

**Università degli Studi di Padova**
Centro Ricerche Fusione (**CRF**)

**Universidade de Lisboa**
Instituto Superior Técnico **(IST)**

**Università degli Studi di Napoli Federico II**

**JOINT RESEARCH DOCTORATE IN FUSION SCIENCE AND ENGINEERING**
Cycle XXXI

# Phenomenology of plasma-wall interaction using liquid metals in tokamak devices

**Coordinator**: Prof. Paolo Bettini

**Supervisor: Dr. Giuseppe Mazzitelli**

**Co-Supervisor: Dr. Flavio Crisanti**

**Ph.D. Student**: Matteo Iafrati

Padova, 29/09/2018




**JOINT Doctorate and NETWORK in Fusion Science and Engineering.**

**Network Partners:**

- Instituto Superior Técnico (IST) Lisboa, Portugal
- Universitá degli studi di Padova, Italy
- Ludwig Maximilians University Munich, Germany

**In collaboration with:**

Consorzio RFX, Italy
IPP Garching, Germany

Università degli Studi di Padova

Dipartimento Centro Ricerche Fusione

*Ph.D. Thesis* Joint Doctorate in Fusion Science and Engineering

# Phenomenology of plasma-wall interaction using liquid metals in tokamak devices

*Supervisor*
Dott. Giuseppe Mazzitelli
ENEA - Head of Fusion Technology Division

*Co-supervisor*
Dott. Flavio Crisanti
ENEA - Università degli studi di Padova

*Ph.D. Candidate*
Matteo Iafrati

”Entrei numa livraria. Pus-me a contar os livros que há para ler e os anos que terei de vida. Não chegam! Não duro nem para metade da livraria! Deve haver certamente outras maneiras de uma pessoa se salvar, senão... estou perdido.”

José de Almada-Negreiros, A Invenção do Dia Claro

Sulle vigne, di notte, ci sono anche stelle. E’ un dio notturno che ti aspetta. Non temere

Cesare Pavese, Dialoghi con Leucò

# Abstract

The goal of the present thesis is to present the theoretical and experimental results concerning the use of liquid metal in tokamak devices. Most of the experimental work has been performed on FTU at the ENEA laboratories in Frascati. The main part of the work has consisted of analyzing the evolution of thermal loads, plasma contamination and plasma edge parameters variations determined by the exposure of liquid metal limiters. A radiative model is proposed to explain the vapor shield effect observed during the past experimental campaigns with the Liquid Lithium Limiter: the results of the simulations and the comparisons made with the experimental data are illustrated. Much time has been spent in the installation, debugging and exploration of two different limiters on FTU: the Cooled Lithium Limiter and the Liquid Tin Limiter. FTU was the first, and up to now unique, tokamak in the world operating with a liquid tin limiter. The results, supported by experimental data and simulations, are reported and discussed. Moreover, a comparison between lithium and tin experiments on FTU is presented. Part of the Ph.D. work has been dedicated to the study and the interpretation of the diagnostics deputy to the main plasma edge parameters measurements. Different Langmuir probes were designed and built for experiments in FTU and other devices too. The old FTU Langmuir probes acquisition system has been successfully moved to a new hardware, and a new software is now performing the data reconstruction. Another part of the work has concerned the implementation *ex novo* of a dedicated laboratory in Frascati focused on the liquid metal features studies, such as wettability, corrosion, and chemical-physical characteristics investigation of the fusion relevant liquid metals (lithium, gallium, and tin). A high vacuum oven was installed for this purpose, and the first test phase ended successfully. Furthermore, a small vacuum chamber was assembled allowing temperature up to 1500°C in a limited volume. This made it possible to increase the testing rate and ultimately to achieve the wetting of small-size tungsten CPS structures with both gallium and tin. In the present work an innovative tungsten coating processes, to avoid corrosion of the structural materials has been investigated. The studies conducted together with the University "La Sapienza" and the ENEA Brasimone research center led to the validation and the realization of a solid and reliable tungsten deposit using the detonation gun machine. During the final period of the Ph.D., liquid tin samples analyses have been carried out after the plasma exposure on ISTTOK tokamak in Lisbon. The results obtained in the heat load calculation and tin effects on plasma are presented, together with a new proposal for the use of CPS-base samples. Finally, a work undertaken in collaboration with the INFN of Frascati and the CERN laboratory in Geneva is reported, regarding the possibility of using liquid lithium as a target for a particle accelerator for muon production.

# Sommario

Nel lavoro di tesi vengono presentati i risultati degli studi e degli esperimenti sull'utilizzo di metallo liquido in macchine tipo tokamak. La maggior parte del lavoro sperimentale è stato svolto su FTU presso i laboratori ENEA di Frascati. L'evoluzione dei carichi termici, un'analisi della contaminazione del plasma dalle impurezze prodotte dai metalli liquidi ed uno studio delle tipiche variazione dei parametri di bordo sono al centro dell'elaborato. Due diversi limiter sono stati installati sul tokamak FTU: il Cooled Lithium Limitered ed il Liquid Tin Limiter. FTU è stato il primo tokamak al mondo, e fin'ora unico, ad operare con un limiter di stagno liquido. I risultati riportati e discussi nella tesi, sono corroborati da dati sperimentali e confrontati con codici di simulazione. Al lettore viene presentata una comparazione nell'utilizzo dei due diversi elementi in un tokamak. Un modello radiativo è stato proposto per spiegare le oscillazioni di temperatura misurate durante gli esperimenti. Una parte del lavoro di dottorato si è soffermata sullo studio delle tipiche diagnostiche devote alla misura dei parametri di bordo: diverse sonde di Langmuir sono state disegnate e realizzate per gli esperimenti in FTU ed in altri dispositivi. Nell'elaborato si riporta il contributo alla realizzazione di un laboratorio dedicato allo studio sul metallo liquido. La finalità è quella di poter meglio comprendere e studiare le proprietà dei metalli di interesse fusionistico, quali litio, gallio e stagno, in termini di bagnabilità, corrosione e caratteristiche chimico-fisiche. Un forno da alto vuoto è stato realizzato per permettere questi studi e la prima fase di test si è conclusa con successo. Per velocizzare e semplificare la procedura bagnamento delle spugne di tungsteno è stata utilizzata una piccola camera da vuoto in grado di arrivare a 1500°C circa. Il bagnamento di strutture CPS è stato ottenuto sia con il gallio che con lo stagno liquido, ed i parametri più importanti del processo sono stati identificati. Nell'elaborato si propone una possibile soluzione al problema della corrosione da parte dello stagno. Infatti, è stato studiato un rivestimento di tungsteno per i materiali di supporto che saranno a contatto con i metalli liquidi al fine di prevenirne la corrosione. Lo studio condotto insieme all'università "La Sapienza" ed al centro ENEA di Brasimone, ha portato alla realizzazione di un robusto, denso e coeso rivestimento di tungsteno mediante la tecnica conosciuta come Detonation Gun. Attualmente è in corso la richesta per un brevetto di processo. La ritenzione di deuterio è stata misurata su vari campioni di stagno liquido esposti al plasma di GyM. Nel trattato si sottolinea l'importanza di queste misure nella necessità di estrapolare dei dati utili ai fini progettuali di un divertore di metallo liquido per un futuro reattore. Negli ultimi mesi del dottorato è stato svolto un lavoro sul tokamak ISTTOK di Lisbona, nella tesi si riportano i risultati ottenuti dall'analisi dei carichi termici sul campione di stagno esposto, proponendo ulteriori sviluppi per gli esperimenti futuri. Per finire, si riassume un lavoro sviluppato in collaborazione con l'INFN di Frascati ed il CERN di Ginevra, riguardo la possibilità di utilizzare

litio liquido come targhetta per un acceleratore di particelle. Il progetto di un acceleratore a muoni è limitato al momento dalle modalità di produzione degli stessi. I materiali convenzionali si sono dimostrati incapaci di sopportare densità di potenza come quelle necessarie per il progetto LEMMA. La proposta del target liquido è argomentata e sviluppata nell'elaborato, un lavoro preliminare di R & D è proposto.

# Resumo

Nesta tese são apresentados os resultados teóricos e experimentais relativos ao uso de metais líquidos num reactor de fusão nuclear tokamak. A grande maioria do trabalho experimental foi realizado no FTU, um tokamak que se encontra instalado nos laboratórios do ENEA em Frascati, Itália. A principal parte do trabalho diz respeito ao estudo da evolução das cargas térmicas, da análise da contaminação do plasma a partir das impurezas produzidas e ao estudo da variação típica dos parâmetros de borda de plasma. Uma das tarefas para a qual vários meses foram dedicados foi a da instalação de dois limitadores diferentes no FTU: o Limitador de Lítio Refrigerado (em inglês Cooled Lithium Limiter) e o Limitador de Estanho Líquido (em inglês Liquid Tin Limiter). O FTU foi o primeiro tokamak do mundo a operar com um limitador de estanho líquido. Os resultados da utilização destes limitadores são positivos, algo que é suportado pelas observações experimentais e simulações. Ambos são relatados e discutidos neste documento. Além disso é apresentada na tese uma comparação entre a utilização de lítio e estanho no FTU. Também é proposto um modelo radiativo o para explicar o efeito do vapor shielding observado durante as campanhas experimentais anteriores com o Limitador de Lítio Líquido. Outra parte do trabalho realizado foi dedicado ao estudo dos diagnósticos típicos para a caracterização dos principais parâmetros de borda do plasma: diferentes sondas de Langmuir foram projetadas e construídas para experiências no FTU e outros dispositivos também. O antigo sistema de aquisição de dados para as sondas Langmuir do FTU foi movido com sucesso para um novo hardware. Alem disso foi também criado um novo software dedicado à reconstrução destes dados. No decorrer deste trabalho revelou-se necessário criar um laboratório em Frascati dedicado ao estudo de características de metal líquido. O principal objetivo desse laboratório é a investigação de metais líquidos relevantes para aplicações em fusão nuclear (lítio, gálio, estanho) em termos de molhabilidade, corrosão e características físicas. Um forno de alto vácuo foi desenhado para essa finalidade. Este foi instalado e a sua operação foi testada com sucesso. Além disso, uma pequena câmara de vácuo foi construida onde uma resistência refratária permite atingir temperaturas até os 1500ºC num volume limitado. Esta montagem experimental possibilitou aumentar a frenquencia com que realizam testes podendo estes depois serem aplicados em maior escala no forno. Foi com este aparato que se conseguiu molhar com estanho e gálio um conjunto de pequenas estruturas de CPS fabricadas a partir de tungstênio. É também proposta uma possível solução para o problema da corrosão de estanho. Investigou-se o revestimento de tungstênio dos materiais estruturais em contato com o metal líquido para evitar a corrosão. Os estudos realizados em conjunto com a Universidade "La Sapienza" e o centro de pesquisa ENEA Brasimone levaram à validação e realização de um depósito de tungstênio sólido e confiável. Durante o período final do doutoramento foi realizada uma análise das amostras líquidas de estanho irradiadas

no tokamak ISTTOK sediado no IPFN em Lisboa, Portugal. A tese mostra os resultados obtidos no cálculo da carga térmica e efeitos de estanho no plasma. A contaminação do plasma foi considerada insignificante. As linhas espectrais de Sn II foram identificadas e utilizadas como indicador para a presença de estanho e investigação do impacto do seu ingresso no plasma. Foram também propostas possíveis melhorias para o atual aparato de exposição de amostras. Estas incluem a polarização das amostras de estanho e a possibilidade de usar uma estrutura CPS. A polarização directa ou inversa das amostras pode ter acesso, respectivamente, a dois mecanimsos de produção de impurezas diferentes, nomeadamente a sputtering ou a evaporação. Os detalhes desta melhoria são discutidos em conjunto com a possibilidade de usar amostras de base CPS. Finalmente, é relatado um trabalho desenvolvido em colaboração com o INFN de Frascati e o laboratório do CERN em Genebra. Neste trabalho explora-se a possibilidade de usar lítio líquido como um alvo para um acelerador de partículas. A projecção de um acelerador de muões é limitada na actualidade devido à dificuldade de produção dos muões. Os materiais convencionais são incapazes de suportar densidades de energia elevadas tais como as necessárias para o projeto LEMMA. A proposta do alvo líquido é discutida no presente documento bem como os resultados preliminares de investigação e desenvolvimento dos planos para um futuro protótipo.

# Contents

# Listing of figures

# Listing of tables

*It is important to do everything with passion, it embellishes life enormously.*

Lev Landau

# 1 Introduction

The energy demand is increasing fast around the world, the developing countries are pushing, with rapid urbanisation, and a new solution for large-scale electricity generation will be required in a short time. Reduction of greenhouse emission, and in particular zero or low $CO_2$ emission sources are strongly needed and thus new energy sources must be developed. Nuclear fusion represents an appealing solution and it should be available as a future energy option by the middle of this century. Nuclear fusion, together with renewable sources, should be able to play a major role in providing a sustainable, secure and safe solution to tackle European and global energy needs.

Inside the stars, fusion reactions take place at high temperatures under the huge gravitational pressures. To make it working on the earth the fuel, in plasma phase, needs to be confined and heated to extremely high temperatures, roughly twenty times more than in the sun core. The easiest way to achieve nuclear fusion in laboratory is the reaction between two hydrogen isotopes: deuterium, extracted from water, and tritium, produced in the reactor itself through the reaction with lithium. When deuterium and tritium nuclei fuse, they form high energetic particle i.e. a helium nucleus and a neutron, as it is shown in figure 1.1.

Nuclear fusion processes are favourable, in term of energy release, up to $^{56}Fe$. It is a promising alternative to the actual carbon-based energy scenario and a worldwide research community is focused on the possibility to make it working for civil energy production. The goal of the actual strategy is to demonstrate [1] the capability to built a power plant in the GigaWatt class. The main advantages would be the very high efficiency in fuel consumption,

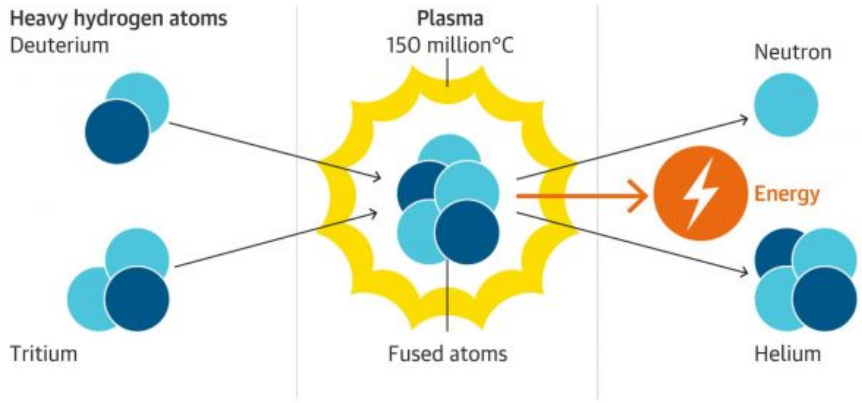


**Figure 1.1:** Two atoms, deuterium and tritium, fuse together, forming a helium nucleus and a neutron.

large fuel availability and its intrinsic green environment impact. The radiative risks are negligible with respect to the conventional fission power plants that nowadays are the only operating nuclear process providing energy to the grid.

## 1.1 Nuclear Fusion

### 1.1.1 Fusion reaction

The class of esoenergetic processes can be sort in two large categories: chemical and nuclear. The chemical reactions are largely diffused in our daily life and we are used to taking advantage of them i.e. energy production, mobility, heating, etc. We characterize the chemical processes as those involving the electrons transitions, whereas nuclear processes are identified as all the reactions implying the nuclei reorganization.

Nuclear fusion and nuclear fission are the processes by which the nucleus of an atom rearrange its protons, moving into a different type of atom; both that processes release energy. The energy is released from the nucleus if the total *Nuclear Binding Energies* is increased.

Nuclear fusion process involves two light nuclei turning into one heavier nucleus. This interaction is driven by the *strong nuclear force*. It is one of the four known fundamental interactions, others being electromagnetism, weak nuclear interaction, and gravitation. This force has a very short action radius i.e. in the order of few *femtometer*, but in such space, it is extremely intense: more than two orders of magnitude greater than the electromagnetic force at the same distance per charge unit. It follows that, if two nuclei have sufficient kinetic energy,

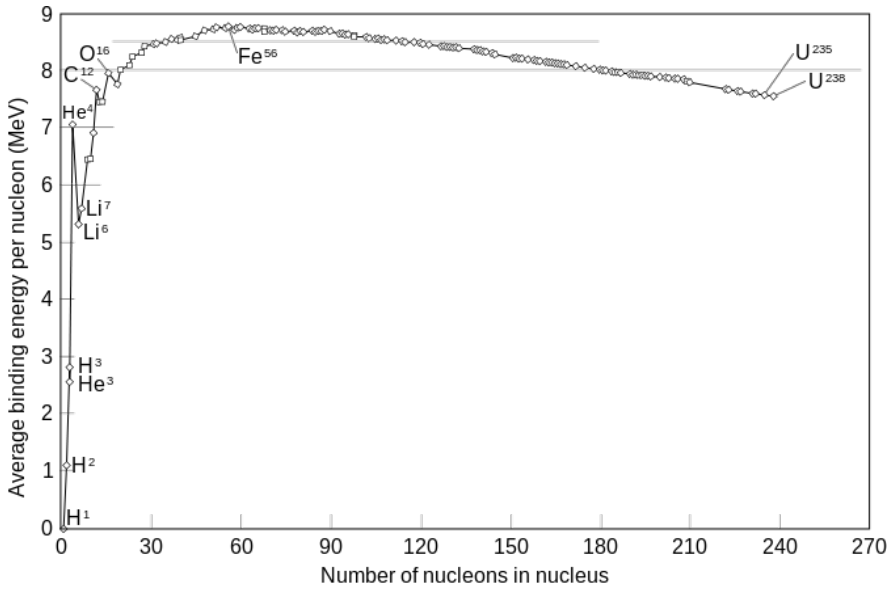


**Figure 1.2:** Average binding energy per nucleon.

they come close enough that the strong nuclear force will prevail on the electromagnetic repulsion, then they fuse together. Usually, the resulting nucleus is unstable and tries to reach stability in different ways:

- nucleus configuration modification, leading to electromagnetic energy emission, i.e. $\gamma$ ray
- subatomic particles ejection, i.e. $\alpha$ or $\beta$ particle
- fragmentation in several smaller elements

Considering the binding energy trend, as shown in fig. 1.2, it clear that fusion is energetically continent for elements lighter than $^{56}Fe$ while fission occurs for heavier elements. We can consider the nuclear energy as the fraction of the binding potential energy realised during the process, usually going in kinetic energy, in the order of a fraction of $MeV$ [*] from the plot 1.2. The typical molecular bound energy is in the order of $1 \div 10eV$ , so the ratio of the released energy between chemical and nuclear reaction is in the scale of $10^4 \div 10^6$ . From the special relativity theory, we can explain the surplus released energy as the mass deficit between the initial and the final products according to $E = mc^2$.

[*] $1eV = 1.6 \cdot 10^{-19} J$

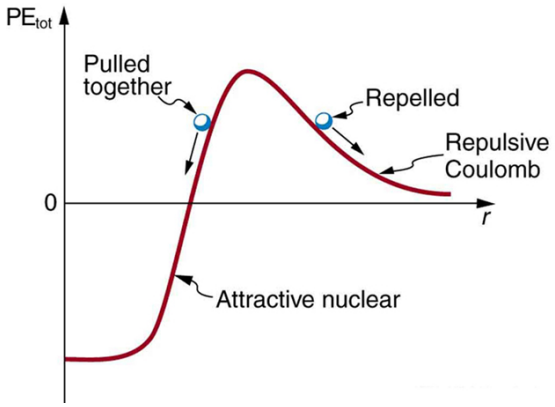


**Figure 1.3:** Schematic rappresentation of the Coulomb barrier.

Fusion process requires a considerable amount of work performed by an external force: the electrostatic repulsion must be overcome before the strong nuclear force can couple the nucleons. We can consider the two body interaction between a first target nucleus $n_1$, and a second one $n_2$ approaching. A force, rise by the interaction of two nuclei with the same charge sign, repels the particle. Due to this coulombian force $F_c$, external work is needed to bring near the two nuclei enough to let fusion happen. The required work increase as $1/r$, where $r$ is the inter-nuclei distance. If $r_f$ is the typical distance where the strong nuclear force overcome the electrostatic repulsion, it is possible to quantify the needed work as

$$U = \frac{e^2 Z_1 Z_2}{4\pi\epsilon_0 r_f} \tag{1.1}$$

We can suppose only the approaching nuclei with a kinetic energy $K$ above $U$ are able to cross the Coulomb barrier. The average energy required to overcome the repulsive barrier between the nuclei in the order of magnitude of the $MeV$ ($Z_1 = Z_2 = 1$ and $r_f = 1\ fm$, have been considered). It means a value in, in terms of plasma temperature [†] the order of $10^9 \div 10^{10}\ K$. In the figure 1.3 the potential trend is shown as a function of the internuclear distance.

The above value is much higher than that actually needed: in the previous estimation, we neglected the quantum tunnel effect [2]. Thanks to it, particles having a kinetic energy lower than that required according to classical physics have nevertheless a finite probability to cross the potential barrier. The overall effect, with the density values achievable on earth, is that the minimum temperature for a reasonable number of fusion reactions is around $10 \div 100\ keV$,

[†] $1eV = 11604K$

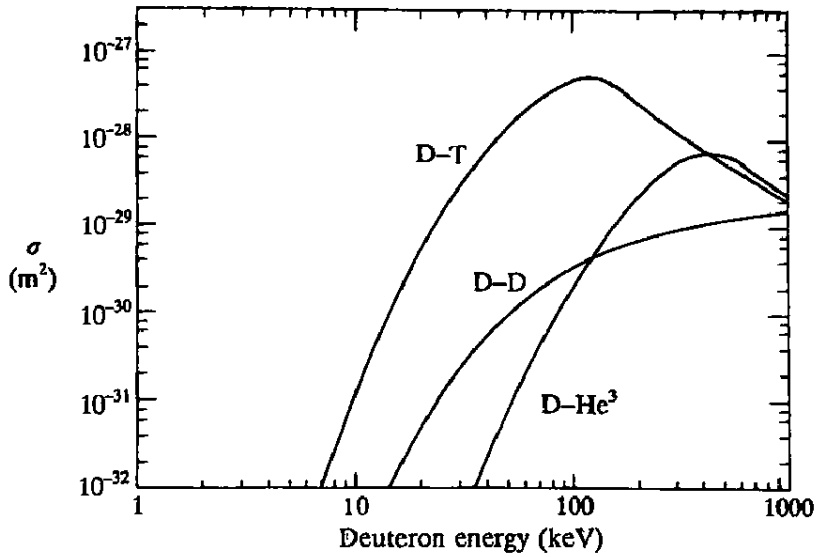


**Figure 1.4:** Cross section for different fusion reaction [3].

depending on the type of reaction.

In figure 1.4 the experimental cross sections for several types of reaction versus the deuterium energy is shown. To estimate the reaction rate in a D-T plasma an integration over the distribution functions $(f_1, f_2)$ of both species is required [3]. The reaction rate per unit volume between particles of two different species with velocities $v_1$ and $v_2$ is given by

$$\mathscr{R} = \Sigma(v_1 - v_2)\,(v_1 - v_2)\,f_1(v_1)\,f_2(v_2) \tag{1.2}$$

assuming the maxwellian distribution for the velocities

$$f_j(v_j) = n_j \left(\frac{m_j}{2\pi T}\right)^{3/2} e^{-\frac{m_j v_j^2}{2T}} \tag{1.3}$$

defining $v' = v_1 - v_2$, then the total reaction rate per unit of volume

$$\mathscr{R} = \int\int \sigma(v')\,v'\,f_1(v_1)\,f_2(v_2)\,d^3v_1 d^3v_2 \tag{1.4}$$

it can be written as

$$\mathscr{R} = 4\pi n_1 n_2 \left(\frac{\mu}{2\pi T}\right)^{3/2} \int \sigma(v') v'^3 e^{\left(-\frac{\mu v'^2}{2T}\right)} dv' \tag{1.5}$$

or how

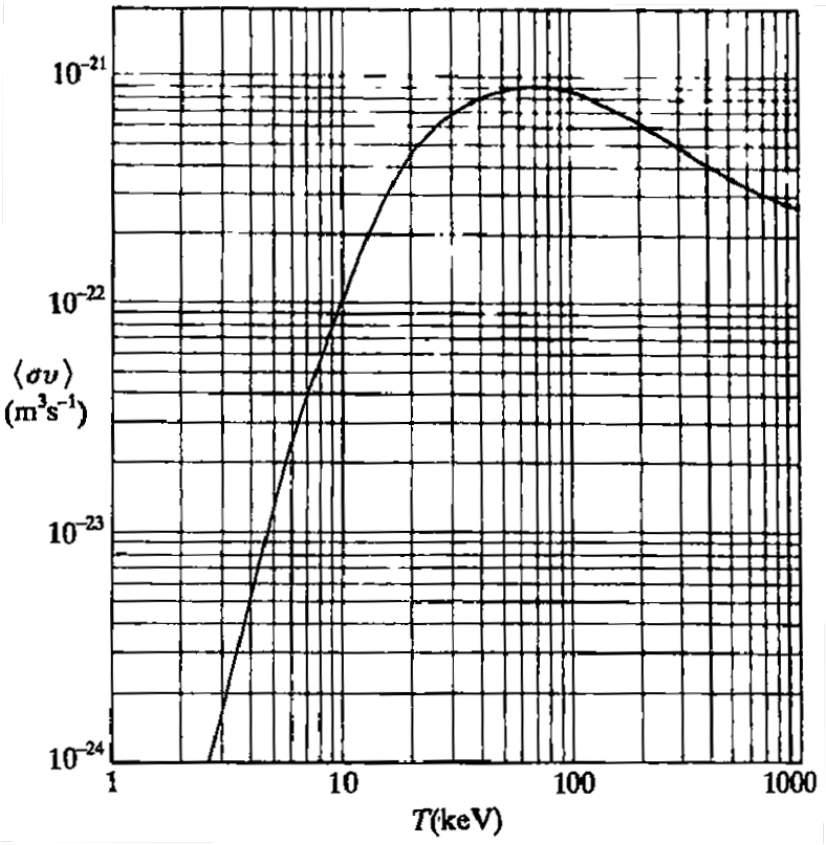


**Figure 1.5:** Product $< \sigma v >$ for DT reaction [3].

$$\mathscr{R} = \sqrt{\frac{8}{\pi}} n_1 n_2 \left(\frac{\mu}{T}\right)^{3/2} \frac{1}{m_1^2} \int \sigma(\varepsilon) \varepsilon e^{\left(-\frac{\mu\varepsilon}{m_1 T}\right)} d\varepsilon \tag{1.6}$$

expressing the cross section in terms of energy of the particles $\varepsilon = \frac{1}{2} m v'^2$. Being interested in estimating $\mathscr{R}$ for DT species we are going to rewrite the equation 1.5 as $\mathscr{R} = n_d n_t < \sigma v >$, which has a maximum for $n_d = n_t$. Figure 1.5 shows the average product $< \sigma v >$ for the D-T reaction as a function of temperature.

Looking to a future fusion plant tritium is a radioactive hydrogen isotope 12.5 years lifetime, so it's not available in nature. Actually, it is produced in fission light-water reactors, but in future, it will be produced in the reactor itself by the nuclear interaction between the neutrons coming from the fusion processes and lithium atoms contained in the blanket modules.

### 1.1.2 Energy balance

In the fusion relevant temperature range (hundreds of millions of Kelvin degrees), all the elements of the periodic table are ionized (the ionization level mainly depends on several factors, among which atomic number and temperature); the fuel inside the reactor is therefore in the plasma state. Once the required condition for fusion reaction is satisfied, the fusion process will provide heat [3]. Assuming a thermodynamic behaviour similar to that of an ideal neutral gas for the nuclear fuel, we can try to quantify the minimum average temperature required for the onset of the thermonuclear reaction:

$$\bar{K} = \frac{3}{2}kT \geq U \tag{1.7}$$

In order to sustain the process, the balance between the heating power and the losses towards the environment must be positive. Supposing a steady state equilibrium in which the temperature remains constant, in order to have a self-sustaining reaction the energy flows must be in equilibrium:

$$P_h + P_p = P_l \tag{1.8}$$

The commonly called ignition is achieved when the produced power $P_p$ and the lost power $P_l$ are equal, i.e. the additional heating power $P_h$ can go null. Defining $Q = \frac{P_p}{P_h}$ we see the ignition corresponds to an energy gain that tends to infinity. We can now write again $Q = \frac{P_l}{P_h} - 1$ and deduce that for a reactor it must satisfied the ratio $\frac{P_l}{P_h} > 2$. In order to develop ignition criteria based on thermodynamic plasma parameters, it is necessary to establish the link between the main plasma parameters and the generated or lost power.

The power produced by nuclear reactions per unit volume in a D-T plasma is

$$P_{Tn} = n_d n_t < \sigma v > \mathscr{E} \tag{1.9}$$

where $\mathscr{E}$ is the unitary released energy. In terms of total density $n = n_d + n_t$ it becomes

$$P_{Tn} = n_d(n - n_d) < \sigma v > \mathscr{E} \tag{1.10}$$

Now by relating the densities of the two species and deriving from one of these we get

$$\frac{\partial}{\partial n_d}(n_d n_t) = \frac{\partial}{\partial n_d}[(n - n_d)n_d] = 0 \Rightarrow n_d = \frac{n}{2} \tag{1.11}$$

so the released power is maximized for $n_d = \frac{n}{2}$. In such optimal mixture the power density is:

$$P_{Tn} = \frac{1}{4} n^2 < \sigma v > \mathscr{E} \tag{1.12}$$

Despite the confinement system, the high temperature plasma continuously loss energy to the external environment. Neglecting the mechanisms responsible for the energy losses, we can quantify the total plasma dissipated power by taking the ratio between the total energy $W$ and the average time it takes to get out of the system.

Starting from the equipartition energy theorem, at a given temperature $T$ each particle contributes with a term $\frac{1}{2}kT$ for each degree of freedom and considering the equal number of ions and electrons $W = \int 3nkTd^3x = 3\overline{nT}kV$. The plasma energy is mainly stored in the form of kinetic energy due to the global thermal agitation. Then defined the energy confinement time $\tau_e$, being an intrinsic system parameter, the level of losses is given by

$$P_l = \frac{W}{\tau_e} \tag{1.13}$$

In experimental plasma devices, the energy losses are balanced by additional heating systems $P_h = P_l$ at the steady state. From equation 1.13 it easily follows

$$\tau_e = \frac{W}{P_h} \tag{1.14}$$

allowing the experimental evaluation of the energy confinement time starting from known quantities.

The expression 1.12 of the power generated by the D-T fusion reaction is split into two parts by kinematic consideration. About $4/5$ of the energy are taken away from the neutron, while the residual $\mathscr{E}_\alpha$, is carried away by $\alpha$ particles. The neutron leaves the plasma without any interaction while the $\alpha$ particles interacts with the surrounding transferring the $3.5\ MeV$ energy to the background plasma by collisions.

The $\alpha$ power density per volume unit is

$$p_\alpha = \frac{1}{4} n^2 < \sigma v > \mathscr{E}_\alpha \tag{1.15}$$

which integrated on the volume becomes

$$P_\alpha = \int p_\alpha d^3x = \frac{1}{4}\overline{n^2 < \sigma v >}\mathscr{E}_\alpha V \tag{1.16}$$

Now we have all the terms it is possible to rewrite the energy balance equation as

$$P_h + P_\alpha = P_s \tag{1.17}$$

and using the equations 1.12, 1.13, 1.16, it becomes

$$P_h + \frac{1}{4}\overline{n^2 < \sigma v >}\mathscr{E}_\alpha V = \frac{3\overline{nT}kV}{\tau_e} \tag{1.18}$$

Given a confined thermonuclear plasma, we want to find when the $\alpha$heating is sufficient to compensate the energy losses and the plasma is able to self-sustain. Keeping constant, for simplicity, density and temperature in the equation 1.18 the energy balance can be rewritten

$$P_h = \left(\frac{3nTk}{\tau_e} - \frac{1}{4}n^2 < \sigma v > \mathscr{E}_\alpha\right) V \tag{1.19}$$

which imposes constraints on the quantity between parentheses in order to reach the plasma self-sustain condition:

$$n\tau_e > \frac{12}{< \sigma v >}\frac{T}{\mathscr{E}_\alpha} \tag{1.20}$$

the right-hand side of the above inequality depends on the temperature and for a D-T mixture has a minimum for $T \sim 30keV$ that corresponds to a numerical value of $n\tau_e > 1.5 \cdot 10^{20} m^{-3} s$. Figure 1.6 shows the $n\tau_e$ product versus temperature. The minimum of the curve is realized for temperatures in the order of tens of keV: it represents the favourable parameters space for the thermonuclear plasma ignition.

Using, close to the minimum, a parabolic $\tau_e$ dependence versus temperature the *triple product* results:

$$\hat{n}\hat{T}\tau_e > 5 \cdot 10^{21} m^{-3}\, keV\, s \tag{1.21}$$

The equation 1.20 also known as the Lawson [4] criterion, citing the author:

> *"Being an engineer I wondered what different parameter ranges there could be for a practical device. People were describing all sorts of things such as colliding beams which have come back in a different form in inertial confinement fusion now, but what I did was to put some parameters on a sheet of paper and then worked out a whole lot of actual numbers that would make sense in that they lay within a practical range."*

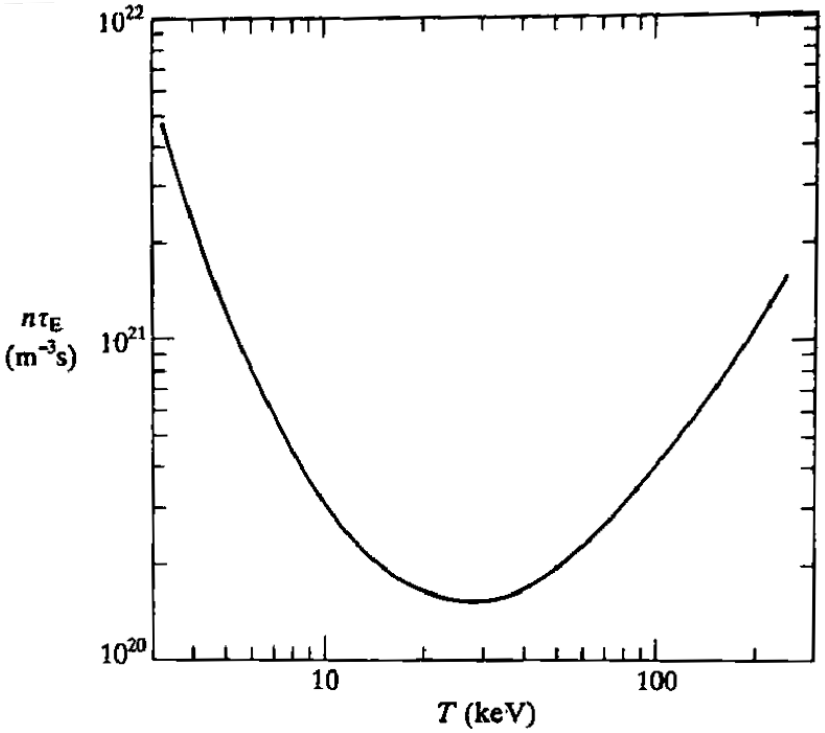


**Figure 1.6:** Rappresentation of the triple product, $n \cdot \tau_E$ is plotted versus $T_e$.

| | Density $[m^{-3}]$ | Temperature $[eV]$ | Typical length $[m]$ | Debye length $[m]$ | Plasma frequency $[Hz]$ |
|---|---|---|---|---|---|
| Interstellar gas | $10^6$ | $0.01$ | $10^{19}$ | $0.7$ | $10^4$ |
| Solar wind | $10^7$ | $10$ | $10^{11}$ | $7$ | $3 \cdot 10^4$ |
| Sun's corona | $10^{12}$ | $10^2$ | $10^7$ | $0.07$ | $10^7$ |
| Sun's core | $10^{32}$ | $10^3$ | $7 \cdot 10^8$ | $2 \cdot 10^{-11}$ | $10^{17}$ |
| Thermonuclear plasma | $10^{20}$ | $10^4$ | $10$ | $7 \cdot 10^{-5}$ | $10^{11}$ |
| Arc discharge | $10^{20}$ | $1$ | $0.1$ | $7 \cdot 10^{-7}$ | $10^{11}$ |
| Thunder | $10^{24}$ | $2$ | $10^3$ | $10^{-8}$ | $10^{12}$ |
| Ionosphere | $10^{12}$ | $0.1$ | $10^4$ | $2 \cdot 10^{-3}$ | $10^7$ |

**Table 1.1:** Main parameters for different types of plasmas.

## 1.2 Introduction to plasma physic

### 1.2.1 The plasma

From a thermodynamics point of view, the succession of matter states from solid to gaseous phase is related with the increase in the average energy per particle of the system. In this perspective, the plasma, also called the fourth stage of matter, takes place above - energetically speaking - to the gas state. The essential condition, if we are talking about plasma, is at least a fraction of the system is in the ionised state.

In the table 1.1 the main parameters for different types of plasmas are summarized.

It is possible to estimate the ionization grade for a given gas starting from the ratio between the two different energy configurations.

Comparing an atom in normal condition with an ionized one, that is the ion-electron pair. Starting from the Boltzmann equation [3], we can write the relation $\frac{\#\ ionized}{\#\ fundamental\ state}$:

$$\frac{n_i}{n_o} = \frac{g_i}{g_o} e^{(\frac{-\chi + \frac{1}{2}mv^2}{kT})} \tag{1.22}$$

where $\chi$ is the ionization potential. The statistical weight of the ionized state is given by

$$g_i = g_{ion} g_{electron} \tag{1.23}$$

where

$$g_{electron} = 2\frac{d^3\overrightarrow{x}\, d^3\overrightarrow{v}}{h^3} \tag{1.24}$$

Given the momentum $p$, and taking an electron with any velocity $\overrightarrow{v}$, the volume $1/n_e$ as its space

$$\frac{dn_i}{n_o} = \frac{g_{ion}}{g_o}\frac{2}{n_e}\frac{4\pi p^2 dp}{h^3}e^{(\frac{-\chi+1/2mv^2}{kT})} \tag{1.25}$$

under isotropic assumption and integrating over speed,

$$\frac{n_i}{n_o} = \frac{g_{ion}}{g_o}2\frac{4\pi m^3}{n_e h^3}e^{(\frac{-\chi}{kT})}\int_0^\infty e^{(\frac{mv^2}{2kT})}v^2 dv \tag{1.26}$$

it is obtained. Now taking $u = \frac{mv^2}{2kT}$ and then $du = \frac{mv}{kT}\, dv$ follows

$$\sqrt{2}(\frac{kT}{m})^{3/2}\int_0^\infty u^{1/2}e^{-udu} = \sqrt{2}(\frac{kT}{m})^{3/2}\Gamma(\frac{3}{2}) = \sqrt{2}(\frac{kT}{m})^{3/2}\frac{1}{2}\Gamma(\frac{1}{2}) = \sqrt{\frac{\pi}{2}}(\frac{kT}{m})^{3/2} \tag{1.27}$$

Then results the Saha equation:

$$\frac{n_i}{n_o} = \frac{g_{ion}}{g_o}\frac{2}{h^3}\frac{(2\pi mkT)^{3/2}}{n_e}e^{(-\chi/kT)} \tag{1.28}$$

From the equation 1.28, it can be noted that the system ionization state depends inversely from the electron density $n_e$, increases as $T^{3/2}$ and it decays very steeply (exponentially) as the energy of the ionization potential increases.

### Debye length

Considering a hydrogen plasma, with $n_i = n_e$; it is globally quasi-neutral, in the sense that averaging over a sufficiently large volume, the electrical charge of the system results null. Quasi-neutrality and collective behaviour are the basic assumption defining a plasma. These are kind of typical assumptions studying ionized gases [5].

Ideally, we can insert a positive test charge into an unperturbed plasma. This particle will tend to attract electrons to itself and to move away from the ions. Given the relationship between the masses, the electrons will accelerate faster than the ions, so for simplicity, we will consider the latter frozen.

The plasma is now described [6] by:

- the spherical electrostatic potential generated by the test charge $\phi(r)$;
- the ion density $n_o$, it will be assumed constant;
- the electrons density, at the first order $n_e(r) = n_o + n_1(r)$;
- the electron distribution function modified by the presence of the electrostatic potential: the Boltzmann factor $e^{-E/kT}$ becomes $e^{(-\frac{1/2mv^2 - e\phi}{kT})} = e^{(-\frac{mv^2}{2kT})} e^{(\frac{e\phi}{kT})}$. The electronic density can now be rewrite as $n_e(r) = n_o e^{(\frac{e\phi}{kT})}$ which tends to $n_o$ for $r \to \infty$

For a single ionization plasma -we chose hydrogen- the Gauss's law become

$$\overrightarrow{\nabla} \cdot \overrightarrow{E} = \frac{\rho_q}{\epsilon_o} = \frac{e}{\epsilon_o}(n_i - n_e) \tag{1.29}$$

Writing the Poisson equation:

$$\overrightarrow{\nabla} \cdot \overrightarrow{E} = -\nabla^2\phi = \frac{\rho_q}{\epsilon_o} = \frac{e}{\epsilon_o}(n_i - n_e) + q\delta(r) \tag{1.30}$$

$$-\frac{1}{r^2}\frac{\partial}{\partial r}(r^2\frac{\partial \phi}{\partial r}) = \frac{e}{\epsilon_o} n_o (1 - e^{\frac{e\phi}{kT}} + q\delta(r)) \tag{1.31}$$

considering the electrostatic potential spherical symmetry $\phi(r)$. It is possible to simplify the non-linear differential equation 1.31 obtained for the $\phi(r)$ with the Taylor approximation. We get:

$$-\frac{1}{r^2}\frac{\partial}{\partial r}(r^2\frac{\partial \phi}{\partial r}) = \frac{e}{\epsilon_o} n_o 1 - [1 + \frac{e\phi}{kT} + \frac{1}{2}(\frac{e\phi}{kT})^2 + ...] \tag{1.32}$$

that in the first order turns out to be

$$\frac{1}{r^2}\frac{\partial}{\partial r}(r^2\frac{\partial \phi}{\partial r}) = \frac{e^2 n_0}{\epsilon_0 kT}\phi \tag{1.33}$$

Looking at the physical dimensions of the term $\frac{\epsilon_o kT}{e^2 n_o}$ we note it is a squared length. So it is straightforward define the quantity $\lambda_D = \sqrt{\frac{\epsilon_o kT}{e^2 n_o}}$, the Debye length.

The term with the $\delta$ in equation 1.31 dominates the function in the region close to the test charge, while the correct solution of potential for more distant points of space is given by the equation 1.33.

Therefore, close to the origin, the potential $\Phi$ tends to:

$$\Phi(r \sim 0) = \frac{q}{4\pi\epsilon_0 r} \tag{1.34}$$

The best way to proceed is to recognize the possibility to write the differential operator in the alternative form

$$\frac{1}{r^2}\frac{\partial}{\partial r}(r^2\frac{\partial \phi}{\partial r}) \equiv \frac{1}{r}\frac{\partial^2}{\partial r^2}(r\phi) \tag{1.35}$$

so the differential equation becomes

$$\frac{\partial^2}{\partial r^2}(r\phi) = \frac{r\phi}{\lambda^2} \tag{1.36}$$

with the exponential solution

$$r\phi = Ae^{-\frac{r}{\lambda}} \tag{1.37}$$

so that the potential become

$$\phi(r) = \frac{A}{r}e^{-\frac{r}{\lambda}} \tag{1.38}$$

It is possible to solve for the constant $A$ by imposing the continuity of the solution close to the origin, obtaining as a final solution

$$\Phi(r) = \frac{q}{4\pi\epsilon_0 r}e^{-\frac{r}{\lambda}} \tag{1.39}$$

From the equation 1.39, we can immediately see that the electrostatic charge potential decays exponentially inside plasma much faster decay than in vacuum. So we can define the $\lambda$ in the exponential as the Debye length $\lambda_D$. This quantity has been here introduced because it plays an important role in the edge physics phenomena and in the Langmuir probe theory. So the Debye length $\lambda_D$ is a very powerful tool that gives us immediately the typical electrostatic potential decay in a given type of plasma.

The numerical approximation is:

$$\lambda_D \backsimeq \sqrt{\frac{kT\ in\ eV}{n\ in\ cm^{-3}}}\, 740\, cm \tag{1.40}$$

The Debye length gives a good estimator of the typical scale for which we can expect the

quasi-neutral plasma behaviour. It is easy to observe Debye length decreases as the density $n_e$ increase, as more particles screen the electrostatic potential, and increases with temperature $T_e$ since the greater energy per particles allows them to remain, on average, at a greater distance from the test charge.

The characteristic values of $\lambda_D$ in case of the FTU tokamak, where the above parameters are respectively $\sim 10^{20} m^{-3}$ and $1\ KeV$, is $\lambda_{D_{FTU}} \approx 2.4 \cdot 10^{-3} cm$. The Debye length expected for a reactor, assuming $\sim 1.5 \cdot 10^{20} m^{-3}$ for density and $20\ KeV$ for the temperature, it is $\lambda_{D_{REAC}} \approx 8.6 \cdot 10^{-3} cm$.

A plasma can be considered strongly influenced by the presence of the magnetic field when the Larmor radius is much lower than its typical dimension $L \approx \sqrt[3]{V}$, namely:

$$\frac{\rho_L}{L} \ll 1 \tag{1.41}$$

If the inequality is satisfied, a particle is generally able to complete at least one rotation around the force lines $\vec{B}$ before leaving the plasma volume. In this situation, it is, therefore, possible to apply at least once the helical motion model.

In case of weak magnetization, the particles travel at most on an arc of circumference under the influence of the Lorentz force before exiting the plasma boundaries and being dispersed. Since the motion is no longer bound to a given direction in space, the overall particles behaviour is therefore comparable to that observed in neutral gases, where the effect of collisions and the internal motion has a random and unlikely direction dominates. A second criterion for establishing the magnetization plasma level is based on the ratio between the gyro-frequency $\Omega_k$ and collisions frequency $f_k$. According to this criterion, the plasma is strongly magnetized if:

$$\frac{\Omega_k}{2\pi f_k} \gg 1 \tag{1.42}$$

that is when each particle is on average able to travel several Larmor orbits before suffering collisions. If the 1.42 is verified, the particle maintains a helical path for a significant time during the interval between two impacts: the general direction of motion remains therefore strongly constrained to the field direction.

Every collision changes instantaneously and randomly $\vec{v}$: typically it displaces the particle in Larmor radius space-scale before the Lorentz force traps it again on a new field line. In the case of a strongly collisional plasma, so if the equation 1.42 is not valid, the particles are continually displaced in every direction due to the collisions.

The collisional frequency $v_k$ tends to decrease with the electron temperature and it tends to increase with electron density. It follows the magnetic field effect being more important in "hot" and not very dense plasmas like those of interest in the fusion field.

### 1.2.2 Magnetohydrodynamics (MHD) theory and plasma confinement

#### Magnetohydrodynamics principles

Magnetohydrodynamics, usually called with the acronym MHD, is the name by which the representation of the plasma is identified as a single fluid. The Euler equations and mass conservation for electrons are respectively written

$$\rho_e \left( \partial_t \vec{v}_e + \vec{v}_e \cdot \vec{\nabla} \vec{v}_e \right) = -\vec{\nabla} p - n_e e \left( \vec{E} + \frac{\vec{v}_e}{c} \wedge \vec{B} \right) \tag{1.43}$$

$$\partial_t \rho_e + \vec{\nabla} \cdot (\rho_e \vec{v}_e) = 0 \tag{1.44}$$

and for ions we have

$$\rho_i \left( \partial_t \vec{v}_i + \vec{v}_i \cdot \vec{\nabla} \vec{v}_i \right) = -\vec{\nabla} p - Z n_i e \left( \vec{E} + \frac{\vec{v}_i}{c} \wedge \vec{B} \right) \tag{1.45}$$

$$\partial_t \rho_i + \vec{\nabla} \cdot (\rho_i \vec{v}_i) = 0 \tag{1.46}$$

they are the starting point for the MHD equations. To obtain the magnetohydrodynamical model we can apply some simplifications [6] [7] we can summarize in five main hypotheses:

- transport currents are neglected, ie $\frac{1}{c}\frac{d\vec{E}}{dt} \approx 0$, which is included in Amper's law and $\vec{\nabla} \wedge \vec{B} = \frac{4\pi}{c}\vec{J} + \underbrace{\frac{1}{c}\frac{d\vec{E}}{dt}}_{0} \Rightarrow \vec{\nabla} \cdot \left( \vec{\nabla} \wedge \vec{B} \right) = 0 = \frac{4\pi}{c}\vec{\nabla} \cdot \vec{J}$ and taking advantage of the properties of the rotor operator gives us a new report on the divergence of the current. This approximation is correct to the extent that the speed of Alfven is much lower than that of light
- the electrons inertia, $m_e \approx 0$, is neglected. This consideration turns out that the electronic motion is so fast that the reorganization is instantaneous and the forces are always balanced; furthermore this also implies that along the magnetic field lines the electron velocity coincides with its thermal velocity. The Euler equation becomes $0 = -\vec{\nabla} p - n_e e \left( \vec{E} + \frac{\vec{v}_e}{c} \wedge \vec{B} \right)$

- Ionic and electronic velocity are similar, that is $|\vec{v}_e - \vec{v}_i| \ll |\vec{v}_{e,i}|$, then the error that will be committed by writing the velocity term in the equations without indicating the species will be small

- for both species (ions and electrons) the pressure gradient is negligible compared to the Lorentz force. The first MHD equation derives from this hypothesis, since it ignores the pressure gradient from the Euler equation for the electrons $0 = \vec{\nabla} p = -n_e e \left( \vec{E} + \frac{\vec{v}_e}{c} \wedge \vec{B} \right)$, we get directly $\vec{E} + \frac{\vec{v}_e}{c} \wedge \vec{B} = 0$;

- finally we assume quasi-neutrality, i.e. $Z n_i \approx n_e$, which puts a constraint on the current $\vec{J} = Z e n_i \vec{v}_i - e n_e \vec{v}_e = e n_e \left( \vec{v}_i - \vec{v}_e \right)$, then combined with the hypothesis of similar velocity becomes $\left| \vec{J} \right| \ll e n_e \left| \vec{v} \right|$.

After these hypotheses, it is possible to derive the fundamental equations of the theory. We write the Euler's equations for both the species

$$\begin{cases} \rho_i \left( \partial_t \vec{v}_i + \vec{v}_i \cdot \vec{\nabla} \vec{v}_i \right) & = -\vec{\nabla} p - Z n_i e \left( \vec{E} + \frac{\vec{v}_i}{c} \wedge \vec{B} \right) \\ 0 & = -\vec{\nabla} p - n_e e \left( \vec{E} + \frac{\vec{v}_e}{c} \wedge \vec{B} \right) \end{cases} \tag{1.47}$$

and adding them we obtain the magnetohydrodynamics Euler equation

$$\rho \left( \partial_t \vec{v} + \vec{v} \cdot \vec{\nabla} \vec{v} \right) = -\vec{\nabla} p - \frac{1}{c} \vec{J} \wedge \vec{B} \tag{1.48}$$

It is one of the fundamental equations of the theory and we can consider it as a direct consequence of Newton's equations. Another very important relation can be derived from Maxwell's equations.

$$\partial_t \vec{B} = -c \left( \vec{\nabla} \wedge \vec{E} \right) \tag{1.49}$$

It is possible to rewrite the Faraday law 1.49 by inserting the MHD hypothesis

$$\vec{E} = -\frac{\vec{v}_e}{c} \wedge \vec{B} \partial_t \vec{B} = \vec{\nabla} \wedge \left( \vec{v} \wedge \vec{B} \right) \tag{1.50}$$

It is beyond this treatment to derive other equations of the theory for which we refer to specific texts. However, those presented above are sufficient to note the intrinsic difficulties due to the non-linear dependence of the system both on the velocity field and on the magnetic field. Furthermore, the ideal magnetohydrodynamical model presented so far can be improved

by adding non-ideal effects (in analogy with fluids) which were not taken into account. This modeling is called visco-resistive magnetohydrodynamics.

### 1.2.3 Magnetostatics and plasma confinement

In this subsection, we assume a small velocity value, not necessarily null, but negligible $\vec{v} \approx 0$. Neglecting the terms with the velocity the Euler's equation is

$$\vec{\nabla} p = \frac{1}{c} \vec{J} \wedge \vec{B} = -\frac{\vec{\nabla} B^2}{8\pi} + \frac{1}{4} \vec{B} \vec{\nabla} \vec{B} \tag{1.51}$$

Introducing the magnetic stress tensor $\Pi_{il}^M$ it is possible to rewrite the equation 1.51 in vector form as

$$\partial_l p \delta_{il} + \partial_l \Pi_{il}^M = 0 \tag{1.52}$$

or more synthetically

$$\partial_l \tilde{\Pi}_{il} = 0 \tag{1.53}$$

with $\tilde{\Pi}_{il} = p\delta_{il} + \Pi_{il}^M$. Following the procedure presented by Fermi and Chandraseckar in 1953 [8], we are going to show that plasma cannot be confined in the absence of external forces [6]. Remember that $\partial_l x_i = \frac{\partial x_i}{\partial x_l} = \delta_{il}$

$$\partial_l \tilde{\Pi}_{il} = 0 \;\Rightarrow\; \left(\partial_l \tilde{\Pi}_{il}\right) x_i = 0 \;\Rightarrow\; \partial_l \left(\tilde{\Pi}_{il} x_i\right) - \tilde{\Pi}_{il} \partial_l x_i = 0 \tag{1.54}$$

we identify the trace of the matrix that describes the previously defined tensor

$$\partial_l \left(\tilde{\Pi}_{il} x_i\right) = \tilde{\Pi}_{il} \delta_{il} = Tr\left(\tilde{\Pi}_{il}\right) \tag{1.55}$$

Recalling that the magnetic stress tensor is defined by

$$\Pi_{il}^M = \left[\frac{1}{4\pi}\left(\frac{B^2}{2}\delta_{il} - B_i B_l\right)\right] \tag{1.56}$$

the magnetic field dependence of the diagonal product is obtained

$$\Pi_{il}^M \delta_{il} = \frac{1}{4\pi}\left(\frac{B^2}{2} 3 - B^2\right) = \frac{1}{8\pi} B^2 \tag{1.57}$$

it follows that the trace of $Tr\left(\tilde{\Pi}_{il}\right) = 3p + \frac{1}{8\pi}B^2$ is strictly positive. Integrating over the entire volume V, the previously found relation begin

$$\int_V d^3x\, \partial_l \left(\tilde{\Pi}_{il} x_i\right) = \int_V d^3x\, 3p + \frac{1}{8\pi}B^2 \tag{1.58}$$

and applying Gauss's theorem

$$\int_V d^3x\, \partial_l \left(\tilde{\Pi}_{il} x_i\right) = \int_{S=\Gamma(V)} dS_l \left(\tilde{\Pi}_{il} x_i\right) = \int_V d^3x\, 3p + \frac{1}{8\pi}B^2 \tag{1.59}$$

Now the term integrating on the surface goes to zero, as wanting to confine the plasma in a region of space, if I choose a larger volume of that occupied by the plasma itself, the external pressure will be zero and the magnetic field will scale with a typical trend such as the dipole $(1/r^3)$. The second term, following the same logical thread [9], can be decomposed into an integral on the volume occupied by the plasma plus the same integral extended to the external volume

$$\int_V d^3x\, 3p + \frac{1}{8\pi}B^2 = \int_{V_{plasma}} d^3x\, 3p + \frac{1}{8\pi}B^2 \; + \int_{V_{ext}} d^3x\, 3p + \frac{1}{8\pi}B^2 \tag{1.60}$$

and it is clear that the second integral must be null. The assertion is absurd. Indeed it should be

$$\int_{V_{plasma}} d^3x\, 3p + \frac{1}{8\pi}B^2 = 0 \tag{1.61}$$

but this is not possible knowing, from the trace calculation $Tr\left(\tilde{\Pi}_{il}\right)$, that the integral argument is strictly positive. The impossibility of solving this equality means that plasma tends to infinite expansion, or it is confined by external forces. In other words, it is not possible to confine a plasma if you do not pay the energy bill. It is common in practice the adoption of external magnetic fields, generated in rigid and artificial conductors, through which the plasma is confined. An example of this is given in figure 1.7, where two magnetic configurations are shown, namely the zeta pinch and the theta pinch. The names, in these cases, are related to the current direction.

**Figure 1.7:** Z-pinch configuration (on the left) and $\theta$-pinch (on the right).

## 1.3 The Tokamak

There are many devices with different configurations and dimensions designed for plasma confinement, the majority of these have an axil symmetric geometry, among them the most important is certainly the Tokamak.

Tokamak is the acronym of *TOroidal'naha KAmera s MAgnitnymi Katushkami*, translated it means toroidal chamber with magnetic coils. This machine appeared for the first time in Russia during the early 50s, its official presentation to the world took place in the International Conferences on the peaceful use of atomic energy in Geneva. The Tokamak's simplified structure is shown in figure 1.8.

The tokamak configuration is obtained by superposing a toroidal magnetic field, $B_\phi$ , order of T, produced by external windings a poloidal magnetic field, $B_\theta \ll B_\phi$, produced mainly by the plasma current, $I_p$ , order of MA, flowing in the toroidal direction. The next big step in tokamak improvements is called ITER: it will be the first fusion device to test the integrated technologies, materials, and physics regimes necessary, in view of the development of a demonstration reactor, for the commercial production of fusion-based electricity. This target involves effort both on basic physics research and technology R& D.

In tokamak, the ionized gas is contained in a toroidal chamber, confined by the strong magnetic field, but the main magnetic field, the toroidal one, it is not sufficient to guarantee this safekeeping. To achieve the plasma equilibrium a poloidal magnetic field is also required. In a tokamak, the poloidal field is produced by the plasma current flowing in the toroidal direction, as seen in figure 1.8. The combination of the toroidal magnetic field $B_\phi$ and of the poloidal field $B_\theta$ gives rise to helicoidal magnetic field lines along the vacuum chamber.

The toroidal magnetic field is produced by the current flowing in the external coils. Tech-

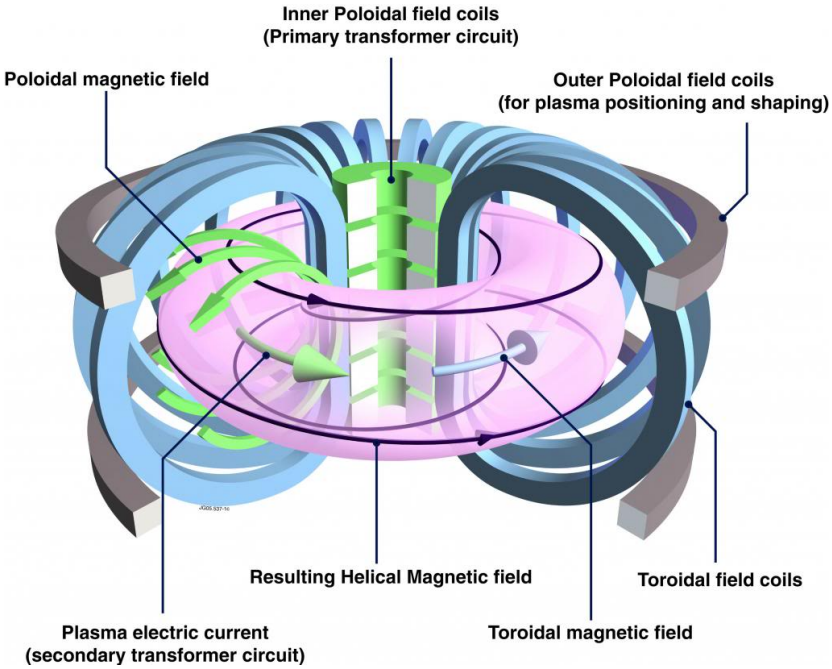


**Figure 1.8:** Essential tokamak structure. A tokamak is a doughnut-shaped vessel in which a helical magnetic field insulates charged particles in the plasma from the surrounding walls. The helical field is produced by combining a toroidal field, and another poloidal field. The former is provided by large external coils, while the latter is generated by a current flowing through the plasma in the toroidal direction. This plasma current arises from a toroidal electric field that is produced inductively by a coil passing through the center of the torus, which acts as the primary winding of a transformer (the secondary winding is provided by the plasma ring). The current flowing in the plasma ring provides the poloidal component of the magnetic field.

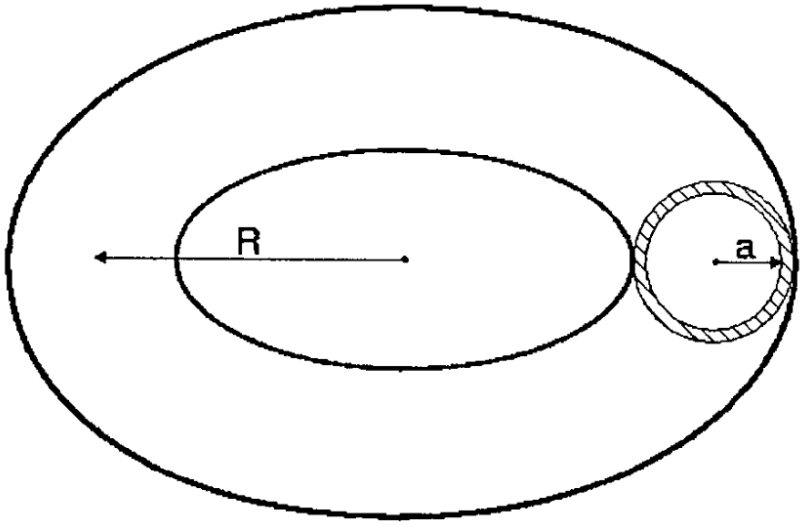


**Figure 1.9:** Toroidal plasma with major radius R and minor radius a, with a single washer: it is usually called poloidal limiter.

nological limits exist on the maximum toroidal field that can be reached. Using conventional copper magnets the limit is primarily imposed by the cooling capacity of the magnets themselves. For a steady state reactor, the losses due to the Joule effect of the conventional magnets would reach very high values which tends to promote the superconducting magnet technology. Tokamaks are often compared to big transformers, a flux variation is produced by the primary winding while the secondary winding is composed by the plasma itself. The plasma current is driven by a toroidal electric field induced by the transformer. Other coils and auxiliary fields are used, as shown in figure 1.8, for the position and shape plasma control.

The plasma is a conductor with a given resistivity, so when the current flow through it the Joule effect $P_J = R \cdot I^2$ dissipate energy in the plasma itself heating it up. This phenomenon is usually called *Ohmmic heating* and it is the common way to start the plasma heating in a tokamak discharge. A conventional conductor would increase its resistivity with temperature and consequentially the energy deposition due to the Joule effect. The plasma behaviour is quite different since its conductivity increase with temperature like as $T^{3/2}$ from the Spitzer theory [10]. It means that as the plasma temperature increase ohmic heating efficiency strongly drops. For this reason in the actual tokamak additional heating is needed to reach the fusion relevant plasma regime $T_e > 10KeV$. The two main additional heating systems are electromagnetic waves or strongly energetic neutrals. In the tokamak machines, the characteristic densities are in the range $10^{18} - 10^{20}m^{-3}$ which is about a factor $10^6$ lower than atmospheric density.

An important parameter to define the typical performance of a tokamak is the $\beta$, defined as

$$\beta = \frac{\langle p \rangle}{\frac{B^2(a)}{2\mu_0}} \tag{1.62}$$

with $\langle p \rangle$ is the average pressure on a poloidal section, a the torus minor radius as usual. This parameter is the ratio between the average kinetic pressure and the magnetic pressure of the field that is used to confine it; the $\beta$-value is therefore indicative of the efficiency of the configuration from the energetic point of view.

Evaluating the equation 1.62 using the typical values of $B_\phi$ and $B_\theta$ in a tokamak, the obtained $\beta$ is about 2-3%; it means that part of the magnetic energy stored in the device is not useful to the confinement. Another important parameter in a tokamak is the *safety factor*, q, defined as

$$q(r) = \frac{rB_\phi(r)}{R_0 B_\varphi(r)} = \frac{\Delta\phi(r)}{2\pi} \tag{1.63}$$

It identifies how close is the spiral drawn by the magnetic field upon a toroidal surface of radius $r$, where $\Delta\phi$ is the toroidal angle necessary to the magnetic field lines to complete the poloidal turn. The safety factor is often expressed as $q(r) = \frac{m}{n} : m$ is the number of toroidal turns needed to complete $n$ fully poloidal rotations. The safety factor is directly linked to the plasma stability, in fact, if a plasma displacement from the equilibrium position occurs, it is possible that one of its components is screwed on the magnetic surfaces with the same periodicity of the field. This condition, which is called resonance, has the effect of making the plasma particularly unstable with respect to this perturbation, for this reason $q$ is also known as the safety factor. If $q$ is irrational all the lines of the field will continue to screw on the toroidal surface without rejoining themselves, and they wipe ergodically the entire surface.

The plasma is contained in a vacuum chamber which also has the important function of minimizing the presence of impurities and therefore keeping as low as possible the plasma contamination. In a fusion relevant plasma impurities give up to a long series of phenomena among these the radiative losses and the fuel dilution. Preventing plasma contamination from impurities is one of the fundamental targets for the success of these experimental machines.

This is the essence of *plasma magnetic confinement*, but up to now, we neglected a very important fact that is essential in our treatment. We put a lot of effort to built a device, the tokamak, with ingenious magnetic field line closed upon themselves, in order to trap the particle in such *magnetic highway*: up to now we assumed the magnet field traps all the particle in closed orbits. This is, unfortunately, not true due to the *radial particles diffusion*, but more importantly, it is impossible to impose an infinite number of closed orbits in a real box. As soon we approach to the vacuum vessel edge, some of the magnetic field lines will go in contact with the solid boundary, we call them *open field lines*. All the particles traveling on these open field lines are destined to hit the solid surface where it gets in contact with the magnetic line itself. In order to protect the vacuum vessel from the energetic particles, it is possible to insert an additional solid part with the specific scope to create a first opened magnetic field line. In this way we shifted the problem of the container integrity, inserting in the machine a sacrificial component which ensures the safety of the vacuum vessel protecting it from the plasma expansion. We can imagine it like a washer inserted in the torus and protecting it, as shown in figure 1.9.

These washers are called *limiters* thus they act to limit the radius of the plasma to being $a$,

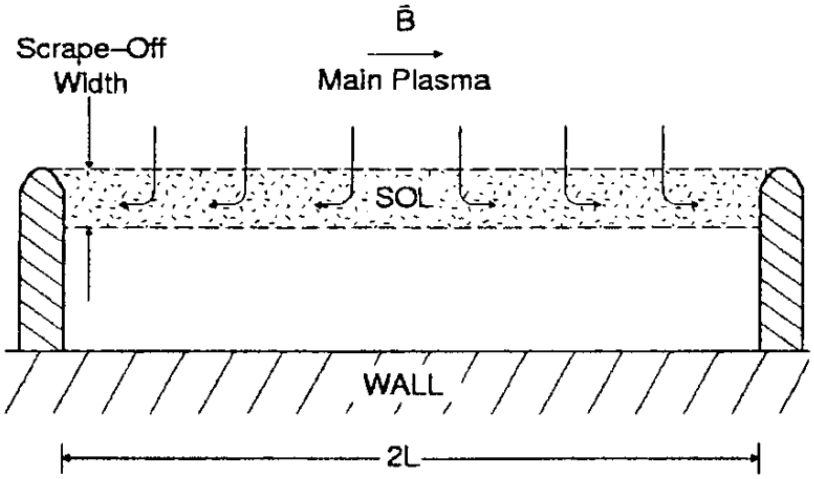


**Figure 1.10:** The SOL has been straightened out. Energy and particles flow from the main plasma into the SOL by slow cross-field transport, followed by rapid transport parallel to B along the SOL to the targets [11].

namely their inner radius. Plasma loss is no longer to the cylinder walls but to the sides of the limiters. This results in the formation of a so called *scraper-off layer*, SOL, in the region $r > a$. The particles crossing the radius $r = a$ move very rapidly to the limiter, because in a magnetically confined plasma the parallel field velocity is much larger than the radial, namely $v_{radial} << v_{parallel}$. The picture is a plasma *scraped-off* in a thin SOL limiting the plasma radius to $\approx a$. We define the *connection length* L to be such that the distance along B, from solid surface to solid surface, is 2L as shown in figure 1.10.

The *Last closed flux surface* (LCFS) is the surface which separates the main plasma from the SOL. It is possible to identify two main relevant limiter configurations: poloidal limiter and toroidal limiter. In addition to the limiter configurations there are equivalent divertor configurations, see figure 1.11. A toroidal divertor is formed by using special external divertor coils located at a specific toroidal location, in order to divert the magnetic field on the poloidal plane at the plasma edge. The toroidal divertor is thus toroidally asymmetric, but it is usually poloidally symmetric. The poloidal limiter is typically poloidally symmetric, of course. Nevertheless, poloidal limiters and toroidal divertors produce essentially equivalent SOLs and for both the connection length is $L \approx \pi R$. Sink action for the toroidal limiter is created by inserting a circular, annular target plate as for the washer used for the poloidal limiter. The equivalent of the toroidally symmetric toroidal limiter is the toroidally symmetric poloidal divertor. This is the divertor configuration most widely used for tokamaks [12]. It is generated by employing an external divertor coil current, $I_D$, parallel to the plasma current, $I_P$.

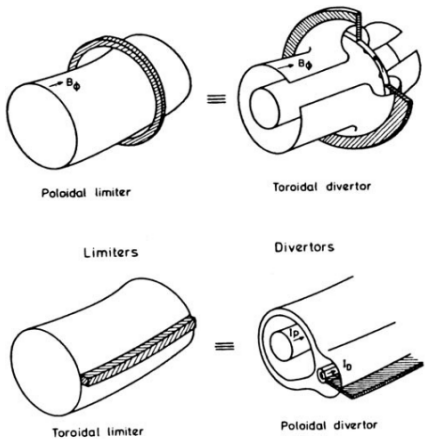


**Figure 1.11:** Various limiter and divertor configurations. (1) Top left the poloidal ring limiter, in the simplest case, is a circular annular plate. (2) Top right the toroidal divertor involves a diversion of the toroidal magnetic field near the edge, making for a configuration analogous to that of the poloidal ring limiter. (3) Bottom left the toroidal limiter consists of a toroidally symmetric, structure attached to the wall. (4) Bottom right the poloidal divertor involves a diversion of the poloidal magnetic field near the edge, making for a toroidally symmetric configuration, analogous to the toroidal limiter [13].

This diverts the polodidal magnetic field, hence the name. Sink action is created by inserting a solid, toroidally symmetric plate: the *divertor target*. The closed flux surfaces are not greatly altered by the fields created by the external current, but the poloidal field at the plasma edge is substantially diverted. For both the toroidal limiter and the poloidal divertor the connection length is considered $L \approx \pi R q$. We are going to spend a few other worlds on the poloidal divertor configuration since, nowadays, it is the most widely used configuration in tokamak devices. The poloidal magnetic fields generated by the parallel currents, $I_P$ and $I_D$, result in an *X-point*, namely a point where the where the poloidal magnetic field $B_\Theta = 0$. The magnetic flux surface passing through the X-point is the *magnetic separatrix*. The flux surfaces existing to the X-point are intercepted by the insertion of the divertor target plate, constituting the sink. The open flux surfaces, which surround the main plasma and extend to the targets beyond the X-point, constitute the SOL; any particles finding themselves on such flux surfaces will quickly hit the targets.

The experiments showed an unexpected impact of the boundary condition on the plasma core performances. It has been found for example that impurity from limiters tend to be ionized in the main plasma, resulting in significant flows, thus also parallel heat convection, all along the length of the SOL. In divertor configurations, by contrast, the ionization can occur primarily near the targets and parallel heat conduction may carry most of the exhaust power over most of the length of the SOL. In figure 1.12 the two configurations are shown. Furthermore, in a divertor

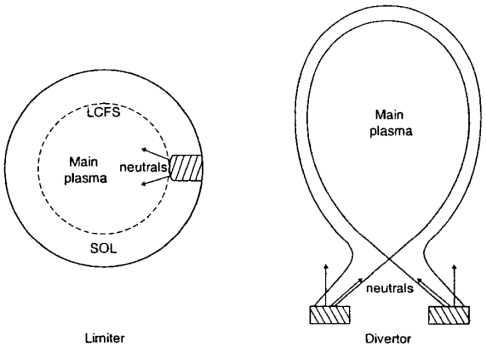


**Figure 1.12:** Limiter versus divertor configuration [13].

configuration would be easier to remove the helium ash in the future fusion reactor. Furthermore, the divertor is essential to access the *H-mode* and the *detached divertor mode*, two operative regime that are extremely important for the success of the future reactor operations.

### 1.3.1 Edge physics

When a solid get in touch with plasma the surface will act as a sink for the plasma fluid. When the charged particles strike to a solid surface they tend to stick to it long enough to recombine. Ions do have a finite probability of back-scattering from a solid surface, they do so mainly as neutrals, picking up electrons from the surface. Electrons also stick to solid surfaces. Thus a solid surface acts as an effective sink for plasma. The particles are subsequently released as neutrals, so it is not a mass sink. For solid surfaces which are insulators or are electrically isolated, opposite charges build up on the surfaces exposed to a plasma, quickly leading to surface recombination.

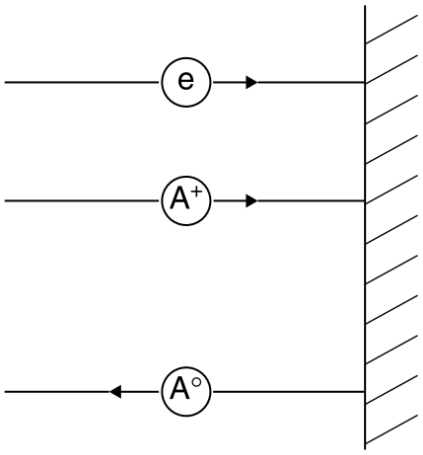


**Figure 1.13:** Charged particles hitting a solid surfaces tend to be adsorbed and to recombine. So typically the result is a neutral atom weakly bound to the surface easy to be desorbed back into the plasma. Thus particle recycling occurs and in steady state the plasma refuels itself

The resulting neutral atoms generally are not strongly bound to surfaces and are thermally re-emitted back into the plasma where they can be re-ionized, usually by electron collision. A steady-state condition, called *re-cycling*, can result if plasma charged pairs are lost to the surface at the same rate as recombined neutrals re-enter the plasma. While no external source of particles is then needed, an external source of energy to provide the ionization power is needed. The solid surface is strongly involved in the plasma source mechanism, it does not only acts as a sink for the particles. The mean free path of the neutrals for ionization may be large compared with the system size, and ionization will occur more or less uniformly throughout the system. In other cases, the ionization mean free path is short compared with system size and so recombination can take place near the ionization source, in particular the plasma source and the plasma sink can be quite close to each other. In that case, the rest of the available volume is then back-filled by diffusion. It is a similar situation of a heat source, such as a radiator, usually placed close to a principal heat sink, such as a window. A solid surface exposed to a plasma initially also acts as a pump in terms of mass, since a lot of particles are initially retained in or on the solid. Such

retention saturates at some level and thereafter a steady-state situation results with the plasma *refuelling itself*. At that point, any external source of fuelling, such as a gas injection, can be turned off and the plasma density will remain constant if no active pumping is used. [11]

If electric field E is applied across a material -plasma for our purpose- the particles respond by moving with an average velocity called the drift velocity, $v_d$. The mobility $\mu$ is defined as $v_d = \mu E$. Starting from this point it is easy to show the dependence of the mobility from the particle mass. Thus

$$v_d = \mu E = \mu \frac{F}{e} = \frac{\mu m a}{e} \tag{1.64}$$

where $m$ is the mass of the particle and $a$ is the acceleration.

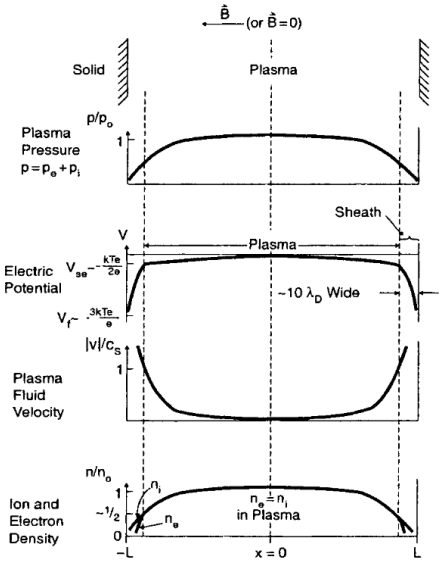


**Figure 1.14:** Schematic of the variation of plasma pressure, electric potential, plasma velocity and ion/electron densities in the plasma between two semi-infinite planes [13].

The drift velocity can be considered the result of a constant acceleration applied for a typical time $\tau$, namely the characteristic time between two collisions.

It is easy to show that

$$\mu = \frac{e\tau}{m} \tag{1.65}$$

Due to their lighter mass, the electrons have definitely a larger mobility than the ion. Now we can apply this concept to the plasma boundary. The electrons quickly reach the surface, in average faster than the ions, and charge up the solid surfaces negatively. Thereafter, an *ambipolar electric field* arises throughout the source region of the plasma, e.g. over length L. This *E-field* retards further electron outflow, at the same time accelerates the ions, so that this *ambipolar diffusion* mechanism of charge produces no net current. This prevents further growth of net charge in the plasma, which remains quasi-neutral. The solid is negatively charged. A positive charge layer *-electrostatic sheath-* forms close to the surface of the material. The charge balance is imperfect in the sheath and a small electric field penetrates into the plasma to the *stagnation point*. The electron flux and the ion flux must be equal: $\Gamma_{si} = \Gamma_{se}$ at the surface.

At the same time parallel electron and ion pressure gradient forces, $-dp_e/dx$, $-dp_i/dx$, arise along the SOL, due to the powerful sink action at the solid surface the pressure is depressed

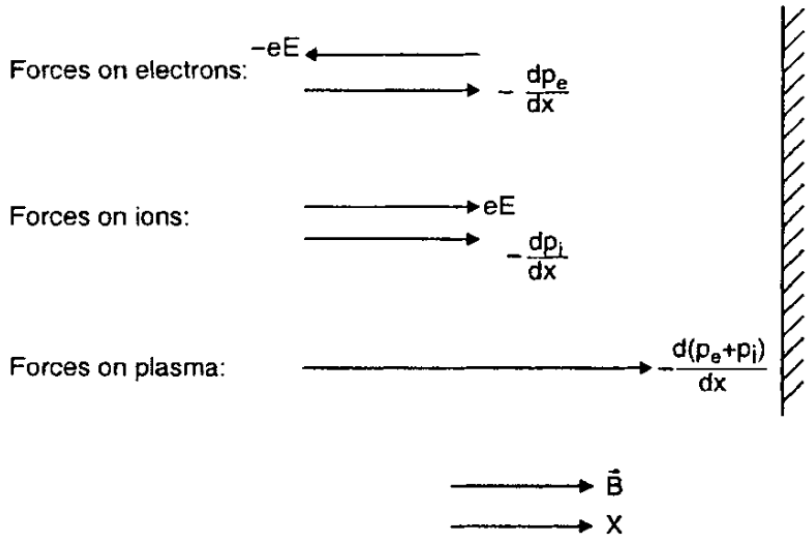


**Figure 1.15:** The electrons are almost balanced, while for the ions the electric field force and the ion pressure gradient force are with the same sign resulting in the ions acceleration. The force on the plasma is due to the total pressure gradient alone since an electric field exerts no force on the quasi-neutral plasma [13].

there, removing plasma momentum. It results that the electrons are nearly in perfect balance between the −eE force (away from surface) and the $-{}^{dp_e}/_{dx}$ force (toward), as shown in figure 1.15, and their net velocity toward the solid surface is extremely subsonic in terms of the electron sound speed (but not relative to the ion or the plasma sound speed). As results, only the tail of the electron distribution can reach the surface. For the ions the two forces, $-{}^{dp_i}/_{dx}$ and $-eE$, are both surface-directed, so accelerating the ions through it.

The sheath region begins where charge neutrality breaks down. The electric potential gradient then becomes quite steep quite abruptly on the boundary side of the sheath edge, where the charge of one sign is increasingly repelled and the other accelerated. For simplicity, we imagine planar symmetry where plasma parameters vary in a direction normal to a planar boundary. This is shown schematically in figure 1.14. The spatial potential profile forms self consistently, its formation depends on the kinetic distribution functions of the charged species, and on ion-neutral collisions even if the Debye length (the sheath thickness has the order of magnitude of a few Debye lengths) is the smallest scale length in the plasma. The breakdown of charge neutrality at the sheath edge implies that the ion drift speed becomes greater than the ion sound speed, $C_s = \sqrt{{}^{k_B T}/_{M}}$, at the sheath edge.

We can try to estimate the radial width of the SOL, $\lambda_{SOL}$, basing on the assumption that the recycling neutrals are ionized in the main plasma and the resulting plasma then diffuses

across the LCFS into the SOL. We can assume the particles have a typical lifetime in the SOL of $\tau = {}^{L}/_{c_s}$, according to the Bohm criterion. The Fick's law of diffusion give us the radial particle flux density, namely $\Gamma_{radial} = -D_\perp \frac{dn}{dr}$, where $D_\perp$ is the cross-field particle diffusion coefficient. Cross-field transport is generally thought to be due to plasma turbulence and it is not possible to evaluate $D_\perp$ from theory. It has to be obtained from the experiments and it is found to be anomalous, means larger than expected from a "classical", i.e. non-fluctuation approach. Typical experimental values are $D_\perp \approx 0.1 - -10 m^2 s^{-1}$. With the above mentioned conditions the particles are able to cross-field the distance $\lambda_{SOL}$ in a time $\tau_\perp = {}^{\lambda^2_{SOL}}/_{D_\perp}$, so that

$$\Gamma_{radial} = \Gamma_\perp = -D_\perp \left.\frac{dn}{dr}\right|_{LCFS} \approx D_\perp \frac{n}{\lambda_{SOL}} \tag{1.66}$$

and given $\Gamma_\perp = n v_\perp \approx {}^{n D_\perp}/_{\lambda_{SOL}}$ and $\lambda_{SOL} = \tau_\perp v_\perp$ we get

$$\lambda_{SOL} = \sqrt{\frac{D_\perp L}{c_s}} \tag{1.67}$$

Taking the typical values for a machine like the Frascati Tokamak Upgrade (FTU) in terms of diffusion coefficient, the average edge temperature of few tens electron volts and the connection length of few tens meters, we obtain $\lambda_{SOL} \approx 1cm$ that results in agreement with the experimental data. Thus the SOL is found to indeed be quite thin. The limiter limits the radial extent of the plasma at $\approx a + \lambda_{SOL}$. A benefit of a thin SOL is that plasma contact with the vessel walls can be avoided, but from the opposite side the plasma surface interaction is highly localized to the leading edges of the limiter, which can, therefore, suffer from severe heating, melting and sputter-erosion. The magnetic confinement is good enough for the plasma core out results to be too good for the edge, and a thicker SOL would be more convenient from the power exhaust point of view.

To have an idea of the power flux for a fully poloidail limiter we can easily divide the power exiting from the last closed magnetic surface by the limiter collecting surface. Using again the typical parameter for FTU, considering 0.4MW exiting from the SOL, the minus radius 30cm and 1cm for the SOL decay length, we get

$$q_{pl} = \frac{P_{SOL}}{2\pi[(a+\lambda_{SOL})^2 - a^2]} \approx 25^{MW}/_{m^2} \tag{1.68}$$

### 1.3.2 FTU: the Frascati Tokamak Upgrade

The Ionised Gas Laboratories were set up in the 1960s at the Frascati National Laboratories, where research on fundamental physics or high-energy physics had already started in 1956. This particular field of research is now carried out under the National Institute of Nuclear Physics (INFN). Since 1976 the research activities on controlled thermonuclear fusion have continued under ENEA programmes, always developed in collaboration with industries and in association with Euratom and CNR. In the following 20 years, the plasma physics laboratories carried out intense studies and research on the generation and physical properties of short-lived dense plasmas, with the objective of seeing whether controlled nuclear fusion could be used as a source of clean energy. The activities led to the construction of the prototype Frascati Tokomak (FT) in the 1970s and then the Frascati Tokamak Upgrade (FTU) in the 1980s.

In 1977 the Frascati Tokamak (FT) began operation. A compact, toroidally shaped experimental machine for studying controlled thermonuclear fusion, it was characterised by a high (10 Tesla) magnetic field, high current density. It achieved the world record in the $n\tau_e$ parameter in the 1979 [14] [15].

FTU is a compact, fully metallic, high magnetic field machine (toroidal field $B_T$ from 2 to 8 T, plasma current $I_p$ from 0.2 to 1.6 MA) with a circular poloidal cross-section (major radius Ro=0.935 m, minor radius a=0.30 m). Additional heating system are available, namely a 140 GHz electron cyclotron (EC) system with power up to 1.5 MW and an 8.0 GHz lower hybrid system with power up to 8.0 MW. The FTU stainless steel vacuum chamber is covered internally, in the high field side, by a toroidal limiter made of molybdenum tiles. In addition, there are an outer molybdenum poloidal limiter and a vertical poloidal liquid metal limiter.

The main characteristics of the FTU tokamak and the plasma parameters typical discharges are reported in the table 1.2.

The compact, high magnetic field devices are characterized by a large current density value that scales approximately with $j \approx {}^{B}/_{R}$, with B being the toroidal magnetic field intensity and R the major radius. Thus, the combination of large B values and small dimensions allows the achievement of large j values. This, in turn, has several advantages:

- The power density $P_\Omega$ associated with the ohmic heating is large, namely $P_\Omega \approx \eta j^2$, where $\eta$ is the plasma resistivity and j the current density. Thus, the plasma can be heated up to relatively high temperatures without the need of strong auxiliary heating systems, please also note $\eta$ decrease with the electron temperature as $T_e^{-\frac{3}{2}}$.

| Quantity | Value |
|---|---|
| Major radius, m | 0.935 |
| Minor radius, m | 0.333 |
| Toroidal magnetic field, T | $\leq$8 |
| Plasma current, MA | $\leq$1.6 |
| Auxiliary heating, MW | $\leq$8 |
| Pulse length, s | 1 – 4.5 |
| Pulse rep. rate, min. | 20 |
| Coil temperature, °C | -192 |
| Flux swing, Wb | 6.4 |
| Load assembly weight, Tons | 90 |
| Toroidal field power, MW | 120 |
| Poloidal field power, MVA | 250 |

**Table 1.2:** Main FTU parameters

- High particle density values can be achieved. Indeed, the particle density n in tokamaks cannot be arbitrarily increased. Above a critical value the plasma disrupts and the equilibrium configuration is lost. The empirical scaling law correlates the maximum allowed particle density with the current density, so high field experiment can easier reach higher values in term of particle density.
- Since the particle density is large, the mean-free-path for the ionization of an impurity atom released from the wall is short and the plasma is effectively screened from the penetration of impurities. Very low $Z_{eff}$ plasma can indeed be obtained.

The particle and energy flux from the plasma core on the wall can extract impurity atoms which penetrate into the plasma. The impurity ions can radiate energy and can dilute fuel, reducing the total amount of fusion power. Thus, impurity penetration must be avoided by a proper choice of the wall materials. FTU have tested several limiter materials, in fact, due to the reduced dimension, the power per unit area is quite large making it a good device to test plasma wall material interaction [16].

One of the most active programmes of the last few years on FTU is the liquid metals programme. FTU showed its feasibility in terms of magnetic field, pulse duration and main plasma parameters stressing and testing the liquid metal concept for a future fusion reactor. The vertical port has been dedicated, since 2005, to the liquid limiters experiments [17]. An overview of the limiters during a plasma pulse is shown in figure 1.16; the central belt is the main fully toroidal limiter (TZM); the equatorial poloidal limiter (TZM) on the left is protecting the vacuum vessel in the low field region; from the bottom left port the liquid

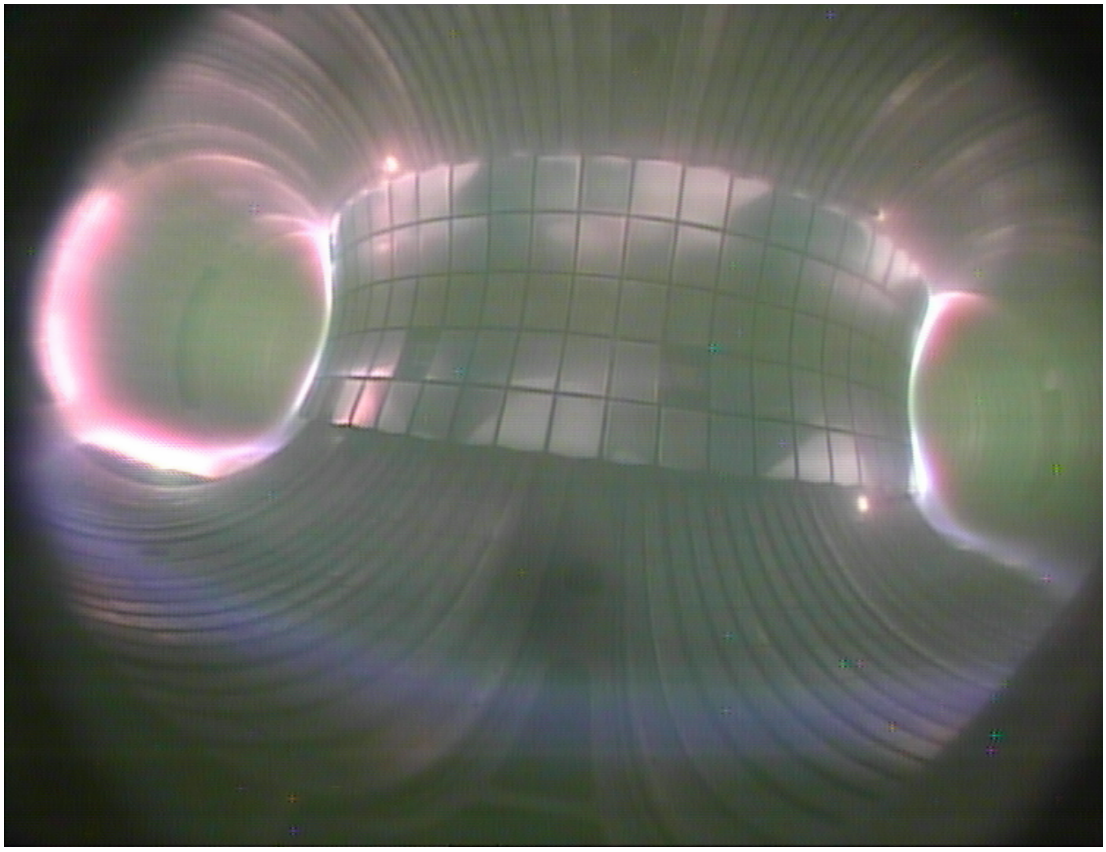

**Figure 1.16:** The Frascati Tokamak Upgrade (FTU) during a typical plasma discharge. All the limiters are visible in the picture: (1) the main belt protecting the vacuum vessel from the high field side is the toroidal limiter; (2) the poloidal movable limiter can be seen on the left of the picture, in the low field side of the machine; (3) on the left bottom of the picture the liquid metal limiter is visible. All the limiters are highlighted from the visible radiation glow, proof of the plasma-surface interaction.

metal limiter is visible (liquid tin limiter is shown in the picture). Wall conditioning procedure is routinely performed on FTU, namely the boronization, to overcome the problem of high $Z_{eff}$ values at low electron density as required by some experimental programs. After this procedure, for an ohmic plasma the total radiated power typically drops from 70-90% down to 35-40% and for Ip=0.5 MA and, $Z_{eff}$ typically decreases up to three times. We will compare the results of the wall condition with boron and the lithization experiments.

*Everything new is actually well-forgotten old.*

Russian saying

# 2

# Liquid metals as alternative plasma facing material

The European Commission, at the beginning of 2012, requested the *European Fusion Development Agreement* (EFDA) (1999 – 2013) to prepare a technical roadmap to fusion electricity by 2050. A roadmap to the realization of fusion energy [1] was proposed, in November 2012, from (EFDA) The document has been developed within a goal-oriented approach articulated in eight different Missions. For each Mission the critical aspects for reactor application, the risks and risk mitigation strategies, the level of readiness now and after ITER and the gaps in the programme have been examined.

We are going to cite a part of the document because it is probably one of the main motivation for the performed work treated in this thesis.

> " A SOLUTION FOR THE HEAT EXHAUST IN THE FUSION POWER PLANT IS NEEDED. *A reliable solution to the problem of heat exhaust is probably the main challenge towards the realization of magnetic confinement fusion. The risk exists that the baseline strategy pursued in ITER cannot be extrapolated to a fusion power plant."*

[1] EFDA - November 2012

As we have already seen, the confinement in a tokamak reactor is the result of magnetic field lines forming a set of closed magnetic surfaces. At the plasma edge a thin $O(1cm)$ region of open field lines is created — the scrape-off layer — through which charged particles and heat flowing out of the core plasma is guided into the so-called divertor where the plasma impinges directly on a material surface. The parallel heat flux in the SOL region of ITER and DEMO is expected to be even higher than the sun's surface. Probably these assumptions gave the main motivation for the second mission, addicted in the above cited roadmap, we partially cite:

> Mission 2. *Heat-exhaust systems must be capable of withstanding the large heat and particle fluxes of a fusion power plant. The baseline strategy for the accomplishment of Mission 2 consists of reducing the heat load on the divertor targets by radiating a sufficient amount of power from the plasma and by producing "detached" divertor conditions. Such an approach will be tested by ITER, thus providing an assessment of its adequacy for DEMO. However, the risk exists that high-confinement regimes of operation are incompatible with the larger core radiation fraction required in DEMO when compared with ITER. If ITER shows that the baseline strategy cannot be extrapolated to DEMO, the lack of an alternative solution would delay the realisation of fusion by 10-20 years. Hence, in parallel with the necessary programme to optimise and understand the operation with a conventional divertor, e.g.by developing control methods for detached conditions, in view of the test on ITER, an aggressive programme to extend the performance of water-cooled targets and to develop alternative solutions for the divertor is necessary as risk mitigation for DEMO. Some concepts are already being tested at proof-of-principle level in 1MA devices (examples are super-X, snowflake, liquid metals). These concepts will need not only to pass the proof-of-principle test but also an assessment of their technical feasibility and integration in DEMO, perhaps by adjusting the overall DEMO system design to the concept, in order to be explored any further. The goal is to bring at least one of the alternative strategies (or a combination of baseline and some alternative strategy) to a sufficient level of maturity by 2030 to allow a positive decision on DEMO even if the baseline divertor strategy does not work. As the extrapolation from proof-of-principle devices to ITER/DEMO based on divertor/edge modelling alone is considered too large, a gap exists in this mission. Depending on the details*

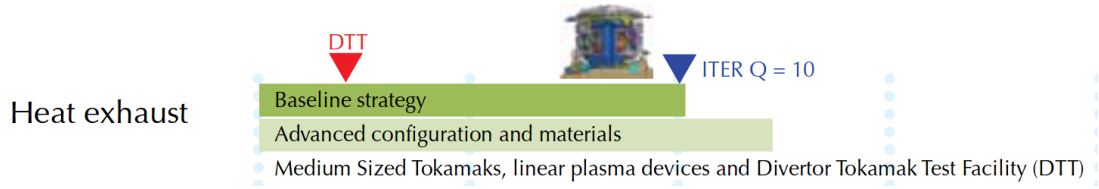


**Figure 2.1:** Focus on the timetable for the Mission2: heat exhaust [1].

> *of the most promising chosen concept, a dedicated test on specifically upgraded existing facilities or on a dedicated Divertor Tokamak Test (DTT) facility will be necessary. The DTT could be either a new or an upgraded facility, entirely devoted to the divertor problem, but with sufficient experimental flexibility to achieve the overall target. The facility needs to be ready in the early 2020's and is a good opportunity for joint programming among the EURATOM member states and for international collaboration. Again, as the extrapolation to DEMO will have to rely on validated codes, theory and modelling effort is crucial for the success of this Mission.*
>
> [1] EFDA - November 2012

Looking to a future nuclear reactor, the performances required by the divertor in terms of thermal and neutron flux resistance will be higher than in ITER. This involves the technological development of solutions able to withstand higher loads. Solid materials are subject to erosion with dust formation, continuous surface deterioration, and their thermo-mechanical properties can change under neutrons fluence. A solution proposed since the beginning of the fusion reactor studies [18] was the use of a liquid metal directly exposed to the plasma, but only recently experiments have been performed to test the viability of this idea. The liquid metal program is currently focused on verifying their compatibility with a future reactor. The results are encouraging but at the same time some problems have emerged. Before a proper treatment to the liquid metal research we introduce the current state of the art in the divertor technologies.

## 2.1 The current strategy

The current strategy is to optimize the operations with the conventional divertor based on plasma detached (fully or at list partial) conditions to be tested on ITER. This strategy is based on different factors:

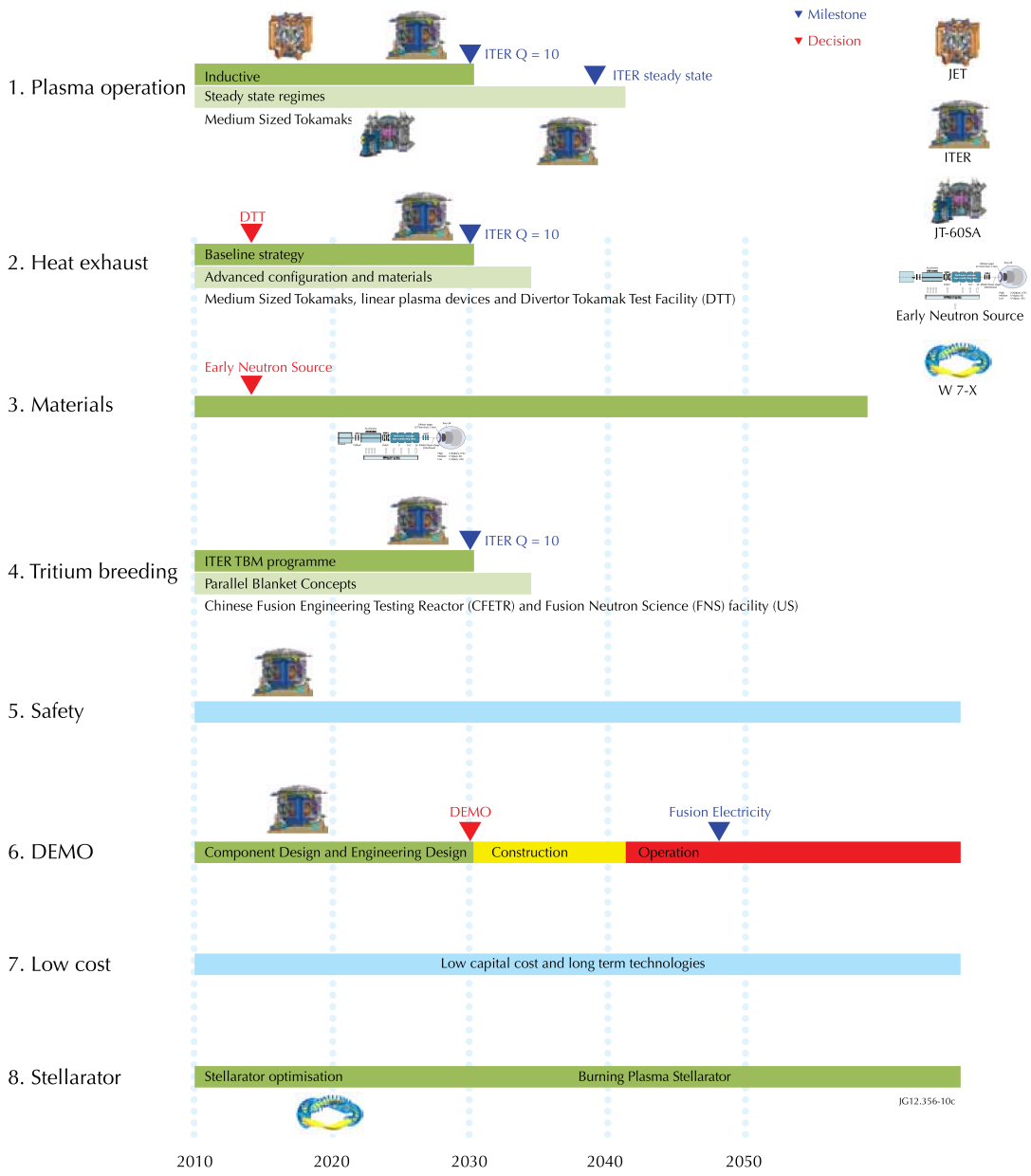


**Figure 2.2:** Complete timetable of the eight missions selected from the roadmap to fusion electricity [1].

- development of plasma facing components able to tolerate large power fluxes $O(5 - -10^{MW}/_{m^2})$
- selection of divertor geometry and magnetic flux expansion to reduce the normal heat flux on the target, i.e. distributing the heat over a larger surface
- removal of plasma energy before it reaches the target via impurity radiation by increasing edge plasma density and injecting impurities in the SOL region, so as to decrease the fraction of the heating power that leaves the vessel via the SOL channel.
- recycling and increase of density lowering the temperature close to the target, with consequent detachment

However, the successful operation of the conventional divertor solution in ITER is not guaranteed:

- the present experiments operate with SOL conditions that are not necessarily those expected in ITER and DEMO
- the simulations with the present SOL models and codes are not fully reliable when extrapolating to ITER and DEMO conditions
- the stability of the detachment front has to be assessed for ITER and DEMO conditions
- there might be problems are related to integration with the core plasma, e.g.: impurity contamination of the core with consequent reduction of fusion performance compatibility of plasma radiation fraction

Therefore a specific project DTT [19] has been launched, by the Italian community, to investigate alternative power exhaust solutions for DEMO, aimed at the definition and the design of a Divertor Tokamak Test facility. This tokamak should be capable of hosting scaled experiments integrating most of the possible aspects of the DEMO power and particle exhaust. A focus on the timetable of the Mission-2 is presented in figure 2.1, where DTT is wished to tackle the power exhaust issue. A summary of the timeline of the total roadmap is given in figure 2.2.

### 2.1.1 ITER DIVERTOR: THE STATE OF THE ART AND LIMITS

We are now going to briefly show the state of the art of the ITER divertor in terms of requirements and technical chooses [20]. The IRF poloidal divertor will be installed in the bottom part of the device. Its main function will be to extract the power coming from the heat flux in

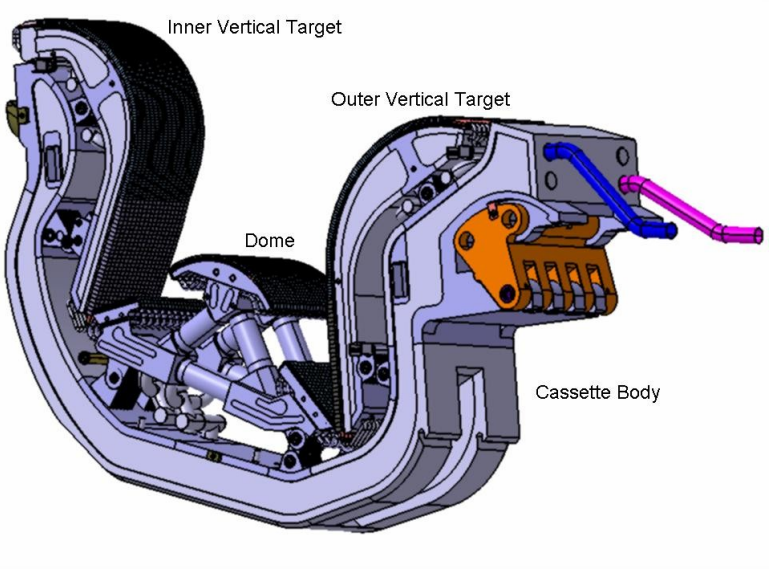


**Figure 2.3:** Schematic view of the ITER divertor consisting of inner and outer vertical targets, dome umbrella, dome particle reflector plates and cassette body [20].

the scrape-off layer (SOL) and radiation at the same time avoiding plasma contamination so preserving the highest possible plasma purity level. It should tolerate high heat loads as it will be the main solid materials interfacing components with plasma, while at the same time it should also providing neutron shielding for the vacuum vessel and superconducting magnets, in the vicinity of the divertor. Various diagnostics for divertor physics studies and machine protection purposes should be hosted in the diveror cassette. The ITER divertor consists of 54 cassette assemblies which will be inserted by remote handling operation. Each cassette assemble includes one Cassette Body and three Plasma-Facing Components (PFCs), namely the inner and outer vertical targets, and the dome. The schematic view is visible in figure 2.3, while in 2.4 the real-size prototype of ITER Divertor Cassette manufactured by Walter Tosto is shown. The inner and outer vertical targets consist of monoblocks with swirl tape in the coolant channel and their lower parts are defined as the high heat flux handling areas, whereas, the dome consists of flat tiles with hypervapotron cooling channel and is exposed to lower heat flux. The hypervapotron principle [21] is based on the boiling/condensation phenomenon in a subcooled water flow boiling with transverse fins separated by slots. The upper part of fins operates at a temperature higher than the critical heat flux temperature while the remaining part operates close to the temperature of stable nucleate boiling onset. These operating conditions produce in slots continuous boiling and condensation processes.

**Figure 2.4:** European real-size prototype of ITER Divertor Cassette manufactured by Walter Tosto [22].

The precipitation-strengthened copper alloy, CuCrZr alloy is used as the heat sink material in forms of pipes and plates. It has a combination of good electrical conductivity, good thermal conductivity, and high strength and it is possible to be joined by fusion welding. The CuCrZr alloy is available in semi-finished products such as rolled plates and cold-drawn tubes. The properties of CuCrZr alloy are sensitive to heat treatment. Dedicated heat treatment is required to obtain the optimal combination of strength, ductility and conductivity, i.e. solution annealing at $980°C$ for 0.5 h followed by quench (typically faster than 1 K/s) and ageing at $475°C$ for 2–4h.

Oxygen free Cu (OFCu) is used as compliant layers at joints and for the swirl tapes. The dpa levels in Cu alloy in the first divertor set were estimated to be maximum 0.4 dpa at area exposed to lower surface heat flux [23]. Low-temperature ($< 300°C$) neutron irradiation of Cu and Cu alloys lead to hardening, increase of yield strength, decrease of elongation and loss of strain hardening capability. The irradiation at $60°C$ to a dose level of about 0.3 dpa can cause significant hardening both in the prime aged and overaged specimens while severely reducing the ductility and work hardening. The tensile response and post-deformation microstructure of the irradiated alloy indicate that the lower density of larger particles produced by overaging at $600°C$ for 1 h improved the resistance to plastic instability and led to some increase in the overall ductility. The radiation effect on tensile properties of Cu alloy show tendency to saturate at doses more than 0.5 dpa. The decrease of CuCrZr conductivity is small (few %) up to a few dpa which is significantly higher than the fluence goal [24]. At the required dose of irradiation the overall change of material properties is considered to be acceptable.

Inconel, alloy 625 and 718 were selected as additional material for the divertor layout respectively as a transition piece of the CuCrZr tube to 316L tube joint, and for the high strength pins for mechanical engagement. Neutron irradiation leads to a slight reduction of tensile and yield strength in the Alloy 718. These changes were taken into account during design assessment.

Tungsten is used as armour materials in form of monoblocks or flat tiles. Tungsten materials are typically produced by sintering process followed by deformation such as rolling and forging.

The dpa levels in W in the first divertor set are estimated to be maximum 0.1 dpa at area exposed to lower surface heat flux [23]. At this dose level, a reduction of thermal conductivity of tungsten is observed at temperatures lower than $800°C$ while there is hardly any effect above $800°C$. The ductile to brittle transition temperature (DBTT) shift to higher temperature range and degradation of tensile properties became noticeable, especially at lower irradiation

temperature. The influence of transmutation in W is considered to be negligible at this dpa level, tungsten would still be usable in ITER since the lifetime fluence of neutrons is much smaller than in a fusion device. A calculation suggests in fact that the end-of-life composition -initially 100% W- in ITER would be about 98% W, 2% Re and 0.03% Os [25].

## 2.2 Liquid metal as alternative solution

The ITER divertor strategy is well assessed in the EFDA roadmap, the divertor realization is currently ongoing but a mitigation of the risk is also carrying on in parallel. In fact, in order to secure the achievement of each mission, appropriate risk mitigation strategies have been developed [1]. For mission two the risk mitigation provides for extending the performance of the actual water-cooled targets and for developing alternative divertor solutions. Some concepts are already being tested at the proof-of-principle level in relativity small devices. These concepts consist essentially in advanced magnetic configurations, i.e. super-X, snowflake, double null, and in the exploration of new materials among which the liquid metals. It is requested to these concepts first to pass the proof-of-principle test, then an assessment of their technical feasibility and integration in a future reactor is necessary. The goal is to have at least one of the alternative strategies, or a combination them, to a sufficient level of maturity by 2030 to allow a major decision on DEMO project even if the baseline divertor strategy does not work.

It is known from the other fields experience (electronics, structural materials, etc) that, to avoid cracking, the surface temperature must be maintained below $T < 0.33T_m$ ( where $T_m$ is the melting temperature in K). This condition is hard to satisfy, for solid materials, under high power quasi stationary heat fluxes. The situation is so dramatic that the technical feasibility of a quasi stationary tokamak reactor may come under the question. Nowadays a proposed solution to the problem has been the creation of a cool, dense radiating layer between the hot plasma and divertor plates.

In the future fusion reactor, the divertor plates should not be subjected to an average power greater than $10^{MW}/_{m^2}$ with transients below $20^{MW}/_{m^2}$, and with an electron temperature below 10 eV [26]. More than 90% of the power should be radiated in the center and/or SOL and the plasma should be partially detached. In this framework, liquid metals are proving to be good candidates as a plasma facing component material.

The liquid metal program is currently focused on verifying if and under what conditions these can be used in a future reactor. The results are encouraging but at the same time

| Property | Liquid metal | | | W |
|---|---|---|---|---|
| | Li | Ga | Sn | |
| Atomic number, Z | 3 | 31 | 50 | 74 |
| Atomic weight | 6.94 | 69.72 | 118.7 | 183.8 |
| Density, $\rho$, $g \cdot cm^{-3}$ | 0.512 | 6.095 | 6.99 | 17.6 |
| Melting point, $T_m$, $°C$ | 180 | 29 | 232 | 3422 |
| Boiling point, $T_b$, $°C$ | 1342 | 2204 | 2602 | 5555 |
| Heat of melting, $\Delta H_m$, $J \cdot g^{-1}$ | 432 | 80 | 59 | 190 |
| Latent heat of vaporization, $\Delta H_v$, $kJ \cdot g^{-1}$ | 21.1 | 3.9 | 2.5 | 4.5 |
| Heat capacity, $C_p$, $J \cdot kg^{-1} \cdot K^{-1}$ | 4420 | 345 | 255 | 140 |
| Thermal conductivity,$k$, $W \cdot m^{-1} \cdot K^{-1}$ @ $T_m$ | 47 | 27 | 32 | 72 |
| Surface tension, $\sigma$, $N \cdot m^{-1}$ @ $T_m$ | 0.400 | 0.685 | 0.554 | |
| Volumetric heat capacity, $\rho\, C_p$, $MJ \cdot m^{-3} \cdot K^{-1}$ | 2.3 | 2.25 | 1.83 | 2.70 |
| Ionization energy, 1st, $10^6 J \cdot g^{-1}$ | 3.61 | 40.4 | 84.1 | 141.6 |
| Ionization energy, 2nd, $10^6 J \cdot g^{-1}$ | 50.6 | 138.0 | 167.6 | 312.5 |
| Ionization energy, 3rd, $10^6 J \cdot g^{-1}$ | 82.0 | 206.6 | 349.3 | |

**Table 2.1:** Properties of fusion relevant liquid metals and W for comparison [37].

a lot of still open questions need answers. A lot of work has been performed on liquid surface plasma facing components (lsPFCs) mostly focus on liquid lithium (Li) [27][28][29] , gallium (Ga) [30][31], tin (Sn) [32][33] and during the last few years on the lithium-tin alloy (Li-Sn)[34][35]. Table 2.1 lists the main properties for pure liquid metals compared with solid tungsten (W), often used in DEMO designs and actual best candidate for the solid divertor solution. Complex interdependent processes in the plasma edge and surface layers of the wall strongly affect the machine performances. Light elements, i.e. Li, Be, B (relatively benign plasma impurities) have been used extensively as impurities getter (particularly for oxygen): it is one of the principal motivation for the ITER Be walls. Furthermore, liquid metals exhibit a self-protection phenomenon, the so-called vapour shield. It has been observed in many different device the liquid metals capability to create a shield of vapour gas in front of the surface reducing the heat load to the substrate during abnormal events for tin, and maybe potentially in continuous mode for lithium [36].

The liquid metals community in fusion plasma research is growing up, as well as the experiments increase a lot in number and achieved results as it is visible also in figure 2.5, from [38]. We briefly summarize some of the liquid metals experiment in fusion relevant plasma device. We report few selected experiments hoping to give a logical thread to the readers and to highlight the most import issues.

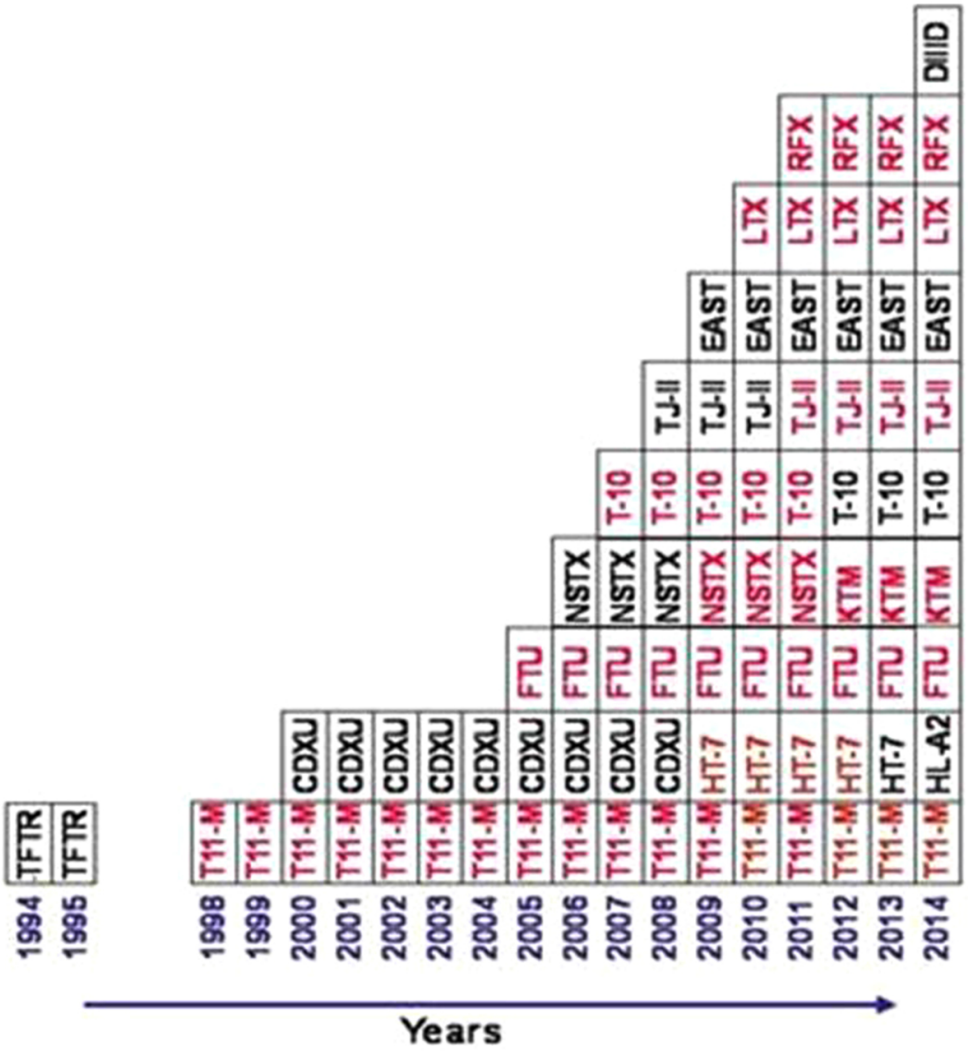


**Figure 2.5:** Lithium progress in the fusion investigations. Each rectangle represents a fusion relevant device investigating Li technology, red text indicates the one with Li CPS, black without CPS [38].

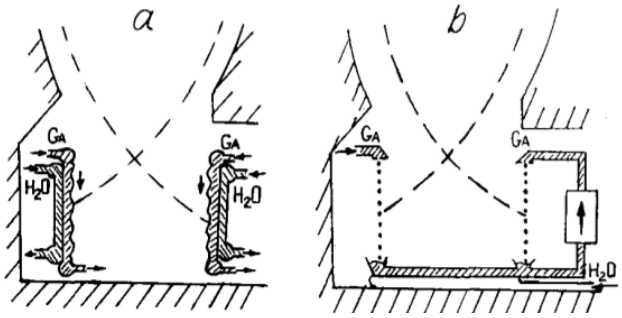


**Figure 2.6:** Liquid metal sheet possible scheme: (a) and jet-drop curtain (b) divertor plates.

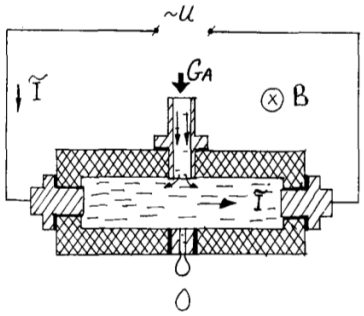


**Figure 2.7:** Principal scheme of the jet-drop shaper [39].

Looking from the historical point of view one of the first articles appeared on J. Fusion Energy hypothesising the use of liquid lithium as PFC is from Christofilos [40]. He was proposing a liquid lithium blanket surrounding the plasma volume with no vacuum wall between the blanket and the plasma. The layer of energetic particles within which the plasma was confined serves as a vacuum wall protecting the plasma from the lithium vapor, which was continuously produced at the surface of the blanket, by ionizing the lithium atoms and ejecting the same along open magnetic lines. To exhaust the heat load generated by the 14 MeV neutrons a thick layer of liquid lithium had to flow moving at $30m/s$.

Other concepts were presented earlier by Badger [18]. These were based on the use of liquid metals flowing inside the vacuum chamber of a tokamak (UWMAK-I and UWMAK-II) in order to extract the heat that was produced by the plasma. Nonetheless, those were only conceptual ideas and it has taken more than one decade before the materialization of a few experiments that allow studying the influence of liquid metals on the behavior of plasmas. A study, called APEX, was initiated mainly from the same UWMAK's authors in early 1998 as part of the US Fusion Energy Sciences Program initiative to encourage innovation and scientific understanding. The primary objective of APEX was to identify and explore novel,

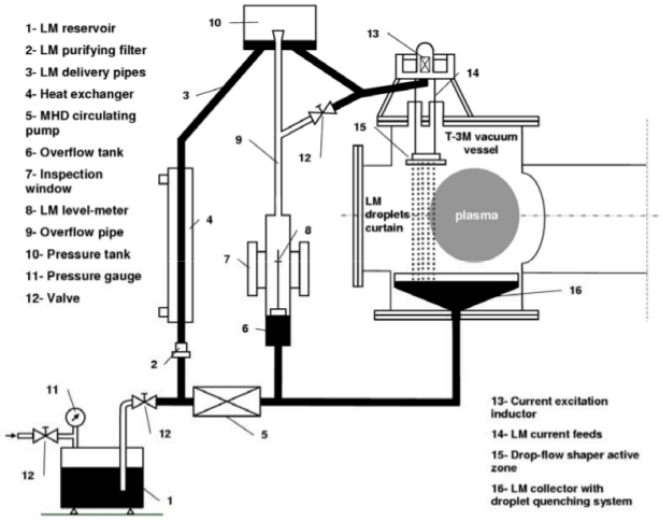


**Figure 2.8:** Scheme of T-3M jet-drop curtain limiter. I-MHD pump. II-jet-drop shaper, III-collector[39].

possibly revolutionary, concepts for the chamber technology that can substantially improve the attractiveness of fusion energy systems. The chamber technology includes the components in the immediate outside of the plasma (i.e. first wall, blanket, divertor, and vacuum vessel) and has a tremendous impact on the economic, safety and environmental attractiveness of fusion energy systems.

The idea to use liquid metals in fusion confinement device was already known in Russia since the 70's device generation. The liquid metal's properties were well known at that time in Russia since the many different application fields and studies, i.e. heat transfer pipeline, fission reactors, spaceship heat shield, etc. The first reported experiments in a tokamak device come from the Soviet Tokamak T-3 in 1986 as described in [39]. The first proposal to use such a limiter was made by the authors of the UWMAK design in 1973 [18]. They cite the UWMAK idea and realized a gallium circuit to test the concept. In fact, it was believed that several technical difficulties related to solid limiter might be overcome using liquid metal flow in contact with the plasma. Figure 2.6 and 2.7 show respectively two possible scheme of the sheet and a concept of the jet-drop shaper.

They decided to work with liquid Gallistan (67% gallium, 20.5% indium and 12.5% tin), or S-GIS, since the additional difficulties in liquid Li handling and the foreseen good properties of Gallium in term of the operational window and power removal efficiency. Gallistan is gallium alloy with a $10.5°C$ melting point and a $1500°C$ boiling temperature. An array of 17 jets decomposing the metal into small droplets (2-4 mm in diameter) before they get in

contact with plasma. The jets were distributed in two rows in the toroidal direction with each one separated 4 mm in the radial direction. Experiments were carried out using the small T-3M tokamak [41] with the following parameters: $R = 95cm$, $a = 16cm$, $B_t = 1T$, $I_p < 40kA$, $Te(0) = 250eV$, $Te(a) = 15 - 30eV$. Drops flowed in a regular jet-drop curtain directed from top to bottom in figure 2.8 and act as a limiter immersed in the plasma at a depth of 3 cm. The drop size was 2-4 mm. The experiments were also performed with a graphite limiter. The results obtained in both regimes were compared. It is to be noted that in these regimes the impurity inflow originated mainly from a limiter. In figure 2.9 are reported the main results. In the conclusion the authors underlined [39]:

- the problem of droplet formation and plasma pollution;
- the problem of the vacuum chamber contamination, but they also add it is believed that the walls boronization would provide an effective recovery of a working chamber;
- they suggest the use of liquid metal divertor plates since it would provide the possibility to overcome some principal obstacles typical for steady state divertor regimes:
  - limitations on fatigue strength;
  - divertor plates erosion;
  - heat removal;
  - simplify the first wall erosion products removal from the working chamber;
- along with some technological improvements needed for liquid metal divertors, in 1992 they suggested the following studies to be carried out:
  - LM divertor behavior under disruptions;
  - plasma-wall interaction, plasma pollution;
  - absorption of hydrogen, deuterium, and tritium.

The main problem detected during the experiments was related to the penetration of small liquid metal droplets into the plasma. These were formed due to the creation of small droplets when they hit the collector surface at the bottom of the chamber, see figure 2.8. After the dismantlement of T-3M, it has been possible to detect the presence of small liquid metal droplets (0.1 – 0.5 mm size) deposited on the chamber walls and on the stationary

poloidal limiter. This was verified even at a large distance from the region where the liquid metal droplets were produced. As a consequence, the colleagues from T3-M proposed the emitter-collector strategy [39] [42] for the use of LM in a tokamak environment. The results obtained in T-3M have shown that the use of gallium alloys in direct contact with plasma could be harmful to the achievement of high performance discharges. In figure 2.9 a the tokamak operation with the carbon limiter and the liquid curtain limiter are compared. The main discharge parameters for C (solid line) and Ga (dotted line) limiters are presented. It is seen that the basic characteristics (plasma density $n_e(t)$ and radiative losses $I_B(t)$ versus time) were similar in both cases. The electron temperature in the limiter shadow was about 15-30 eV. As has been verified, the penetration of a large amount of high Z impurities into the plasma generates high levels of radiation losses which are responsible for the degradation of the machine performance or even, in extreme situation to abruptly ending the discharge in a so called *disruption*.

After several years, the possibility to use liquid lithium as plasma facing component received a new impulse on the base of the experiments done in the TFTR Tokamak. In TFTR lithium pellets were injected into the plasma resulting in a significant (and unexpected) improvement of the performance [43]. Another factor that had some influence on the option to use lithium was that this material will always be required in fusion reactors since it works as a tritium breeder. Lithium plasma compatibility is mainly due to its low atomic number (Z = 3) that allows this element to have a much lower contribution to plasma radiative losses when compared with the typical heavier impurities in tokamaks: oxygen, iron, chromium, nickel, molybdenum, etc.

Perhaps one of the most serendipitous discoveries in TFTR was considered the beneficial effect of lithium pellet injection into the discharge [44]. Originally implemented as a current profile diagnostic, the injection of lithium pellets resulted in a significant increase in the neutron rate and confinement time during the beam heated portion of the discharge. The experiments done in TFTR have shown the formation of a protective ionized lithium layer between the hot plasma and the tokamak walls without having a significant contribution to the plasma impurity content increase [45]. Lithium pellet conditioning leads to reduced edge densities and improved neutral beam penetration, which then peaks up the density profile and improves confinement. Four principal benefits have resulted from lithium conditioning of TFTR:

- increased D-T fusion power (up to 10.7 MW) for the given input power;

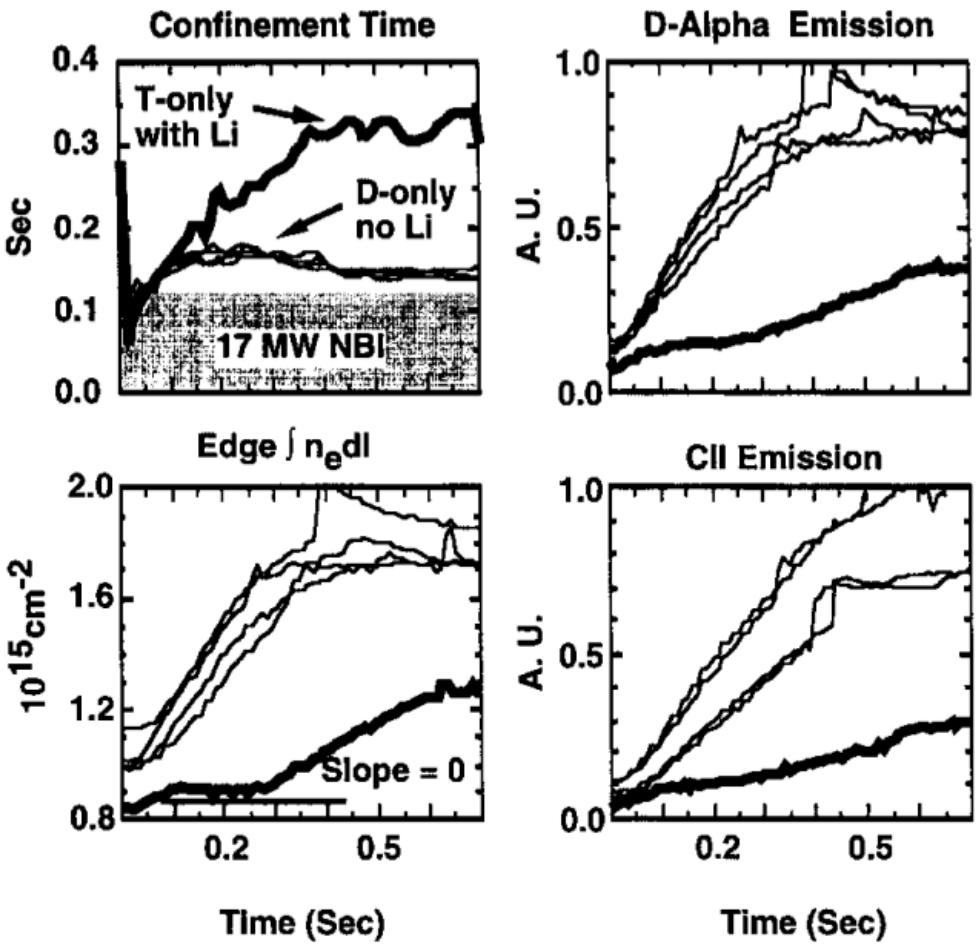


**Figure 2.10:** Reductions in edge electron density and $D_\alpha$ and $C_{II}$ line emission and corresponding increase in energy confinement time for a T-only discharge with good lithium conditioning (thick line) and several D-only discharges for comparison (thin lines) [43].

- significant enhanced of the energy confinement time, up to $\tau_E = 330ms$;
- lithium conditioning enabled supershot operation at high values of plasma current (up to 2.7 MA) and stored energy, through its apparent elimination (or reduction) of the sawtooth instability at high plasma currents;
- lithium conditioning, enhanced values of the Lawson product of a factor 60, up to $n_e\tau_E T \approx 10^{21} m^{-3}\, s\, keV$ [44], [46]

Figure 2.10 shows the suppression of edge plasma density and material influx from the limiter with lithium conditioning in TFTR. Reduced edge density and $D_\alpha$ and $C_{II}$ emissions have been observed to correlate with increased $\tau_E$ in supershots without lithium conditioning.

The authors also report a decrease of the lithium beneficial effects after about 300ms. They commented it could be related to the dilution of lithium close to the limiter (limiter is considered the main impurity source). So they suggested to implementing a continuously resupply lithium system to the limiter during neutral beam injection. We will recall this concept later.

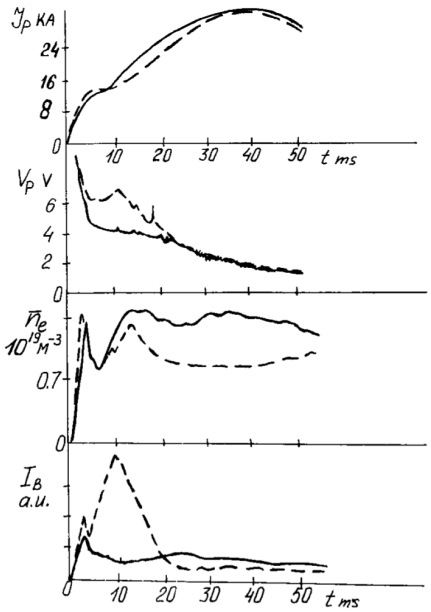


**Figure 2.9:** Experiments on T-3M with jet-drop curtain limite. The figure presents the main discharge parameters for C (solid line) and Ga (dotted line) limiters. In the plots are respectively shown: $J_p(t)$ - discharge current; $V_p(t)$ - loop voltage; $n_e(t)$ - plasma electron density; $I_B(t)$ - radiative losses. Pictures from [39].

In 1998, a *Capillary Porous System (CPS)*, has been tested in the Russian tokamaks T11-M and T-10. The experimental setup, for the two tokamaks, is shown in figure 2.11. The main T-11M parameters are: $R = 0.7m$, $a = 0.25m$, $J_p = 70 - -100kA$, $B_T = 1.2T$, $\Delta t = 0.2s$). The main T-10 parameter are: $R = 1.5m$, $a = 0.35m$, $J_p = 200 - -300kA$, $B_T = 2.5T$, $\Delta t = 1s$). The CPS consists in a solid porous matrix (metal with micro-channels or metallic mesh) wetted with liquid metal, lithium in the T11-M experiments. Due to surface tension forces in the capillary channels, lithium is driven through the porous structure and it is held on the surface. These forces counteract the electromagnetic forces applied to the metal by the induced currents and so overcome one of the main problems, the droplet formation, observed in the T3-M liquid curtain limiter. The use of lithium showed the same increase in performances as previously observed in TFTR.

The $Z_{eff}$ decrease up to one, the high and medium $Z$ impurities were suppressed, and the plasma recycling reduction has been confirmed from the T-10 wall lithizated experiments [47].

During the period 1998 – 2009, many experiments have been performed, in T11-M [38], with liquid lithium limiters. The main results we summarize here are:

- surface tension forces in the CPS allow the liquid Li splashing suppression;
- surface tension forces ensure PFC regeneration during the long experimental campaign;

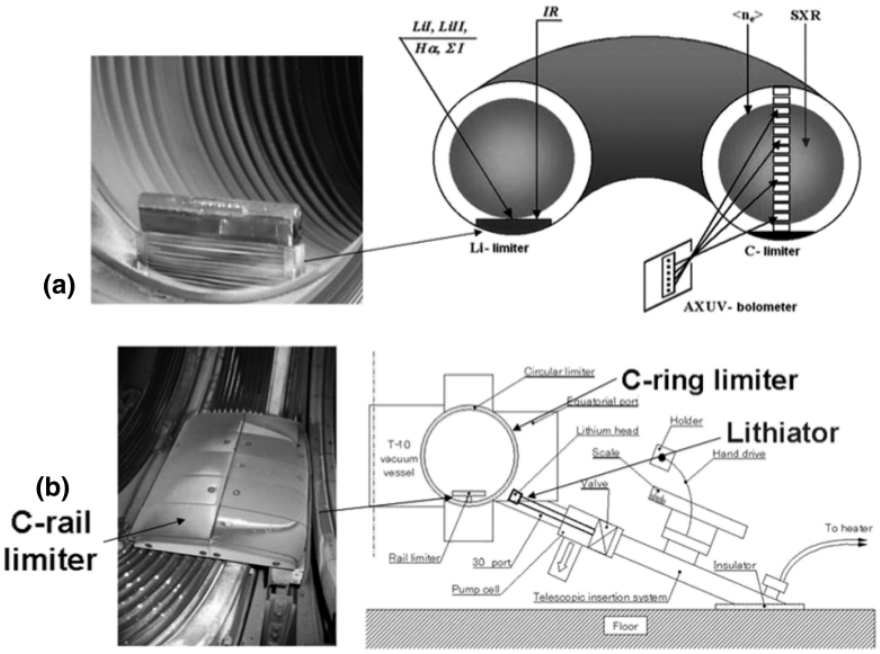


**Figure 2.11:** Schemes of Li experiments in T-11M (a) and T-10 (b) [38].

- liquid Li PFC erosion in the tokamak scrape-off layer(SOL) is a strong function of Li temperature [48]

- Li non-coronal radiation (radiation of non-fully stripped lithium ions) has been found really important. It can cool the tokamak boundary plasma and thus protect the PFC from the high power load during quasi-steady state and disruption regimes. The authors, Mirnov et al., propose the idea of a permanent circulation of Li ions between the plasma and the tokamak PFC, which prevents the full stripping of Li ions up to the coronal model limit. Them supposition is based on the T-11M experiments: a large fraction of the total ohmic heating power was dissipated on the vessel wall by lithium UV radiation [38]. Their estimation shows that for cooling ITER periphery by UV Li radiation about $7g \cdot s^1$ of Li would be needed. A very high value that requires a way to collect the evaporated lithium (closed loop) for a possible use in tokamak;

- the solid matrix of the CPS limiter has high resistance to disruptions [49];

- the temperature of hydrogen desorption for liquid Li has been observed in the window between $320 - 500°C$ [48];

- the *lithium screening* effect can be a practical basis of the closed Li loop [38] [49] concept in steady-state tokamak operations with a Li emitter and collector. The physical origin of lithium screening is still not clear enough. A proposed explanation from the authors

is related to the large difference between the low first (5.8 eV) and high second (75 eV) lithium ionization potentials. As a result, the lithium ions in the plasma SOL ($T_e = 10 - 30eV$) should be mainly in the first ionization state and them friction with the main plasma ions—driven of neoclassical accumulation of high-Z ions into the plasma center should be low.

In figure 2.12 and 2.13 the lithium emitter–collector concept, in two different approaches, is shown. It considers the creation of a lithium circulation loop close to the vessel and plasma periphery with the primary hot limiter ($400 - 700\,^{\circ}C$) as a Li emitter and the secondary limiter in its shadow as a colder Li collector. In many current Li experiments the role of the cold Li collector is played by the entire vessel surface. The Li emitter can work as the main tokamak limiter (see T-11M) but it can also operate as a secondary limiter positioned in the shadow of the main limiter (see T-10, FTU) or in the divertor SOL. Both the limiter were successfully tested during 2000 shots, with a power load up to $10MW \cdot m^{-2}$ and a shot duration of 0.1 – 0.2 s. About 20% shots were concluded by disruptions. The main difference from the SS mesh limiter to the W felt was the increase in heat conductivity of the active CPS layer up to two or three times. No signs of runaway electrons or disruptions were observed on the limiter surface. The same result has been also reported from the FTU liquid lithium experiments [50].

NSTX is an low aspect ratio spherical torus, $R_0$ = 0.85m, a = 0.67 m, $B_T$ < 0.55 T, $I_P$ < 1.5 MA, up to several seconds pulse time. This machine was designed to provide access to new physics regime with very high $\beta$, within the 30 to 43% range, high plasma elongation K < 2.7, and triangularity $\delta$ < 0.8), high bootstrap current and high pressure driven sheared flow [51]. This device is able to produce plasmas with various configurations: inner wall (center stack, CS) limited, single null diverted (LSN) and double null diverted (DN) [52]. A major accomplishment of the NSTX lithium research is the demonstration of the H-mode plasma performance improvements with lithium [53]. At the beginning Li experimentation on NSTX started with a few milligrams of lithium pellets injected into the plasma, and then it has evolved to a dual Li evaporation system (LITER) able to evaporate up to ~160 g of lithium onto the lower divertor plate. Since 2010, the NSTX research with lithium has focused on the effect of liquid lithium divertor (LLD) on the plasma performances. The LLD plate is a copper substrate with a thin (~ 0.2 mm thick) stainless steel layer covered by a ~50% porous molybdenum coating to promote uniform lithium filling by capillary action. During H-mode confinement, plasma performance improvements with lithium divertor coating have been observed with LLD as well. The divertor heat flux reduction observed in NSTX with a

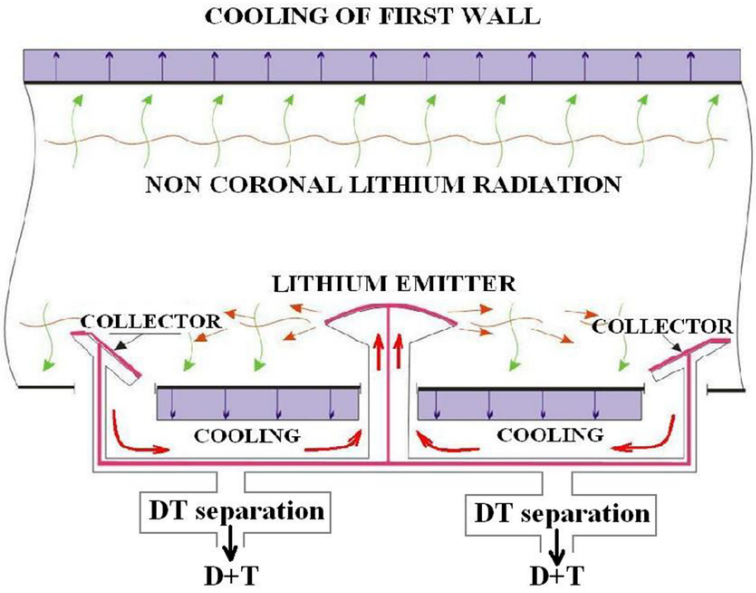


**Figure 2.12:** The principal scheme of the lithium emitter–collector concept with Li emission, plasma cooling by non-coronal Li radiation, Li collection and transport back to the emission region [38].

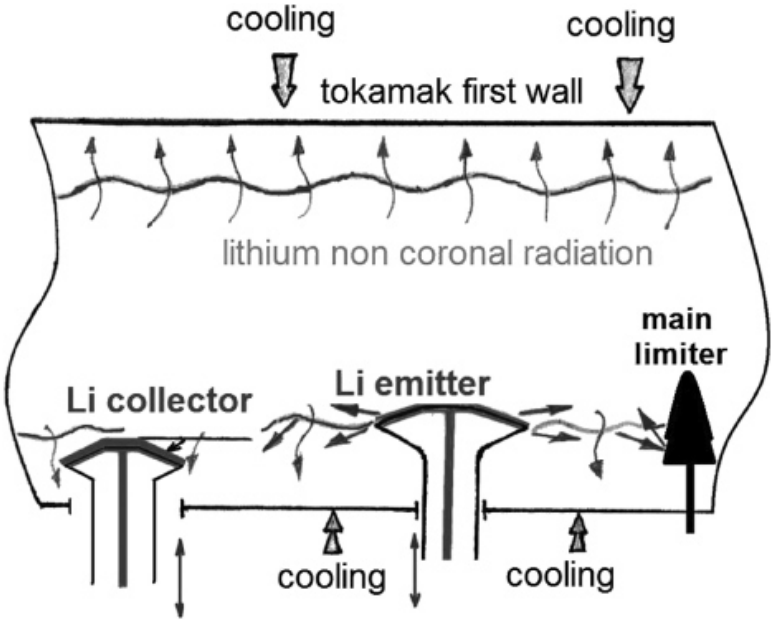


**Figure 2.13:** The principal scheme of the lithium emitter–collector concept with several identical Li limiters in the tokamak chamber, which can change their emitter and collector roles in turns the badminton model [38].

modest lithium application suggests a very interesting possibility of lithium for handling the divertor heat flux.

A conceptual design for a pre-filled liquid lithium divertor target for the National Spherical Torus Experiment Upgrade (NSTX-U) has been presented by Rindt [54]. The target, CPS based, will be supplied with lithium from an internal reservoir. Liquid lithium transport to the surface will be facilitated by capillary forces acting in the structure, which will provide a much larger availability of liquid material at the surface compared to the evaporative scheme used before. The authors point out a list of the main requirements of the future system looking at the NSTX-U specifics request, but also having the possibility to investigate the extrapolation to a reactor:

- high Z fusion relevant material for the substrate
- the component must survive surface temperatures up to 1000 K
- expected stationary heat flux up of 10 MW $m^2$; edge localized modes (ELMs) of 130 kJ in 2 ms at a frequency of 10 Hz, for maximum 5 s.
- avoid droplet
- possibility to pre-loaded the PFC before the installation in the machine
- possibility to clean the surface for diagnostic purpose

LLD has to survive to this heat flux and temperature that means no plastic deformations or recrystallization, and no dry spots on the surface allowing erosion of the high Z material should occur.

During the last years the liquid metals community has grew a lot and lot of effort has been put to achieve thrilling results. We do not have time to analyse all the past experiments so we focused on the small presented group which can be consider pioneer in this field.

A complete overview of the liquid metals experiment performed until now is given by [37].

It is interesting to point out that where liquid lithium has been exposed to plasma (FTU[50, 55, 33], TJII [56, 34, 35], T11 and T10 [28, 57, 27]) or was injected as micro pellets or was strongly evaporated (in the amount of several hundred grams, NSTX [58, 29], EAST [59, 60, 61]) no lithium accumulation was observed in the center of the discharge.

The negligible evaporative flow of lithium up to the surface temperature of 645K becomes unacceptable above 750K. However, it should be noted that the evaporative process creates a cloud of radiant lithium that protects the underlying structure.

Finally, the CPS has been adopted for the concept of liquid metal divertor for DEMO by EUROFusion [1].

## 2.3 Capillary Porous System - CPS

As it indicated in final reports of the EFDA power exhaust (PEX) tasks, the liquid metals in a matrix of Capillary Porous System (CPS) could be a viable solution for the plasma facing materials. The key advantage of liquid metals is the possibility of surface renewal. The CPS provides it by the natural way owing to capillary forces and ensures the liquids confinement on PFC surface.

A detailed study on the liquid-CPS substrate interaction is required for a good choice. Capillary effect requirement in self-healing and liquid stability under magneto hydrodynamic(MHD) forces are determined by the good wetting of CPS material and by the value of surface tension forces.

As mentioned above, the capillary forces in CPS are the main reason for liquid metal stability under MHD effect and its self-healing ability. Capillary effect strongly depends on the wetting angle and on the surface tension of liquids, following the empiric law $P_c = {}^{2\sigma cos(\Theta)}/_{r_{eff}}$, where $\sigma$ is the surface tension coefficient; $\Theta$ is wetting angle; $r_{eff}$ is the effective radius of CPS pore. Assuming the ideal wetting $\Theta = 0$ the estimated capillary pressure $P_c$ vary proportionally with the surface tension for all the above fusion relevant metals. For liquid gallium and tin, the capillary pressure is higher by factor 1.7 and 1.4 respectively in comparison with Li. However, in reality no one of the mentioned element can achieve the total wetting. Surely lithium it the best of the three from this point of view. Wetting angle of 23° is probably the best achieved with tin [62]. The best structural material should be neutron resistant, particularly in terms of secondary unstable isotope; CPS could be ideally DPA damage free. Experiments in DIFFER, performed by P. Rindt, pointed out the CPS working capability is not affected even after a major damage of the porous structure.

The ability of the CPS to confine the liquid metals is determined by the equation

$$P_C > \Delta P_L + \Delta P_G + \Delta P_F + \Delta P_{MHD} \tag{2.1}$$

with $P_C$ the CPS capillary pressure, $\Delta P_L$ the hydraulic pressure drop in the CPS, $\Delta P_G$ the difference in hydrostatic pressure, $\Delta P_F$ the pressure delta due to surface evaporation and $\Delta P_{MHD}$ the pressure due to MHD forces on liquid metal [63] [64]. Capillary pressure in CPS can be estimated from Darcy's law as

$$P_C = \frac{2\sigma cos\,(\theta)}{r_{eff}} \tag{2.2}$$

where $\theta$ is the wetting angle, $r_{eff}$ the effective porous structure radius and $\sigma$ the metal surface tension. The hydrodynamic pressure variation is

$$\Delta P_L = \frac{8m\mu L_{CPS}}{S_{CPS}\varepsilon r_{eff}^2 \delta} \tag{2.3}$$

where m is the evaporation rate, $\mu$ la dynamic viscosity, $L_{CPS}$ the length of the module, $S_{CPS}$ its surface, $\varepsilon$ the volumetric porosity, $\delta$ the metal density. The hydrostatic pressure is simply

$$\Delta P_G = \delta g h \tag{2.4}$$

The pressure due to surface evaporation can be well approximated as half of the lithium vapor pressure $P_{ev}$ [64], which strongly depends on the temperature

$$\Delta P_G = \frac{P_{ev}}{2} \tag{2.5}$$

The pressure variation due to the MHD effects induced on liquid lithium are approximated as

$$\Delta P_{MHD} = \frac{B^2 L_{CPS} v \left(1 + \frac{l}{\gamma}\right)^2 \gamma^2}{\rho l^2} \tag{2.6}$$

where $B$ is the magnetic field, v the linear velocity, $\delta$ ed $l$ due parameters of the CPS structure and $\rho$ la electrical resistivity of the liquid. In the range of temperatures between $400°C$ e $800°C$ , replacing the numerical values of the above mentioned contributions $\Delta P_L + \Delta P_G + \Delta P_F + \Delta P_{MHD}$ magnitude of $10^3 Pa$ are obtained. These pressures are certainly lower than the capillary pressure of the CPS valued up to $10^5 Pa$. This argument ensures that the liquid metal consumption can be compensated when the CPS is used as PFC. The possibility of using the CPS as a first wall during conventional discharges or disruptions strongly depends on the inequality

$$P_C > P_{EM} \tag{2.7}$$

where $P_{EM}$ is the peak pressure generated by the plasma during a disruptive event. The

value of $P_{EM}$ has been estimated for the Liquid Lithium Limiter operated in FTU (EM Loads Lithium Limiter, LTC, Frascati, 23th Sept. 2003) resulting at most in the order of $10^4 Pa$, a value that continues to be lower with $10^5 Pa$. Therefore, the possibility of using the system as the first surface exposed to plasma during the experiments is confirmed.

This technique provides for the presence of a capillary structure, such as a finely woven wire mesh, in which the melted lithium is contained. The capillary forces of the structure itself can compensate for the electromagnetic forces induced by the plasma current on the liquid, as demonstrated experimentally in several devices.

### 2.3.1 Liquid metals operative window

Depending on the impurity and its atomic number the influence on the plasma can be quite different like as fuel dilution for lithium or radiative collapse for tin. In the framework of the liquid metals use as PFC a limit on the material influx to the plasma needs to be set. Coenen [65] proposed to define the limits with respect to the incoming plasma flux, let say magnitude of $10^{24}$ $m^{-2}$ $s^{-1}$. Usually sputtering yields is in the order of 0.1 – 1%, it means an evaporation limit of about $10^{22}$ $m^{-2}$ $s^{-1}$ is a good starting point for the threshold. Of course the maximum plasma pollution is strongly dependent on the impurity species and them capability to reach the plasma core. A different estimation is possible taking in to account the radiative losses and impose that the impurity concentration has to not afflict the plasma performances in terms of radiative losses.

This consideration is more stringent and the tolerable evaporation flux goes down to $10^{20}$ $m^{-2}$ $s^{-1}$. Another key parameter is the re-deposition efficiency, which could extend a lot the so-called *operative window*. This term is usually used to describe the temperature range we can use a certain liquid metal in a tokamak. Taking for example Li and Sn, the second allows for comparably high surface temperatures due to low evaporation and material losses even when not considering re-deposition efficiency. A good picture is given by Coenen in figure 2.15a. The boundary temperature are given essentially starting from the melting point until the maximum acceptable level of the evaporative flux. But an upper limit could also be set due the compatibility between the liquid and the support structure. Liquid metals are really corrosive and this undesirable effect increase with temperature. So at a certain temperature we could have corrosion issue with the substrate material instead be blocked from the plasma pollution. In figure 2.14 an overview of the different vapour pressure as a function of the surface temperature is given. For lithium and tin the coloured area highlights the operative window for both considering as acceptable a flux of $10^{22}$ $m^{-2}$ $s^{-1}$.

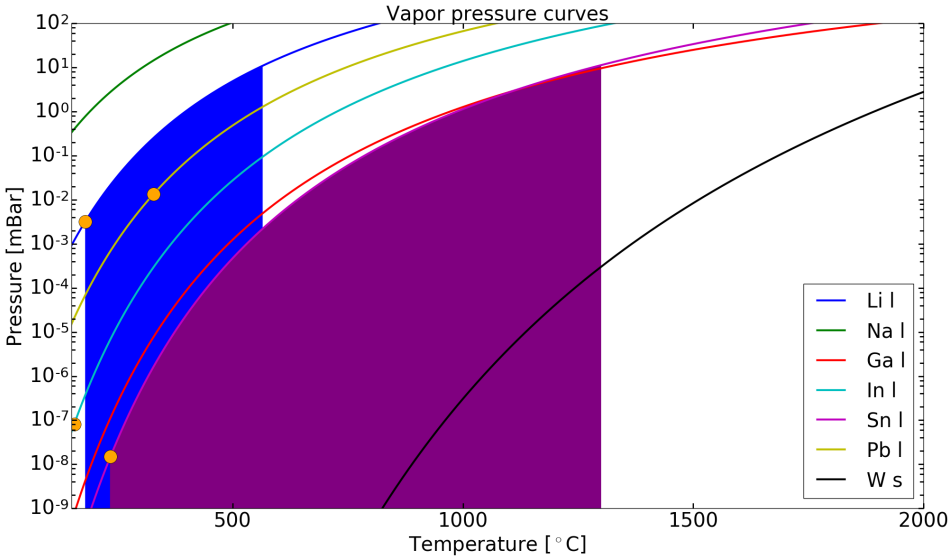


**Figure 2.14:** Vapor pressure versus temperature for a set of liquid metals. Tugsten has been showed to simply the comparison to the readers. In blue and violet are respectively highlithed the operative windows for Li and Sn assuming as acceptable a flux of $10^{22}$ $m^{-2}$ $s^{-1}$. The yellow dots indicate the melting point.

For pure elements the Antoine equation is good estimator of the vapor pressure as a function of surface temperature. In particular such quantities are correlated by $p_{ev} = 10^{(a-\frac{b}{T_s+c})}$ where $p_{ev}$ is the vapor pressure in bar and $T_s$ the temperature in K, $a, b, c$ are experimental coefficients found in [66] and [67]. The vapor flux in atoms per second could be calculated starting from the vapour pressure as in equation

$$\phi = \frac{p_{ev} e^{-\frac{\Delta H}{K_B T_s}}}{\sqrt{2 k_B T_s \pi m}} \tag{2.8}$$

where $\Delta H$ is the enthalpy of vaporization, $k_B$ is the Boltzman constant, $T_s$ the surface temperature and $m$ is the element's atomic mass.

In figure 2.15b are visible the evaporation rate of Li and Sn as a function of surface temperature. It is clear, from the picture, the importance of the intrinsic operative temperature window that each element has in a tokamak or fusion relevant device.

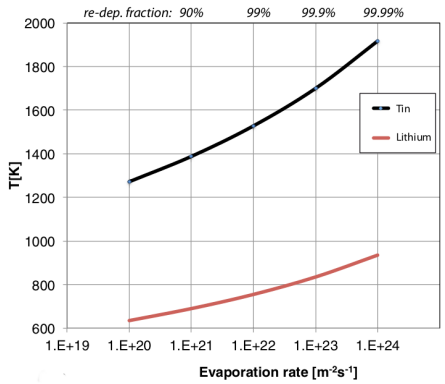


**(a)** The upper bound of the operation window in function of the considered re-deposion, from Coenen [65].

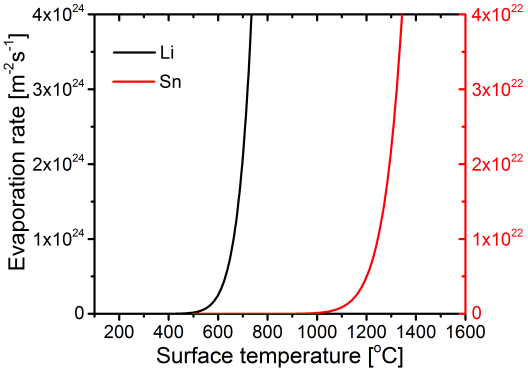


**(b)** Evaporation rate of Li and Sn as a function of surface temperature. Cortesy of M. Poradziński [68].

**Figure 2.15:** Operative windows and evaporation rate for lithium and tin.

*I will drive flat out all the time... I love racing.*

Gilles Villeneuve

# 3 Tokamak experiments

In this chapter, the liquid metals experiments carried on the Frascati Tokamak Upgrade are shown. The liquid lithium limiter and the liquid tin limiter systems are described starting from the engineering features, after that the impacts of liquid materials on plasma performances are singularly analysed and reported. A phenomenological model is proposed to explain the vapor shield effect observed with the liquid lithium limiter. The results of the first experiments with the liquid tin limiter are presented. After that, the thermal analysis of the tin sample exposed in the ISTTOK tokamak is illustrated.

## 3.1 Lithium Limiters

### 3.1.1 Liquid Lithium Limiter

In 2005 the first experiment with a *Liquid Lithium Limiter (LLL)* took place in Frascati [50]. The limiter was developed in collaboration and provided by the *Federal State Unitary Enterprise "Red Star"*. The tokamak FTU was equipped with three modules lithium limiter, it was supposed to operate in the shadow of the main limiter in order to investigate the *lithization* phenomena. The use of lithization as wall conditioning technique was one of the first motivation to test the lithium limiter in FTU, so it first purpose was to act as *lithium evaporator*. Similar experiments have been performed also in RFX-Mod device in Padua [69]. The limiter overview is given in figure 3.1.

The Liquid Lithium Limiter was based on the *Capillary Pore Systems (CPS)* structures.

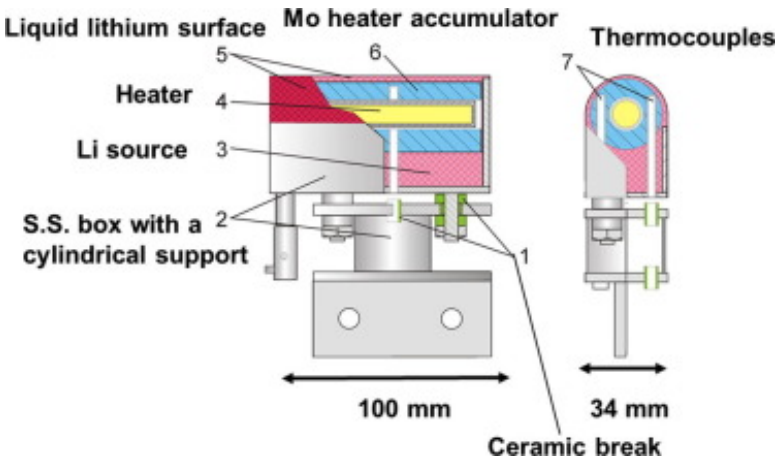


**Figure 3.1:** Structure of a liquid lithium limiter module: 1. ceramic break; 2. AISI 304 stainless steel frame; 3. liquid lithium tank; 4. electrical heater; 5. CPS surface interacting with plasma, 1mm thickness and pores radius of 15 $\mu$m; 6. Mo heater accumulator; 7. thermocouples housing.

The single unit is shown in the figure 3.1, it consists of: (1) ceramic break; (2) stainless steel frame and support structures; (3) liquid lithium tank; (4) electrical heater; (5) CPS surface interacting with plasma, 1mm thickness and pores radius of 15 $\mu$m; (6) heater accumulator; (7) thermocouples housing; removable protective stainless steel foil.

The main parameters of the LLL are summarized in table 3.1.

A crucial point was the CPS solution assessment in a tokamak environment. It was very important to demonstrate the CPS capability of liquid metal confinement and surface refilling for a long series of possible applications and studies. The whole system has been designed to be inserted from the bottom of the machine (PORT-01).

The structural materials are all non-magnetic, compatible with the chemical aggressiveness of lithium up to $600°C$ [70] and with a low vacuum degassing coefficient:

- boxes, support elements, capillary mesh are in stainless steel;
- the heat accumulator is in pure molybdenum;
- the electrical insulators are in pure alumina;
- the heating element resistors are made of W-20Re tungsten alloy;
- the lithium used is natural lithium ($^6Li$ - 7.42%; $^7Li$ - 92.58 %) LE-1 quality complies with the Russian standard GOST 8774-75.

In the figure 3.2 the system is shown in its entirety.

Analytical models and finite element calculations supported the system design [71]. In particular, it was necessary to study the compatibility with the mechanical stresses induced by sudden changes in temperature and stresses induced by electromagnetic forces, figure 3.3.

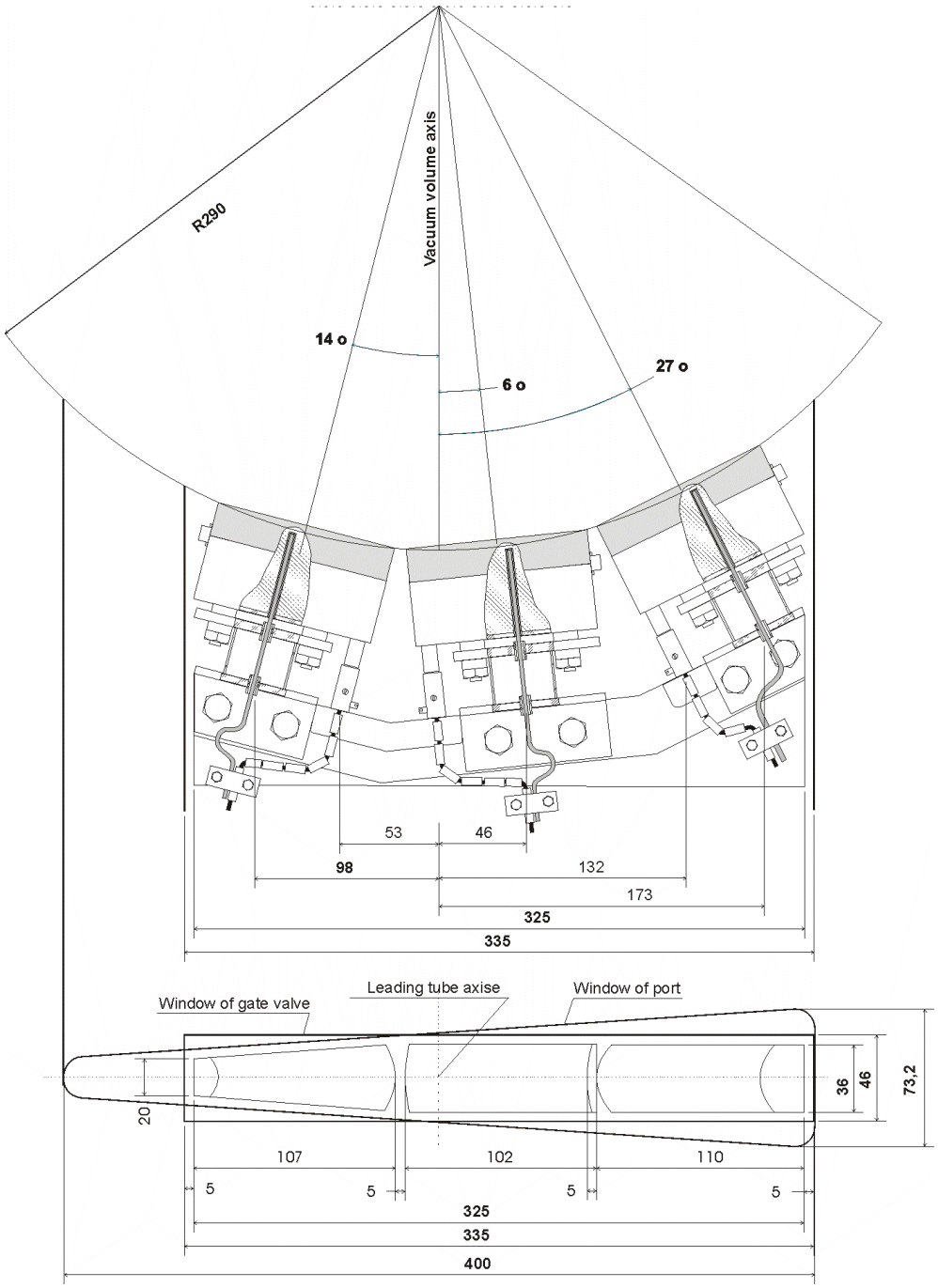


**Figure 3.2:** LLL system viewed from the front and from the top with respect to the size of the the vacuum chamber access port. All the measures are in millimiters.

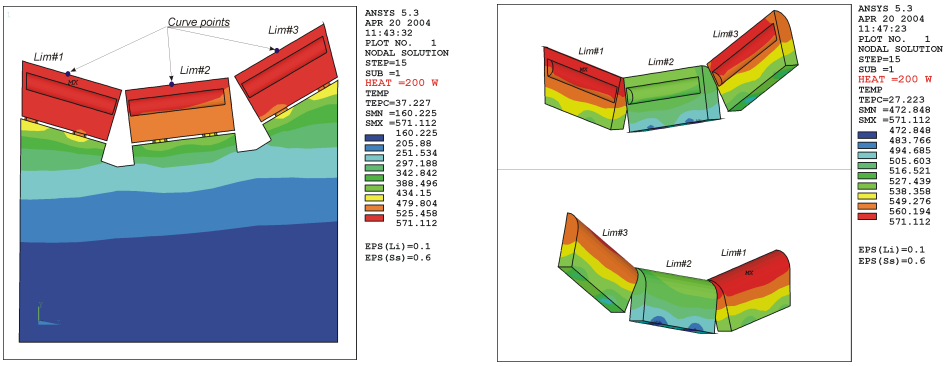


**Figure 3.3:** Temperature distribution in the lithium limiters and support plate for steel emissivity of 0.6 and 200 W power for each heater

| Main technical parameters of Lithium Limiter | Value |
|---|---|
| Total area of opened lithium surface | $170\,cm^2$ |
| Total lithium surface interacting with plasma | $85\,cm^2$ |
| Lithium volume | $165\,cm^3$ |
| Total lithium mass | $82\,g$ |
| Lithium surface temperature provided by heater | $180 - 500°C$ |
| Numbers of plasma shots | $> 1000$ |
| Capillary pressure | $10^5\,Pa$ |

**Table 3.1:** Table summarizing the main parameters of the LLL in-vessel element.

The distributed load of a heat flow of $10\,{}^{MW}/_{m^2}$ on the surface of liquid lithium is shown in the figure 3.4.

The temperature of the surfaces of the three modules was monitored during plasma discharge using infrared sensors. Scheme of the cryostat and photo-detector connected to the optical channel are given in figure 3.5 and 3.6 respectively.

Response times of common commercial infrared sensors in the order of $5 \div 40\,ms$ and their reduced applicability to metal surfaces with low emissivity required the development of a dedicated device for monitoring the temperature of the lithium limiter for FTU. The light was collected and carried into the photodiode by IR fibers.

The device installed on FTU in autumn 2005 was inclusive of four HgCdTe photodiodes, shown in figure 3.6, located at the bottom of a cryostat, visible in the figure 3.5, immersed in a liquid nitrogen storage vessel from the capacity of 16l, polycrystalline infrared optical fiber in silver halides and a focusing lens in Ge with anti-reflective coating.

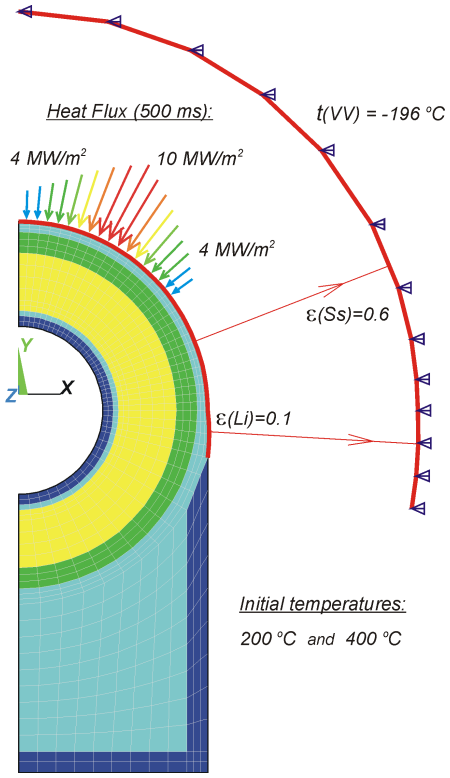


**Figure 3.4:** Finite element simulation model for the analysis of the thermal transient to which the single module is subjected during a plasma shot. The emissivity of lithium and steel is taken into account.

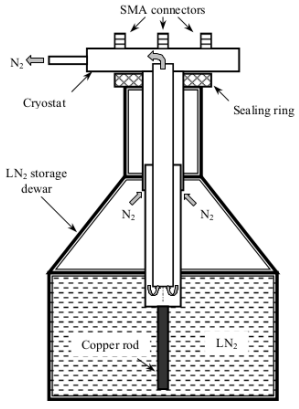


**Figure 3.5:** Cryostat of the photo sensors

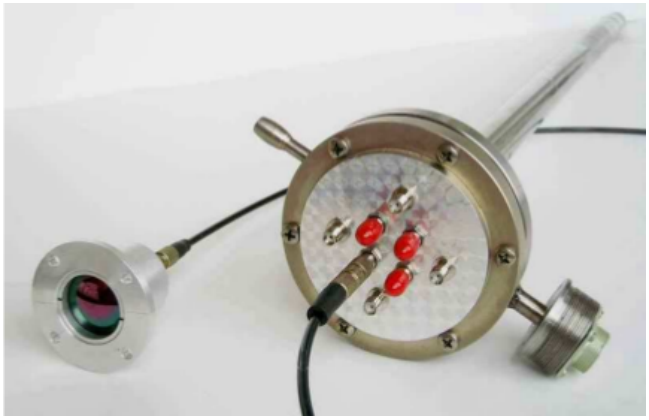

**Figure 3.6:** LLL photo sensors.

The liquid lithium limiter is shown in plasma as a mirror surface, whose emissivity in the temperature range of interest $200 \div 800°C$ it's around $5 \div 10\%$ of blackbody radiation. It was considered appropriate to move into the middle and far infrared optical band with a cut-off of the wavelength of $\lambda_{co} = 6.7\mu m$ for three of the four channels and $\lambda_{co} = 9\mu m$ for the last channel in order to lower the lower limit temperature if desired.

Part of the data collected in the past during the campaigns with the liquid lithium limiter in the years 2008/2009 have been the subject of successive elaborations. In particular in the development of a phenomenological interpretation of the data, as will be shown in the next section.

### 3.1.2 Cooled Lithium Limiter

The *Cooled Lithium Limiter (CLL)* was inserted in the framework of the EFDA plasma-wall interaction research to further investigate plasma physics and technology for a CPS based solution in a future fusion reactor. Since the positive results achieved with the LLL also from the point of view of the power exhaust, it was decided to study more in detail this aspect with a new lithium limiter. This type of basic unit can be applied, for example, both in device type limiter and divertor type. The FTU CLL system consists of the following components including secondary systems also used in the previous version of the Liquid Lithium Limiter, references in figure 3.7:

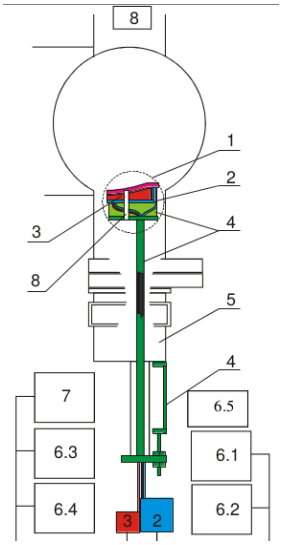


**Figure 3.7:** Overview of the CLL system.

- element with CPS structure where lithium is housed, it is the element actually in contact with plasma (1)
- cooling and heating system for the thermal stabilization of the lithium surface (2)
- lithium power supply system for possible on-site lithium refill (3)
- load-bearing structure with positioning mechanism (4)
- empty volume for visual inspection (5)
- vacuum (6.1), inert gas (6.2), pressurized air (6.3), supply (6.4), cold water (6.5) secondary systems,

CV1...CV4 - check valve
ET - expansion tank
EH1 - electrical heater 0.5 – 1 kW
EH2 - electrical heater 1.5 – 3 kW
EH3 - electrical heater 70 W
EH4 - electrical heater 140 W
HC1...HC2 - hydraulic cylinder
IP - insulated plug of water pipes
LD - lithium dispenser
PV1...PV6 - pneumatic control valve
PR - pressure reducer
PC - pneumatic power cylinder
P1 - vacuum meter
P2 - pressure meter
P3 - pressure meter
RV - relief valve
TR1...TR4 - throttle regulator
T1...T14 - thermocouple
V1...V2 - ball valve
V3, V9 - needle valve
V4...V6 - needle valve
V7...V8 - control valve
WT1...WT2 - water tank

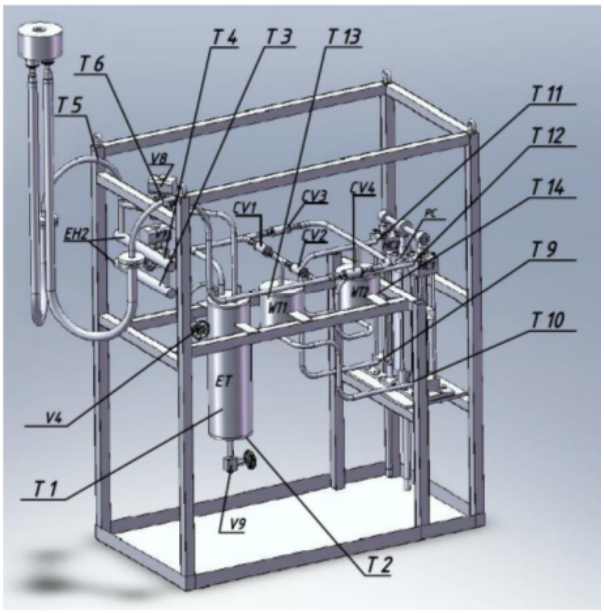


**Figure 3.8:** Schematic view of the CLL system, including hydraulic and electric circuits.

- automatic control unit for the cooling / heating system with diagnostics (7)
- dedicated diagnostics (infrared sensors, Langmuir probes, etc.) (8).

The CLL is positioned on a mobile support structure through which is possible to access the visual inspection of the limiter without necessarily breaking the vacuum and compromising the chemical composition of the lithium surface. In tables 3.2 and 3.3 the main parameters of the experiment are shown. The CLL heating system is able to operate in two modes: the first, *Pause mode*, represents the stationary condition between the plasma shots, the element is brought to the temperature of 200 °C, the second mode, *Plasma-mode* instead activates few moments before of plasma discharge up to 10 seconds later allowing higher heat removal capability. Figure 3.9 shows the system pressure as a function of temperature, so that water remains in a liquid state beyond the normal boiling temperature. The two modes differ substantially due to the water flow to the CLL element.

The functional scheme and the general view of the system are presented in figures 3.8, 3.10. The heat removal ( 100kW) from the system as well as its heating are due to the same water flow at 200°C. The water is heated up to this temperature by two electric resistors (EH1-1, EH1-2),

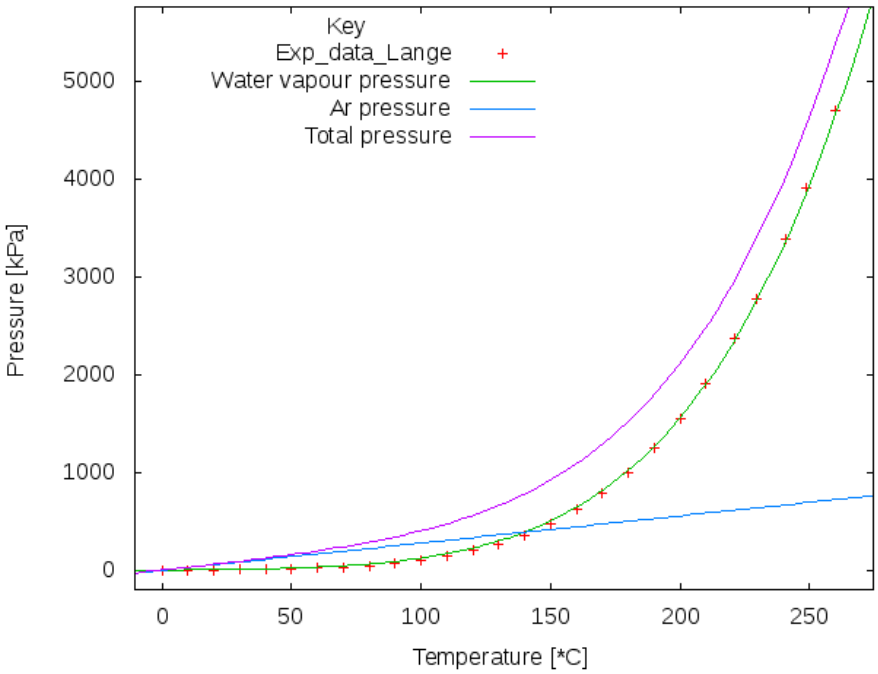


**Figure 3.9:** CLL system pressure versus water temperature [72].

| Parameter | Value |
|---|---|
| Power flux to the surface | up to $10MW \cdot m^{-2}$ |
| Discharge duration | up to 5s |
| Plasma current | < 1.6 MA |
| Toroidal magnetic field | < 8 T |
| Expected number of shots | > 100 |
| Initial lithium surface temperature | >190 °C |
| Lithium surface temperature during the plasma interaction | up to 800 °C |
| Power of heat removal | up to 100 kW |
| Plasma interaction area | 100 $cm^2$ |
| Lithium amount (volume/weight) | up to 80 $cm^3$ / 40 g |
| Element dimensions (LxHxW) | 330 x 205 x 32 mm |

**Table 3.2:** Main parameters of the invessel element.

| Parameter | Value |
|---|---|
| Heat transferring liquid | Distilled water |
| Total water volume | 15l |
| Air pressure in the secondary system | 0.7 MPa |
| Ar pressure in the water system | 0.8 MPa |
| Heating power | |
| -> Plasma mode | 1kW |
| -> Pause mode | 7kW |
| Heat removing power | <100kW |
| Time of operation | |
| -> Pause mode | $\infty$ |
| -> Plasma mode | 15s |
| Typical water temperature | |
| Pause mode | 220 – 230 °C |
| Plasma mode | 200 – 210 °C |
| Maximum pressure in the system | 5 MPa |
| Typical water flow rate | |
| -> Pause mode | 0.05 l/s |
| -> Plasma mode | 0.5 l/s |
| Overall dimensions outvessel system L x H x W | 158 x 145 x 63 cm |
| Total system weight | 170 kg |

**Table 3.3:** Main parameters of the outvessel system.

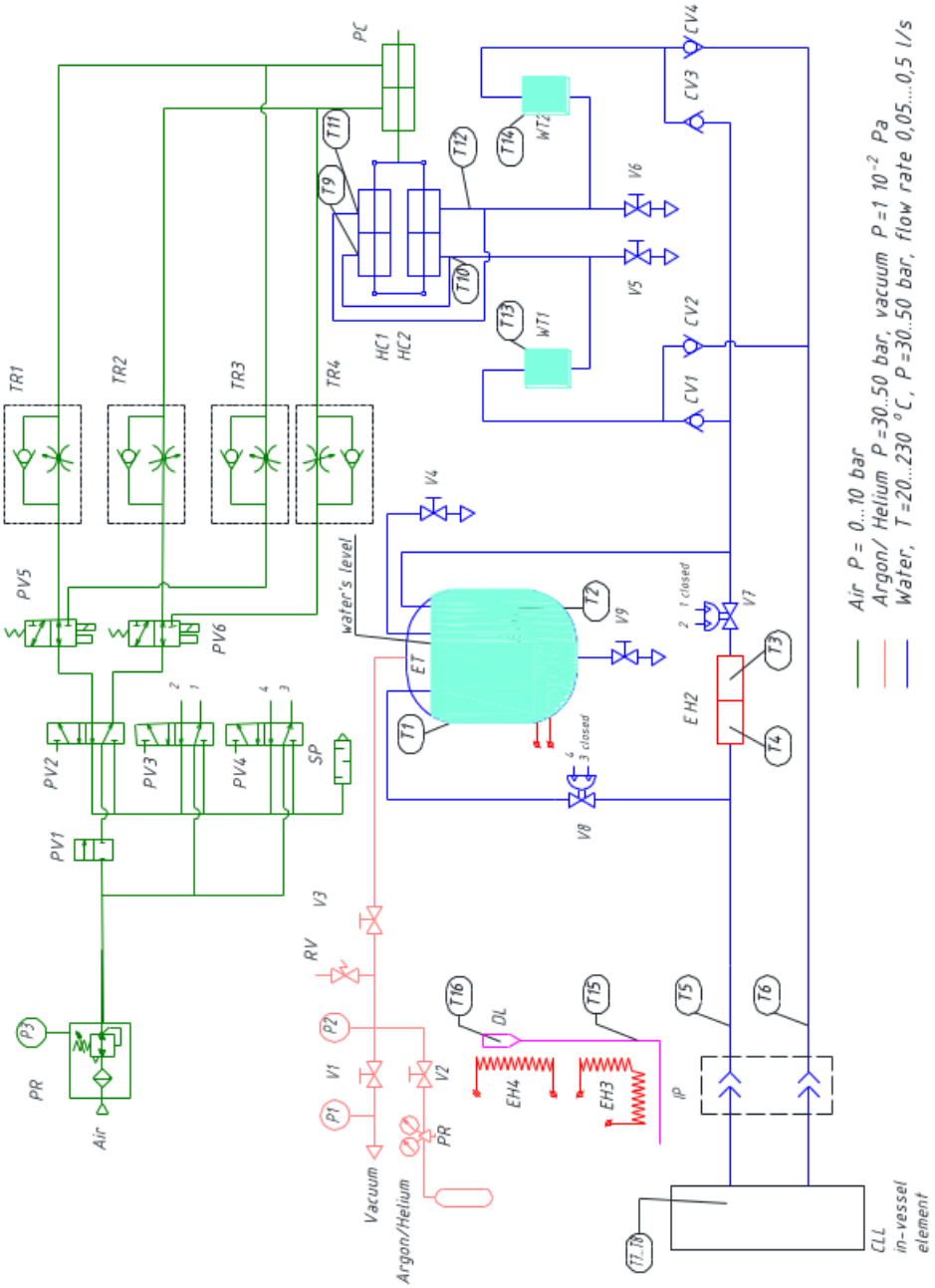


**Figure 3.10:** Schematic view of the CLL system, including hydraulic and electric circuits [72].

the first is located in the ET water expansion tanks, while the second is located on the water rise line towards the CLL element. The temperature in the expansion vessel is around 230 °C and it is always greater, at least twenty degrees than that of the rest of the system. This ensures that the whole circuit is pressurized, avoiding possible local boiling phenomena and therefore the formation of air bubbles. The circulation of the cooling liquid is carried out by the hydraulic cylinders HC1, HC2, with the possibility to adjust the pistons sliding speed and therefore tune the water flow. With reference to the figure 3.10 the complete refrigerant flow circulation cycle is as follows: WT1-CV1-ET-V8-CLL-CV4-WT2-CV3-ET-V8-CLL-CV2-WT1. The water tanks WT1 and WT2 have the function of heat exchangers, they cool down the water before it is pushed by the hydraulic cylinders and cycle restarted. This limitation is due to the fact that the sealing gaskets of the cylinders HC1, HC2 cannot operate at temperatures higher than 60 °C. The whole system is protected against overpressure by means of a safety valve with a pre-set value of 59bar. Before being put into operation, the system is pumped under vacuum at about $10^{-3}$ bar, then filled with distilled water. An initial pressure of Ar in the system of 0.8MPa is injected. The final version of the system includes a lithium distributor with electric heaters (EH3, EH4) and thermocouples (T15, T16), to possibly refill the dispenser with lithium. Dispenser contains about 140 $cm^3$ of lithium, equivalent to 70g. The lithium refilling procedure can be performed at the temperature of 200 °C of the CLL and 250 °C of the dispenser. The system is equipped with a monitoring unit and a control unit for temperature regulation. They are connected to the computer for remote control and for data acquisition via RS-485 interface and USB / RS-485 AS4 conversion unit. The first setup resulted in quite large temperature fluctuations (about tens of degrees) as shown in figure 3.11c. In order to understand the origin of such high temperature fluctuations, the command of the PID controller was analysed and a new specific controller was implemented which also allows a higher control frequency of the electric heater [72].

The PID analysis is summarised in figure 3.11. The relation between the water temperature fluctuations and the current flowing in the resistance is shown. The system exhibits a clear relationship between the oscillations and the working frequency of the PID controller actuator, in fact, as is visible from the picture 3.11 the temperature fluctuation tends to be dumped as soon the controller actuation time is decreased. The initial control strategy was able to open and close the current circuit in bunches with a characteristic time in the order of a tenth of a second. So it has been decided to develop a new actuation system able to work at a higher frequency. It has been chosen a random turn-on solid state relay that is able to close the circuit immediately after the command signal and open it again as soon as the zero-crossing. An

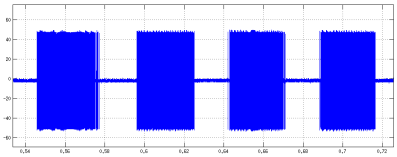

**(a)** Current through the heater resistor.

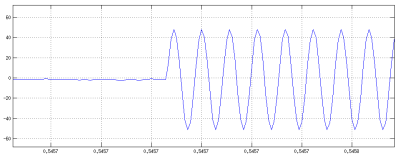

**(b)** Detail, current through the heater resistor.

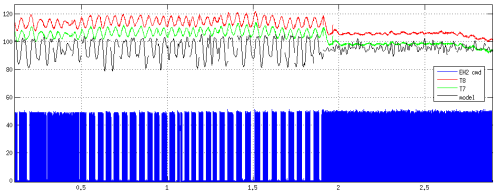

**(c)** Analysis of the current through the heater resistor. The actuation time of the controller seem too low for the FTU CLL water circuit. In plot in a.u. are shown the water temperature close to in-vessel element (red and green curves), the current through the heater resistor (blue) and the Fourier analysis of the current signal cut at the characteristic time of the water system [72].

**Figure 3.11:** Analysis of the electric heater actuation. The control stratergy and the typical heating bunch is shown in figure 3.11a and in detail in figure 3.11b. In figure 3.11c the temperature and the actuation are shown, increasing the actuation frequency the oscillation are dumped [72].

example of this is given in figure 3.12, where the current through the resistor and the relay command are plotted.

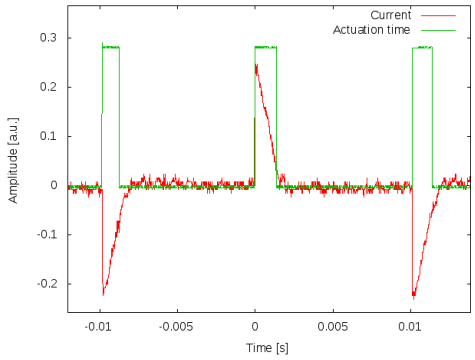


**(a)** Current through the heater resistor.

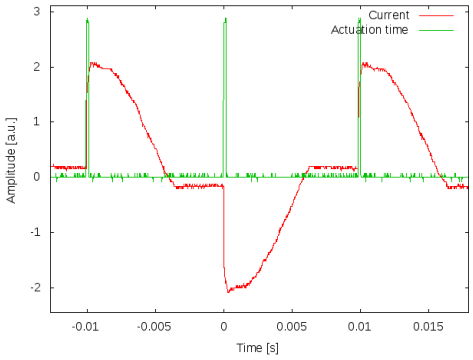


**(b)** Detail, current through the heater resistor.

**Figure 3.12:** Current, in red, through the heater resistor with the new random turn on SSR in a.u., the relay command is plotted in green.

The new control system, developed during the debugging phase in Frascati, has shown the possibility to operate without the previously observed oscillations. Unfortunately the CLL

was damaged before the FTU experimental campaign resumed, the molybdenum tube of the in-vessel unit cracked preventing the plasma exposure of the cooled lithium limiter.

Anyway, it was decided to operate the limiter without the active cooling for a short experimental campaign. However, this did not allow the limiter to get too close to the last closed magnetic surface also due to the reduced structural rigidity. The goal of this campaign was to continue the work started on the diagnostics set up and in particular on the Langmuir probes and on the infrared camera [73], [74]. During those experimental days, the old CAMAC acquisition system of the Langmuir probes began to move towards the new PXI. This allowed to have more memory available and to be able to memorize the entire duration of the shot, which was not possible with the old system as it was limited to a few hundred milliseconds. The old lithium limiter was sent back to the factory for the reparation and it is now available in Frascati. Unfortunately since its arrival in the laboratory, it has not been possible to perform any experimental campaign on FTU due to a major fault in the power supply system.

## 3.2 Vapor shield model

We are going to introduce the experimental results and analysis obtained with the lithium limiters.

The simplified scheme of the FTU lithium experiment is shown in figure 3.13 together with on overview of the available diagnostics.

The following results are referred to a medium density shot $n_e = 1.0 \cdot 10^{20} m^3$, with $I_p = 0.5MA$, magnetic field $B_T = 6T$. In this case, the LLL was placed at the shadow of the main toroidal limiter at a distance of $D_{lcms} = 1.5cm$ from the vacuum chamber walls and at about 2 cm behind the LCMS. This discharge was characterized by stable conditions of plasma current and density and absence of MHD events. In figure 3.15 a visible picture of the FTU plasma operation with the lithium limiter. The green light is given by the $Li^+$ most intense line in the visible spectra. The most interesting features for this shot are represented by its radiative characteristics related to the temporal behaviour of the Li surface temperature.

In figure 3.14a, starting from the top, it is visible the temporal trend of the Li surface temperature for the LLL central unit followed by the evolution of the neutral Li and $Li^+$ emission line intensities and of the total plasma radiation.

The temporal window of the plots corresponds to the flat top of the plasma current and it has been chosen to point out the increase of the lithium surface temperature ($T_{s_{Li}}$) and of neutral Li and $Li^+$ emission line intensities under the plasma heat flux. This trend continues

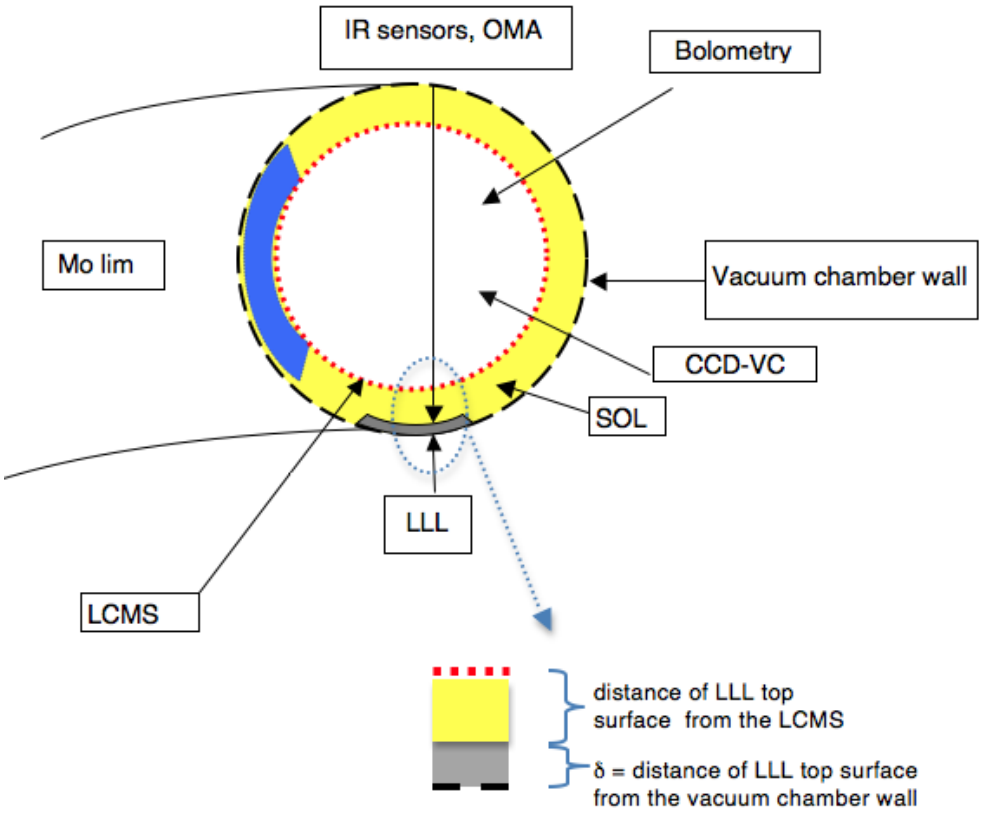


**Figure 3.13:** Schematic view of LLL experiment - IR: infrared sensors for measurement of lithium surface temperature; OMA: Optical Multi-channel analyzer looking at the LLL; Bolometry: bolometric signals for the measurement of total radiation losses; CCD-VC: Video camera for observing the visible plasma radiation - LCMS and SOL indicate the last closed magnetic surface and the Scrape-off layer respectively. The distance of LLL top surface from the LCMS can be varied shot by shot.

until, for $t > 1.29s$, an increase of the bolometric signal takes place that is accompanied with a decrease of $T_{s_{Li}}$. This effect is due to the growth of evaporated Li flux and to the strong Li radiation in non-coronal equilibrium that leads to a reduction of the heat flux on the lithium surface. The decrease of the neutral Li line (see Li in figure 3.14a) explains the behaviour of LLL surface temperature that rises again until evaporated atoms produce the same effect as previously observed. A clear evidence of an oscillation of LLL surface temperature is visible on a larger time scale in figure 3.14b for the three modules. A similar phenomenology was also previously observed in stable plasma discharges with thermal loads as high as $2^{MW}/_{m^2}$ as will be shown later in figure 3.32b. A discrepancy was noticed between the experimental conditions and the results of the ANSYS code simulations. With ANSYS in fact, a continuous rise of the

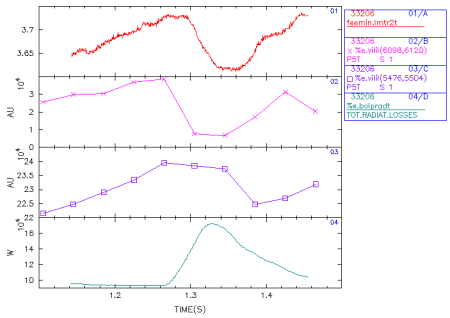


**(a)** Starting from the top: surface temperature, line intensity for LiI, line intensity for LiII, bolometric signal versus time

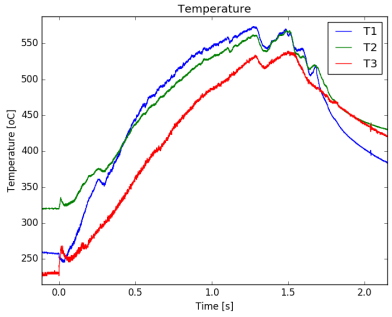


**(b)** Temperature from the middle point of each module of the LLL

**Figure 3.14:** Overview of a shot with the liquid lithium limiter

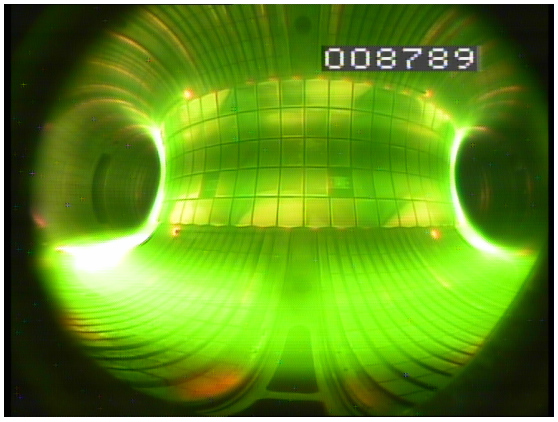


**Figure 3.15:** Visible picture of the FTU plasma during the lithium limiter experiments.

Li temperature was found and explained by the absence in the code of a dissipation term for the plasma heat flux. Another thing is to be noted in figure 3.14a, i.e. the minimum value of the $Li^+$ spectral line appears shifted at a longer time than that of neutral Li atoms. One of the most discussed topics in the use of liquid metals as PFC is the vapour shield phenomena of which G. G. Van Eden gives an exhaustive explanation in [32]. A zero dimensional code has been developed and applied to the data collected on FTU using the LLL. Two fundamental terms for the model development, namely the power flux evaluation and the cooling rate, will be singularly analysed below.

### 3.2.1 Power flux evaluation

In this subsection, the theory and the approximation used for the power flux evaluation [75] [76] on the limiter are reported. When the surface of a semi-infinite region, initially at temperature $T = T_i$, is cooled (or heated) at temperature $T = T_\infty$, we can write $T - T_\infty$ as a function of: temperature difference from the initial state $T_i - T_\infty$; t time; x position, with the axis x perpendicular to the surface of the semi-infinite solid, the other two spatial coordinates are considered invariants of the system; $\alpha$ heat diffusion coefficient (or thermal diffusivity), defined as the relationship between thermal conductivity and the product between density and specific heat of the body, i.e. $\alpha = \frac{k}{\rho c_p}$, $\alpha$ is measured in $m^2/s$ .

$$T - T_\infty = h(t, x, \alpha, T_i - T_\infty) \tag{3.1}$$

Taking advantage of a dimensional analysis we can reduce the five variables that play in two dimensionless groups

$$\underbrace{\frac{T - T_\infty}{T_i - T_\infty}}_{\vartheta} = f\underbrace{\left(\frac{x}{\sqrt{\alpha t}}\right)}_{\xi} \tag{3.2}$$

Position and time collapse in a single dimensionless variable. We define $\Delta T = T_i - T_\infty$ and we rewrite the boundary conditions $T_i$ and $T_\infty$ using the mathematical formalism

$$T(x = 0) = T_\infty \quad or\ using\ \vartheta \quad \vartheta(\xi = 0) = 0 \tag{3.3}$$

$$T(t = 0) = T_i \quad or\ using\ \vartheta \quad \vartheta(\xi = \infty) = 1 \tag{3.4}$$

Now it is possible to transform the equation to the partial derivatives, which describes the heat conduction, in an ordinary differential equation in the variable $\xi$.

$$\frac{\partial^2 T}{\partial x^2} = \frac{1}{\alpha}\frac{\partial T}{\partial t} \tag{3.5}$$

We can write

$$\frac{\partial T}{\partial t} = \Delta T\frac{\partial \vartheta}{\partial t} = \Delta T\frac{\partial \vartheta}{\partial \xi}\frac{\partial \xi}{\partial t} = \Delta T\frac{\partial \vartheta}{\partial \xi}\left(-\frac{x}{2t\sqrt{\alpha t}}\right) \tag{3.6}$$

$$\frac{\partial T}{\partial x} = \Delta T \frac{\partial \vartheta}{\partial x} = \Delta T \frac{\partial \vartheta}{\partial \xi}\frac{\partial \xi}{\partial x} = \Delta T \frac{1}{\sqrt{\alpha t}}\frac{\partial \vartheta}{\partial \xi} \tag{3.7}$$

$$\frac{\partial^2 T}{\partial x^2} = \Delta T \frac{1}{\sqrt{\alpha t}}\frac{\partial^2 \vartheta}{\partial \xi^2}\frac{\partial \xi}{\partial x} = \Delta T \frac{1}{\alpha t}\frac{\partial^2 \vartheta}{\partial \xi^2} \tag{3.8}$$

Substituting the 3.6 and the 3.8 in the 3.5 we get

$$\frac{d^2\vartheta}{d\xi^2} = -\frac{\xi}{2}\frac{d\vartheta}{d\xi} \tag{3.9}$$

in which you can see from the notation the transition to total derivatives. Calling $\frac{\partial \vartheta}{\partial \xi} = \chi$ so the equation 3.9 becomes

$$\frac{d\chi}{d\xi} = -\frac{\xi}{2}\chi \tag{3.10}$$

such equation integrated once provides

$$\chi \equiv \frac{d\vartheta}{d\xi} = C_1 e^{-\frac{\xi^2}{4}} \tag{3.11}$$

integrating a second time

$$\vartheta = C_1 \int_0^{\xi} e^{-\frac{\xi^2}{4}} d\xi + \vartheta(0) \tag{3.12}$$

Now taking into account the boundary conditions 3.3 and 3.4, $\vartheta(0) = 0$ and for $C_1$

$$\vartheta(t=0) = 1 = C_1 \int_0^{\infty} e^{-\frac{\xi^2}{4}} d\xi = \sqrt{\pi} \qquad \Rightarrow \qquad C_1 = \frac{1}{\sqrt{\pi}} \tag{3.13}$$

so the general solution of the heat conduction problem in semi-infinite solid approximation with the aforementioned boundary conditions can be written as

$$\vartheta = \frac{1}{\sqrt{\pi}} \int_0^{\xi} e^{-\frac{\xi^2}{4}} d\xi = \frac{2}{\sqrt{\pi}} \int_0^{\frac{\xi}{2}} e^{-s^2} ds \equiv erf(\xi/2) \tag{3.14}$$

According to the Duhamel principle the solution of a problem with a non-zero source (ordinary non-homogeneous differential equation) can be obtained as an overlap of solutions of the problem with null sources (homogeneous ODE), but having the initial data of the source in a given $\tau$ in the range $0 < \tau < t$ Considering, for example, the Cauchy problem for

the ordinary non-homogeneous differential equations

$$\begin{cases} \frac{dy}{dt} = ay + f(t) \\ y(0) = 0 \end{cases} \tag{3.15}$$

and applying the just expressed Duhamel principle we solve for $\quad \forall\, 0 < \ tau < t$

$$\begin{cases} \frac{dz(t,\tau)}{dt} = az(t,\tau) & a\,\epsilon\,(0,\infty),\ \ f\,\epsilon\,C([0,\infty)) \\ z(\tau,\tau) = f(\tau) \end{cases} \tag{3.16}$$

whose solution is

$$z(t,\tau) = f(t)e^{a(t-\tau)} \qquad t > \tau \tag{3.17}$$

and overlapping we get the solution

$$y(t) = \int_0^t z(t,\tau)d\tau = \int_0^t f(\tau)e^{a(t-\tau)}d\tau \qquad t > 0 \tag{3.18}$$

Duhamel principle can be applied to heat conduction problem in order to simplify the analytic solution. The equations of heat transmission under appropriate conditions can be written as:

*If* $v = F(x, y, z, \lambda, t)$ *represents the temperature in* $(x, y, z)$ *at the time t in a solid with initial temperature equal to zero, while the surface temperature is* $\phi(x, y, z, \lambda)$*, then the solution to the problem is given by*

$$v = \int_0^t \frac{\partial}{\partial t} F(x, y, z, \lambda, t - \lambda)d\lambda \tag{3.19}$$

It is possible to say that when the surface temperature is zero from $t = -\infty$ to $t = 0$ and $\phi(x, y, z, \lambda)$ from $t = 0$ to $t = t$, the temperature at time t is given by

$$v = F(x, y, z, \lambda, t) \qquad t > 0 \tag{3.20}$$

when the surface temperature is zero from $t = -\infty$ to $t = \lambda$ and $\phi(x, y, z, \lambda)$ from $t = \lambda$ to $t = t$ we have

$$v = F(x, y, z, \lambda, t - \lambda) \qquad t > \lambda \tag{3.21}$$

furthermore, when the surface temperature is zero from $t = -\infty$ to $t = \lambda + d\lambda$ and $phi(x, y, z, \lambda)$ from $t = \lambda + d\lambda$ at $t = t$ we can find

$$v = F(x, y, z, \lambda, t - \lambda - d\lambda) \qquad t > \lambda + d\lambda \tag{3.22}$$

Then, if the surface is at zero temperature from $t = -\infty$ to $t = \lambda$, $\phi(x, y, z, \lambda)$ between $t = \lambda$ and $t = \lambda + d\lambda$ and again zero between $t = \lambda + d\lambda$ and $t = t$ we get

$$v = F(x, y, z, \lambda, t - \lambda) - F(x, y, z, \lambda, t - \lambda - d\lambda) \tag{3.23}$$

recalling the definition of the difference quotient, it is rewritable as

$$\frac{\partial}{\partial t} F(x, y, z, \lambda, t - \lambda) d\lambda \qquad t > \lambda \tag{3.24}$$

In this way dividing the the interval $I = (0, t)$ in many small intervals and adding the contributions obtained, the result of the problem for the surface temperature $\phi(x, y, z, t)$ is in the form

$$v = \int_0^t \frac{\partial}{\partial t} F(x, y, z, \lambda, t - \lambda) d\lambda \tag{3.25}$$

When the surface temperature does not vary from point to point, but it is only a function of time this result can be summarized in the following statement:

*If $v = F(x, y, z, \lambda, t)$ represents the temperature in (x, y, z) at the time t in a solid whose initial temperature is zero while the surface temperature is held at a given value, the solution of the problem when the surface is at temperature $\phi(t)$ is given by*

$$v = \int_0^t \phi(\lambda) \frac{\partial}{\partial t} F(x, y, z, t - \lambda) d\lambda \tag{3.26}$$

The 3.26 immediately follows from the previous statement if we consider the $F(x, y, z, \lambda, t)$ rewritable in the simplest form $\phi(\lambda) F(x, y, z, t)$.

So, now we can derive the heat transfer and heat flows in semi-infinite solid approximation. In the case of a surface x = o at a given temperature V, with initial temperature zero, the temperature of the solid is expressible in the form $v = V \left(1 - erf \left(\frac{x}{2\sqrt{\alpha t}}\right)\right) = V\, erfc \left(\frac{x}{2\sqrt{\alpha t}}\right)$. We remember the definition of K, thermal conductivity as the ratio, in stationary conditions, between the heat flow and the temperature gradient that causes it. The units of K in the International Unit System are $[W][m^{-1}][K^{-1}]$. We can verify that the heat flux

$$f = -K\frac{\partial v}{\partial x} \tag{3.27}$$

satisfies the same differential temperature equation

$$K\frac{\partial^2 f}{\partial x^2} = \frac{\partial f}{\partial t} \qquad x > 0,\ t > 0 \tag{3.28}$$

thus for a given heat flux function of time $q(\lambda)$ (turned on at a certain moment $0 < \lambda < t$), we write the solution

$$f = q(\lambda)\, erfc\left(\frac{x}{2\sqrt{\alpha t}}\right) \tag{3.29}$$

from the equation 3.27 and properties
* of the $erfc(x)$

$$\begin{aligned} v &= \frac{q(\lambda)}{K}\int_x^\infty erfc\left(\frac{x}{2\sqrt{\alpha t}}\right)dx = \\ &= \frac{2q(\lambda)\sqrt{\alpha t}}{K} i\, erfc\left(\frac{x}{2\sqrt{\alpha t}}\right) = \\ &= \frac{2q(\lambda)}{K}\left\{\sqrt{\frac{\alpha t}{\pi}}e^{-\frac{x^2}{4\alpha t}} - \frac{x}{2}\, erfc\left(\frac{x}{2\sqrt{\alpha t}}\right)\right\} \end{aligned}$$

The temperature evaluated in x = 0 can be simplified as

$$v = \underbrace{q(\lambda)}_{\phi(\lambda)}\underbrace{\frac{2}{K}\sqrt{\frac{\alpha t}{\pi}}}_{F(t)} \tag{3.30}$$

now you can apply the equation 3.26 and defining $\tau = t - \lambda$, it follows

---

*

- $i^n erfc(x) = \int_x^\infty i^{n-1} erfc(\xi) d\xi$
- $i^0 erfc(x) = erfc(x)$
- $i\, erfc(x) = \frac{1}{\sqrt{\pi}} e^{-x^2} - x\, erfc(x)$

$$v = \frac{\sqrt{\alpha}}{K\sqrt{\pi}} \int_0^t \frac{q(t-\tau)}{\sqrt{\tau}} d\tau \tag{3.31}$$

The derived equation 3.31 has been used for the evaluation of the power flux density impinging on the limiter. The first step of the present investigation has been to estimate the heat flux on LLL by using the heat equation and the Fourier law with the semi-infinite body approximation [75] in order to reproduce the experimental lithium surface temperature versus time as given by IR measurements in figure 3.14b. The starting point is represented by the relation between the surface temperature evolution and the surface power density in semi-infinite solid approximation 3.31, that gives the surface temperature rise at the time $t$ after the arbitrary function heat flux $q(t)$.

It is possible to recognize that the equation is the convolution integral of the functions $f(\tau) * g(t-\tau)$.

Starting from the convolution theorem

$$h(x) = \int_{\mathbb{R}^n} f(\tau) g(t-\tau) d\tau = f * g \tag{3.32}$$

that suggests a method to evaluated the power flux values from the known temperature values. The convolution theorem affirms that the Fourier transform of the convolution of two functions is equal to the product of the transforms and that by using the reverse Fourier transform it is possible to obtain the relation shown on the right side of the following equation

$$\mathcal{F}\{f * g\} = \mathcal{F}\{f\} \cdot \mathcal{F}\{g\} \quad \Longrightarrow \quad f * g = \mathcal{F}^{-1}\{\mathcal{F}\{f\} \cdot \mathcal{F}\{g\}\} \tag{3.33}$$

To apply this method for the simulation of the heat propagation, it has been necessary to use a self-developed algorithm based on the Discrete Fourier Transform (DFT). In this way it is possible to write the following equation 3.34:

$$q(t) = \mathcal{F}^{-1}\left\{ \frac{2}{C} \frac{\mathcal{F}\{T(t)\}}{\mathcal{F}\left\{\frac{1}{\sqrt{|\lambda|}}\right\}} \right\} = \frac{2}{C} \mathcal{F}^{-1}\left\{ \mathcal{F}\{T(t)\} \cdot \sqrt{|\lambda|} \right\} \tag{3.34}$$

where $\lambda$ correspond to $t - \tau$. In our case, the absolute value of the heat source has been calculated during the 1.5s plasma pulse length. In order to validate the proposed method using the Fast Fourier Transform, originally self-implemented in C code, the same data samples

were also analysed with two additional different way for the heat load reconstruction. The first consists of the well validated Cook and Felderman method [77] which decomposes the convolution integral in the sum indicated in the equation 3.35. Another method, again used for verification, was to directly convolve the time and temperature vectors using the functions as in the formula 3.32, this last one confirmed the agreement with the previous two, but also shows to be the slowest. The second method directly uses the NumPy Python convolution operator [78]. The numerical value of the *kernel* of convolution integral could be computed by the Cook and Felderman method [79], [77], which gives the exact solution for the problem in the semi-infinite body approximation. This is shown in the equation 3.35:

$$q_{cf}(t_n) = \frac{2}{\sqrt{\pi}} \frac{k}{\sqrt{\alpha}} \sum_{j=1}^{n} \frac{T_j - T_{j-1}}{\sqrt{t_n - t_j} + \sqrt{t_n - t_{j-1}}} \tag{3.35}$$

where the heat flux, $q_{cf}$, is given at the discrete time instant, $t_n$. As before, it is a function of thermal conductivity, $k$ and thermal diffusivity, $\alpha$. Finally, $T_j$ is the surface temperature at the time instance $t_j$.

In figure 3.16a is shown the final heat load reconstruction that better approximates the Li surface temperatures given by infrared LLL sensors (T1, T2,T3).

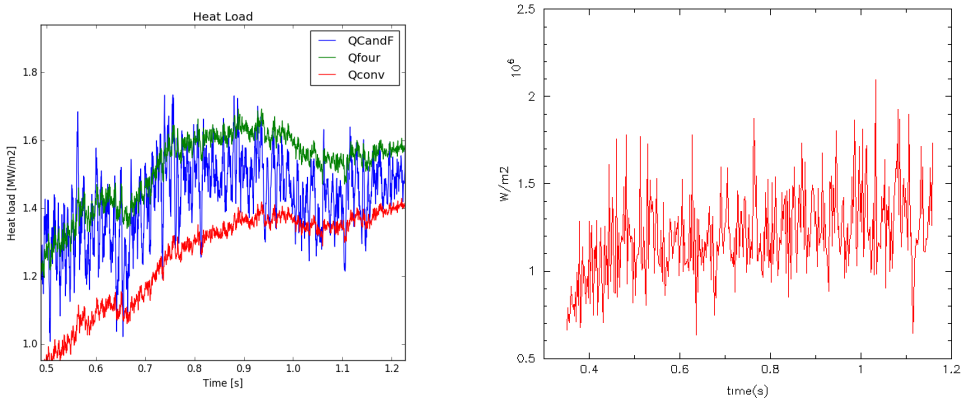


**(a)** Heat load evaluated from the fots sensors measurement with three methods: Cook and Felderman, direct convolution, using the Fourier transform.

**(b)** Evaluated heat load from the langmuir probe close to the LLL.

**Figure 3.16:** Comparison of the heat load as deduced from the IR camera and from the Langmuir probes measurements.

The above results are in agreement with the expected heat load taking into account the typical discharge parameters. Furthermore analogous results were obtained by using the

experimental data from the LLL two Langmuir probes, in figure 3.16b, in similar shots and the Stangby formula for the evaluation of the thermal load [80]. This fact is visible from the comparison between figure 3.16.

### 3.2.2 Cooling Rate calculation

In this section, we are going to estimate the cooling rate for lithium, since it has been found it can play a very important role during the so-called vapour shield phenomena. As starting a point we introduce the radiative phenomena in plasma and we define the main process will be included in the calculation. To evaluate the intensity of the emitted radiation it is important to know the mechanisms by which the particles exchange energy between themselves and with the outside. The density of electrons and ions currently reached in fusion relevant devices usually vary between $10^{13}$ and $10^{15 part/cm^3}$, the typical temperature is in the range $10^5$ to $10^8 K$. In reality, talking about temperature for a laboratory plasma is not entirely correct, since the concept of temperature is applied, strictly speaking, only to systems in thermodynamic equilibrium. For a plasma, thermodynamic equilibrium means that the particle distribution functions (ions, electrons, neutral atoms) in the velocity space are Maxwellian curves characterized by the same temperature; that the density of the atoms in the various states of ionization and excitation follows the Saha-Boltzmann's law; that the electromagnetic radiation present in the system is described by the Planck equation. These conditions are practically never verified in the laboratory plasmas. The Planck function does not describe the radiation, but the Maxwell collision frequency and the Saha-Boltzmann equation are good approximations: in this case we speak of local thermodynamic equilibrium (LTE). Even this situation, is not usually verified in tokamak plasmas. One of the most prevalent reasons for failure to achieve LTE equilibrium is found in low density plasmas: excitation and ionization of atoms occur mainly by collisional processes between particles, while de-excitation takes place with radiative phenomena [3].

Such situation is found in the solar corona and is therefore called coronal balance or coronal equilibrium. In the coronal model, ionization and excitation are considered exclusively due to electronic collisions, while reverse processes occur due to spontaneous decay, radiative recombination, and dielectronic recombination.

The density of the various ionization states, $n\,(z)$, as a function of time, for a plasma that is not in conditions of local thermal equilibrium, must be calculated by making a balance between all the mechanisms that increase the concentration and those that decrease, practically taking into account the collisional ionization and radiative recombination. It would then

solve a system of equations like:

$$\frac{dn\left(z\right)}{dt} = n_e\left\{-n\left(z\right)S\left(z\right) + n\left(z-1\right)S\left(z-1\right) - n\left(z\right)\alpha\left(z\right) + n\left(z+1\right)\alpha\left(z+1\right)\right\} \tag{3.36}$$

with z between 0 (neutral atom) and Z (fully ionized atom) for each atomic species present. If the times are sufficiently long for the establishment of a quasi-stationary situation, we can place $\frac{dn(z)}{dt} = 0$. This condition allow us to close the previous equation in the so-called coronal equilibrium system

$$\frac{n\left(z\right)}{n\left(z+1\right)} = \frac{\alpha\left(z+1\right)}{S\left(z\right)} \tag{3.37}$$

The $\alpha$ and S coefficients depend only on temperature, if the $\alpha$ and $n_e$ dependency are neglected. From the equilibrium equation the fractional abundance curves can be calculated $f\left(z\right) = \frac{n(z)}{\sum_z n(z)} = \frac{n(z)}{n_{imp}}$ depending on the temperature, assuming $\sum_{z=0}^{z=Z} n\left(z\right) = 1$.

The presence of impurities in the plasma produces abundant energy losses. There are two types of processes mainly involved: the increase of the breaking radiation (bremsstrahlung) due to the typically high charge value of the impurities and the radiation that comes from atomic excitation and recombination processes (line radiation).

In a stationary situation, neglecting the effect of the transport in coronal equilibrium regime, the irradiated power is proportional to the electronic density $n_e$ and to the density of impurities $n_I$. The radiative power can be written as

$$P_R = n_e n_I L_z \tag{3.38}$$

where the term $L_z$, which takes the name of cooling rate, is only a function of temperature.

For low Z impurities, like lithium we are interested in, the maximum radiative loss occurs at a relatively low temperature, of the order of few eV.

So now, we can finally compute the cooling rate function for lithium starting from the ion balance, as suggested from the equation 3.36. A similar model called the Onion Skin Collisional-Radiative model (OSCR) has been already successfully applied in other fusion relevant device [81]. The model calculates the coronal and non coronal equilibrium as a function of the parameter $\tau_p n_e$. The starting point is the well known ion balance system under the coronal equilibrium hypothesis $\sum_{z=0}^{z=N} \frac{dn_z}{dt} = 0$.

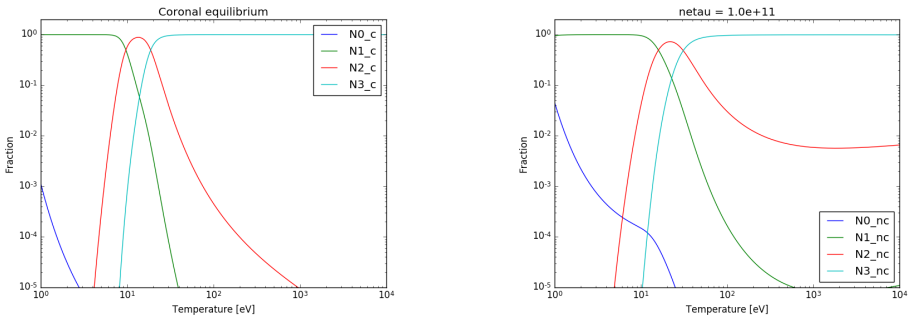


**(a)** Coronal equilibrium ion balance.

**(b)** No coronal ion balance $n_e\tau = 10^{11}\ \ s \cdot cm^{-3}$.

**Figure 3.17:** Comparison in the ion balance calculation.

The density evolution of the ionized state $z$ is given by the rate system

$$\begin{aligned} \frac{dn_z}{dt} \quad = \quad & n_{z+1}n_e\alpha_{z+1}(T_e, n_e) - n_z n_e \alpha_z(T_e, n_e) + \\ & n_{z-1}n_e S_{z-1}(T_e, n_e) - n_z n_e S_z(T_e, n_e) + \\ & \sigma_z - \frac{n_z}{\tau_z} \end{aligned} \tag{3.39}$$

The system 3.39 without the last row not include any particle source or losses, more the $\tau_p n_e$ parameter tends towards to infinity, more the system approach to the coronal equilibrium, i.e. $\tau_p n_e \to \infty$.
In the lithium case the equation 3.39 results in the following system

$$\begin{pmatrix} -S_0 - \frac{1}{\tau_p n_e} & \alpha_1 & 0 & 0 \\ S_0 + \frac{1}{\tau_p n_e} & -S_1 - \alpha_1 - \frac{1}{\tau_p n_e} & \alpha_2 & 0 \\ \frac{1}{\tau_p n_e} & S_1 & -\alpha_2 - S_2 - \frac{1}{\tau_p n_e} & \alpha_3 \\ \frac{1}{\tau_p n_e} & 0 & S_2 & -\alpha_3 - \frac{1}{\tau_p n_e} \end{pmatrix} \begin{pmatrix} n_0 \\ n_1 \\ n_2 \\ n_3 \end{pmatrix} n_e = \begin{pmatrix} 0 \\ 0 \\ 0 \\ 0 \end{pmatrix} \tag{3.40}$$

Where $\alpha_z$ and $S_z$ represent, respectively the recombination and the ionization rate coefficients, $\sigma_z$ is the source term for a given ionization state and $\tau_p$ is the particle confinement time.

Two particular solutions of the system 3.40 are shown in figures 3.17a and 3.17b respectively for $\tau_p n_e = \infty$ and $\tau_p n_e = 10^{11}\ \ s \cdot cm^{-3}$. The curves get smooth and move toward higher

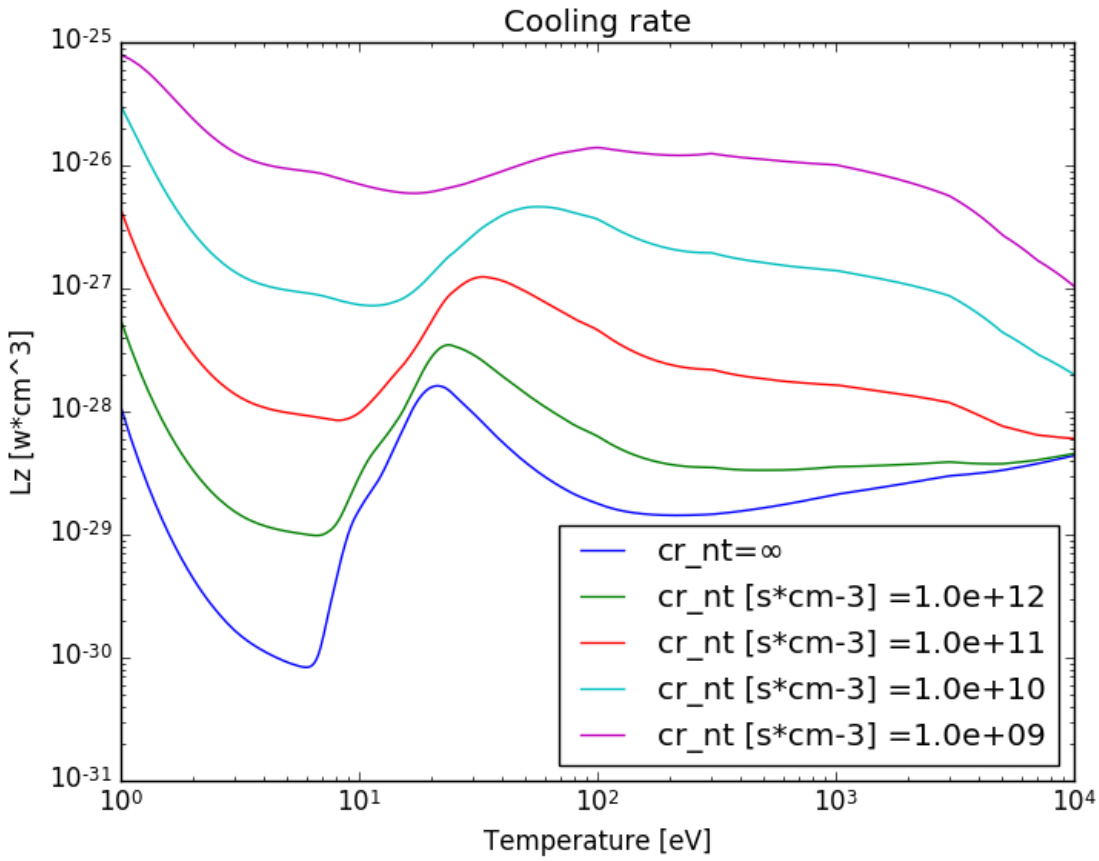


**Figure 3.18:** Lithium cooling rate $L_z$ versus electron temperature. Different curves are shown in function of the $n_e\tau$ parameter, $\tau_p n_e \to \infty$ approach the coronal equilibrium.

temperature as the $\tau_p n_e$ value decrease. Once having the ion balance it is possible to get the cooling rate function $L_z$ integrating all the radiation losses for each ion state $z$ i.e. line, bremsstrahlung and recombination radiations. More details are in [82]. The data used in the computations are from [83] and [84]. Lithium confinement time, $\tau$, in the Scrape-Off and in the Radiative Layer region may be considered as a very important parameter. Furthermore, if it is small, then lithium ions will not reach the coronal equilibrium before they return to the wall. In this case the lithium radiated power can exceed of orders of magnitude the intensity expected for the coronal equilibrium as calculated in figure 3.18.

If the coronal equilibrium is not satisfied, is quite reasonable expects a lithium radiation roughly an order of magnitude higher for the typical periphery parameter i.e. in FTU $T_e = 20eV$, $n_e = 10^{13} cm^{-3}$, $\tau = 10^{-3} s$. This flexible tool allows a simple modelling of the

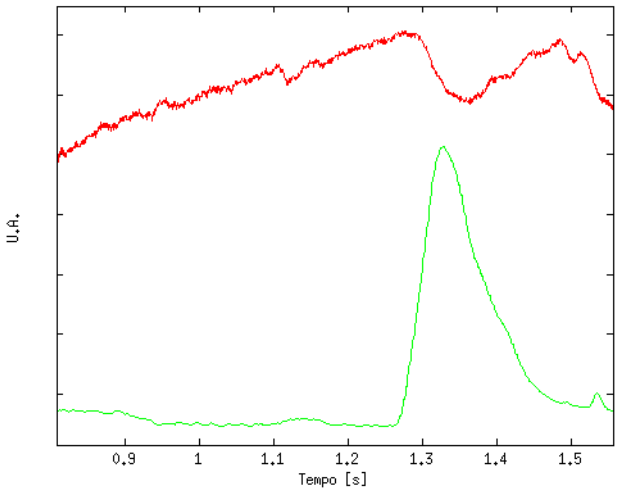


**Figure 3.19:** The figure shows in arbitrary units surface temperature [RED] and the radiative losses [GREEN] evolution during the pulse.

impurity behaviour in many experimental setup. These results will be applied to estimate the power radiated by lithium impurity influx in the Scrape-Off and in the Radiative Layer region on FTU.

### 3.2.3 Phenomenological model

We are finally ready to build a simple phenomenological model taking into account the main experimental evidence observed on FTU. The heat source has been taken constant for the 1.5s plasma pulse length and the absolute value has been calculated as shown in the previous section. Starting from this we try to understand the phenomena previously observed in figure 3.14a (last two plot in the bottom) between 1.3s and 1.5s that is the strong increase in the bolometric losses suddenly followed by the surface temperature decrease. If we subtract from the constant heat source a function with the same shape of the bolometric signal, see figure 3.19, and we solve again the heat equation we can reproduce the experimental data. So, it has been the starting point for a deeper investigation of the phenomena.

It is to underline that in our conditions, with a Li surface temperature close to 550°C, evaporation represents the main mechanism of Li erosion. A large fraction of Li re-deposition is expected from the ERO code [55]. This is because the lower energy for thermally evaporated lithium particles results in a shorter mean free path for ionization than that of sputtered lithium, which results in the large re-deposition fraction, greater than 0.9. We considered this

as a reference value. The lithium sputtering rate for FTU has been evaluated in [55] and [85].

The first step has been to reproduce the thermal behaviour of the target. Different approaches are available starting from the heat equation $\frac{\partial T}{\partial t} - \alpha \nabla^2 T = \dot{q}$. Setting a source term $\dot{q}$, the dimensional unit of this quantity will be $[\frac{W}{m^3}]$, as for the two other terms $\frac{\partial T}{\partial t}$ and $\alpha \nabla^2 T$. We are interested in the surface flux density in $[\frac{W}{m^2}]$ impinging on the target surface. Using a referenced technique in [86], given $q_w$ the surface flux density at the wall, $k$ the thermal conductivity, $L$ the characteristic length of the target in the $x$ direction, it is trivial to demonstrate that $q_w = -k\frac{\partial T}{\partial x}|_{x=0} = k\left[\frac{\dot{q}}{k}x - \frac{\dot{q}L}{2k}\right]_{x=0} = -\frac{\dot{q}L}{2}$. It is possible to find the equivalent power volumetric density to apply in $x = 0$ to reproduce the experimental data. During such procedure a fit has been performed in order to derive the correct thermal parameter for the simulation, particularly the characteristic length L. The heat equation can be numerically solved with some approximation. The spatial gradient has been evaluated and averaged in a few points, the length of the metal layer has been varied to fit the experimental data. The final value that minimizes the differences between the experimental data and the equation solution has been found about 8mm, this number is compatible with the distance of the liquid surface from the molybdenum heat accumulator that we consider thermalized at the initial temperature $T_{s_0}$. The above approximations allow for a quick implementation but a deeper analysis could improve the method and better investigate the taken assumption. The main advantage of this approach is that the steady state regime can be simulated in case of a purely conductive heat sink for a thermalized cooling system.

It is possible to use, as another approach, the analytic solution for the semi-infinite body approximation consisting of the convolution integral expressed in equation 3.31. This case the formal equation well reproduce the experimental data without any need for fitting the thermal parameter. It offers a fast implementation and a well known background theory. Of course the limitation of this analytical approach is that it is valid until the semi-infinite body approximation is good.

The two methods have been compared using the same experimental data, and they showed a good agreement. So, it has been decided to use and report the second one, based on the equation 3.41, since its easier implementation.

The experimental data suggest a plasma detachment similar behaviour. Pitcher et al. [87] indicates the detachment phenomena coming when the product $n_z n_e L_z L$, where L is intended integrated along the connection length, is relevant compared with the available heat flux in the upstream point. Nevertheless the changes in the parallel thermal conductivity $\kappa_{//}$, due to the local electron temperature drop, haven't been considered. The pressure along the

field line has been taken constant. The heat source to the target has been approximated as a sum of different contribution $q_t = q_{pla} - q_{ev} - q_{rad}$ respectively: the constant heat source from the plasma, the enthalpy variation energy taken by the phase change, the irradiated energy near the target. The $q_{ev}$ contribution has been evaluated to be about a hundred times smaller than $q_{rad}$, so the first one has been neglected.

The experimentally observed phenomena call back a plasma detachment effect, from the data it is evident from the strong decrease of the heat load impinging the limiter.

The surface temperature $T_s$ and the impurity density $n_z$ close to the limiter have been linked using the following equations system:

$$\begin{cases} T_s(t) = T_{s_0} + \frac{\sqrt{\alpha}}{K\sqrt{\pi}} \int_0^t \frac{q_t(\tau)}{\sqrt{t-\tau}} d\tau \\ \dot{n}_z(T_s, t) = \alpha_s\left(T_s\right) \cdot \phi(T_s) - \frac{n_z(T_s,t)}{\tau_i} \\ q_t(t) = q_{//} - \int_0^L n_z n_e L_z(t_e, n_e, \tau_c) ds \end{cases} \tag{3.41}$$

where

$$\phi(T_s) = \frac{p_0 e^{-\frac{\delta H}{K_B T_s}}}{\sqrt{2 K_B T_s \pi m_{Li}}} \cdot \sigma \tag{3.42}$$

$$\alpha_s(t) = \frac{1}{1 + e^{-(p_0(t-\tau') - p_{pla})}} \tag{3.43}$$

In the formulas $T_s$ is the surface temperature, $q_t$ is the heat flux evaluated on the target. The parameters for the evaporation of lithium are: $p_0$ is the vapour pressure, $\Delta H$ is the enthalpy of vaporization, $m_{Li}$ is the lithium atomic mass, $K_B$ the Boltzmann constant, $\sigma$ is the target surface. The integral, in the bottom formula of the system, take into account the radiative losses along the particle path in the parallel direction, namely the typical connection length $L$. The first equation of the system 3.41 is the typical heat equation solution in semi infinite body approximation where the source from the plasma is reduced from the radiative losses induced by the impurity density near the target. The impurity density is given by the second equation of the system 3.41 linking the vapour flux $\phi(T_s)$ expressed in 3.42 with the surface temperature. An additional phenomenological term $\alpha_s(T_s, t)$, equation 3.43, is added in order to take in to account the observed threshold in the vapour flux. The plasma pressure simply given as $p_{pla} = nKT$ play a crucial role in the vapour cloud formation: only when the vapour pressure, $p_{ev}$, is significantly greater of the plasma pressure the neutral impurity accumulates

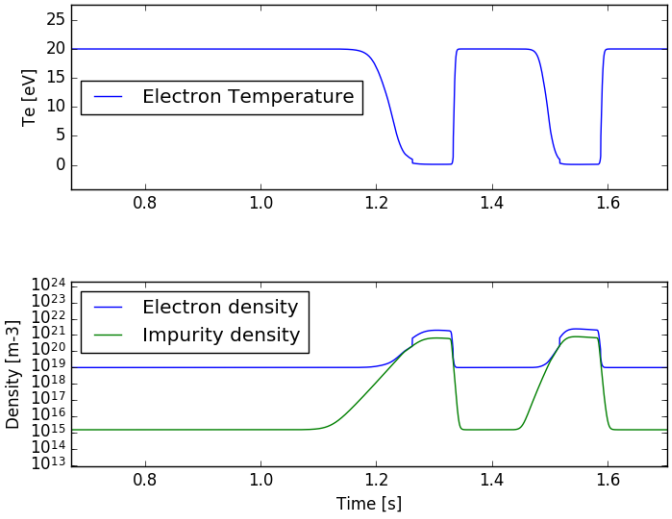


**Figure 3.20:** Local electron density and temperature as predicted by the model.

in front of the target. Such behaviour has been also reported in [32]. The aforesaid pressure drop has a strong surface temperature dependence, i.e. exponential. The idea is that as the neutral cloud increase in density, it increases also the probability for the radiative processes, that play as a trigger for the phenomena. The $\tau'$ characteristic time has been introduced as observed from the positive slope of the bolometric signal. It summarizes the time that is needed for the vapour cloud ionization. In particular $\tau'$ can include the atomic process times. The term $\frac{N(t)}{\tau_i}$ is the impurity loss expressed in function of them characteristic confinement time $\tau_i$. It is the typical time that a lithium ion spends on the field line bound the limiter. The surface temperature predicted from the proposed model is shown in figure 3.21, while a detail of the electron density and temperature is given in figure 3.20.

It is worth noting that the Li atoms source is strictly dependent on the surface temperature, at least in the operational regime where the evaporation starts to dominate on physical sputtering (T > 530 °C). The strong dependence of the Li atom flux from the surface temperature can play an important role in the control of heat removal from the liquid surface.

The agreement between experiment and model is quite good, not only qualitatively, but also quantitatively. It indicates that the most important processes taking part to the vapor shield phenomena have been taken into account. If we do not stop the simulation after 1.5s the temperature tends to evolve to a steady state regime showing stationary oscillations constant in frequency and in amplitude, as it is visible in picture 3.22a, where the temperature evolution

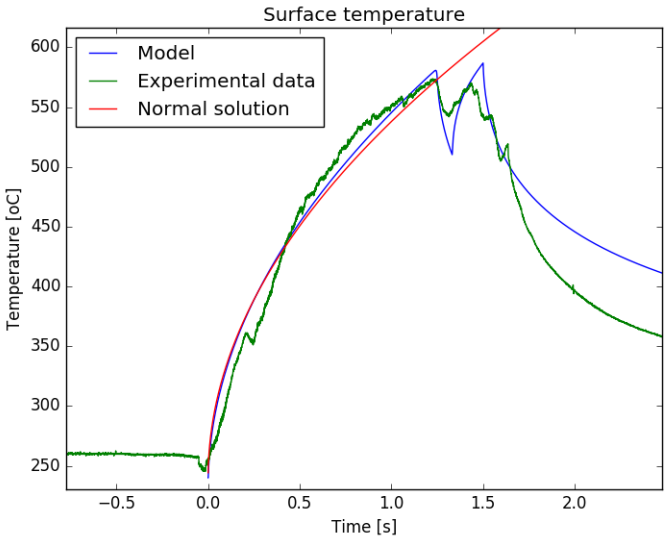


**Figure 3.21:** The figure shows the experimental data (green), the solution of the heat equation (red) and the proposed model (blue). The simulation has been stopped synchronously with the plasma current shut down.

is plotted in arbitrary units. A similar behaviour has been also observed from G.G. Van Eden during the experiments performed in Pilot-PSI using liquid metals [88]. This is reported in figure 3.22b(a), particularly referring to the edge temperature.

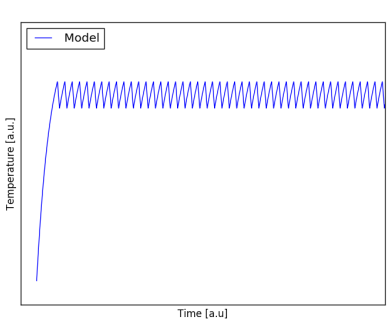


**(a)** The simulation performed without imposing the end of the plasma pulse. It is pobbible to notice the costant frequency and amplitude foreseen for the temperature oscillations.

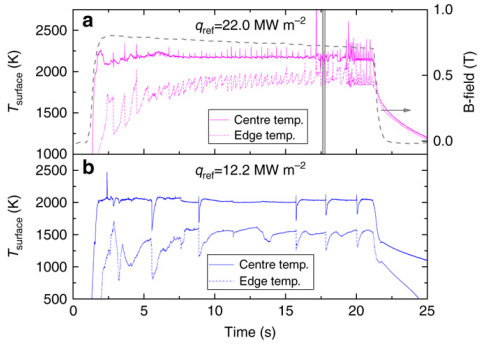


**(b)** Evolution of the liquid tin surface temperature observed in Pilot-PSI. The authors report fast temperature oscillations around a constant base value regularly observed during the plasma discharges. Figure from G. G. van Eden [88]

**Figure 3.22:** Proposed model on the left side; evolution of the liquid tin surface temperature observed in Pilot-PSI [88] on the right.

## 3.3 Liquid Tin Limiter

The liquid Sn in a Capillary Porous System (CPS) matrix has been suggested as a high potential plasma facing material in a steady state operating fusion reactor owing to its physiochemical properties. Up to now, FTU has been the only tokamak in the world to have tested a *Liquid Tin Limiter* (TLL). Nowadays the most liquid metal PFC intensively studied in fusion relevant devices are lithium based. They demonstrated promising results in plasma parameters improvement and plasma facing surface long-life operation. One of the main limits for lithium-based PFC is the operative temperature window; it is mainly determined by maximum surface temperature taking Li flux to the plasma within the acceptable level. The liquid tin has a high potential for application as the PFC base material due to its low chemical activity. The high boiling point of tin gives good hope in higher operation limit in comparison with lithium and a good capability for withstanding heat load as high as tens of $^{MW}/_{m^2}$. However, tin (Z=50) is a high Z material and plasma pollution must be avoided. Therefore, the experimental investigation of these aspects has been one of the main research activities of the FTU tokamak during the last experimental campaigns. The main reasons for the experimental study on PFC based of liquid Sn were the comparison with lithium-based PFC under tokamak conditions and its influence on plasma parameters.

As already mention in section 2.3, liquid tin offer large operating window (300 < T < 1300 °C) with negligible evaporation, low or negligible activation and low hydrogen/deuterium/tritium retention [89] [90]. Moreover, for T > 1300 °C the thermal shield formed in front of the divertor plates by evaporated tin atoms can play an important role in the power mitigation [32]. Due to the high atomic number tin meets the high core radiation requirement, but the maximum tolerable tin concentration for DEMO should be less than $10^{-3}$ of the electron density to be sustainable [68].

The liquid tin limiter (TLL), designed for FTU, in collaboration with the *Federal State Unitary Enterprise "Red Star"*, meets the following criteria:

- tin can be melt before the plasma operation using an embedded electrical heater;
- cooling system based on a mixture of atomised water and gas with the opportunity for power flux monitoring;
- possibility of plasma facing surface temperature control and stabilization at plasma effect on desirable level in the range of 300–900 °C;
- easy movement with respect to LCMS of plasma column;

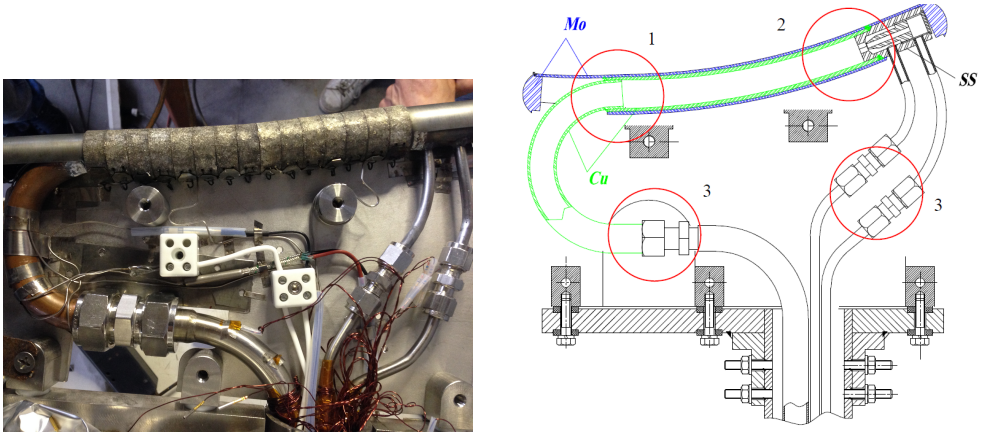


**(a)** Picture of the liquid tin limiter. The CPS structure filled with tin is visible on top. On the right the two cooling channel for water and gas, on the right the single pipe for the atomized mixture. The molybdenum screen prevents the contact between tin and copper. The electric heater is wrapped around the copper pipe.

**(b)** Exploded diagram of the tin limiter. The main part are represented, the red circles evidence the joint part. Particularly the number 3 are fast connection allowing the limiter head removal from the dedicated vacuum box where it is placed.

**Figure 3.23:** Overview of the liquid tin limiter in-vessel element, a picture on the left and the technical drawing on the right.

- possibility of visual inspection and tin refilling.

The principal component of TLL design is the in-vessel plasma facing element, visible in figure 3.23a, covered with CPS made from tungsten (W) felt (pressed W wire with a diameter of $50\mu m$ and pore size of $30\mu m$) and filled with Sn. The main TLL in-vessel element parameters are listed in table 3.4. Taking into account the tin corrosive activity to structural materials, the Sn filled CPS is installed on molybdenum protective screen. In figure 3.23b the technical drawing of the tin limiter is presented. The element is equipped with an electrical heater to keep the original liquid state of Sn (T > 232 °C) and cooling channel for effective removal of incoming heat during plasma discharge. The effective cooling of the in-vessel element is performed by evaporation of fine dispersed cooling media (water spray in gas) that comes from an atomizer incorporated into the element structure. Such cooling scheme is compatible with the high temperature operation, ensure the low pressure of cooling media and quick response of the cooling system on the temperature change of plasma facing surface. The out-vessel system permits proper operation of an in-vessel element at design conditions with automatic remote control of electrical heater and atomizer. A data acquisition system with detectors of temperature, pressure and Langmuir's probes provide monitoring of the limiter

| Parameter | Value |
|---|---|
| Power flux, $^{MW}/_{m^2}$ | up to 10 |
| Operation time, s | up to 10 |
| Initial surface temperature, °C | 250 - 330 |
| Surface temperature during plasma pulse, °C | 300 - 1500 |
| Heat removal capacity from cooling system, J | $o(10^5)$ |
| Plasma facing area, $cm^2$ | 85 |
| Liquid Sn volume, $cm^3$ | 10 |
| Limiter size LxWxH, cm | 27 × 2.6 × 40 |

**Table 3.4:** Main parameters of the liquid tin limiter in-vessel element.

operation parameters. The calorimeter accumulator is included in the system for monitoring of the incoming energy flux from plasma on the TLL surface. During operation the energy flux incoming from the plasma discharge is removed and comes to the calorimeter as the flow of the heated mixture of vapour and spray of cooling media. This mixture is bubbled through the specified volume of water in the calorimeter. Change of water temperature T in the calorimeter during system operation permits estimate the value of incoming energy, from the energy balance equation for calorimeter including all the expected energy losses terms.

As is well known the majority of metals (stainless steels, Al and Cu alloys, etc.) excepting refractory metals and beryllium are not compatible with liquid tin at the temperatures supposed for the PFC operation [91]. The corrosive effect of liquid Sn on TLL structural materials was studied with samples of compact and porous materials in static isothermal conditions [92]. The tin limiter installed in FTU has been pre-assembled and tested in the factory: several tests on tin behaviour and on the wetting properties has been performed. The samples surface has been preliminarily cleaned by an electrochemical method to provide reliable and reproducible results. Freshly cleaned samples were placed into niobium container filled with molten Sn and exposed during 1 hour in a vacuum furnace at different temperatures. Sn impact evaluation has been performed with SEM metallography and element distribution map analysis. As it has been detected, the 316-type stainless steel is completely incompatible with Sn at T ≥ 400 °C and dissolved just after wet [62]. Only Mo and W alloys are resistant to Sn up to T < 1400 °C and demonstrated no corrosion effect (dissolution, compound formation, Sn permeation) on a surface of these materials. In addition, tungsten and molybdenum have high heat conductivity that with the high corrosion resistance make them the favourite candidate materials for PFC with liquid tin. For this reason the tungsten wire for the CPS and molybdenum tube for protective screen have been chosen in presenting TLL design. The use of copper

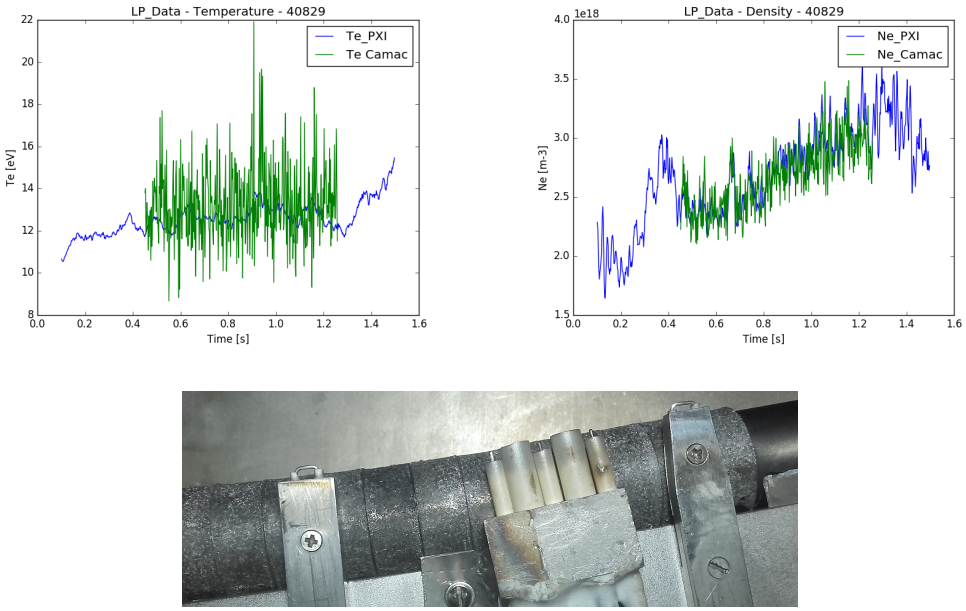


**Figure 3.24:** Comparison between the old (CAMAC) and the new (PXI) LP acquisition system on FTU. Reconstructed temperature is on the top right, density is on the top left, the old system results are in green, the new are plotted in blue. The main upgrade is the possibility to record the LP data during the all plasma pulse without any limitation in memory. Detail of the tin limiter from the inspection window is given on the bottom. The LP with them peculiar electrode shape are visible at the far end of the picture.

as cooling channel material is possible only with a protective screen, i.e. molybdenum or tungsten, due to the tin corrosive effect.

The liquid tin limiter operations on FTU are monitored using several diagnostics: four dedicated Langmuir probes (LP), a fast IR camera looking at the surface temperature, visible and VUV spectroscopy. A detail of the Langmuir probes installed on the TLL is given in figure 3.24. The unusual shape of the probes (a closed arc) is used to check shot by shot the status of the molybdenum electrodes. Before each plasma shot a sinusoidal voltage is acquired at the probe ends, if its results interrupted a warning signal comes out. This system permits to know if the collection probe area has been changed after an abnormal event such as a disruption. When the probe is operating a switch is open, the circuit is interrupted and the probe can work as usual with a simple electrode exposed to plasma [93]. The old acquisition system (operating with the lithium limiter) was limited in memory and only a few hundreds millisecond could be stored during the plasma shot. At the end of the experiments with the lithium limiter and before the tin limiter installation lot of work has been performed on the Langmuir probe system, the data acquisition system has been moved to a new ADC with

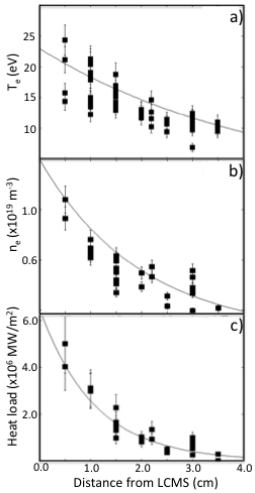


**Figure 3.25:** Starting from the top pannel electron temperature $T_e$, electron density $n_e$, heat load q versus the distance from the LCMS. The lines are the exponential curve fits. The fitting result are respectively $\lambda_T = (4.0 \pm 0.6)\, cm$, $\lambda_n = (2.0 \pm 0.3)\, cm$, $\lambda_e = (1.2 \pm 0.2)\, cm$.

higher memory and time resolution. At the same time a new reconstruction algorithm has been developed and it is currently working during tokamak operation for all the LP present in the machine. In figure 3.24 the comparison between the two system is shown, while a scan along the Scrape-Off Layer using the Langmuir probes is presented in figure 3.25. The scan was performed moving the limiter shot by shot towards the plasma. The profile have been fitted with an exponential function and the results are in agree with the FTU standard values and with the simple SOL scaling law $\lambda_e = \left(\frac{1}{\lambda_n} + \frac{3}{2}\frac{1}{\lambda_T}\right)^{-1}$ [80].

The transition to the new Langmuir probe system for FTU has required to develop a new interface with the FTU pre-shot control system based on VAX. First of all, an off-line test procedure was developed to verify the correct functioning of the overall system and particularly to check the status of the electrodes inside FTU, before the plasma operation, using the original closed electrode methodology. The systematic acquisition of the sine wave before the shot is also used to check the status of the signal generators and the power amplifiers supply the probes: two of the most fragile components of the system. In the old time the probe characteristic reconstruction was carried out by acquiring only the current and assuming the voltage as a perfect sine triggered 3.5s before the plasma shot. Since, the availability of many more channels on the new PXI hardware, the acquisition of all the voltage waveforms was implemented, thus improving the fidelity of the reconstructed data. Furthermore, the possibility of using the reciprocating probe arrays has been prepared, but not yet tested during

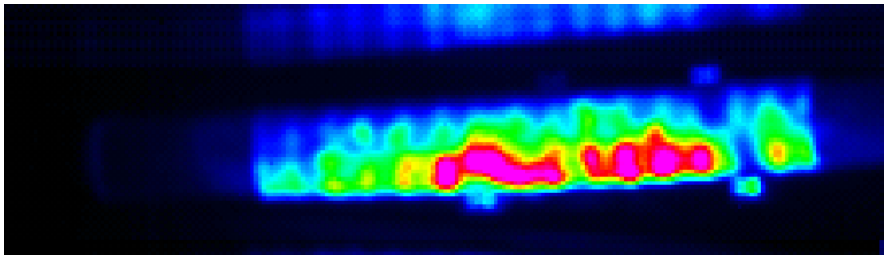

**Figure 3.26:** IR picture of the tin limiter durign the plasma shot as recorded from the camera. The high field side is on the left, the low field side of the tokamak on the right.

plasma operations, due to a long FTU shutdown. The combs with the probes are pushed inside FTU with a very fast hydraulic system, the position is actually read by an encoder and acquired by the PXI. In this way the reconstruction software can provide the temperature and density profile to the user.

A fast IR camera up to 1375Hz in frame rate directly looking at the liquid metal limiter is available on FTU. Starting from the temperature map and applying the procedure shown in section 3.2.1 it is possible to derive the heat load distribution along the limiter during the plasma pulse. An example is presented in figure 3.26. The heat loads derived from the camera using the algorithms in section 3.2.1 have been compared with the Langmuir probes results and the ANSYS code. The limiter geometry and the plasma shape have been inserted in ANSYS, the power flux density is an input and the foreseen surface temperature map the output of the code. Looking at the picture in figure 3.26 it is possible to notice an asymmetry in the heat load distribution. To have a better understanding of the experimental results, it was important to explain the observed heat load profile on the TLL. For this reason a dedicated reconstruction of the magnetic field lines have been done and compared with the limiter position during the experiments. Taking in to account the typical e-folding length for the FTU SOL a simple geometrical calculation has been performed to check the consistencies of several different measurements on the TLL. The tin limiter has a bending radius of 129cm, so it cannot match the typical plasma shape for FTU

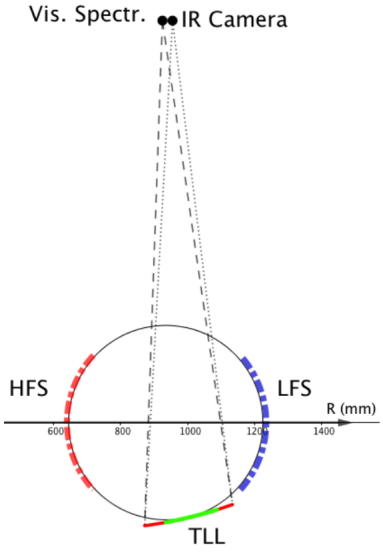


**Figure 3.27:** The bending radius of TLL is much larger of plasma radius. The toroidal limiter in red, the poloidal limiter in blue and the visible diagnostics aperture are shown.

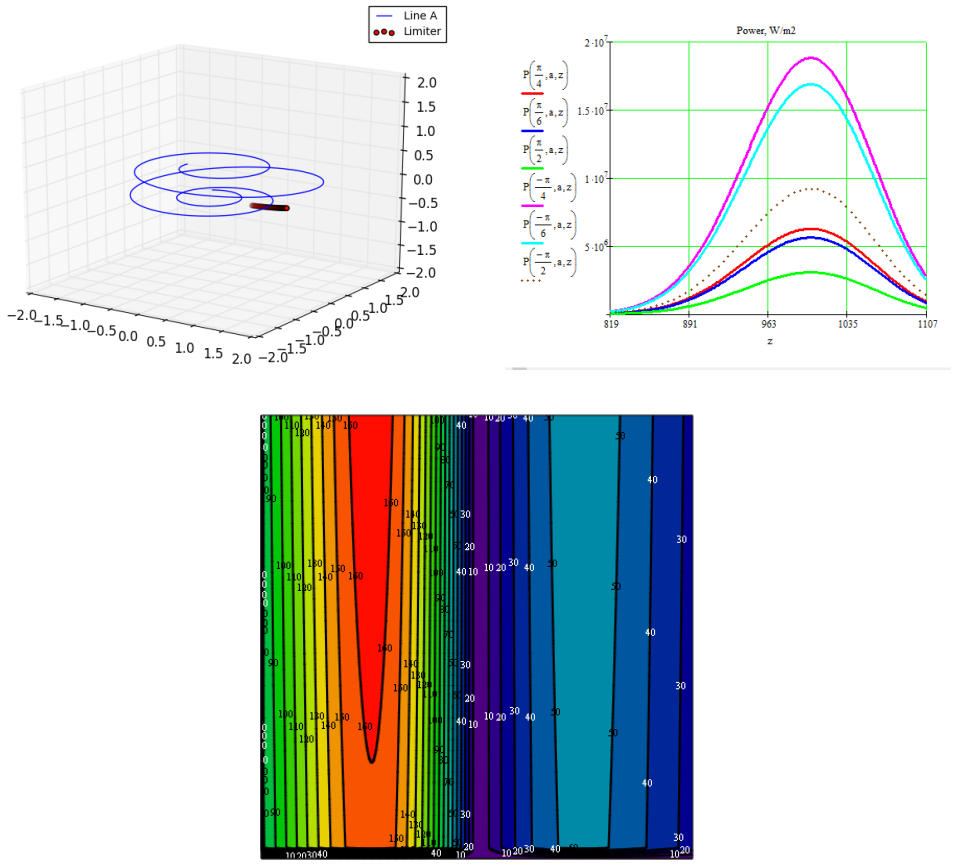


**Figure 3.28:** Top left the connection length is shown starting from the limiter. The reconstruction has been performed taking into account the real magnetic field during the plasma pulse as given from the ODIN code [94] [95]. Top right the expected heat load are plotted in the poloidal plane. Z is the radial distance from the torus axis, the angle indicates the impact point with the cylinder shape limiter starting from zero on the top, i.e. $\pi/2$ is the surface unitary vector parallel to the toroidal direction point through the plasma current. Bottom the results are displayed in colour map to facilitate the comparison with the experimental picture from the IR camera.

with a minor radius a = 29cm. The tin limiter geometry in comparison with the toroidal and poloidal limiter of FTU is presented in figure 3.27. Taking the plasma reconstruction and the limiter position it is possible to map each point on the surface with the real distance from the LCMS. The results are shown in figure 3.28: the radial heat load distribution perfectly agree with the limiter distance from the last closed magnetic surface, while the two side asymmetry can be explained by the difference in the connection length from the two sides.

During the last experimental campaign on FTU with the TLL, several shots have been dedicated to the tin spectroscopy investigation. In addition to the usual survey spectrometer SPRED (10-30 nm), a 2m grazing incidence Schwob-Fraenkel XUV spectrometer [96] observ-

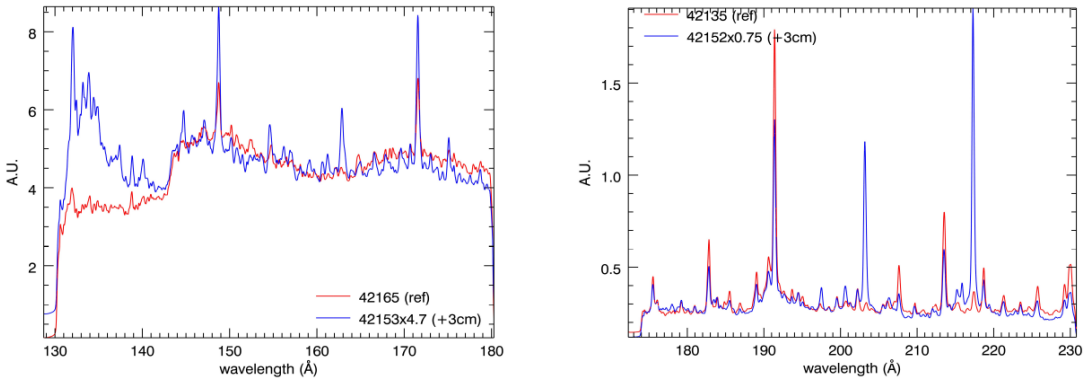


**Figure 3.29:** Comparison of different spectral range during the liquid tin experiments in FTU. In one case the TLL is fully retracted (red), in the other with the TLL at 0.5cm from the LCMS (blue). The curves are normalized to the same background level [97].

ing the emission in the range from 1 to 34 nm, was installed on FTU, looking at the plasma through a fixed, equatorial line-of-sight. Considerable effort was devoted to updating and expanding a comprehensive list of theoretical and experimental wavelengths for all the ions to be observed. A scan has been performed with the high resolution Schwob spectrometer in order to identify spectral lines from Sn in different ionization stages, to monitoring the performances and the impact on plasma parameters of the TLL. A picture of this is given in figure 3.29. Few more tin lines have been identified, in addition to those previously observed with the lower resolution SPRED spectrometer. Furthermore, the Sn line brightness has been seen to increase towards the end of the discharge, but without of causing a measurable variation in the $Z_{eff}$ value. The tin lines have been isolated against the metal-dominated background spectrum typical of FTU plasmas in a limited range of plasma parameters.

During the campaign the machine worked mainly with the following conditions: $B_T$ = 5.3T, 0.5MA < $I_p$ < 0.8MA, $T_e$ < 1.6 keV, $n_e < 4 \cdot 10^{20} m^{-3}$. The vertical position of the TLL was varied shot by shot basis from being flush with the vacuum vessel (totally in the toroidal limiter shade) up to be almost at the LCMS. Many more lines remain to be identified, and higher ionization stages are not to be excluded. In figure 3.29 the observed spectral range for two discharges are presented, one with and one without the TLL. The blue curves are normalized to the same background level. More detail can be found in [97] [98].

The surface temperature of the hottest region of the limiter for pulse 41546 is plotted versus time in figure 3.30, together with the plasma current, and the measured SnXXI line emission. The Sn line emission starts to increase at 0.8s when the surface temperature reached

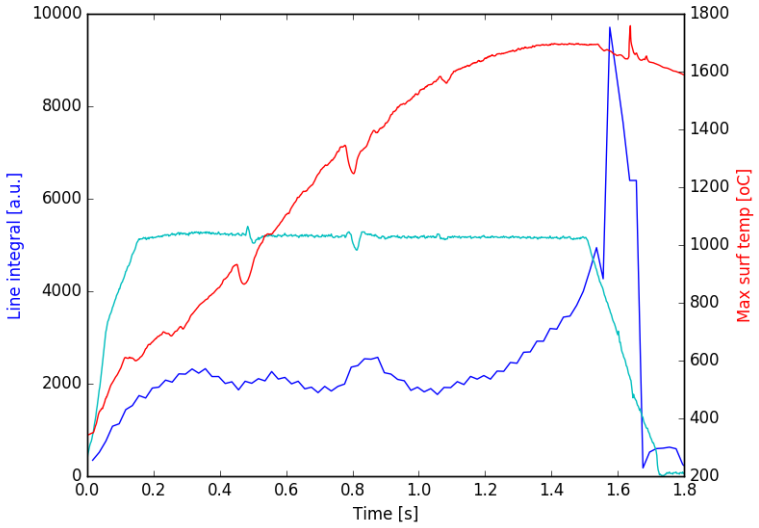


**Figure 3.30:** Plasma current (cyan line, x10kA looking at the left Y axis), the surface temperature (red line, in Celsius) and the SnXXI 20.4nm line emission (blue line, a.u.) are plotted versus time. The three overshoots in the plasma current and surface temperature traces were due to problems on the power supply of the vertical field control coils.

about 1300°C. A problem with the magnetic vertical field is also visible on the plasma current in three different bumps. After one second from the plasma start, the maximum surface temperature is well above 1300°C and the tin line begins to grow almost exponentially. In such pulse, starting from 0.5s, the tin limiter was closing the LCMS as indicated from the ODIN magnetic reconstruction code [94] [95]. The heat load for the shot 41546 has been deduced from the IR camera with the previously described techniques, and in addition, the 3D simulation with the ANSYS code has been performed to check the results reliability. The value of 18 $MWm^{-2}$ was found, also in agreement with the Langmuir probe measurements.

The molybdenum and oxygen lines usually dominate the spectrum of the discharge in which the toroidal TZM FTU limiter acts as the main limiter, while the lines of tin exclusively dominate the spectrum of the pulse in analysis at the end of the discharge, as shown in the third panel in figure 3.33a. In this spectrum are clearly visible the intense band emission between 13-14nm due to the emission of different ions SnIX - SnXII and the intense Zn-like and Cu like lines respectively at SnXXI 20.4nm and SnXXII 27.6nm. The same lines were also observed in tin injection on MAST [99]. Some of the Sn lines were also identified with the SPRED instrument and used to perform a spatial scan of the plasma cross section, on a shot-by-shot basis of repetitive discharges. The instrument was tilted upward so that the impact parameter of its line-of-sight varied from 0 to 23 cm in steps of few cm at the time,

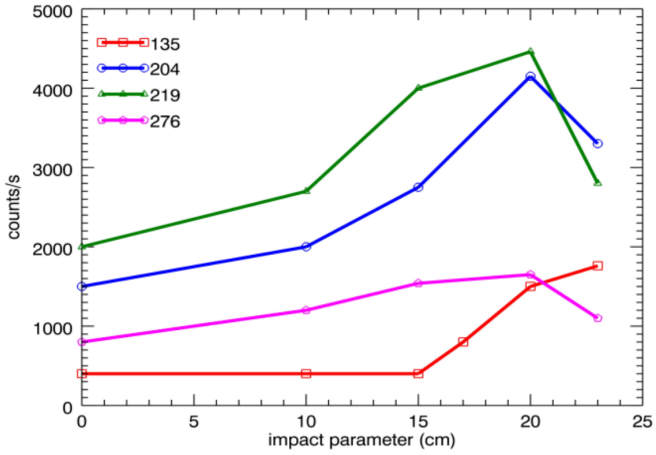


**Figure 3.31:** Spatial scan of the plasma cross section in discharges with TLL at 0.5cm from the LCMS. The impact parameter of its line-of-sight varied from 0 to 23 cm in steps of few cm [97].

while the TLL was kept in the same position, 0.5cm from the LCMS. The results are reported in figure 3.31, the lines peak off-axis, as to be expected for these intermediate ionization stages, in fact, SnXXI 20.4nm has an ionizing potential of 608eV, and SnXXII 27.6nm has 645eV. Unfortunately, theoretical data regarding ionization equilibria for Sn are not easily available prevented more detailed analysis of these experimental results.

The electron temperature at the plasma center ranged from 1.0 to 1.4 KeV that it means that taking into account SnXXI and SnXXII ionization potentials, these ions should exist around half radius, i.e. well inside the last closed magnetic surface, as figure 3.31 confirms. The TLL interacting surface is about $10^{-2}$ - $10^{-3}$ times the toroidal limiter surface, this can explain the lack of tin lines, when sputtering and not evaporation is the dominant tin production mechanism as also confirmed by visible spectroscopy [98]. Furthermore, prompt tin redeposition on the limiter itself could contribute to reducing the tin influx in the discharge as suggested also in [100]. The effect of complete dominance of liquid metal lines in the spectrum when evaporation is strong has been already observed on FTU with lithium [50], and a proof is given in figure 3.33a.

A possible explanation of this phenomena is the creation of a thin layer of the evaporated atoms on the toroidal limiter tiles, so that the Mo sputtering is strongly reduced. After having operated several pulses in strong tin evaporation regime, a few discharges without the liquid metal limiter are sufficient to clean main limiter surface and the tin emissions are no more detectable.

FTU operations with lithium and tin limiters show several import aspects, both the lithium

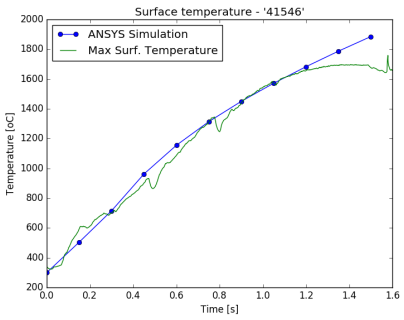


**(a)** Ansys model vs the TLL experimental surface temperature.

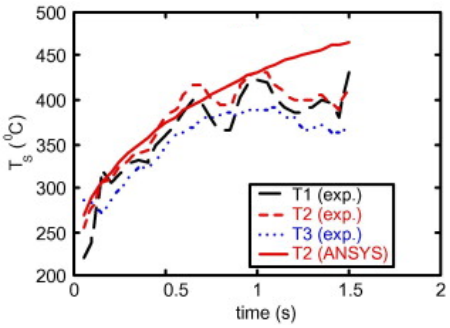


**(b)** Ansys model vs the LLL experimental surface temperature [50].

**Figure 3.32:** Comparison of the operative window for lithium and tin limiter.

and the tin limiters have been exposed to several different plasma discharges with transient heat load up to ten $^{MW}/_{m^2}$, without damages on the CPS surface. A possible interpretation is the vapor shield self-protection phenomena has been proposed with tin in [32]. The lithium limiter has shown a flattening of the surface temperature, as shown in figure 3.32b, which deviates from the heat conduction model provided by ANSYS code. The flattening of the surface temperature can be linked to the surface evaporation phenomena. Also using the tin limiter, the deviation from the ANSYS model has been observed above relevant tin evaporation temperature, as shown in figure 3.32a. Such effect has been achieved placing the TLL at a few millimeters from the LCMS: the temperature evolution has clearly moved from the ANSYS simulated at a high temperature level. The operative temperature window, larger for tin than lithium, strictly depends on the respective vapour pressure curves. Referring to figure 3.32a, probably the lack of the oscillations was related the the different plasma pressure due to the pulse setup and to the limiter position. In this case, we suppose, it was higher then the vapor tin pressure.

As previously described during the strong evaporation regime, with both metals, the VUV spectra have been completely dominated by lithium or tin, as is visible in figure 3.33a. Starting from that an estimation of the impurity content in the discharge from the Z-effective measurement has been provided. Assuming that lithium or tin are the only impurity the effective charge $Z_{eff}$ is $Z_{eff} = \frac{Z^2_{imp} \cdot n_{imp} + Z^2_H \cdot n_H}{n_{tot}}$. Substituting in the equation the values for the selected pulses we got respectively $n_{\%_{Li}} = (1.0 \pm 0.8)\%$ and $n_{\%_{Sn}} = (0.05 \pm 0.03)\%$. With the tin limiter, we observed the absence of any impurity lines on the UV spectra until the surface temperature reached a sufficiently high level, approximately $1500°C$,

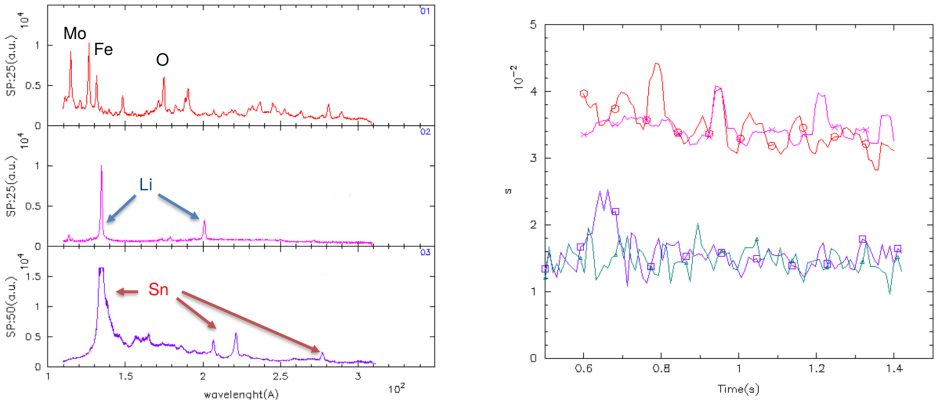


**(a)** Comparison of different spectra during the FTU pulse. Starting from the top a normal discharge with the usual toroidal main limiter, in the middle a pulse with the lithium limiter, finally in the bottom with the tin limiter.

**(b)** Confinement time from JETTO simulation on FTU pulses. Starting from the bottom: (a - purple) metals dominating spectra (Mo, Fe, O); (b - cyan) tin main impurity after many shots withtin limiter; (c - purple) lithium main impurity after the "lithization campaign"; (d - red) after a fresh boronization.

**Figure 3.33:** Comparison of the machine working with the usual TZM limiter, the liquid lithium limiter and the liquid tin limiter.

where evaporation becomes important. The JETTO code [101] was also used to compare two similar discharges without and with the liquid metal limiters in strong evaporation regime. A picture of that is reported in figure 3.33b. Starting from the bottom metals dominating spectra (Mo, Fe, O) is shown in purple with and tin dominated spectra in cyan, the two confinement times are within the error bars (10-15%) and they are practically the same without any appreciable degradation in plasma performance. A different story is with lithium reported in purple, the confinement time when FTU is lithium dominated is compared with the machine performance as after a fresh boronization, the red line in the plot. This behaviour was expected from the already performed experiments with lithium injection in many devices, furthermore a detail report of the beneficial lithium effects on plasma is in [50].

In summary, the experiments performed so far demonstrate the possibility for liquid materials of withstanding high transient heat loads, with the added quality of self-healing properties. Technological improvements have followed the liquid metals experiments on FTU. Several CPS meshes have been tested, several layouts have been investigated and different diagnostic tools have been applied. The experience with lithium and tin fixes the physical (i.e. the operative window) and technological constraints for the next design phase.

This work concern the analysis of the liquid metal samples exposed to ISTTOK plasmas, which are well described in [102, 90]. The *Instituto Superior Técnico TOKamak*, ISTTOK, is a high aspect ratio tokamak with a circular cross-section. Its main ISTTOK parameters are: $R = 46$ cm, $a = 8.5$ cm, $B_T = 0.5$ T, $I_p = 4$ kA. This device can operated in AC-mode [103], meaning that each discharge consists of a lot of smaller pulses of alternated plasma current. This operation mode extends the length of discharge allowing for better analysis of the plasma sample interaction dynamics. The typical parameters in the edge plasma, relevant in this treatment, are: electron and ion temperature, $T_e \sim T_i = 15 - 30$ eV, electron density, $n_e = 0.5 - 3 \times 10^{18}$ m$^{-3}$, particle flux $\Gamma^{D+} = 1 - 7 \times 10^{22}/\text{m}^2\text{s}$, a radial decay length of the particle flux of $\sim 2 - 3$ cm and discharge duration of 1 s. It mean each shot consisting of forty alternating pulses with a duration of $\sim$ 25 ms as seen in the top panel of figure 3.34. In the IST tokamak a stainless steel manipulator host the sample holder with a bore cup where the liquid metals are exposed to the plasma. An electric heater is used to melt the sample. The samples preparation took place in a separate vacuum chamber as described in [102, 90]. They were heated up and the temperature was kept until the end of outgassing phase, so the pressure became stable. The samples were then allowed to solidify and transfer to the tokamak. Once there the sample was degassed again, moved to the selected minor radius for plasma exposure and reheated. The sample was exposed from a lower vertical port of the tokamak with surface parallel to the machine's horizontal plane at a normalised radial position of $r/a = 0.7$. The sample was irradiated under deuterium plasmas in the liquid state.

The spectroscopy setup on ISTTOK is composed of a spectrometer (CVI 1/2 Digikröm), a fast EMCCD camera (iXon Ultra 888) and an optical alignment system fitted to the vessel's horizontal port. A bundle of ten optical fibres connects the in-vessel optics to the spectrometer allowing simultaneous measurements of the spectral emission spanning from the scrape-off layer to the inner part of the plasma core. The system is focused such that each sampled volume is separated 2.5 mm from the adjacent. The surface temperature of the samples was monitored using one of two pyrometers - optris CTlaser 3ML or 2MH - focused on the sample from the top connector of the port according to the relevant temperature ranges:

- 3ML covers the interval of 50°C to 400°C
- 2MH goes from 385°C to 1600°C

In order to provide the pyrometers calibrations a type-k thermocouple was placed in the

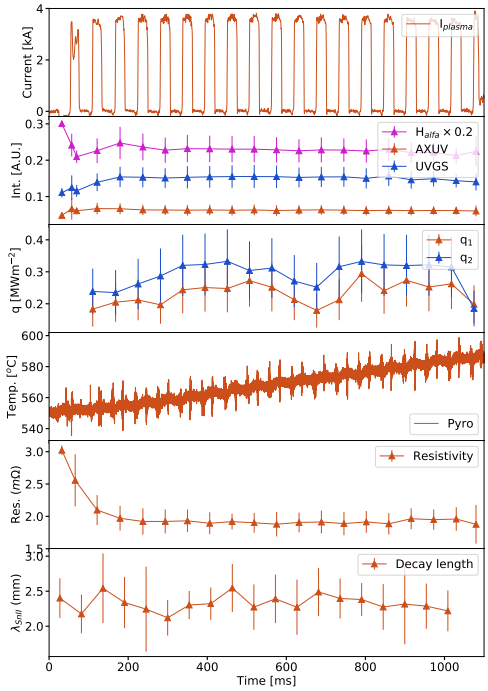


**Figure 3.34:** Compilation of the signals acquired on the shots of the liquid tin experimental campaign.

liquid metal next to the pyrometer's focal point. The calibration was done in a mock-up setup with the same experimental conditions as the tokamak. In previous liquid metal experiments at ISTTOK, it was observed that the combined action of the holder cartridge heater and the plasma heating did not bring the liquid metal temperature above 450 $^oC$. This means that the tin evaporation is negligible according with the curves in figure 2.14.

There were two pinhole diode bolometers installed inside the vacuum vessel at a distance of $\approx \pi/2$ on the toroidal direction from the liquid metals holder, they can be used to monitor the local impurity content during the tokamak discharge evolution. Finally, there is a set of Langmuir probes mounted on a moving manipulator. Several probes are installed in ISTTOK for different purpose, i.e. plasma fluctuation measurement, flux measurements, etc. In this work the electrodes have been swept with a sinusoidal tension in order to get the classical edge parameters like as electron temperature and electron density.

We are now focusing on an experimental campaign dedicated to the liquid tin exposure in ISTTOK. Looking at figure 3.38 the situation for the whole experimental campaign is shown. During the discharges the sample temperature raised by the action of the electrical heater and by the plasma effect, however all the bolometric measurement remains fairly constant.

Since the bolometric signals can be considered a proxy for the effective plasma charge, the fact that they remain constant supports the hypothesis that the tin influx in the discharge is minimal and the plasma performance was mostly unperturbed. This agrees with the very low vapor pressure and the very low sputtering contribution related with the small exposed area. On the fourth panel of figure 3.34 the typical evolution of the surface temperature during a discharge is shown. The surface temperature of the sample was monitored using pyrometers which focused on the sample from the top connector of the port. In the top panel, the plasma current, putting the attention on the positive current cycles while the negative ones systematically failed. This characteristic is also observable also from the pyrometer, in fact the IR diagnostic time resolution is lower of the single plasma pulse. Furthermore, the plasma equilibrium is different in the positive and in the negative case having an effect on the vertical position. The result is a different power flux on the sample that can be observed from the pyrometer. The temperature evolution is correlated to this displacement, in fact, during the positive cycles the temperature increases, but in the absence of plasma, the sample starts cooling down. However, since the manipulator's head is thermally isolated, the cumulative behaviour is a steady temperature increase throughout the discharge, the average temperature slowly increased during the experimental campaign as is shown in the fourth panel of figure 3.38. Starting from the sample surface temperature evolution, it is possible to derive the impinging heat flux. The same analysis already shown in section 3.2.1 have been applied also to the ISTTOK experimental data. But since the fewer amount of available data we decided to use a simplified approach. Particularly, two different methods have been used to derive the thermal flux. The solution for the temporal evolution of the temperature [75], $T$can be written as:

$$\begin{aligned} T(x,t)\Big|_0 &= T(0,0) + \frac{q}{k}\int_x^\infty erfc\left(\frac{x}{2\sqrt{\alpha t}}\right)dx\Big|_0 \\ &= T(0,0) + \frac{2q}{k}\sqrt{\frac{\alpha t}{\pi}} \end{aligned} \tag{3.44}$$

where $q$ is the heat flux, $k$ is the thermal conductivity and $\alpha$ the thermal diffusivity. Since the temporal evolution of the surface temperature is recorded it is possible to fit equation 3.44 with the experimental data to derive the heat flux. However, this solution assumes the heat flux to be constant throughout the considered interval. If this assumption is not satisfied the exact analytic solution of the equation 3.5 is a convolution integral whose value can be

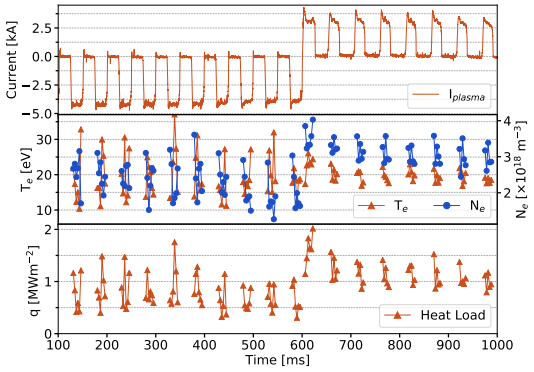


**Figure 3.35:** Temporal evolution of the plasma current and the Langmuir probe derived quantities. In panel three the heat loads to the probe which are derived from the other quantities. The signal are processed such that they are only shown averaged plasma current is present.

determined numerically with the given boundary condition. This alternative technique is therefore also capable of deducing transient heat loads. The numerical value of this integral is given by the Cook and Felderman method [79], [77], already described in section 3.2.1, which gives the exact solution for the problem in the semi-infinite body approximation.

In the third panel of figure 3.34 the heat fluxes estimated from the two discussed above methods are shown for one particular discharge. The heat flux $q_1$, the one plotted in brown, corresponds to convolution integral solution while $q_2$, the one in blue, is the fit with the simple analytic approximation, assuming the stationary, given by the equation 3.44. Both estimations are shown averaged for each AC-period to simplify the comparison between the two methods. This is of particular importance for selecting the intervals under which the heat flux can be considered constant.

The data available from the Langmuir probes has been used to cross-check the heat fluxes values on the target as estimated from the pyrometer. Using the classical electrostatic probe theory, with all the known approximations, it is possible to deduce the parallel heat flux from the electron temperature and density, i.e. $q_{\parallel} = \gamma \frac{T_e I_{sat}}{A_{pr}}$, where $T_e$ is the electron temperature, $I_{sat}$ the saturation current and $A_{pr}$ is the probe surface perpendicular to the flux pipe. The energy transfer factor, $\gamma$, has been considered like for FTU, $\approx 7 \div 8$, Heat loads between 0.5 to 1.2 MWm$^{-2}$ has been observed which is fully compatible with the expected values. Moreover the previous measurements at ISTTOK on the power flux density performed by Gomes [31] are in agreement with the actual experimental data. The average heat load measured with the Langmuir probes is within the same order of magnitude as those derived from the pyrometer signals. Within the same shot the centroid of the plasma column fluctuates

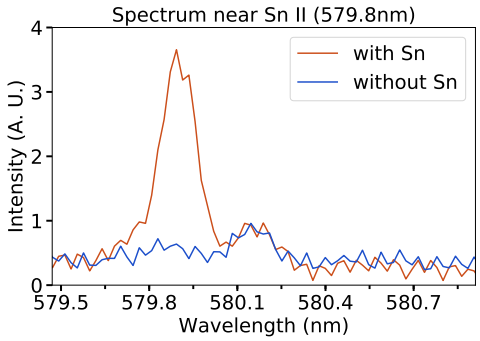


**Figure 3.36:** Typical spectrum acquired near the Sn II 579.80 nm line during an ISTTOK discharge in brown. For comparison the same spectra is shown for a discharge without tin.

around some different equilibrium position. That position varies from shot to shot as well as between AC-periods of the same shot. This is particularly true for plasma current of opposing directions. The distance between the plasma and the sample surface is one of the main parameter determining the deposited energy. The particular case shown in figure 3.35 displays two distinct moments with different plasma edge parameters and heat loads reaching the sample surface. Nonetheless, for the duration of this campaign the average heat load is in the order of few hundreds of $\mathrm{kWm}^{-2}$ which could be enhanced if both positive and negative cycles of the AC discharge had occurred.

Plasma resistivity was derived from the ratio between plasma current and loop voltage, i.e. $R_{plasma} = V_{loop}/I_{plasma}$ to have a rough idea of the global impact on plasma of the exposed sample. On ISTTOK discharges, this quantity depends on many parameters and so it is vulnerable to calculation errors: it is only calculated and shown for flattop-averaged values of loop voltage and plasma current. Resistivity for a normal discharge is shown in the fifth panel of figure 3.34 and the campaign evolution of this quantity is shown in figure 3.38. The plasma resistivity was mostly unaffected by the sample exposition during this campaign, in fact, the value does not deviate significantly from the typical value for ISTTOK. Furthermore, if the overall growth in resistivity is attributed exclusively to change in $Z_{eff}$ then, according to the Spitzer's resistivity formula, the averaged nuclear charge of the plasma will be modified by a factor of 10% or less. This does not differ significantly from that of other experimental days and normal operation fluctuation.

Moving to the spectroscopic analysis during the campaign in analysis and in the previous experiments with liquid tin at ISTTOK the most intense lines of SnI (303.41, 317.50, 326.23, 452.47 nm) where never identified. Several SnII candidates where found (579.8, 556.19 and

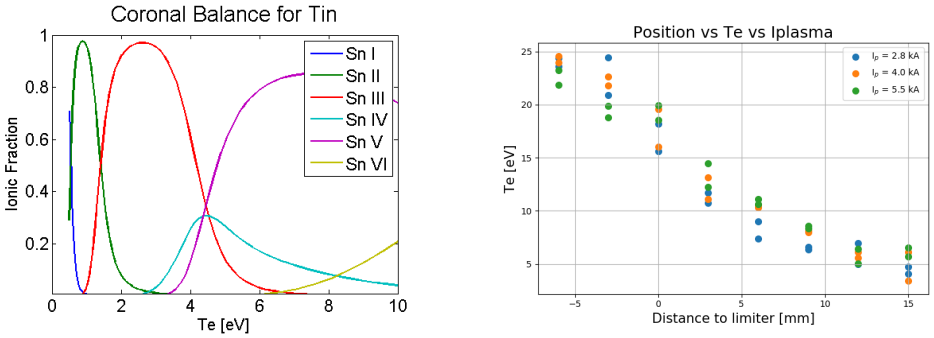


**(a)** Tin coronal balance for the first six ionization stages. Rates coefficients given by FLYCHK [105].

**(b)** Electron temperature on ISTTOK versus the radial distance to the limiter.

**Figure 3.37:** Tin coronal balance on the left. Electron temperature profile on ISTTOK on the right.

558.88 nm). Above the second ionisation state, the lines documented in literature [104] are below detection threshold or in a spectral range not accessible with the optical setup. From all the observed lines the SnII 579.8 nm was the one with the highest relative intensity and was therefore used as a good indicator for tin presence in the discharge.

The coronal balance, reported in figure 3.37a, indicates that the observed Sn lines are compatible with a plasma region where the temperature should not be higher than 3 eV. Electrostatic probe measurements of the ISTTOK scrape off layer show that such region is located outside of the last closed magnetic surface roughly 10mm away from the limiter. This is shown in figure 3.37b where three sets of points are for different plasma currents, the temperatures are determined by the electrical characteristic of a langmuir probe.

The typical failure rate of two following cycles in ISTTOK discharge in the order of 50% was not related to the introduction of tin samples but was unfortunately outside of control. A picture of this is in the plasma current panel of figure 3.34. Such behaviour was already present before and after the experimental campaign in analysis. An asymmetry was observed during the shots dominated by either positive or negative current periods, reflecting of course in the plasma position. The strong correlation with the discontinuity observed between shots 41990 and 41992 is visible in figure 3.38. The average plasma position has a strong impact on most the tokamak diagnostics, and particularly to the light based since the intersection between the plasma column and line of sight is modified. This is the case of the $H_\alpha$ and bolometry. The LCMS position also determine with which part of the vessel wall (and of the fully poloidal limiter) the plasma is interacting. There is also an impact on the comparison between the heat loads to the sample as derived from the pyrometry signals and the Langmuir probe signals.

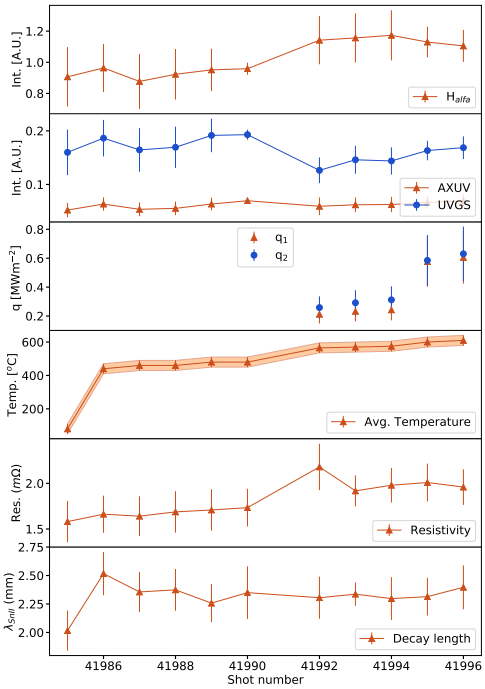


**Figure 3.38:** Summary acquired signals during the experimental campaign. Each panel shows the shot-averaged evolution of the values throughout the experimental campaign for the same signals which are previously shown in figure 3.34.

Since the sample is inserted from the bottom and the Langmuir probe from the top of the machine a deviation in the horizontal position of the plasma results in a reverse heat load measurements. The heat loads measured by pyrometer and by the Langmuir probes are in the same order of magnitude. We found the thermal load on the tin samples systematically lower than what observed by the electrostatic probes and by Gomes measurements [31]. A possible explanation is that the holder size is not negligible, so perturbing the local plasma.

To conclude several diagnostics were used to analyse the interaction of ISTTOK's deuterium plasmas with the liquid tin samples. The evolution of the tin surface temperature was monitored by two pyrometers and two different methods were used to deduce the plasma impinging power flux density. This was found to be in the order of hundreds kWm$^{-2}$ which is supported by Langmuir probe analysis and previous measurements.

Plasma pollution caused by tin has been found very low. All the observed measurements are consistent with practically negligible evaporation and very low sputtering. The low amount of tin ions escaping from the sample are quickly or already ionise which is consistent with the spectroscopy data. The ISTTOK plasma conditions at which the sample is exposed are

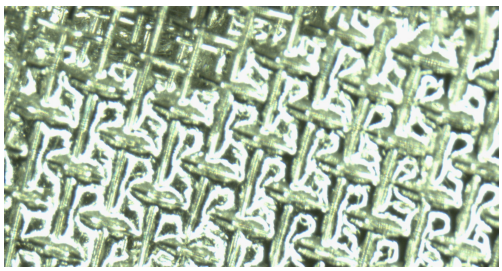

**Figure 3.39:** Photograph of a tungsten mesh wetted by tin in the Frascati Liquid Metals Laboratory ready for the exposure on ISTTOK .

below the threshold for the onset the evaporation regime for tin. It has been proposed, for the future, to upgrade the manipulator's sample holder with the possibility of sample polarisation as well as the introduction of a capillary porous system. In figure 3.39, a tungsten mesh wetted with tin in the Frascati Liquid Metals Laboratory is shown. The idea is to fit the actual ISTTOK manipulator dimensions and allow different exposure schemes and the exploitation of other ports on ISTTOK using the CPS technology. Furthermore, polarising the sample the evaporation threshold can be obtained and surpassed. This would allow to separately study, on ISTTOK, the two primary mechanisms of impurity production for liquid metal PFC, we mean evaporation and sputtering.

The experimental evidences reported above allow to extrapolate for a future setup. Sputtered and evaporated ions will have different initial population: we expect the ions, produced mostly by energetic collision, already ionised, while the evaporated tin should be neutral. The idea is that the neutral atoms evaporated would have a velocity distribution peaked to the thermal velocity of the surface, a small fraction of eV, against tens eV for the sputtered one. Using negative polarisation it will be possible to attract and accelerate ions to the target and reach the observed tin sputtering by deuterium ions as reported by [106]. Having a sweep up to 200V it would be possible to study the effect of the highly energetic ions bombarding the liquid surface and observe its effect on plasma pollution. On the other hand it is possible to largely increase the local heat flux by polarising the target with a positive biasing voltage such that the electrons are attracted. A collecting area of $125mm^2$ is considered, keeping in mind the typical edge parameter for ISTTOK, the average current for the negative sample polarisation is in the order of 0.2A which means an additional heat flux of about $0.15^{MW}/_{m^2}$. This value is too small to affect the target significantly in terms of surface temperature increase. Instead with the direct bias of 200V and limiting the current at 3A it is possible to increase the power flux density to the target of $4.5^{MW}/_{m^2}$. Such value is relevant and could push the

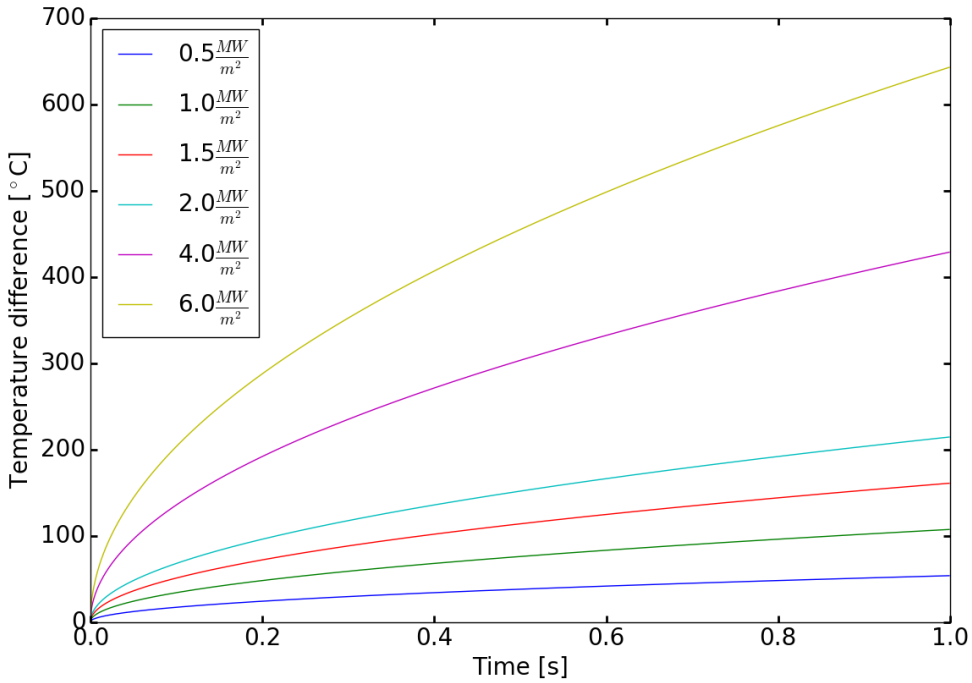


**Figure 3.40:** Surface temperature simulation versus time for different heat flux density.

final surface temperature of the sample high enough to have access to the evaporate regime, as shown in figure 3.40.

*Excellent! And now?*
*Light, just light, making everything below it a toy world.*
*Very well, we'll make the glasses accordingly.*

Edgar Lee Masters, Spoon River Anthology

# 4

# Technological aspects of liquid metals

In this chapter topics concerning liquid metals interesting for fusion applications will be discussed. During the development of the thesis, part of the time has been devoted to experimental activities investigating the mechanisms that dominate the metals behaviour in the liquid state, and particularly in which way these aspects affect their application in tokamaks. Furthermore, practical aspects of liquid metal and relative technology have been studied to consciously participate in the liquid limiters operations improvements on FTU and in the conceptual design of possible future liquid plasma facing component structures.

## 4.1 Introduction to liquid metals theory

How does a liquid look like on the microscopic scale? We can figure out it like a molecular ensemble in rapid motion, with a mean kinetic energy of $\frac{3}{2}k_BT$ so that the environment of each one must be continuously changing. This statement is true for a classic interpretation of the kinetic energy, derived from the equipartition energy. Quantum corrections are never found to be important in liquid except for low atomic weight elements which remains liquid at very low temperature. Imaging we can sit on a single molecule and record its neighbour's positions for any instant of time, we can ask what kind of average environment we will observe [107].

At one extreme is what may so-called the *quasi-crystalline* models, in which the local coordination just above the melting point is treated as very similar to that which prevail in

the solid phase just below [108]. Any evidence can suggest the mean separation between neighbouring molecules change less on melting than might be expected from the increase in volume which occurs; it is the mean number of the nearest neighbours - the so-called *coordination number* - which is altered. This is the sort of evidence that has been often used to justify the quasi-crystalline approach, the extra volume in the liquid phase is commonly ascribed to *holes* in the liquid structure. In the simplest model the holes may be treated as actual vacancies in a crystal lattice, but more general they could be dislocated, grain boundaries between crystallites or any sort of misfit that arises when the long-range order of the solid is destroyed.

One of the difficulties getting in contact with quasi-crystalline model is to explain the observed increase of entropy on melting, which, is typical of the order of $k_B$, Boltzmann constant, per atom in simple monoatomic substances. This is shown in table 4.1. We are going to examine with more detail this argument by introducing the entropy in liquid metals. Anyway, it emerges that if crystals exist in liquids they must be very small, in the order of few molecules. An argument supporting the fact that they could not be even as big as this, because the presence of them would make it impossible for a liquid to supercool. In ideal circumstances Turnbull and Cech [109], suggest almost all liquid metals can supercool through as much as 20% of their melting temperature. It is possible to overcome this argument by various hypotheses: if the crystallites in a liquid have something to do with a state of free rotation, i.e. a potential barrier could exist inhibiting the growth of one at the expense of another. Anyway, if crystallites exist, at all, they are so small and so irregular and so continuously swapping molecules between themselves and changing orientations that the observer sitting on a molecule in a liquid would hardly recognise their existence. Maybe, over a relatively long period of time, it would be possible to identify an average correlation between the position of neighbouring molecules, reminiscent of the solid lattice correlation [107].

At the opposite extreme from the quasi-crystalline picture lies the model of *random close-packed* (RCP) spheres, particularly investigated by Berna [110], [111], [112]. The RCP can be imagined on the macroscopic scale, for example, by pouring a lot of rigid bearing balls in a container with irregular surfaces -since smooth sides would encourage a regular lattice formation, in other words crystallization- and shaking them together until they could not be further compressed. Several methods for disclose the characteristic coordination patterns exist in the literature. The conclusions could be:

- the mean number of neighbours which virtually make contact, so that are very close, with some central sphere, is about 8;

- if the entire volume of the system is divided up into *Voronoi polyhedra* [*], and each polyhedron is associated with a sphere, then the mean number of faces per polyhedron is close to 13. All these neighbours lie quite close, within $\sqrt{2}$ diameters of the central sphere;

- the Euler's theorem implies that the mean number of edges per face on the polyhedra should be very close to 5 [113]. A high incidence of five-sided faces is indeed observed, and five-fold rings of neighbouring atoms are associated with these. Such feature is unfamiliar to any crystal lattice with translational symmetry, so that it exists an essential difference between the RCP state and any arrangement described by the quasi-crystalline.

The volume increase needed to pass from a truly close-packed arrangement of rigid spheres to a random close-packed is roughly the 15%, which is quite close to the expansion that it is observed for the rare gases melting, as reported in table 4.1. Anyway, the weak point of this model is its static character. A computational approach to the dynamic models shows that the increase of volume on melting is greatly affected by the kinetic energy of the molecules. This argues that in the solid just before melting they are already quite well separated.

### 4.1.1 Entropy in liquid metals

From the point of view of the quasi-crystalline model is a matter of interest to look at the increase of the entropy on melting $\Delta S$, which can of course be determined from the latent heat of melting [107]. However, it is really interesting to compare the total entropy of the liquid phase, as determined from specific heat measurements down to very low temperature, with the quantity

$$S_{pg} = Nk_B log\left(e\frac{\Omega}{N}\left(\frac{2\pi e m_A k_B T}{h^2}\right)^{\frac{3}{2}}\right) \tag{4.1}$$

where $N$ is the number of molecules in the volume $\Omega$ and $m_A$ the atomic mass of the specimen, while of course $k_B$ the Boltzmann constant, $e$ the elementary charge and $h$ the Planck constant. The formula 4.1 describes the entropy of a perfect gas at the same temperature and volume considered for the liquid in analysis. The difference $S_E = S - S_{pg}$ is known as the *excess entropy*. It is a negative quantity since the spatial coordinates are more ordered

[*] In the simplest and most common case, that of the plane, given a finite set of points S, the Voronoi diagram for S is the partition of the plane that associates a region $V(p)$ to each point $p \in S$ so that all points within the $V(p)$ region are closer to each other than to any other point in S.

| Substance | Increase of volume on melting % $\Delta\Omega/\Omega$ | Increase of entropy on melting $\Delta S/Nk_B$ | Excess entropy at melting point $-S_e/Nk_B$ |
|---|---|---|---|
| A | 14.3 | 1.7 | 3.6 |
| Kr | 15.1 | 1.7 | - |
| Xe | 15.3 | 1.7 | - |
| Li | 1.6 | 0.80 | 3.7 |
| Na | 2.5 | 0.85 | 3.55 |
| K | 2.5 | 0.87 | 3.61 |
| Rb | 2.5 | 0.87 | - |
| Cs | 2.6 | 0.87 | - |
| Cu | 4.4 | 1.16 | 3.6 |
| Ag | 3.8 | 1.13 | 3.85 |
| Au | 5.1 | 1.11 | 4.0 |
| Be | 7.0 | 1.13 | 3.7 |
| Mg | 3.1 | 1.17 | 3.45 |
| Zn | 4.2 | 1.28 | 3.9 |
| Cd | 4.0 | 1.24 | 4.15 |
| Hg | 3.6 | 1.18 | 5.1 |
| Al | 6.0 | 1.39 | 3.6 |
| Ga | -3.2 (+1.5) | 2.2 (1.1) | 4.75 |
| In | 2.0 | 0.92 | 4.4 |
| Tl | 2.2 | 0.85 | 4.05 |
| Si | -9.6 | 3.6 | (2.5) |
| Ge | -5.0 | 3.2 | (1.0) |
| Sn | 2.6 | 1.67 | 4.2 |
| Pb | 3.5 | 0.96 | 4.1 |
| Sb | -0.9 | 2.61 | 3.2 |
| Bi | -3.4 | 2.40 | 3.9 |
| Te | 4.9 | 3.0 | 2.6 |

**Table 4.1:** The volume and entropy variations of simple liquids. The parameters in parenthesis for Ga are for metastable $Ga$B supercooled at $-16.3°C$. Table from [107].

in the liquid phase than in a perfect gas. Some values for $S_E$ are shown in table 4.1, and it is possible to notice several substances can be grouped together as for example the rare gases, the Body Centered Cubic (bcc) metals (Li, Na, K, Rb, Cs, Tl), semimetals, etc. By comparison the variation in $S_E$ seem to be unsystematic and relatively small with low dispersion.

We can deduce that when these simple substances melt they tend to lose the structural features. We can we also note they tend to decrease the differences that distinguish them from one other. For example Sb and Bi are semi-metals in the solid phase, however the contraction occurring during melting seems to bring them in the metallic properties space. Ga shows a large $S_E$ normalized value, it is possible that Ga has a more ordered structure just above the melting point than the average liquid metals. The same argument it is valid also for Hg.

Some model [114] from the begin of the last century observed that the thermal entropy of an Einstein solid, $S_s$, is given in terms of the characteristic vibration frequency (for solid) $\nu_s$ by the formula

$$S_s = 3Nk_B \, log\left(\frac{k_B T}{h\nu_s}\right) + O\left(\frac{h\nu_s}{k_B T}\right)^2 \tag{4.2}$$

If we now assume that a similar formula can be written also for liquid and applying the basic logarithmic property we immediately get

$$S_s - S_l = \Delta S \approx 3Nk_B \, log\left(\frac{\nu_s}{\nu_l}\right) \tag{4.3}$$

so that an entropy increase of order of $Nk_B$, as shown in table 4.1, can be explained by a drop of roughly 40% in $\nu$ passing from the solid to the liquid phase. Using the Dulong–Petit law [115], or remembering that at high temperature the electrical resistivity of solid metals should scale with $\nu_s^{-2}$, we can rewrite the previous equation 4.3 as

$$S_s - S_l = \Delta S \approx \frac{3}{2}Nk_B \, log\left(\frac{\rho_l}{\rho_s}\right) \tag{4.4}$$

where $\rho_l$ and $\rho_s$ are respectively the liquid and solid electrical resistivity. Such approximation works with reasonable accuracy in most of the case. Unfortunately, this simple theory it is not fully coherent. The $\nu$ increase on melting is too large compared with the typical molecular motion in liquid [107], and also $\rho_l$ and $\rho_s$ depends upon more factors than just $\nu_l$ and $\nu_s$. The main error is probably to consider all the entropy of a liquid due to the thermal agitation of its molecules. But in this way, we ignore the *configurational entropy* arising from disorder in the rest position where the molecules are instantaneously vibrating towards. In support of

this, taking in example a simplified quasi-crystalline model, if we consider all the extra volume, introduced on melting, as available for vacancies creation, we get a configurational entropy, $S_c$, equal to

$$S_c = Nk_B \left(\frac{\Delta\Omega}{\Omega}\right)\left(1 - log\left(\frac{\Delta\Omega}{\Omega}\right)\right) \tag{4.5}$$

It amounts up to $0.2Nk_B$ if $\frac{\Delta\Omega}{\Omega}$ is 5% and so it is not negligible at all. So, the presence of very small crystallites in the liquid seems to justify the magnitude of $\Delta S$.

### 4.1.2 Specific heat, surface tension, and surface entropy

The studies of liquid metal features, and particularly the surface properties, has been found extremely useful handling with the wetting and corrosion experiments. At the melting point the specific heat at constant volume, $C_\Omega$, is quite close to the Dulong and Petit [115] value of $3Nk_B$, as in the monoatomic solid. It is a surprise, since a good part of the specific heat in solids is attributed to the excitation of transverse vibrational modes which an ideal fluid is unable to support. Nevertheless, real liquids are viscous, and their viscosity at the melting point is sufficient for transverse mode propagation with little attenuation [116]. The liquid viscosity rapidly falls on heating and the transverse mode energy storage become less important. With this argue we can point out, as in [117], that $C_\Omega$ diminishes with temperature tending to a value of about $2Nk_B$ at the critical point temperature, $T_c$, consistent with the idea that at this point the transverse vibrations are no longer contributing. In a monoatomic perfect gas, which cannot sustain vibrational modes, $C_\Omega$ is $\frac{3}{2}Nk_B$. Since $C_\Omega$ is larger than $(C_\Omega)_{PG}$, the excess entropy should rise on heating. In example, assuming $-4Nk_B$ at the melting point, we should end to $-2Nk_B$ at the critical point, as suggested by the following equation [107]:

$$-4Nk_B + \frac{3}{2}Nk_B\, log\left(\frac{T_C}{T_M}\right) \approx -2Nk_B \tag{4.6}$$

The specific heat remains negative since the molecular structure still retains some degree of order. The ratio between the specific heats at constant pressure and constant volume follows from the thermodynamic formula

$$\gamma = \frac{C_p}{C_\Omega} = 1 + \alpha^2 \frac{\Omega T}{\beta C_\Omega} \tag{4.7}$$

where $\alpha$ is the volume expansion coefficient and $\beta$ the isothermal compressibility.

| Metal | $d\mathscr{F}/dT$ $dyne\, cm^{-1} K^{-1}$ | Surface entropy per atom units of $k_B$ |
|---|---|---|
| Li | -0.14 | 0.80 |
| Na | -0.1 | 0.85 |
| K | -0.06 | 0.78 |
| Rb | -0.06 | 0.94 |
| Cs | -0.05 | 0.78 |
| Ag | -0.13 | 0.65 |
| Al | -0.165 | 0.68 |
| In | -0.096 | 0.61 |
| Sn | -0.083 | 0.55 |
| Cu | +0.75 | -2.9 |
| Zn | +0.5 | -2.2 |
| Cd | +0.5 | -2.9 |
| Hg (25 °C) | -0.20 | 1.2 |

**Table 4.2:** Surface entropies of liquid metals. All the data are for temperature close to $T_M$, except in the case of Hg [107].

Given this preamble we are going to the main purpose of this subsection, the surface tension. We use the symbol $\mathscr{F}$ to indicate the surface tension of liquid metals, it is measured in force per unit length. Its SI unit is newton per meter, $N/m$, which could also be replaced by surface free energy per area, $J/m^2$. The surface tension for liquid metals is quite large, compared with many non-metallic liquids, but it is not unexpected. Approximations based on the *Jellium model* [107] are capable of giving an answer of the right order of magnitude. In the normal course of the events $\mathscr{F}$ is a decreasing function of temperature; it goes to zero at the critical temperature following the empirical law $(T_c - T)^n$, where n seems generally to be a little bigger than one. This means that the *surface entropy* per unit of area, or $-d\mathscr{F}/dT$, is a positive quantity. The surface entropy corresponding to the area occupied by a single atom in the surface layer is typically rather less than $k_B$. There are some liquid metals for which $d\mathscr{F}/dT$ is reported to be positive, notably Cu, Zn, and Cd. Table 4.2, summarize the surface entropy for a list of several liquid metals.

The problem of the surface entropy dependences can be afford according with the Debye theory. In such case the entropy is associated with the excitation of vibrational modes. If the

wavelength is large compared with the atom dimensions the dispersion relationship can be well approximate by

$$\omega^2 = q^3 \mathscr{F}/\rho \tag{4.8}$$

where $\omega$ is the angular frequency for a vector $q$ and $\rho$ is the density. It follows that the number of distinct ripple modes on a surface A is given by

$$\mathscr{N}(\omega) = \frac{A}{3\pi}\left(\frac{\rho}{\mathscr{F}}\right)^{\frac{2}{3}} \omega^{\frac{1}{3}} \tag{4.9}$$

the quantity on the left side of the equation 4.9 is commonly called *density of states*. We can define the cut-off frequency $\omega_{max}$ by the condition

$$\int_0^{\omega_{max}} \mathscr{N}(\omega) d\omega = \frac{A}{a} \tag{4.10}$$

where a is the surface area occupied by a single molecule. It can be considered in the order of $\approx\ 1.09 \cdot \left({}^{m_A}/_{\rho}\right)^{2/3}$. So we can now image to replace the role of the Debye temperature, $\Theta_D$ in the Debye theory with a characteristic surface temperature $\Theta_S$ given by the equation

$$\Theta_S = \frac{\hbar\omega_{max}}{k_B} = \frac{\hbar}{k_B}\left(\frac{4\pi}{1.09}\right)^{3/4}\left(\frac{\mathscr{F}}{m_A}\right)^{1/2} \tag{4.11}$$

It follows from the Debye theory for temperature higher than $\Theta_S$

$$\mathscr{F}(T) = \mathscr{F}(0) - \frac{k_B T}{A}\int_0^{\omega_{max}} \mathscr{N}(\omega)\left\{log\left(\frac{k_B T}{\hbar\omega}\right) - \frac{1}{24}\left(\frac{\hbar\omega}{k_B T}\right)^2 + \dots\right\} d\omega \tag{4.12}$$

where $\mathscr{F}(0)$ is the surface free energy in absence of modes. At the end of the story, after having separate the contribution from the bulk modes to the surface entropy we approach at the final formula

$$-a\frac{d\mathscr{F}}{dT} = k_B\left\{log\left(\frac{\Theta_D}{\Theta_S}\right) + \frac{5}{12}\right\} \tag{4.13}$$

where the terms of order $O\left({}^{\Theta}/_{T}\right)^2$ have been neglected above the melting point.

For liquid metals the ratio $\frac{\Theta_D}{\Theta_S}$ lies in the range between 1.4 and 2.1 so the surface entropy per atom is expected to be close to $k_B$. This theory can explain most of the entries in table 4.2

with reasonable precision. Nevertheless, Cu, Zn and Cd clearly remains anomalous, asking for an unusual degree of ordering in the arrangement of the ions near the surface. A possible explanation suggested by [107], is that the liquid surface is virtually crystalline. Given the melting entropy of such elements of about $1.2k_B$ per atom, it corresponds to roughly three layers of ions ions crystalline in order to take account of this results, but unfortunately not good references are cited in support of this statement.

## 4.2 Liquid Metal Laboratory in Frascati

Recently a dedicated laboratory has been installed in Frascati focused on the study of the liquid metals properties. The main aim of such laboratory it to investigate the liquid metals behaviour outside the tokamak environment and to improve actual knowledge and technologies in this field.

For this purpose a new high vacuum oven, shown in figure 4.1 has been installed in the laboratory, in addition, a smaller vacuum chamber has been set up to speed up the experiments on small mock-ups and to test the procedures before replicating them within the larger oven.

The small size camber consists in a vacuum volume of roughly 80cm$^3$. The stainless steel cylinder is actively cooled by water, a quartz window placed on top of the chamber allowing a visual inspection of the overall process. A small microscope up to 1000X looks at experiments recording or taking pictures. The heat is provided by a refractory metal resistance (usually tantalum but may be substituted with molybdenum or rhenium) in which flows current. The AC power is supplied by a Variac directly connected to the grid and then a transformer to increase the current. The maximum supply voltage is 5V RMS and the current up to 150A RMS. At this moment the temperature is measured with a platinum rhodium TYPE B thermocouple directly in contact with the bottom part of the resistor, the crucible with the liquid metal bath, usually a small box made by a molybdenum sheet, is placed in the upper part of the resistor. The large oven instead consists of two different vacuum chambers. A larger cylindrical chamber, the one actually heated, and a smaller chamber equipped with an inspection window, an opening to load the samples and a manipulator. An overview of the oven is given by the picture in figure 4.1.

The furnace is heated by irradiation, three resistors of pure molybdenum in which flows AC current provide for the energy transfer. The hot chamber is surrounded by four cylindrical molybdenum screens and two more in stainless steel, all of them are inserted in the AISI 316 vacuum container which is actively cooled by water. Two vacuum systems rotative plus turbo-

molecular pumps provide a limit vacuum of about $10^{-8}$ mBar after degassing operations for both the zones. The large chamber is also accessible by opening the oven cover for a bigger working access. Nowadays the oven allows a cylindrical space hot chamber with a diameter of 160mm and a height of 250mm. In this volume, the heat distribution can be considered homogeneous. The heating resistors, surrounding that zone, are powered by a three-phase transformer capable of delivering up to 1kA RMS at 14V RMS at the stationary. The resistors are delta connected and the delivered current is controlled by remote using an SCR module. The sizing of the resistance in molybdenum was calculated by evaluating the rise in temperature of the same until the equilibrium was reached at the stationary level. The data relating to the variation in resistance as a function of temperature were taken from [118], while those related to the emissivity of molybdenum from [119]. The resistors were built by weaving 7 molybdenum 0.8mm diameter wires for a total length of about 5m. The final value of the built-in resistors makes it possible to reach a dissipated power of 10kW which perfectly fits, within a small safety margin, the maximum power that can be delivered by the system.

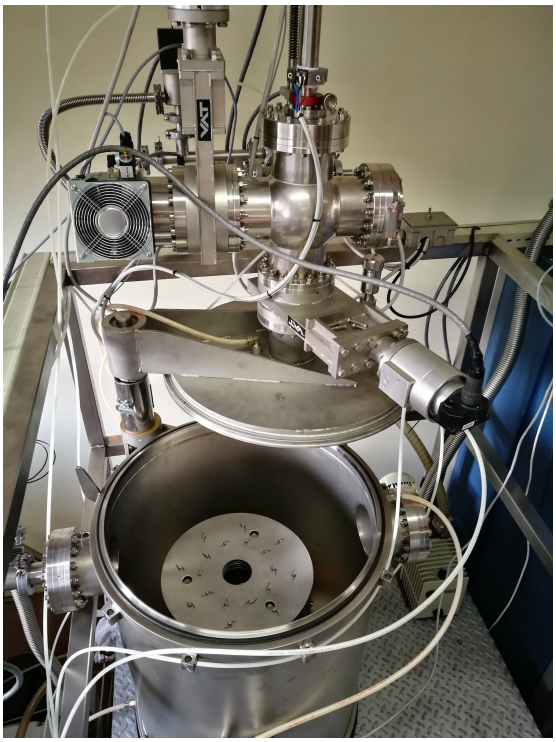

**Figure 4.1:** The high vacuum oven relised for the liquid metals experiments.

The oven is currently being tested, the first tests up to 1200°C have been successfully

achieved. In this configuration, the maximum temperature that can be reached in the hot chamber is about 1500 °C. The first experiments were wettability tests of the porous structures using gallium and tin. We decided to postpone the tests with liquid lithium since much more information could be found in literature on this subject [120] and because handling liquid lithium requires more strictly safety measurements.

These experiments were carried out on a small scale experimental setup described above and shown in the figure 4.2. First of all the tungsten mesh were cleaned by chemical action, in particular using citric acid or hydrochloric acid in the ultrasonic tank. The same treatment, in citric acid, was also reserved for the tin or gallium flakes in a solid state. The meshes, previously cut, were placed inside a molybdenum container together with a small piece of gallium or tin. The whole assembly was put in contact with tantalum resistance and the temperature gradually raised. Below we briefly report the first qualitative results still subject to further analysis.

Wetting with both materials, gallium and tin, has been archived. The procedures were recorded with an optical microscope and clearly highlight the moment of the transition. Both for gallium and tin it was noted that the temperature at which wetting occurs is about 800-850 °C for gallium and 1000-1100 °C for tin with 10% of uncertainty on temperature measurement. The error is dominated by the thermocouple position and by the difficulty of making a good thermal contact between the thermocouple and the tantalum resistance. However, these values are consistent with the few found in literature and reported by Lyublinski in [92], the authors affirm that the wettability tests of molybdenum and tungsten with tin has shown that Mo is effectively wetted by tin at about 950 °C , while W is wetted well at about 1050 °C.

Now, it is out of doubt the great importance in wetting experiments of the surface tension of the liquid metal. As we already described in the previous section the surface tension of liquid metals has a strong dependence on the temperature and this explains why it is necessary to reach high temperatures during this wetting experiments. Equally important is also the compatibility between the two surfaces, and in particular the presence of an oxide layer on the liquid metal surface. It is in fact well known that the liquid metal in general, gallium and tin in our case, are always covered by a thin layer of oxide [121] [122] which prevents adhesion between the two surfaces. Laboratory experiments suggest that at very high temperatures this layer might be decomposed, or that a mechanical break of such oxide surface is followed by a sudden wetting. The verification of this statement was given us in two identical experiments carried out in the small vacuum chamber: in the first case a liquid metal sphere was placed above the mesh, in the second case it was positioned on its side, in contact with the sharp tips

of the tungsten wires. In the first case, the wetting was not even archived reaching more than 1300 °C, while in the second it was obtained just over the already mentioned 1000 °C. The Russian colleagues have noticed the same phenomenology [123] and the common solution used to solve the problem is to immerse the tungsten sponge in a deep liquid metal bath, so avoiding the interaction with the oxidized liquid surface. The wetting experiments in the small chamber are reported in figure 4.2.

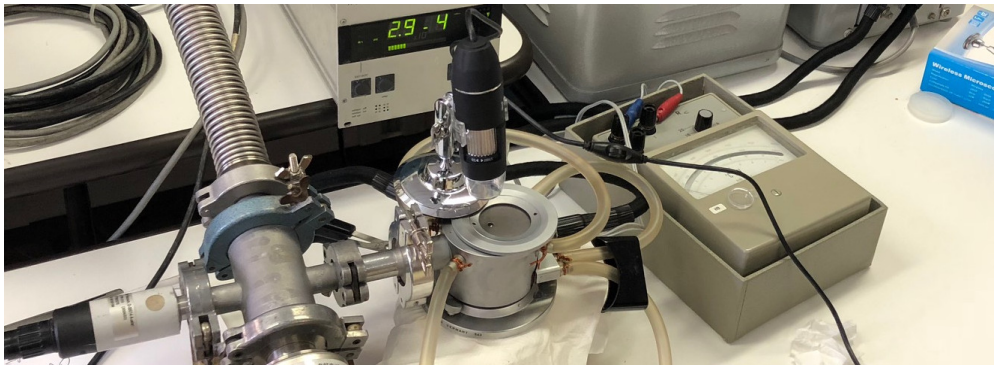


**Figure 4.2:** The little vacuum chamber used to test the reliability of the wetting process on small samples.

A few tents of samples have been produced so far, using tungsten meshes with 50$\mu$m wire diameters spaced 200$\mu$m each other, as shown in figure 4.3. In addition, tungsten felts with wire diameter size 40$\mu$m have also been successfully wetted. These samples will be soon analyzed by the Scanning Electron Microscope to proceed with their characterization. Furthermore, they will be exposed to various plasma experiments. The samples will be used to expose liquid metals in the linear device GyM in Milan: usually in GyM the liquid metals are exposed using the horizontal manipulator and the magnetic cusp configuration (as will be described in the next paragraph), using the CPS technique will be possible to operate with the vertical samples holder. This will allow an increase of a factor of ten in terms of plasma density, it will offer the possibility for the sample polarization, and for actively cooling it with water. Two meshes, one soaked by tin and one by gallium, are currently at the Campus Tecnológico e Nuclear laboratories in Lisbon where a characterization using the ion beam analysis techniques will be performed. Then, the two samples will be exposed on ISTTOK's plasma giving the possibility to operate with the CPS in the Portuguese tokamak.

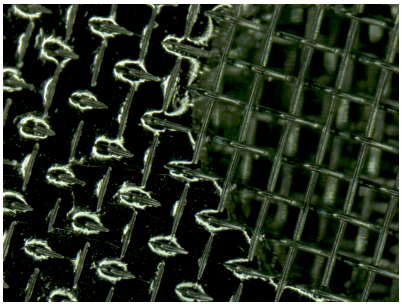

**(a)** Detail of the CPS during the wetting phase.

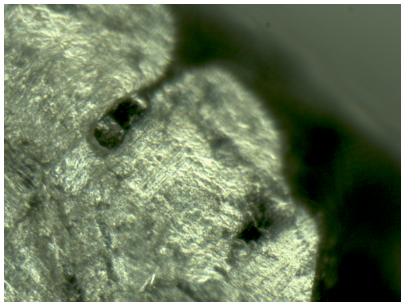

**(b)** Cross-section of the tunsten matrix filled with tin.

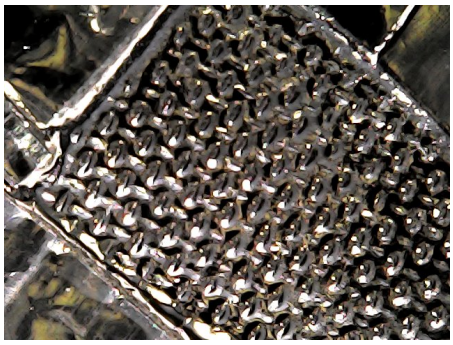

**(c)** Tungsten CPS wetted with tin.

**(d)** Tungsten CPS wetted with gallium.

**Figure 4.3:** Overview of the wetting tests performed in the liquid metals laboratory using the small vacuum chamber. Tungsten mesh 50$\mu$m pore size is always shown, tin and gallium wetting has been achieved.

Studying about liquid metals corrosion are also ongoing. Lithium has not been used in the laboratory also because lithium data are available in literature. Since it is considered a good candidate as a blanket material many references have been found. Anyway, in the case of a CPS based divertor the liquid metal is static and the expected corrosion level is lower than the test usually performed on the lithium corrosion evaluation [124]. Lithium differs in its properties from other alkali metals: it generally results more aggressive, in its attack on many metals, than either sodium or sodium-potassium alloys [125]. Anyway, copper and copper alloys have typically poor resistance to lithium attack, while no corrosion was observed on molybdenum in lithium up to 700°C. A summary is given in figure 4.4.

Liquid gallium is very aggressive in its attack on most the solid metals. It has strong corrosion reaction with the most of the aluminium and copper based alloy. In case of aluminium based alloy the corrosion product is generally loose, promoting a corrosion diffusion area with uniform gallium concentration. Liquid gallium not only causes uniform corrosion process to the surface of the copper based alloy, but also has good compatibility with the corrosion layer and can form gallium covered area on the corroded surface [126]. First experiments

| MOLTEN METALS | CONTAINER METALS |
|---|---|
| Alkali metals | Fe, Co, Cr, Nb, W, Ta, Mo, Re |
| Mg | Fe, Nb, Be, W, Ta, Re, Mo, Cr |
| Zn | Nb, Zr, Ta, W, Cr, Ti, Ir, V |
| Cd | Nb, Ta, W, Mo, Fe, Cr |
| Hg | Fe, W, Ta, Re, Mo, Nb, Rh, Ni, Be, Co |
| Pb | Fe, Co, Ir, Zr, Rh |
| Sn | W, Mo, Ta, Nb, Os, Ir |
| Bi | W, Zr, Fe, Ta, Rh, Cr, Ti, V, Co |
| Ga | W, Ta, Mo, Nb, Os, Ir |
| Tl | Fe, W, Ta, Mo, Nb, Co |
| In | Fe, W, Ta, Mo, Nb, Co |

**Table 4.3:** Metal for possible use as containers, listed by Brewer [125] in order of decreasing preference, based on availability and attack opposition.

in laboratory show us the perfect incompatibility of liquid gallium with aluminium alloy also at low temperature. In addition, gallium compatibility with stainless steel and Nicrobell (a nickel-chromium alloy with 1.4% of silicon which provides high oxidation resistance and strength at temperatures up to 1250°C) are definitely excluded. Few hours in a liquid gallium pool at 500°C were sufficient to completely dissolve the external shield of any thermocouples used for the temperature monitoring. It has a high affinity for all common metals and the few pure metals successfully compatible at high temperatures with gallium are tungsten, rhenium, beryllium, and tantalum. [125]. The mechanism of attack on solid metals by gallium differs widely from metal by metal, and strongly depends on temperature. Molybdenum, for example, reacts with gallium forming more than one reaction product, one of which is in a solid solution [127].

Tin as PFC candidates for nuclear fusion applications, is a bit facilitated than gallium, because of its lower corrosive attitude [92]. Nerveless, most of the metals and alloys commonly attacked by liquid aluminium and zinc are also usually attacked by liquid tin, especially at high temperature [125]. It is well known and documented the tin and tin solders attack to copper in the range 250 °C to 450 °C. Several attempts to alloy tungsten and tin were unsuccessful. Northrup et al. [128] found that tungsten wire is not dissolved in molten tin heated to 1680°C. Corrosion study [92] show Mo is not attacked by liquid Sn, and it is compatible with such element up to at least 1000 °C.

The problem of the corrosion of the support structures, in contact with the liquid metal,

is an open issue and must be addressed for the design of a future liquid metal divertor. In the next section, a tungsten coating to protect the support materials and cooling structures, in particular the copper pipe, is presented and described in detail. The deposition technique used allows obtaining a coherent tungsten thickness even on complex geometries and on large parts without the need for a vacuum chamber. Being able to obtain such coating, it allows to minimize the distance between the liquid metal surface and the coolant and therefore a greater ability to remove heat at the stationary condition.

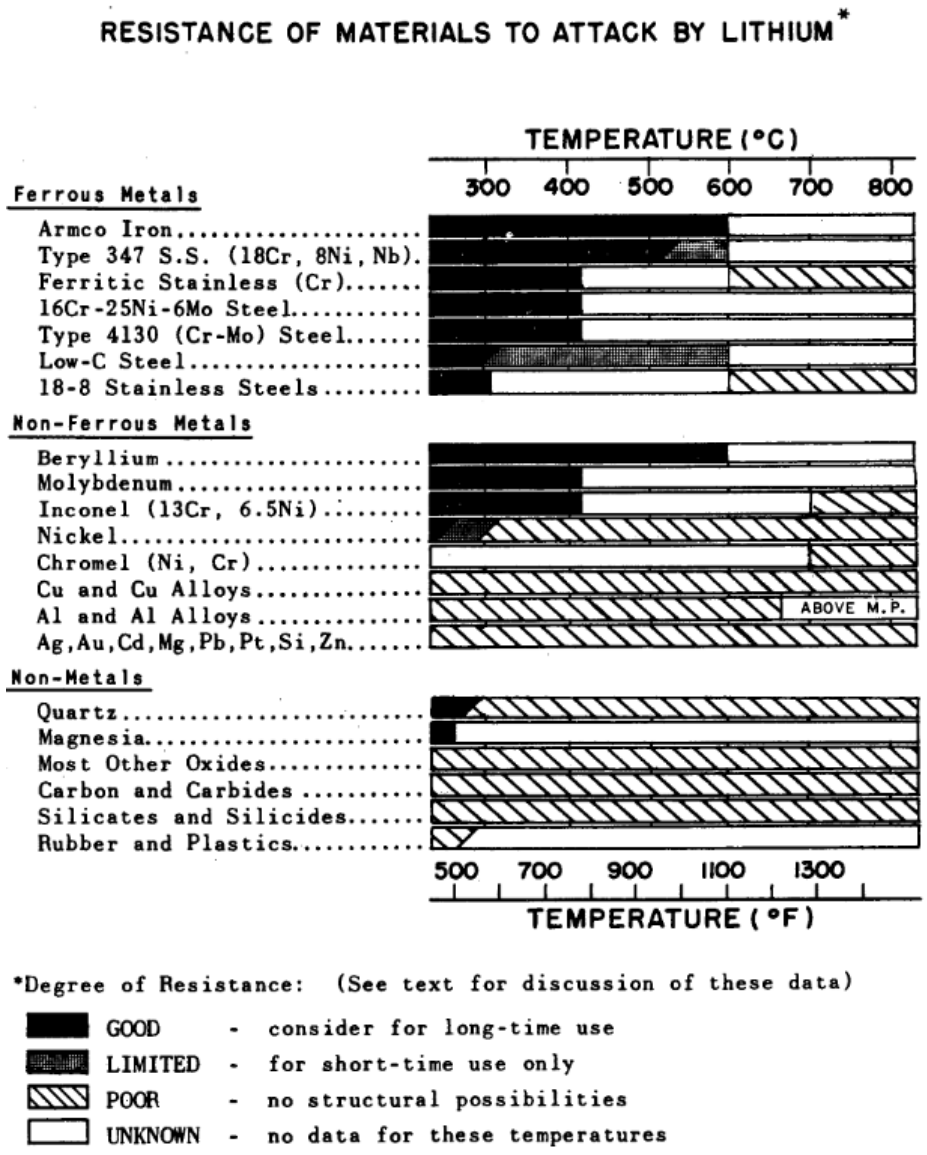


**Figure 4.4:** Overview of material resistance by lithium attack [125].

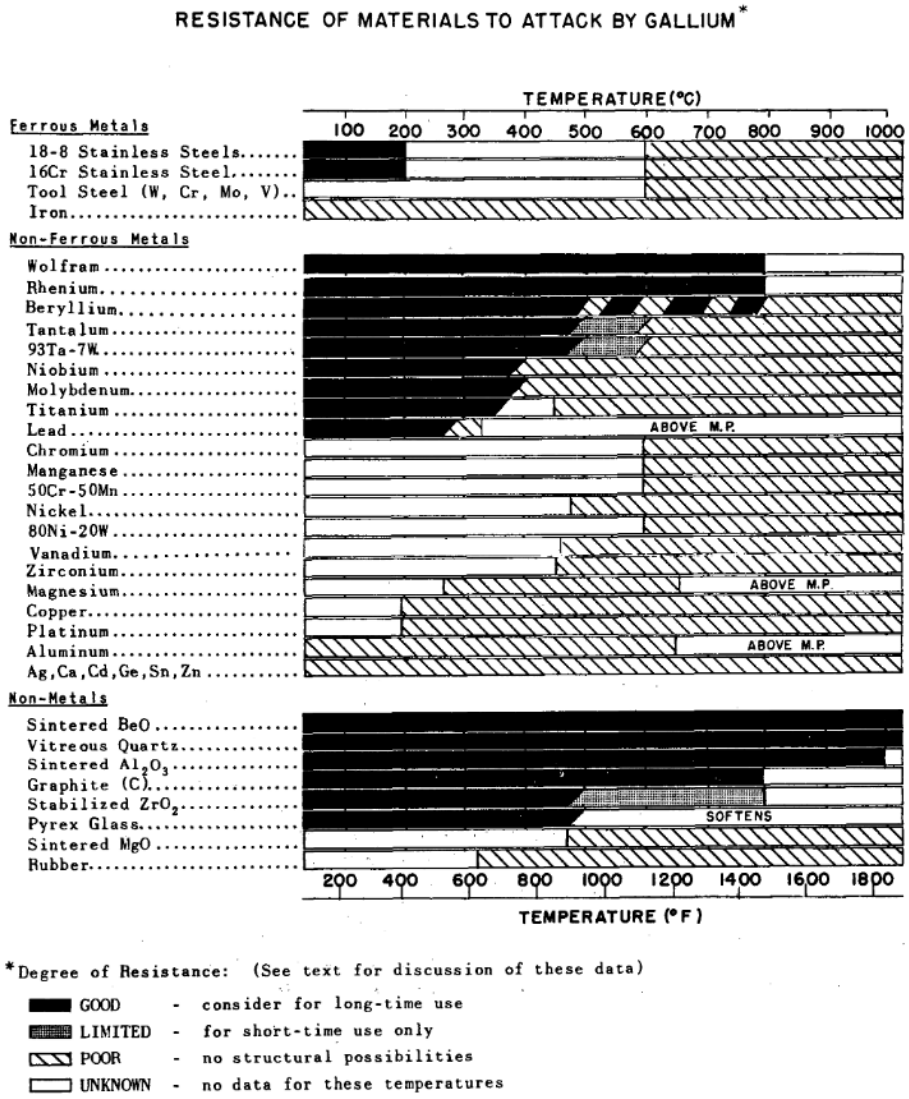


**Figure 4.5:** Overview of material resistance by gallium attack [125].

## 4.3 Detonation spray

Thermal spraying is an effective and low cost method to achieve surface coatings. It is a cost-effective way to protect critical components from wear, corrosion, fatigue, oxidation and high temperatures. Such coatings are used in a wide range of applications [129], i.e. industrial process, automotive, aerospace, etc., moreover their application and diffusion is growing fast too.

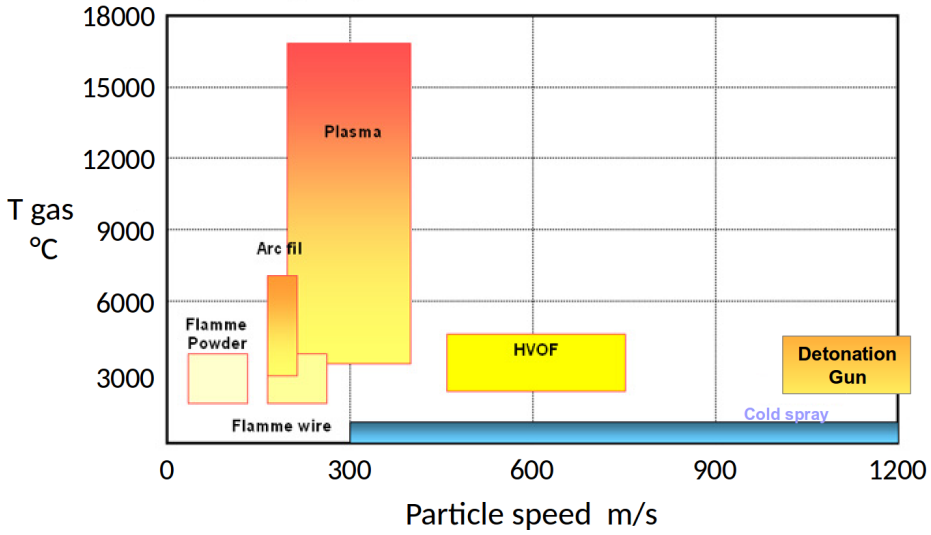


**Figure 4.6:** The plot indicates the working space covered by different deposition techniques. Often the working temperature of the process or the particle speed are crucial parameters, since high temperature or strong impact could damage the substrate material.

Many commercial thermal spray coating techniques are available nowadays:

- Wire Arc Spray
- Plasma Spray
- High-Velocity Oxy Fuel (HVOF)
- Flame Spray
- Detonation Gun Spray
- Cold Spray.

In figure 4.6 the working space for the most important commercial techniques is reported. Basically the thermal spray idea relay on applying a consumable material to a substrate by melting (or making it plastic/squashy) the material in droplets and impinging the softened or molten droplets on the substrate to form a continuous coating. The choice of the best deposition technique depends on the application requirements (level of adhesion, size, shape) and on the substrate material constraints (metallurgy, physical chemists properties). Also availability and cost of the equipment play an important role in the decision of the best deposition strategy. For our purpose, we want to shield the support structure by a protective

layer, that prevents the liquid metal corrosion. One of the main requirements is the possibility to cover a large surface with complex geometries as, for example, the copper pipes of the ITER divertor's cooling system. For tungsten deposition, chemical vapour deposition and plasma spray technique are mentioned in literature. The first is limited to small achievable thickness, and both require a vacuum chamber to avoid tungsten oxide formation. Tungsten oxide, in fact, being a volatile oxide, would not deposit on the surfaces.

Detonation gun is a thermal spray coating process giving an extremely good adhesive strength, low porosity and surface coating with mainly compressive residual stresses [130]. High deposition rate, reliability, and low cost are some features offered by the detonation gun solution. Furthermore, one of the advantages of this technique lies in the possibility of working directly in the atmosphere with the protection given by the inert gas (nitrogen) used during the process.

A precise amount of combustion fuel consisting of oxygen and acetylene is fed through a tubular barrel closed, at one side, by the combustion chamber. A picture of the detonation gun machine is given in figure 4.7. In order to prevent the possible back firing a blanket of nitrogen gas is allowed to cover the gas inlets. Furthermore, the nitrogen buffer also determines the combustion delay time and the partial barrel cleaning. Simultaneously, a predetermined quantity of the coating powder is fed into the barrel or in the combustion chamber. Generally, the gas mixture inside the chamber is ignited by a simple spark plug, in our case a propane mixture is used to trigger the reaction. The combustion of the gas mixture generates high pressure shock waves (the detonation wave), which propagates through the gas stream.

Depending upon the stoichiometry, the temperature of the hot gas stream can go up to 4000 °C and the velocity of the shock wave can reach up to 3500m/s. The hot gases generated during the detonation violently hit the powder, accelerate and heat the particles to a plasticizing stage. Typically the interacting time is barely sufficient to melt only the particle skin. These particles then come out of the barrel and impact the component resulting in the typical very dense and strong coating. The coating thickness achieved per shot depends on many variables i.e. the stoichiometry of the combustion gases, the powder particle size, the total gas amount, the shot frequency and the distance between the barrel end and the substrate. Depending on the wanted coating thickness and the coating and substrate material the detonation spraying cycle can be repeated at the rate from 1 to 10Hz.

The detonation chamber and the barrel are finally flushed again with fresh nitrogen for cleaning purpose. In fact, residual powder particles or of non-detonated gas in the chamber could affect the correct detonation process. The typical operative cycle of the proposed process

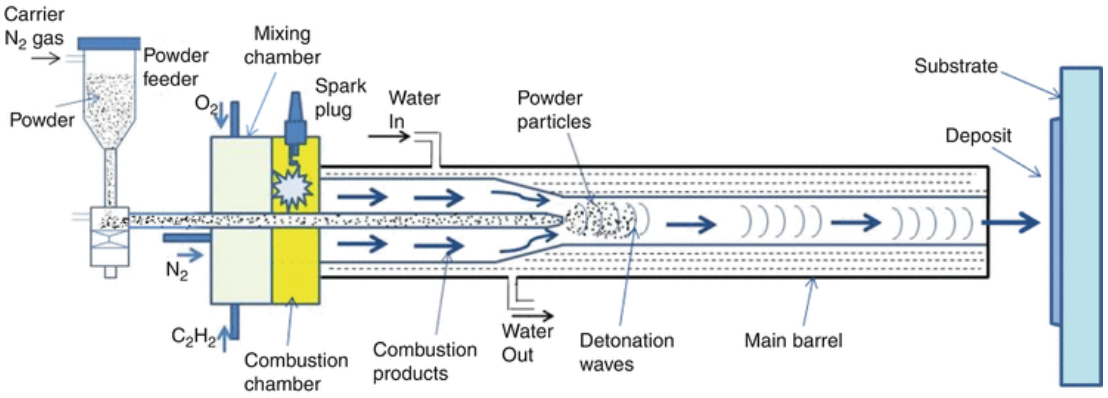


**Figure 4.7:** The thermal spraying techniques, which include the "Detonation Gun", essentially consist in generating a flow of gas at high temperature and speed inside which the powders of the material that will make the coating are injected. During the path in the torch of the deposition torch, the gas jet can reach a temperature up to about 4000 °C and a speed of about 3500m/s before impact with the surface to be coated. The powder particles, therefore, injected into the gas flow, greatly increase their temperature and speed until they reach temperature and speed values close to those of the gas before impacting on the surface to be coated. The particles crushing one on the other, cooling, form the coating.

lasts 250ms and it is reported in table 4.4. Once the detonation cycle is completed the overall procedure is repeated until the required thickness of the coating is reached. Among all the possible coating material (ceramics, refractory metals) tungsten has been selected as one the best candidate for nuclear fusion application. There is no metallurgical bond formation between the substrate and the deposited coating, and the adhesion between them is purely mechanical. This type of anchorage is well documented on specialized literature with adhesion levels that can exceed 70MPa in pure traction [130, 131]. Tungsten deposit has been successfully achieved and the request for the process patent is actually going on. According to literature is it the first time that detonation gun machine has been used to deposit pure tungsten. Specifically, the optimization of the amount of propane, nitrogen, oxygen, and acetylene inserted in the machine and injection times during the operating cycle of the machine are claimed. The powders consumption (and consequently the deposition rate) is estimated to be in the order of kilograms of powder per hour of operation. The deposition yield of this technique can reach values in the order of 70% (mass obtained coating / mass of powders used). All the work related to this task has been performed in the ENEA research center in Brasimone using the *Detonotaion Gun* device.

In figure 4.9, Scanning Electron Microscope (SEM) analysis of the tungsten covered Cr-CuZr sample is shown. Thicknesses from a few tens of microns up to millimeters has been obtained. The uniform deposition on large surfaces is obtained by moving the torch and/or

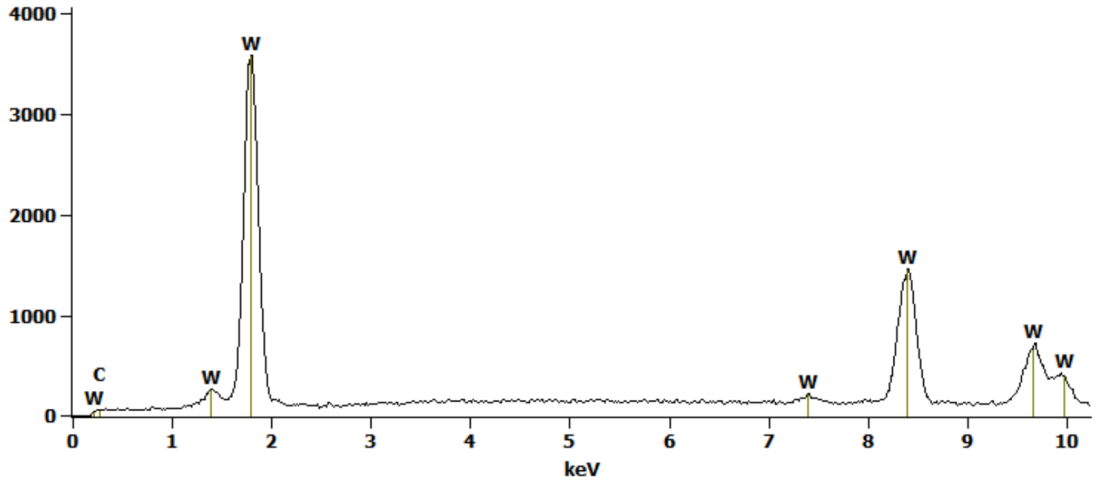


**Figure 4.8:** Energy Dispersive X-ray Spectrometry

the substrate. Contamination of the coating was investigated by the *Energy Dispersive X-ray Spectrometry* (EDS) technique, as shown in figure 4.8 and was found to be negligible. Anyway, the mechanical adhesion and the resistance to thermal cycling or strong thermal gradient are primary requirements.

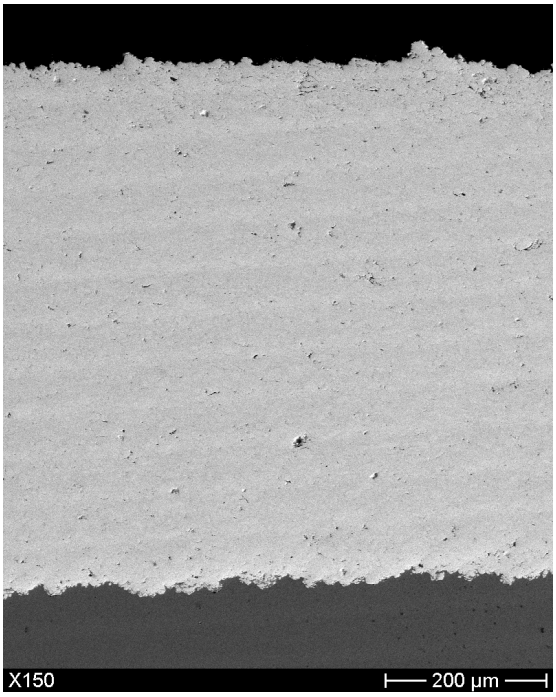


**Figure 4.9:** Scanning Electron Microscope (SEM) analysis of the CrCuZr sample tungsten covered using DS technique.

| Parameter | Nozzle size [mm] | Actuation time [ms] |
|---|---|---|
| 1. Barrel | - | ———95—-150——- |
| 2. Acetylene | 2.0 | 3-38——————— |
| 3. Acetylene | 1.8 | 3-38——————— |
| 4. Oxygen | 2.2 | 3-20——————— |
| 5. Oxygen | 2.2 | 3-38——————— |
| 6. Nitrogen | 2.2 | ———-115—-196—– |
| 7. Nitrogen | 2.0 | ———-115—-196—– |
| 8. Feeder powder 1 | - | —-50–85——————— |
| 9. Feeder powder 2 | - | ———————— |
| 10. Spark | - | ————–136——– |
| 11. Cycle time | - | 1————————250 |

**Table 4.4:** Example of a typical cyclogram of the detonation machine gun

## 4.4 Tin retention

Liquid Sn samples have been exposed in GyM to $D_2$ plasma for retention experiments, at operating pressures ranging from $7 \cdot 10^{-5}$ to $1 \cdot 10^{-4}$ mbar. Since the samples were liquid and no CPS structure was available, they have been irradiated in a double-cusp magnetic configuration, obtained by current inversion in two coils. This configuration allowed to tilt the magnetic field lines driving the plasma ions on the horizontal target holder [89]. Each sample consists of ~3g of solid Sn (purity 99.9%) press fitted into a steel tray holder of overall size 20.4 x 18.4 $mm^2$. The samples have been kept in vacuum (0.1 mbar) for 1 hour at a temperature of 400 °C to remove any impurities and then were re-solidified in vacuum at room temperature (20 h). Then they were placed in GyM at 6 cm below the machine axis, with the long side perpendicular to the machine axis. In retention experiments the samples were heated up to 300°C by a IR lamp placed under the rear side of the sample holder. Thermal Desorption Spectrometry (TDS) measurements have been carried out two months after plasma exposure at ENEA Frascati laboratory on a sample exposed to the same deuterium fluence than the ones sent to the other laboratories and on a reference, not exposed, sample. The vacuum chamber is connected to the Quadrupole Mass Spectrometer (Balzers QMG 421) the sample is inductively heated to minimize the background effect of the chamber walls. The samples were heated up to 700 °C with a temperature ramp of about 6 °C /minute. Masses 2 (H2), 3 (HD) and 4 (D2) were monitored. Few months after the irradiation in GyM one sample was moved to Lisbon to perform *Ion Beam Analysis* (IBA) in the *Campus Tecnológico e Nuclear* (CTN), *Instituto Superior Técnico* (IST), Universidade de Lisboa. The

*Nuclear reaction analysis* (NRA) spectra were collected at a scattering angle of 140° using a silicon surface barrier detector with a large depletion layer. A mylar foil with a thickness of $6.6 \cdot 10^{20 at/cm^2}$ was placed in front of the NRA detector, assuring that only the protons emitted from the $^{2}H(^{3}He, p_0)^{4}He$ are collected in the NRA spectra.

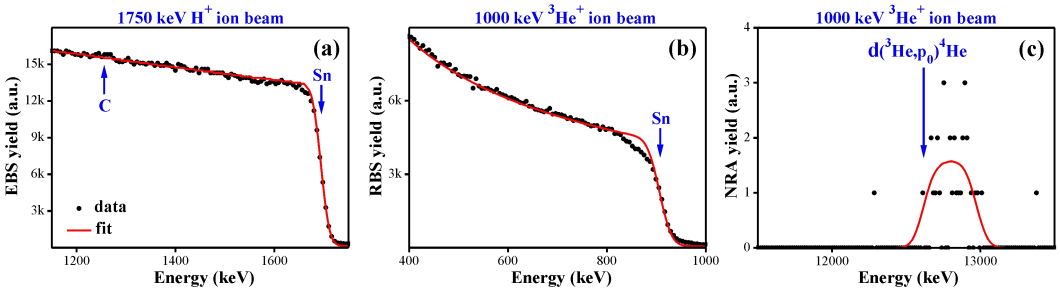


**Figure 4.10:** (a) RBS with incident 1.75 MeV proton beam; (b)(c) RBS and NRA analysis with incident 1.0 MeV 3He+ ion beam, respectively.

The measure has been performed close to the maximum cross section for the reaction using a 1MeV $^{3}He^{+}$ incident beam [132]. The incident $^{3}He^{+}$ ions, scattered by the Sn nuclei (Rutherford scattering), were collected simultaneously in an additional *Rutherford backscattering spectrometry* (RBS) spectra in order to normalize the available proton yields in the NRA spectra and to compute the deuterium content. Four different points with superficial diameters of 1 mm were analysed. IBA is particularly helpful to check the presence and the deposition of carbon (C) in the irradiated surfaces. This is commonly performed by using proton beams with incident energies close to a huge resonance for the elastic scattering of protons by $^{12}C$, $^{12}C(p,p)^{12}C$. For the present experimental geometry, were the RBS detector (pin diode) is placed at a scattering angle of 165°, a resonant energy is close to 1742 keV, and therefore, the present RBS experiment was performed with an incident proton beam of 1.75 MeV. Corresponding cross sections for the $^{12}C(p,p)^{12}C$ elastic scattering were calculated from the SigmaCalc code [133]. All the RBS and NRA chemical analysis has been performed using the NDF code [134].

The vertical arrows in figure 4.10(a) indicates the energies for superficial C and Sn in the RBS spectra collected with incident proton beams. In figure 4.10(b) and 4.10(c) the vertical arrows point out the corresponding energies for superficial Sn and deuterium in the RBS and NRA spectra collected from incident $^{3}He^{+}$ beams. The Rutherford backscattered yield of $^{3}He^{+}$ ions scattered by the Sn nuclei has been used to normalize the NRA yield induced by

the $^{2}H(^{3}He, p_0)^{4}He$ reaction.

The analytical RBS results put in evidence that, if a C content exists in the irradiated Sn surface, the corresponding amount is really negligible and it should be not higher than 1-2 at.%. From the NRA spectra it is evident that very low deuterium contents are present in the surface at the different analysed points. It is possible to resolve the deuterium depth profile with a fit line considering medium retained amounts of 0.18 at% along a depth profile of 1000 nm [89]. Other retention measurements have been performed by Loureiro [90]. The quantified D amount on the surface is factor of two lower than those measured in the present work, While the reported deuterium fluence is roughly fifty times lower.

The value of deuterium retained obtained with TDS from the bulk sample is $1.0{\cdot}10^{15 at/cm^2}$, very similar to that obtained with NRA from a near-surface layer. Therefore it can be deduced that deuterium is adsorbed on the surface of Sn samples and does not penetrate into the bulk.

After the first measurement carried out on the sample exposed in GyM and reported in [89], three new samples were exposed to different integrated fluences, respectively 2, 3, and 4 hours. The first sample, analysed in [89], was exposed during 2.5 hours.

The samples were irradiated with the same procedure described above. Preliminary results are still under investigation and a quantitative assessment of deuterium content is not available. The figure 4.11 shows the integrated number of counts, which is directly proportional to the deuterium content in the sample, versus the exposition time. The result from the previous sample has been confirmed and the magnitude in deuterium retention for the range of fluences between $1 \cdot 10^{24 at/cm^2}$ and $5 \cdot 10^{24 at/cm^2}$ remains in the same range. In the plot 4.11 the sample previously measured in the [89] work has been positioned in blue. Furthermore, is also confirmed that all the deuterium is trapped within the first 1000nm from the surface.

Moreover, in order to investigate the impact of sample storage in the atmosphere at room temperature, the latter three samples have been analysed twice: one week after the plasma irradiation and two months later. The experimental data perfectly overlap in the plot in figure 4.11, so there is no evidence of the time decay phenomena in therm of deuterium content, at least for the time scale considered. Anyway, it is not possible to exclude, a priori, a typical decay time much shorter than one week or much longer than 5 months. In any case, further analyses are already planned. The quantitative data, relative to the plot in figure 4.11 will be available soon.

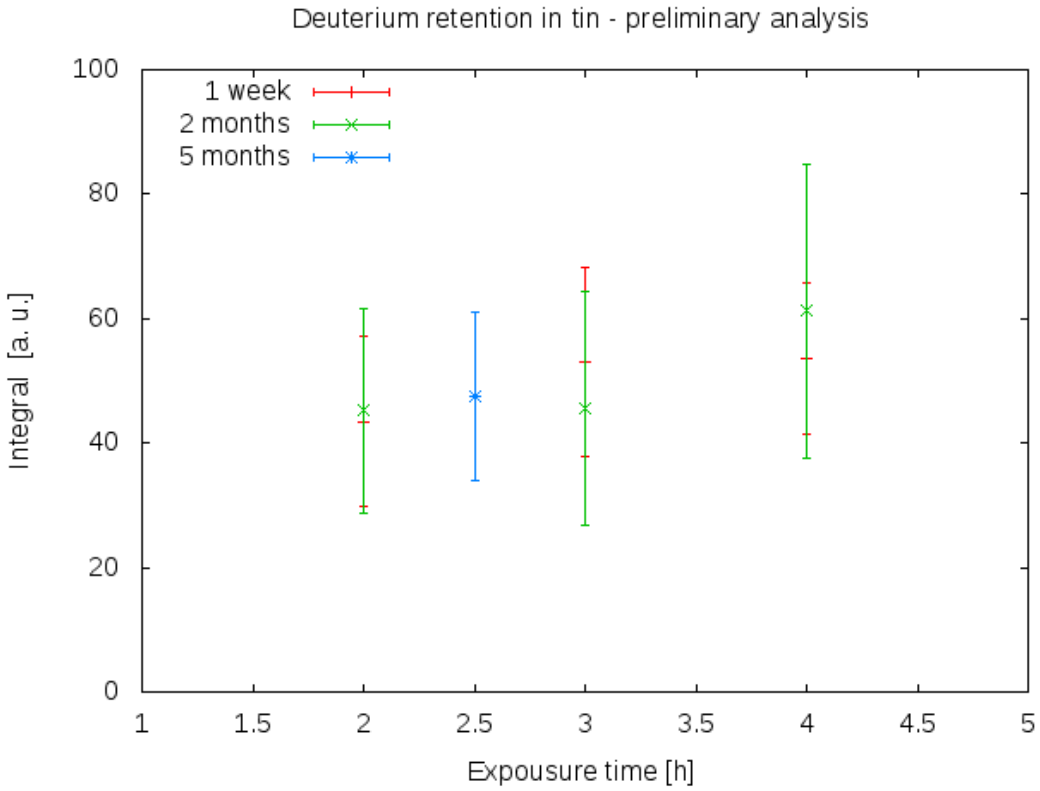


**Figure 4.11:** Preliminary results on new irradiated samples in GyM analysed in the CTN laboratory.

*There are two possible outcomes: if the result confirms the hypothesis, then you've made a measurement. If the result is contrary to the hypothesis, then you've made a discovery*

Enrico Fermi

# 5

# Spin-off liquid lithium positron target

In this chapter, the proposal and the study of a liquid lithium target for a muon accelerator are presented. One of the main limitations for the LEMMA project is the impossibility of using conventional solid materials to reach the desired production rate due to the too high density of deposited power. So far, the R & D activities and development of a future experimental set-up developed in collaboration with INFN and CERN will be presented.

## 5.1 The LEMMA idea

A new scheme to produce muon beams characterised by very low emittance, in such a way to avoid the need for cooling, using a positron beam of about 45 GeV interacting on electrons on target is being studied by our group. This scheme is challenging and innovative, and needs a full design study to be developed. In particular, one of the novel topics to be investigated is the interaction between the positron beam stored in a low emittance ring with a thin target, to be inserted directly in the ring chamber to produce muons. Produced muons will then be immediately collected at the exit of the target and transported to two $\mu^+$ and $\mu^-$ accumulator rings.

Even if the idea of building a muon collider is not new at all, the first proposals date back to several decades ago, this hypothetical machine is gaining more and more interest today as a possible new generation of experiment, able to overtake the main limitations of actual colliders, and in particular of LHC. Even if the Large Hadron Collider has already delivered

numerous years of data, due to the great effort needed to conceive and build such frontier machines it is already now the time to study how to carry on the research on fundamental particle physics in the future. In this context, design studies are now ongoing on a Future Circular Collider (FCC) [135], to be built at CERN, with a circumference of about 100km and unprecedented energies and luminosities for both hadron and lepton cases. However, even with respect to such huge and powerful machines, a muon collider would still retain some advantages that make it worth studying. The majority of these advantages comes from the use of muons itself. In fact, being 200 times heavier than electrons, a beam of muons will suffer much less of Synchrotron Radiation emission, that is the limit of circular $e^+$ e colliders, giving the possibility to reach much higher energies. The advantages, however, are not only related to the accelerator, but also to the physics itself. In fact, focusing for example on the Higgs boson, we know that its coupling goes with the mass to the square, $m^2$, meaning that we expect a much higher production of Higgs boson at a muon collider [136]. In spite of these advantages there are also some critical points that have hindered so far the design of a muon collider. First of all, muons decay in few μs. That means that the whole chain, from generation to acceleration up to the interaction, must be performed in a very short time. The traditional muon production scheme leads inevitably too large emittance beams. In fact, muons are conventionally produced by colliding protons on target, and then exploiting the mesons, π and k, decay. Muons are thus produced with a variety of angles and energies, implying the necessity of beam cooling to lower the emittance of the beam.

In this novel scheme, a primary beam of positrons interacts with a fixed target, the positron beam having a energy (45 GeV) just above the threshold for the reaction $e^+e \rightarrow \mu^+\mu$ [137] [138]. The essential advantage of this *direct muon production* is that low emittance is possible. In fact, it happens that the angle between the two muons goes with square root af the center of mass energy, namely $\sqrt{s}$, and is however small close to the threshold. Moreover, also the energy difference between the two muons produced is small just above the threshold, and thus it is also the energy spread of the muon beam. As a result, exploiting direct muon production it is possible to create a muon beam that has already at creation small emittance, that in turns means that good luminosity is reachable with reduced muon fluxes, thus resulting in reduced backgrounds. Finally, also the losses from decays are reduced. In fact, the asymmetric scheme allows to obtain two already boosted muons, which will have higher lifetime and which are both possible to collect.

On the other side with respect to such advantages, this novel scheme has its main limitation in the production rate, since the cross section for the process is about 3 orders of magnitude

lower than the one for the conventional one, i.e. microbarn ($\mu$b) versus millibarn (mb). Such a small cross section makes the choice of the target material crucial. In fact, the number of produced $\mu$ pairs $N_{\mu\mu}$ can be parametrised as

$$N_{\mu\mu} = N_{e^+}\rho_{e^-}L\sigma_{e^+e\to+} \tag{5.1}$$

Where $N(e^+)$ is the number of $e^+$, $\rho_{e^-}$ is the target electron density, $L$ is the target length and $\sigma_{e^+e^-\to\mu^+\mu^-}$ is the cross section for the process in analysis.

- the ideal target is $e^-$ dominated
- the dominant process is collinear radiative Bhabha scattering ($\sigma_{rb} \approx 150mb$) $\to$ $(\rho_{e^-}L)_{max} = \frac{1}{\sigma_{rb}} \approx 10^{24} \div 10^{25} cm^{-2}$ [139] [140] [141]
- Muon beam emittance increases with $L$

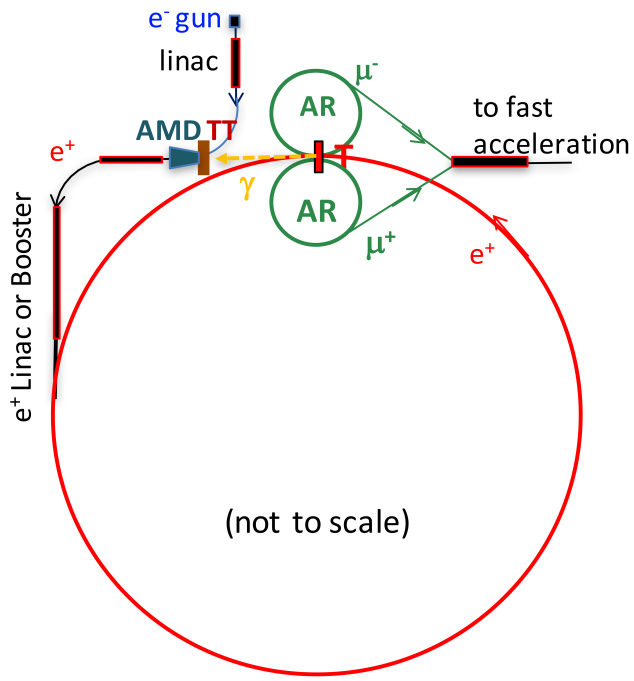


**Figure 5.1:** Actual design of the LEMMA accelerator complex, as described in the text.

So, the criteria to follow to choose the target are basically three: first of all, to minimise the emittance a thin target is needed. In fact, having a thick target would mean that muons are produced all along its thickness, resulting in an increase in beam emittance. Secondly, the need to maximise the production rate requires a high density target. Lastly, the positron loss should be reduced as much as possible, since to rise the number of produced muons is it possible to conceive a recirculating scheme in which the positron beam interacts several times in the target. This last point would require a low Z target, in order to limit the effect of bremsstrahlung, that would reduce the positron beam lifetime. It is straight away clear that these requirements are somehow

| Parameter | Unit | Value |
|---|---|---|
| Circumference | km | 6.83 |
| Energy | GeV | 45 |
| Bunches | # | 100 |
| $e^+$ bunch spacing | ns | 200 |
| $e^+$ freq | MHz | 5 |
| Beam current | mA | 240 |
| $e^+$ / bunch | # | $3 \cdot 10^{11}$ |
| $e^+$ flux on target | # $s^{-1}$ | $1.5 \cdot 10^{18}$ |
| Beam dimension | $\mu$m | 10 - 100 |
| $U_0$ | GeV | 0.51 |
| SR power | MW | 120 |

**Table 5.1:** Positron accumulator ring 6.3 km, main parameters table

conflicting with each other, and so a careful study relying on Monte Carlo simulation is being performed. A possible trade off between the conflicting requirements could be represented by not too heavy materials (like Be, C and Li)and not too thin targets. The other fundamental aspect to be considered in order to maximise the production rate is the positron source, that has to be as intense as possible.

### 5.1.1 Accelerator schema

The accelerator scheme currently proposed is shown in figure 5.1, and starts from a standard electron gun; these electrons collide with a conventional Heavy Target (HT) to produce $e^+$ e pairs. Then, an Adiabatic Matching Device is used to collect positrons, that are accelerated and injected in the main positron ring. At the current design stage, this is a 6.3km 45GeV storage ring in which a target for muon production (T) is inserted, in such a way to make positrons collide with it several times. In such a configuration, muons are produced with an energy of 22GeV and a Lorentz $\gamma$ factor of about 200, implying that they will live about 500$\mu$s. In correspondence of the production target there are two separate accumulation rings, followed by a fast acceleration that injects both muon beams in the actual collider. A first set of parameters for the positron ring and a very preliminary set of parameters for a possible muon collider exploiting the proposed scheme are respectively shown in table 5.1 and 5.2. However, what is worth to stress is that, thanks to the very small emittance, a luminosity comparable to the conventional one is possible with much lower muon fluxes.

| Parameter | Unit | Value |
|---|---|---|
| Luminosity | $cm^{-2}\,s^{-1}$ | $5.09 \cdot 10^{34}$ |
| Beam Energy | GeV | 3000 |
| $\mu$ mass | GeV | 0.1057 |
| $\mu$ lifetime | s | 0.06 |
| $\mu\, c \cdot \tau$ | m | $1.87 \cdot 10^{7}$ |
| Ring circumference | km | 6 |
| Bending field | T | 15 |
| Bending radius | m | 667 |
| Gamma factor | | 28393 |
| Turn before decay | # | 3114 |
| Beam current | mA | 0.048 |
| Revolution frequency | mA | $5.0 \cdot 10^{4}$ |
| Number of bunches | # | 1 |
| $\mu$/bunch | # | $6.0 \cdot 10^{9}$ |

**Table 5.2:** 6 TeV $\mu$ collider draft parameters

## 5.2 Proposed Liquid Lithium target

The target assessment is a central and very important task for the achievement of the LEMMA project goal. The conventional strategy for the muon production typically consists in $\pi$ or k decay, they are usually generated by proton beams on a solid material. Since the cross section of such process is large, the demands on the target in terms of power density are acceptable for conventional material. The biggest problem, however, remains the huge spread in terms of momentum on the particles produced from the mesonic decay.


**Figure 5.2:** The muon beam exiting from the target tent to reproduces the dimensions and characteristics of the incoming positron beam.

As previously described, the muon threshold direct production allows a low emittance beam with a considerable gain in terms of the final machine luminosity. Simulations show that muon beam exiting from the target tent to reproduces the dimensions and characteristics of the incoming positron beam, an intuitive schema is given in figure 5.2. It follows that to minimize the spatial dispersion it is convenient to focus the positron beam as much as possible, which however implies a smaller volume where the energy is deposited. Power

deposition in the order of several hundreds kilowatts for low and medium Z materials is expected in the intersection volume between the particle beam and the target. The $\mu^+\mu^-$ pairs produced per interaction are given in equation 5.1, it is evident that the target plays the role of electrons containers, electrons which will take part in the annihilation process with positrons. The nuclei, unfortunately, we could not take them out, only dilute the electrons and induce bremsstrahlung losses.

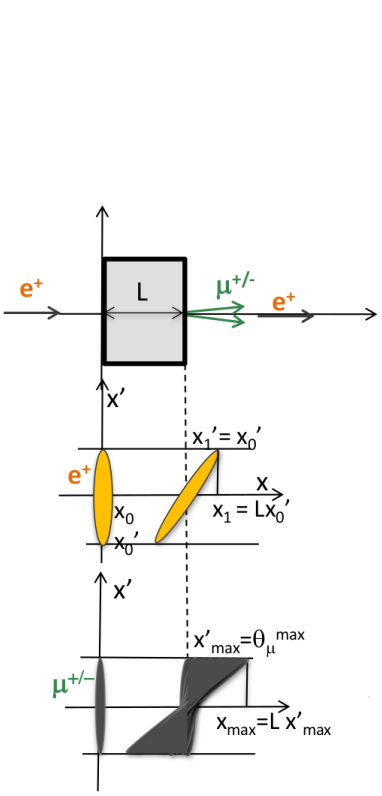


**(a)** The target length L could be seen as a drift along the spatial direction, muons are uniformly produced along the target and the aperture angle is simply shifted and point by point through the interaction line.

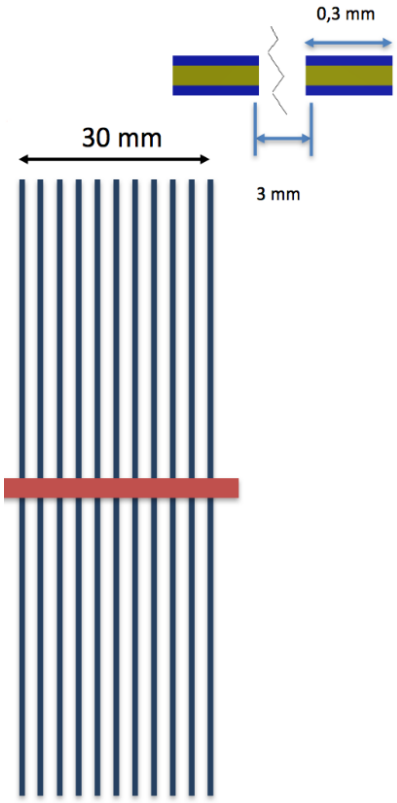


**(b)** Solid rotating graphite target using the comb layout to take in to account the needed for power removal.

**Figure 5.3:** Target lenght contribuition to the muon emittance on the left, rotating grafite target on the right.

Ideally, for what has been said so far, the ideal would be a pure electrons target, but this is obviously impossible for any conventional material. Other proposals involving plasma targets have been investigated but their treatment goes beyond the scope of this thesis.

Coming back now to the general target analysis, the dominant process in low and medium

Z materials is collinear radiative Bhabha scattering ($\sigma_{rb} \approx 150mb$) $\rightarrow$ $(\rho_{e^-} L)_{max} = \frac{1}{\sigma_{rb}} \approx 10^{24} \div 10^{25} cm^{-2}$. The emittance production angle contribution is mainly determined by the target thickness (L) and the center of mass energy (s) of the incoming beam.

From the point of view of the $e^+$ beam the target length L is a drift along the spatial direction, muons are uniformly produced along the target and the aperture angle is simply shifted and point by point through the interaction line. A picture of this is given in figure 5.3a, while simulations performed using GEANT4 [142, 143, 144] are reported in figure 5.4. The emittance contributions due to muon production angle can be expressed as

$$\epsilon_\mu \approx \frac{L\theta_\mu^2}{12} \tag{5.2}$$

where

$$\theta_\mu = \frac{4m_e}{s}\sqrt{\frac{s}{4} - m_\mu^2} \tag{5.3}$$

Therefore, to summarize we would like to have a very thin target to minimize the emittance, a high electron density target (high Z) to maximize the production rate, as much low as possible atomic charge to minimize losses due to positrons (very low Z material). The target material is crucial for the positron beam lifetime too, as is shown in figure 5.4. Different material options can be summarised as follow:

- Heavy materials, thin target (Mo, W, Hg)
  - thin target minimize the emittance, in fact $\epsilon_\mu \, \alpha \, L$,
  - the $e^+$ bremsstrahlung losses would prevails, the amount of power loss in the target could reach the value of several MW and this is incompatible with any material. Furthermore it is not realistic from the point of view of the main beam power supply and beam optics, the spread in energy particles before and after the target cannot be matched and the most of the beam would be lost;
  - the $\mu^+\mu^-$ production efficiency decrease with Z as $\eta_{max} \approx \frac{\sigma_\mu}{(Z+1)\sigma_{bhabha}} \approx 10^{-7}$

- Very light materials, thick target (liquid H, liquid He)
  - the muons production is maximized, value up to $10^{-5}$ can be reached;
  - the target length necessary increase, even if the liquid target option is considered L approach to the order of several meters having an impact on the muons emittance;

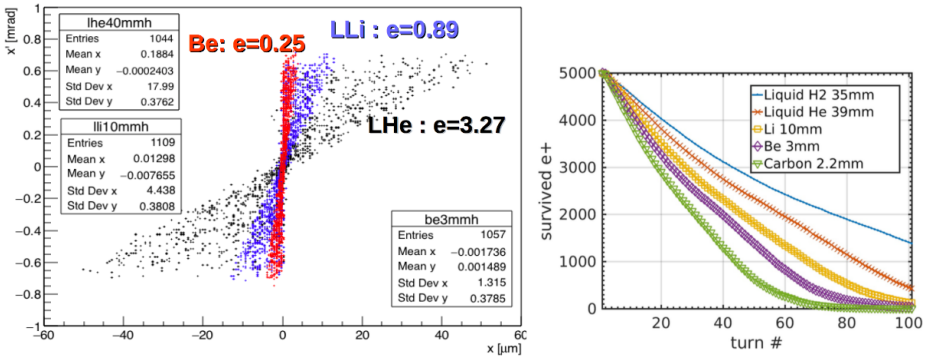


**Figure 5.4:** The simulations using GEANT4 [142, 143, 144] of the beam emittance just after the target, liquid helium, liquid lithium and solid berillium have been analysed. The expected positron beam lifetime is also reported on the right versus the differet target materials.

  - nevertheless the power handling would be very challenging, the huge needed power removal capability in a liquid hydrogen or helium bath is almost impossible

- Light materials (Li, Be, C)

  - they combine a relatively low muon emittance and small $e^+$ loss
  - the muon production efficiency is still acceptable $10^{-6}$

The most standard solution involves the use of a rotating graphite plate, the plate would be inserted in the accelerator vacuum chamber, and it must rotate at such a speed as to avoid the phenomenon of the pile up as the frequency of the bunches is 5MHz. Assuming a radius of 10cm and a beam of 10$\mu$m in the transverse dimension, this reflects in a rotation speed of about 24000 RPM. The graphite target must dissipate about 200kW of power in the stationary regime, which in this case would be done by radiation. Taking into account the graphite emissivity, the needed surface to dissipate all the power results in the order of several meters square assuming an optimistic working temperature of 2000°C. Obviously, a single target cannot fit this requirement since the peaked temperature surface would be a corona with the same width of the beam, more or less.

The only solution we found would be to use a comb target, as shown in the figure 5.3b, composed by many graphite plates. In this way, introducing cooled copper in the empty space the desired surface could be obtained. Anyway, the assembly complexity and the enormous

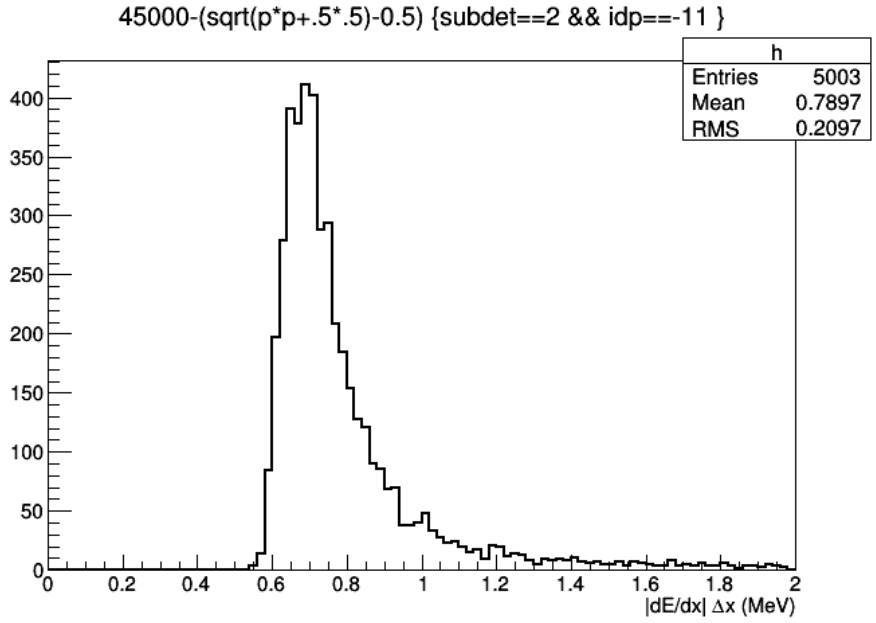


**Figure 5.5:** The simulation of the deposited energy per particle using lithium target 10mm. The simulation have been performed using GEANT4 [142, 143, 144].

mechanical difficulty making the target structure rotating so fast suggests this choice as high risks and maintenance demanding. The mechanical reliability of graphite, which operates at such high temperatures, has not been evaluated yes; in the event of target breaking, the removal and replacement operations could cause long shut down of the accelerator complex. To summarise, a solid choice would be more conventional and the technology is well known. The target would be composed of few components, so easier, very cheap and vacuum compatible. Moreover, the area surrounding the target would be one with the most intense activation, having something moving at very high speed in such harsh environment sounds like undesirable. In any case all the operation near the target, whatever it is, must be performed in remote handling.

Moving our attention on an other not to heavy material we find lithium. The use of flowing liquid lithium as a target for the particle accelerator as been proposed. The experience reach during the Ph.D. using liquid metals and the knowing of fusion relevant experiments, such as IFMIF [145, 146], supported this proposal.

So, most of the work has been performed, of course, on the liquid lithium solution. In figure 5.5 the simulation of the deposited energy per particle in 10mm lithium target using GEANT4 [142, 143, 144], is shown. Using the input from the simulation it is possible to

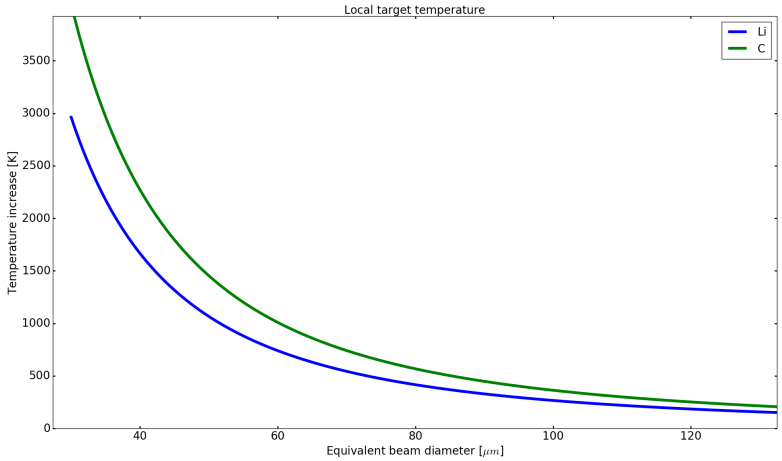


**Figure 5.6:** The simulation of the temperature increse per bunch both for lithium and graphite versus the positron beam equivalent diameter.

deduce the power density deposited in the lithium crossed volume by the positron beam.

A simple estimation is given by:

- $P_{target} = 1.6 \cdot 10^{-13} \frac{J}{MeV} \cdot 1.5 \cdot 10^{18} \frac{e^+}{s} \cdot 0.8 \frac{MeV}{e^+} \approx 200kW$
- $\frac{\Delta E}{e^+} = 0.8Mev \qquad \Delta V = 7.85 \cdot 10^{-5} cm^{-3}$
- $\frac{\Delta E}{\Delta V} = 1.02 \cdot 10^4 \frac{MeV}{cm^3 e^+}$ Assuming a beam diameter of $100\mu m$
- $\Delta T = 10^4 \frac{MeV}{cm^3 e^+} \cdot \frac{1}{0.512 \frac{g}{cm^3} \cdot 3.582 \frac{J}{g \cdot K}} \cdot 1.6 \cdot 10^{-13} \frac{J}{MeV} \cdot 3 \cdot 10^{11} \frac{e^+}{bunch} \approx$

$$2.7 \cdot 10^2 \frac{K}{bunch}$$

The $\Delta T$ is the temperature increase per single bunch in the lithium volume interacts with the particle beam, $5 \cdot 10^5$ bunch per second would cross the volume, of course a stationary scenario of the target is not realistic. In figure 5.6 the temperature increase per single bunch is plotted versus the equivalent beam diameter, lithium and graphite are simulated. The basic idea is to use a liquid lithium cascade with a sufficiently high velocity so that the single positrons bunch interact time by time with a *fresh* lithium volume avoiding pile-up. After these preliminary evaluations a set of detailed simulation has been performed in collaboration with ENEA Brasimone and them expertise with liquid metals loop technologies, and several different layouts have been discussed together.

The first problem was related to the pile up effect. Furthermore, we understood the power density issue depends only on the beam transverse surface and not on its shape, this remains true even for the muons production rate. So that, the beam is intentionally corrected to obtain a circular shape along the ring, we asked to the optics experts the possibility to have an elliptical beam in the interactive zone, receiving a positive response. Then we proposed to use an elliptical beam with the axes dimensions 10x500$\mu$m and we calculated the relative increase in temperature due to the single bunch: it is 430°C. Now, given the beam height and the time distance, 200 ns, between two consecutive bunches, it is straightforward calculate the minimum speed that lithium liquid needs to avoid the pile up phenomenon that corresponds to 50m/s. Thanks to the experience on this subject of the ENEA Brasimone colleagues we understood that such speed is feasible with lithium from the engineering point of view.

The initial idea was a 1cm inner diameter tube intersecting the accelerator vacuum pipe and so the beam at a given point. This solution, attractive because simple and safe, however, has presented the problem of the tube walls containing the liquid metal. Various calculations and simulations have been carried out with different materials and thicknesses, evaluating: the impact of the walls on the positron beam, the increase in emittance of the produced muons and the structural capacity of the pipe itself. Unfortunately, the required safety margins have not been achieved mainly because of the strong structure vibrations induced by the large mass of liquid metal moves at such high speed.

Thus, the solution for this issue is to install the pipe, containing the liquid metal, in a separate vacuum box and then cut the tube letting the positron beam interacts only with liquid lithium. The vacuum box would be separated from the accelerator primary vacuum by two thin beryllium windows placed about 4 meters away from the interaction point. The positron beam would be defocused near such windows, the energy loss and the performance degradation would be negligible in this case. The impact of lithium vapor on the positron beam in the box volume was estimated, since the beam path in such box is very small compared to the length of the ring, its contribution to the total emittance of the beam was considered negligible.

The simulations carried out with the Brasimone's colleagues, and show in the figure 5.7, well agree in absolute value with the foreseen temperature increase estimated before. Furthermore, a detailed analysis shows the temperature increase is extremely localized and the system's bulk temperature variation is quite low, only a few tens Celsius degrees: this fully confirm the system power handling. The use for the liquid target has many operational advantages, but also, obviously, a considerable complication of the system from the point of view of the

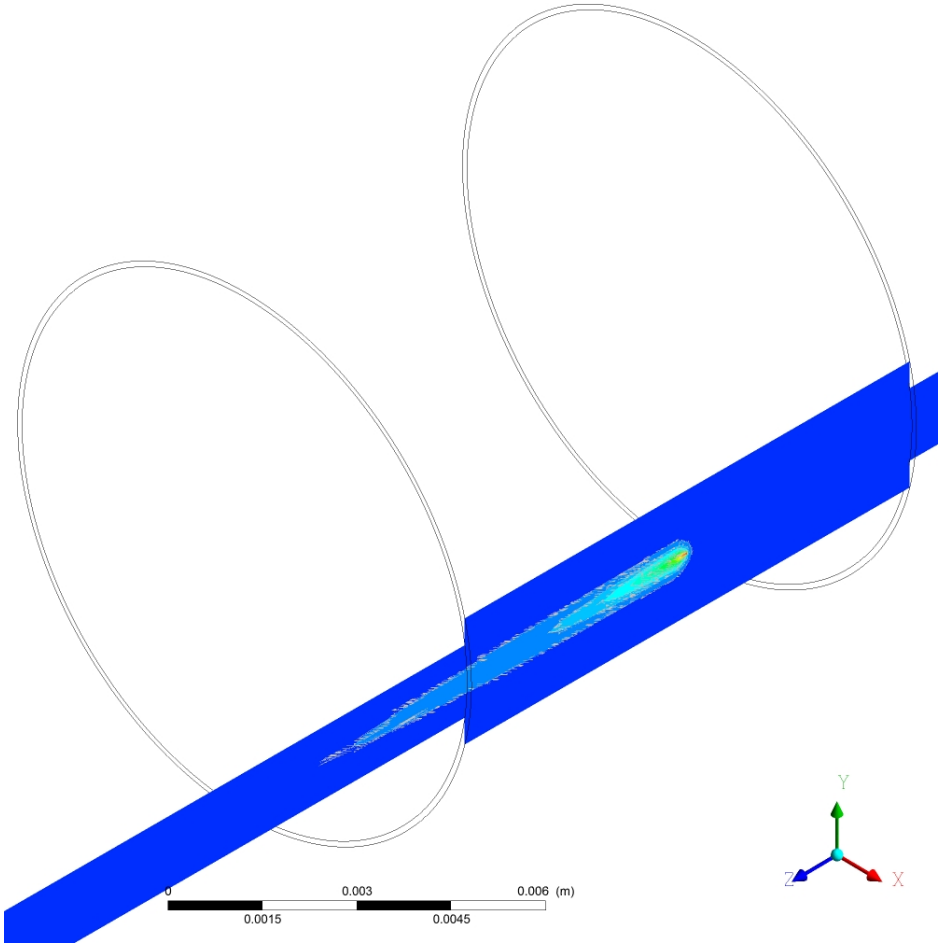


**Figure 5.7:** Simulation of the temperature distribution along the lithium flowing target.

chemical and radioactive safety.

Unfortunately, a few references have been found regarding the interaction between positrons and liquid metals. One of these is in [107], where the authors report the phenomenology of interaction between a MeV positron beam and various liquid metals. A theoretical treatment of the positron annihilation, with the electrons contained in the liquid metals, is offered to the reader, here some interesting experimental observations are reported. One of the major doubts lies in the ability of the positron beam to generate perturbations and oscillations that could destabilize the liquid metal cascade in front of the beam, thus making the experiment vain. The authors in [107] report an unexpected increase in the average life time of the positrons in the metals when they are melted. A customary explanation of this effect is that positrons can find *voids* in the more open structure offered by the liquid phase, where they can stay in relatively low energy far from the ions. However, this picture is not persuasive, since there is no evidence that appreciable size voids occur in liquid more often than vacancies in solid close to the melting point, as shown in the previous chapter. Perhaps, a different approach could be that positrons do not take advantage of voids already present in the liquid before they arrival, instead the positrons would create voids by them-self repelling the surrounding ions. Currently, the lack in knowledge on this topic should be cover by performing dedicated experiments.

At the moment both solutions, the solid and the liquid one, are being studied in parallel. In the meantime, preliminary tests were carried out at CERN during August 2018 on the production rate of muons using various materials, i.e. Be and C. An experimental campaign, the first one, is foreseen with a liquid lithium system in July 2019 at the SOREQ research center in Israel [147, 148]. The Israeli colleagues have a facility for neutrons production starting for protons on a liquid lithium target. We are evaluating with them the use of such target and the possibility to scan the parameters operative range with the protons beam. Then the idea would be to move the target to a collimated electron beam reaching more interesting power densities for our purpose. Another very attractive possibility would be the installation of a liquid lithium target facility in the DAΦNE particle accelerator in Frascati. This device is, in fact, an electron-positron ring operating in the GeV range of energy. The Frascati collider would not be available before 2020.

# 6 Conclusion

In the thesis, various aspects of the use of liquid metal in tokamak devices have been addressed. Nuclear fusion and magnetic confinement have been introduced, as well as the basic principles of plasma physics. According to the European roadmap, the power exhaust problem has been pointed out and the actual approach to tackle it has been traced. Power exhaust is one of the most challenging issues on the path towards electricity produced by nuclear fusion plants. In this framework, two liquid metal limiters have been installed and utilised as plasma facing component on FTU. Starting from the achieved results with the liquid lithium limiter, a radiative model has been developed in order to explain the data collected during previous campaigns. The observed vapor shield phenomenon has been studied taking into account the vapor pressure, the plasma pressure, and the main radiative processes. The simulations show a good agreement with the experimental data, and extrapolations suggest a stationary regime for the temperature oscillations in terms of frequency and amplitude. Such effects strongly reduce the power flux density reaching the liquid surface, since a lot of power is lost by radiation, and it could be a key self-protecting feature for the future liquid-base plasma facing component.

Hence, for the first time in the world, a liquid tin limiter has been tested in tokamak. The CPS-base limiter has been exposed on the FTU pulse, without active cooling, to heat loads up to 18 MW $m^{-2}$. This limiter has acted as main limiter during several plasma discharges, showing its capability to withstand heat load in the same range of the FTU toroidal limiter.

The comparison between the lithium and the tin limiter has experimentally validated and

put in evidence the importance of the operative window for the two metals. In fact, the tin surface reached the evaporation regime as already previously observed with lithium, in both cases the VUV spectra was completely dominated by the metal impurity. A reasonable explanation for this would be a prompt redeposition on the main toroidal limiter reducing or preventing the molybdenum atom sputtering. The experiments with tin have shown very low plasma pollution and the plasma performances have not been affected by the tin impurities, while the well documented beneficial features doping plasma with lithium have been observed too. Actually, it is of primary import to tackle and stress the stationary operations regime, and the assessment of an integrated plasma scenario compatible with liquid metals is mandatory.

In parallel with the plasma compatibility investigation, the technical issues related to the use of liquid metals have been systematically approached. A laboratory in Frascati is now devoted to the study of liquid metal features, like wetting and corrosion. Dedicated tools have been adapted and installed thanks to the experience gained with the two liquid metal limiters. The issue of how to support structure corrosion for a future liquid metal CPS-base divertor has been considered. Tungsten coating deposition using detonation gun has been successfully achieved for the first time. It looks like a reliable and robust solution to definitely overcome the problem and a process patent is currently in progress.

The thermal analysis of liquid tin samples exposed to ISTTOK tokamak plasma was the central part of the activity performed in Lisbon where also deuterium retention has been studied. The latter is an important information, needed by the scientifical community dealing with liquid metal divertor design. Many new informations have been collected and detailed measurements and activities are planned for the future.

To sum up: one part of the thesis has been focused on the plasma interaction phenomenology with liquid metals, while another part has concerned the more technological aspects related to them compatibility with a future reactor integrated scenario. The scientific community working on liquid metal has grown a lot during the last decades and is now approaching to a very important challenge: to propose a Liquid Metal Divertor solution for DEMO. The effort to afford the conceptual design of a liquid metal divertor has been one of the main guideline to orient the Ph.D. work. The appealing feature of liquid metals, like as the self-healing surface, the absence of neutron damage, the possibility to have finally achieved a long lifetime plasma facing component are leading towards the liquid metal divertor solution as a real possibility to overcame the power exhaust problem.

Rather than being focused on a specific aspect the work developed in this PhD has simultaneusly adressed several scientific and technical aspects of liquid metal applications

on tokamaks. Many original contributions have been made with the intent to prepare the introduction of a liquid metal divertor on the Divertor Test Tokamak.

Finally, an example of collaboration and synergy with other laboratories in the different field is given by preliminary work undertaken in collaboration with the INFN of Frascati and the CERN of Geneva. The study of a future muon collider has been tackled, the amazing challenge consists in the direct production of the $\mu^+ \mu^-$ pair starting from a positron beam that interacts with a target material. The experience on liquid metals has led to propose a liquid lithium target, actually emerging as a practical solution to overcame the high power density issue on the material itself. R & D activities and planning for dedicated experiments are currently in progress and many attractive prospective are showing up.

# References


[1] [Online]. Available: https://www.euro-fusion.org/fileadmin/user_upload/EUROfusion/Documents/Roadmap.pdf

[2] M. Razavy, *Quantum Theory of Tunneling*. WORLD SCIENTIFIC, 2003. [Online]. Available: https://www.worldscientific.com/doi/abs/10.1142/4984

[3] J. Wesson and D. Campbell, *Tokamaks*, ser. International Series of Monogr. OUP Oxford, 2011. [Online]. Available: https://books.google.it/books?id=XJssMXjHUroC

[4] J. D. Lawson, "Some criteria for a power producing thermonuclear reactor," *Proceedings of the Physical Society. Section B*, vol. 70, no. 1, p. 6, 1957. [Online]. Available: http://stacks.iop.org/0370-1301/70/i=1/a=303

[5] R. Goldston and P. Rutherford, *Introduction to Plasma Physics*. CRC Press, 1995. [Online]. Available: https://books.google.it/books?id=7kM7yEFUGnAC

[6] G. Montani, "Lecture notes from plasma electrodynamics," 2014.

[7] B. Scott, *An Introduction to Magnetohydrodynamics (MHD),or Magnetic Fluid Dynamics*. Berlin, Heidelberg: Springer Berlin Heidelberg, 2005, pp. 51–74. [Online]. Available: https://doi.org/10.1007/11360360_3

[8] S. Chandrasekhar and E. Fermi, "Problems of gravitational stability in the presence of a magnetic field." *Astrophysical Journal*, vol. 118, no. 1, p. 116, 1953.

[9] V. D. Shafranov, "On magnetohydrodynamical equilibrium configurations," *J. Exptl. Theoret. Phys. (U.S.S.R.)*, vol. 33, no. 1, pp. 710 – 722, 1957. [Online]. Available: http://www.jetp.ac.ru/cgi-bin/dn/e_006_03_0545.pdf

[10] R. S. Cohen, L. Spitzer, and P. M. Routly, "The electrical conductivity of an ionized gas," *Phys. Rev.*, vol. 80, pp. 230–238, Oct 1950. [Online]. Available: https://link.aps.org/doi/10.1103/PhysRev.80.230

[11] P. C. Stangeby, *The Plasma Boundary of Magnetic Fusion Devices*, I. of Physics Publishing Bristol and Philadelphia, Eds. IOP Publishing Ltd., 2000.

[12] G. McCracken and P. Stott, "Plasma-surface interactions in tokamaks," *Nuclear Fusion*, vol. 19, no. 7, p. 889, 1979. [Online]. Available: http://stacks.iop.org/0029-5515/19/i=7/a=004

[13] P. C. Stangeby, "A tutorial on some basic aspects of divertor physics," *Plasma Physics and Controlled Fusion*, vol. 42, no. 12B, p. B271, 2000. [Online]. Available: http://stacks.iop.org/0741-3335/42/i=12B/a=321

[14] L. Pieroni, "Experimental results from present day high field tokamaks," 12 1981.

[15] F. D. Marco, L. Pieroni, F. Santini, and S. Segre, "High magnetic field tokamaks," *Nuclear Fusion*, vol. 26, no. 9, p. 1193, 1986. [Online]. Available: http://stacks.iop.org/0029-5515/26/i=9/a=005

[16] F. Romanelli, "Frascati tokamak upgrade (ftu): Results and developments," Enea, Tech. Rep., 1997.

[17] G. Pucella, E. Alessi, L. Amicucci, B. Angelini, M. Apicella, G. Apruzzese, G. Artaserse, F. Belli, W. Bin, L. Boncagni, A. Botrugno, S. Briguglio, A. Bruschi, P. Buratti, G. Calabrò, M. Cappelli, A. Cardinali, C. Castaldo, F. Causa, S. Ceccuzzi, C. Centioli, R. Cesario, C. Cianfarani, G. Claps, V. Cocilovo, F. Cordella, F. Crisanti, O. D'Arcangelo, M. D. Angeli, C. D. Troia, B. Esposito, D. Farina, L. Figini, G. Fogaccia, D. Frigione, V. Fusco, L. Gabellieri, S. Garavaglia, E. Giovannozzi, G. Granucci, M. Iafrati, F. Iannone, M. Lontano, G. Maddaluno, S. Magagnino, M. Marinucci, D. Marocco, G. Mazzitelli, C. Mazzotta, A. Milovanov, D. Minelli, F. Mirizzi, A. Moro, S. Nowak, D. Pacella, L. Panaccione, M. Panella, V. Pericoli-Ridolfini, A. Pizzuto, S. Podda, G. Ramogida, G. Ravera, D. Ricci, A. Romano, C. Sozzi, A. Tuccillo, O. Tudisco, B. Viola, V. Vitale, G. Vlad, M. Zerbini, F. Zonca, M. Aquilini, P. Cefali, E. D. Ferdinando, S. D. Giovenale, G. Giacomi, A. Grosso, V. Mellera, M. Mezzacappa, A. Pensa, P. Petrolini, V. Piergotti, B. Raspante, G. Rocchi, A. Sibio, B. Tilia, R. Tulli, M. Vellucci, D. Zannetti, I. Bogdanovic-Radovic, D. Carnevale, A. Casolari, M. Ciotti, C. Conti, P. Dinca, V. Dolci, C. Galperti, M. Gospodarczyk, G. Grosso, L. Lubiako, M. Lungu, J. Martin-Solis, C. Meineri, F. Murtas, A. Nardone, F. Orsitto, E. P. Cippo,

Z. Popovic, D. Ripamonti, A. Simonetto, and U. Tartari, "Overview of the ftu results," *Nuclear Fusion*, vol. 57, no. 10, p. 102004, 2017. [Online]. Available: http://stacks.iop.org/0029-5515/57/i=10/a=102004

[18] B. Badger, M. Abdou, R. Boom, and R. e. a. Brown, "Uwmak-i, a wisconsin toroidal fusion reactor design," *University of Wisconsin report UWFDM-68 Madison*, 1973. [Online]. Available: http://www.sciencedirect.com/science/article/pii/S0920379614005924

[19] F. Crisanti, R. Albanese, G. Granucci, R. Martone, and P. Sonato, "The divertor tokamak test facility proposal: Physical requirements and reference design," *Nuclear Materials and Energy*, vol. 12, pp. 1330 – 1335, 2017, proceedings of the 22nd International Conference on Plasma Surface Interactions 2016, 22nd PSI. [Online]. Available: http://www.sciencedirect.com/science/article/pii/S2352179116300813

[20] T. Hirai, S. Panayotis, V. Barabash, C. Amzallag, F. Escourbiac, A. Durocher, M. Merola, J. Linke, T. Loewenhoff, G. Pintsuk, M. Wirtz, and I. Uytdenhouwen, "Use of tungsten material for the iter divertor," *Nuclear Materials and Energy*, vol. 9, pp. 616 – 622, 2016. [Online]. Available: http://www.sciencedirect.com/science/article/pii/S2352179115301046

[21] *Transfert de flux supérieur à 1 kW/cm2par double changement de phase entre une paroi non isotherme et un liquide en convection forcée*, September 1970.

[22] W. Tosto. (2018) Walter tosto staff. [Online]. Available: http://www.waltertosto.it/news/ultime-news/completati-con-successo-i-prototipi-per-divertor-cassette-iter

[23] R. Villari, V. Barabash, F. Escourbiac, L. Ferrand, T. Hirai, V. Komarov, M. Loughlin, M. Merola, F. Moro, L. Petrizzi, S. Podda, E. Polunovsky, and G. Brolatti, "Nuclear analysis of the iter full-tungsten divertor," *Fusion Engineering and Design*, vol. 88, no. 9, pp. 2006 – 2010, 2013, proceedings of the 27th Symposium On Fusion Technology (SOFT-27); Liège, Belgium, September 24-28, 2012. [Online]. Available: http://www.sciencedirect.com/science/article/pii/S0920379613002718

[24] S. Zinkle and S. Fabritsiev, "Copper alloys for high heat flux structure applications," *Nucl. Fusion Suppl.*, vol. 5, no. SUPPL., 1994.

[25] G. Cottrell, "Sigma phase formation in irradiated tungsten, tantalum and molybdenum in a fusion power plant," *Journal of Nuclear Materials*, vol. 334, no. 2, pp. 166 – 168, 2004. [Online]. Available: http://www.sciencedirect.com/science/article/pii/S0022311504005094

[26] G. Federici, W. Biel, M. Gilbert, R. Kemp, N. Taylor, and R. Wenninger, "European demo design strategy and consequences for materials," *Nuclear Fusion*, vol. 57, no. 9, p. 092002, 2017. [Online]. Available: http://stacks.iop.org/0029-5515/57/i=9/a=092002

[27] I. Lyublinski, *Fusion Eng. Des.*, vol. 89, pp. 2816–2821, 2014.

[28] S. Mirnov and V. Evtikhin, "The tests of liquid metals (ga, li) as plasma facing components in t-3m and t-11m tokamaks," *Fusion Engineering and Design*, vol. 81, no. 1, pp. 113 – 119, 2006, proceedings of the Seventh International Symposium on Fusion Nuclear Technology. [Online]. Available: http://www.sciencedirect.com/science/article/pii/S0920379605004874

[29] H. Kugel, J. Allain, M. Bell, R. Bell, A. Diallo, R. Ellis, S. Gerhardt, B. Heim, M. Jaworski, R. Kaita, J. Kallman, S. Kaye, B. LeBlanc, R. Maingi, A. McLean, J. Menard, D. Mueller, R. Nygren, M. Ono, S. Paul, R. Raman, A. Roquemore, S. Sabbagh, H. Schneider, C. Skinner, V. Soukhanovskii, C. Taylor, J. Timberlake, M. Viola, and L. Zakharov, "Nstx plasma operation with a liquid lithium divertor," *Fusion Engineering and Design*, vol. 87, no. 10, pp. 1724 – 1731, 2012, the 2nd International Symposium of Lithium Application for Fusion Devices. [Online]. Available: http://www.sciencedirect.com/science/article/pii/S0920379611005187

[30] L. Begrambekov, A. Zakharov, A. Pustobaev, and V. Telkovsky, *Atomnaya Energiya*, vol. 64, 1988.

[31] R. Gomes, H. Fernandes, C. Silva, A. Sarakovskis, T. Pereira, J. Figueiredo, B. Carvalho, A. Soares, C. Varandas, O. Lielausis, A. Klyukin, E. Platacis, and I. Tale, "Interaction of a liquid gallium jet with the tokamak ISTTOK edge plasma," *Fusion Engineering and Design*, vol. 83, no. 1, pp. 102 – 111, 2008. [Online]. Available: http://www.sciencedirect.com/science/article/pii/S0920379607004243

[32] G. van Eden, "Vapour shielding of liquid metal walls in nuclear fusion devices," Ph.D. dissertation, Department of Applied Physics, 5 2018, proefschrift.

[33] M. Iafrati, G. Mazzitelli, M. L. Apicella, G. M. Apruzzese, J. P. S. Loureiro, I. Lyublinski, A. Vertkov, A. Berlov, G. Maddaluno, F. Crescenzi, A. Mancini, and FTU team, "Comparison between liquid lithium and liquid tin limiters in FTU," 2017, , O5.132 in the procedings from 44th EPS Conference on Plasma Physics in Belfast June 2017 (to appear in Plasma Phys. and Controlled Fus.). [Online]. Available: http://ocs.ciemat.es/EPS2017PAP/pdf/O5.132.pdf

[34] F. L. Tabarés, E. Oyarzabal, D. Tafalla, A. Martin-Rojo, D. Alegre, and A. de Castro, "First liquid lithium limiter biasing experiments in the tj-ii stellarator," *Journal of Nuclear Materials*, vol. 463, pp. 1142 – 1146, 2015, pLASMA-SURFACE INTERACTIONS 21. [Online]. Available: http://www.sciencedirect.com/science/article/pii/S0022311514008940

[35] T. Estrada, T. Happel, L. Eliseev, D. López-Bruna, E. Ascasíbar, E. Blanco, L. Cupido, J. M. Fontdecaba, C. Hidalgo, R. Jiménez-Gómez, L. Krupnik, M. Liniers, M. E. Manso, K. J. McCarthy, F. Medina, A. Melnikov, B. van Milligen, M. A. Ochando, I. Pastor, M. A. Pedrosa, F. L. Tabarés, D. Tafalla, and T.-I. Team, "Sheared flows and transition to improved confinement regime in the tj-ii stellarator," *Plasma Physics and Controlled Fusion*, vol. 51, no. 12, p. 124015, 2009. [Online]. Available: http://stacks.iop.org/0741-3335/51/i=12/a=124015

[36] T. W. Morgan, P. Rindt, G. G. van Eden, V. Kvon, M. A. Jaworksi, and N. J. L. Cardozo, "Liquid metals as a divertor plasma-facing material explored using the pilot-psi and magnum-psi linear devices," *Plasma Physics and Controlled Fusion*, vol. 60, no. 1, p. 014025, 2018. [Online]. Available: http://stacks.iop.org/0741-3335/60/i=1/a=014025

[37] R. Nygren and F. Tabarés, "Liquid surfaces for fusion plasma facing components—a critical review. part i: Physics and psi," *Nuclear Materials and Energy*, vol. 9, pp. 6 – 21, 2016. [Online]. Available: http://www.sciencedirect.com/science/article/pii/S2352179115301307

[38] S. Mirnov, "Plasma-wall interactions and plasma behaviour in fusion devices with liquid lithium plasma facing components," *Journal of Nuclear Materials*, vol. 390-391, pp. 876 – 885, 2009, proceedings of the 18th International Conference on Plasma-Surface Interactions in Controlled Fusion Device. [Online]. Available: http://www.sciencedirect.com/science/article/pii/S0022311509002554

[39] S. Mirnov, V. Dem'yanenko, and E. Murav'ev, "Liquid-metal tokamak divertors," *Journal of Nuclear Materials*, vol. 196-198, pp. 45 – 49, 1992, plasma-Surface Interactions in Controlled Fusion Devices. [Online]. Available: http://www.sciencedirect.com/science/article/pii/S0022311506800103

[40] N. C. Christofilos, "Design for a high power-density astron reactor," *Journal of Fusion Energy*, vol. 8, no. 1, pp. 97–105, Jun 1989. [Online]. Available: https://doi.org/10.1007/BF01050784

[41] A. A. Abagyan, A. A. Alferov, V. F. Babal'yants, D. G. Baratov, V. N. Dem'yanenko, S. B. Leonov, S. P. Maksimov, S. V. Mirnov, V. N. Mikhailov, V. V. Myalton, V. S. Semenov, M. M. Fiks, and V. P. Fokin, "T-3m tokamak materials testing stand," *Soviet Atomic Energy*, vol. 58, no. 4, pp. 286–292, Apr 1985. [Online]. Available: https://doi.org/10.1007/BF01207217

[42] S. Mirnov, A. Belov, N. Djigailo, A. Dzhurik, S. Kravchuk, V. Lazarev, I. Lyublinski, A. Vertkov, M. Zharkov, and A. Shcherbak, "Experimental test of the system of vertical and longitudinal lithium limiters on t-11m tokamak as a prototype of plasma facing components of a steady-state fusion neutron source," *Nuclear Fusion*, vol. 55, no. 12, p. 123015, 2015. [Online]. Available: http://stacks.iop.org/0029-5515/55/i=12/a=123015

[43] C. Skinner, E. Amarescu, G. Ascione, W. Blanchard, C. Barnes, S. Batha, M. Beer, M. Bell, R. Bell, M. Bitter, N. Bretz, R. Budny, C. Bush, R. Camp, M. Casey, J. Collins, M. Cropper, Z. Chang, D. Darrow, H. Duong, R. Durst, P. Efthimion, D. Ernst, N. Fisch, R. Fonck, E. Fredrickson, G. Fu, H. Furth, C. Gentile, M. Gibson, J. Gilbert, B. Grek, L. Grisham, G. Hammett, R. Hawryluk, H. Herrmann, K. Hill, J. Hosea, A. Janos, D. Jassby, F. Jobes, D. Johnson, L. Johnson, J. Kamperschroer, M. Kalish, H. Kugel, J. Langford, S. Langish, P. Lamarche, B. Leblanc, F. Levinton, J. Machuzak, R. Majeski, J. Manikam, D. Mansfield, E. Mazzucato, K. McGuire, R. Mika, G. McKee, D. Meade, S. Medley, D. Mikkelsen, H. Mynick, D. Mueller, A. Nagy, R. Nazikian, M. Ono, D. Owens, H. Park, S. Paul, G. Pearson, M. Petrov, C. Phillips, S. Raftopoulos, A. Ramsey, R. Raucci, M. Redi, G. Rewoldt, J. Rogers, A. Roquemore, E. Ruskov, S. Sabbagh, G. Schilling, J. Schivell, G. Schmidt, S. Scott, S. Sesnic, B. Stratton, J. Strachan, T. Stevenson, D. Stotler, E. Synakowski, H. Takahashi, W. Tang, G. Taylor, W. Tighe, J. Timberlake, A. von Halle, S. von Goeler, R. Walters, R. White, J. Wilson, J. Winston, K. Wong, K. Young,

M. Zarnstorff, and S. Zweben, "Plasma wall interaction and tritium retention in tftr," *Journal of Nuclear Materials*, vol. 241-243, pp. 214 – 226, 1997. [Online]. Available: http://www.sciencedirect.com/science/article/pii/S0022311597800414

[44] J. Terry, E. Marmar, H. R.B., and et al., "Iaea proced," in *Plasma Physics and Controlled Nuclear Fusion Research*, 1991.

[45] J. L. Terry, E. S. Marmar, J. A. Snipes, D. Garnier, and T. Group, "Imaging of lithium pellet ablation trails and measurement of q profiles in tftr," *Review of Scientific Instruments*, vol. 63, p. 5191, 1992. [Online]. Available: https://aip.scitation.org/doi/abs/10.1063/1.1143849

[46] J. Strachan, D. Mansfield, M. Bell, J. Collins, D. Ernst, K. Hill, J. Hosea, J. Timberlake, M. Ulrickson, J. Terry, E. Marmar, and J. Snipes, "Wall conditioning experiments on tftr using impurity pellet injection," *Journal of Nuclear Materials*, vol. 217, no. 1, pp. 145 – 153, 1994. [Online]. Available: http://www.sciencedirect.com/science/article/pii/002231159490314X

[47] V. V. et al, "Experiments with lithium gettering of the t-10 tokamak," in *Proc. 22nd Int. Conf. on Fusion Energy 2008*, V. IAEA, Ed., 2008.

[48] S. Mirnov, E. Azizov, A. Alekseev, V. Lazarev, R. Khayrutdinov, I. Lyublinski, A. Vertkov, and V. Vershkov, "Li experiments on t-11m and t-10 in support of a steady-state tokamak concept with li closed loop circulation," *Nuclear Fusion*, vol. 51, no. 7, p. 073044, 2011. [Online]. Available: http://stacks.iop.org/0029-5515/51/i=7/a=073044

[49] V. A. Evtikhin, I. E. Lyublinski, A. V. Vertkov, S. V. Mirnov, V. B. Lazarev, N. P. Petrova, S. M. Sotnikov, A. P. Chernobai, B. I. Khripunov, V. B. Petrov, D. Y. Prokhorov, and V. M. Korzhavin, "Lithium divertor concept and results of supporting experiments," *Plasma Physics and Controlled Fusion*, vol. 44, no. 6, p. 955, 2002. [Online]. Available: http://stacks.iop.org/0741-3335/44/i=6/a=322

[50] M. Apicella, G. Mazzitelli, V. P. Ridolfini, V. Lazarev, A. Alekseyev, A. Vertkov, and R. Zagórski, "First experiments with lithium limiter on ftu," *Journal of Nuclear Materials*, vol. 363-365, pp. 1346 – 1351, 2007, plasma-Surface Interactions-17. [Online]. Available: http://www.sciencedirect.com/science/article/pii/S0022311507002711

[51] M. Ono, S. Kaye, Y.-K. Peng, G. Barnes, W. Blanchard, M. Carter, J. Chrzanowski, L. Dudek, R. Ewig, D. Gates, R. Hatcher, T. Jarboe, S. Jardin, D. Johnson, R. Kaita, M. Kalish, C. Kessel, H. Kugel, R. Maingi, R. Majeski, J. Manickam, B. McCormack, J. Menard, D. Mueller, B. Nelson, B. Nelson, C. Neumeyer, G. Oliaro, F. Paoletti, R. Parsells, E. Perry, N. Pomphrey, S. Ramakrishnan, R. Raman, G. Rewoldt, J. Robinson, A. Roquemore, P. Ryan, S. Sabbagh, D. Swain, E. Synakowski, M. Viola, M. Williams, J. Wilson, and N. Team, "Exploration of spherical torus physics in the nstx device," *Nuclear Fusion*, vol. 40, no. 3Y, p. 557, 2000. [Online]. Available: http://stacks.iop.org/0029-5515/40/i=3Y/a=316

[52] M. ONO and N. Team, "Nstx: Facility/research highlights and near term facility plans," *Princeton Univeristy Report*, November 2008. [Online]. Available: https://www.osti.gov/servlets/purl/941507-cBmFLa/

[53] H. W. Kugel, M. G. Bell, J.-W. Ahn, J. P. Allain, R. Bell, J. Boedo, C. Bush, D. Gates, T. Gray, S. Kaye, R. Kaita, B. LeBlanc, R. Maingi, R. Majeski, D. Mansfield, J. Menard, D. Mueller, M. Ono, S. Paul, R. Raman, A. L. Roquemore, P. W. Ross, S. Sabbagh, H. Schneider, C. H. Skinner, V. Soukhanovskii, T. Stevenson, J. Timberlake, W. R. Wampler, and L. Zakharov, "The effect of lithium surface coatings on plasma performance in the national spherical torus experiment," *Physics of Plasmas*, vol. 15, no. 5, p. 056118, 2008. [Online]. Available: https://doi.org/10.1063/1.2906260

[54] P. Rindt, N. L. Cardozo, J. van Dommelen, R. Kaita, and M. Jaworski, "Conceptual design of a pre-loaded liquid lithium divertor target for nstx-u," *Fusion Engineering and Design*, vol. 112, pp. 204 – 212, 2016. [Online]. Available: http://www.sciencedirect.com/science/article/pii/S0920379616305555

[55] R. Ding, G. Maddaluno, M. Apicella, G. Mazzitelli, V. P. Ridolfini, A. Kirschner, J. Chen, J. Li, and G.-N. Luo, "Modelling of lithium erosion and transport in ftu lithium experiments," *Journal of Nuclear Materials*, vol. 438, pp. S690 – S693, 2013, proceedings of the 20th International Conference on Plasma-Surface Interactions in Controlled Fusion Devices. [Online]. Available: http://www.sciencedirect.com/science/article/pii/S0022311513001542

[56] J. Sánchez, M. Acedo, A. Alonso, J. Alonso, P. Alvarez, E. Ascasíbar, A. Baciero, R. Balbín, L. Barrera, E. Blanco, J. Botija, A. de Bustos, E. de la Cal, I. Calvo,

A. Cappa, J. Carmona, D. Carralero, R. Carrasco, B. Carreras, F. Castejón, R. Castro, G. Catalán, A. Chmyga, M. Chamorro, L. Eliseev, L. Esteban, T. Estrada, A. Fernández, R. Fernández-Gavilán, J. Ferreira, J. Fontdecaba, C. Fuentes, L. García, I. García-Cortés, R. García-Gómez, J. García-Regaña, J. Guasp, L. Guimarais, T. Happel, J. Hernanz, J. Herranz, C. Hidalgo, J. Jiménez, A. Jiménez-Denche, R. Jiménez-Gómez, D. Jiménez-Rey, I. Kirpitchev, A. Komarov, A. Kozachok, L. Krupnik, F. Lapayese, M. Liniers, D. López-Bruna, A. López-Fraguas, J. López-Rázola, A. López-Sánchez, S. Lysenko, G. Marcon, F. Martín, V. Maurin, K. McCarthy, F. Medina, M. Medrano, A. Melnikov, P. Méndez, B. van Milligen, E. Mirones, I. Nedzelskiy, M. Ochando, J. Olivares, J. de Pablos, L. Pacios, I. Pastor, M. Pedrosa, A. de la Peña, A. Pereira, G. Pérez, D. Pérez-Risco, A. Petrov, S. Petrov, A. Portas, D. Pretty, D. Rapisarda, G. Rattá, J. Reynolds, E. Rincón, L. Ríos, C. Rodríguez, J. Romero, A. Ros, A. Salas, M. Sánchez, E. Sánchez, E. Sánchez-Sarabia, K. Sarksian, J. Sebastián, C. Silva, S. Schchepetov, N. Skvortsova, E. Solano, A. Soleto, F. Tabarés, D. Tafalla, A. Tarancón, Y. Taschev, J. Tera, A. Tolkachev, V. Tribaldos, V. Vargas, J. Vega, G. Velasco, J. Velasco, M. Weber, G. Wolfers, and B. Zurro, "Confinement transitions in tj-ii under li-coated wall conditions," *Nuclear Fusion*, vol. 49, no. 10, p. 104018, 2009. [Online]. Available: http://stacks.iop.org/0029-5515/49/i=10/a=104018

[57] S. Mirnov and V. Lazarev, "Li experiments at the tokamak t-11m in field of steady state pfc investigations," *Journal of Nuclear Materials*, vol. 415, no. 1, Supplement, pp. S417 – S420, 2011, proceedings of the 19th International Conference on Plasma-Surface Interactions in Controlled Fusion. [Online]. Available: http://www.sciencedirect.com/science/article/pii/S002231151100050X

[58] M. Ono and R. Kaita, "Recent progress on spherical torus research," *Physics of Plasmas*, vol. 22, no. 4, p. 040501, 2015. [Online]. Available: https://doi.org/10.1063/1.4915073

[59] H. Guo, J. Li, X. Gong, B. Wan, J. Hu, L. Wang, H. Wang, J. Menard, M. Jaworski, K. Gan, S. Liu, G. Xu, S. Ding, L. Hu, Y. Liang, J. Liu, G. Luo, H. Si, D. Wang, Z. Wu, L. Xiang, B. Xiao, L. Zhang, X. Zou, D. Hillis, A. Loarte, R. Maingi, and the EAST Team, "Approaches towards long-pulse divertor operations on east by active control of plasma–wall interactions," *Nuclear Fusion*, vol. 54, no. 1, p. 013002, 2014. [Online]. Available: http://stacks.iop.org/0029-5515/54/i=1/a=013002

[60] Z. Chen, Y. Song, Q. Yang, J. Hu, G. Zuo, J. Ren, S. Zhang, H. Xu, Y. Wang, and W. Zhao, "Preliminary design and performance study of east liquid lithium limiter based on cps," *Fusion Engineering and Design*, vol. 89, no. 11, pp. 2685 – 2690, 2014. [Online]. Available: http://www.sciencedirect.com/science/article/pii/S0920379614004578

[61] G. Z. Zuo, J. S. Hu, S. Zhen, J. G. Li, D. K. Mansfield, B. Cao, J. H. Wu, L. E. Zakharov, and the EAST Team, "Comparison of various wall conditionings on the reduction of h content and particle recycling in east," *Plasma Physics and Controlled Fusion*, vol. 54, no. 1, p. 015014, 2012. [Online]. Available: http://stacks.iop.org/0741-3335/54/i=1/a=015014

[62] A. Vertkov, I. Lyublinski, M. Zharkov, G. Mazzitelli, M. Apicella, and M. Iafrati, "Liquid tin limiter for ftu tokamak," *Fusion Engineering and Design*, vol. 117, pp. 130 – 134, 2017. [Online]. Available: http://www.sciencedirect.com/science/article/pii/S0920379617300522

[63] V. Evtikhin, I. Lyublinski, A. Vertkov, V. Belan, I. Konkashbaev, and L. Nikandrov, "Calculation and experimental investigation of fusion reactor divertor plate and first wall protection by capillary-pore systems with lithium," *Journal of Nuclear Materials*, vol. 271-272, pp. 396 – 400, 1999. [Online]. Available: http://www.sciencedirect.com/science/article/pii/S0022311598007934

[64] V. Evtikhin, A. Vertkov, I. Lyublinski, B. Khripunov, V. Petrov, and S. Mirnov, "Research of lithium capillary-pore systems for fusion reactor plasma facing components," *Journal of Nuclear Materials*, vol. 307-311, pp. 1664 – 1669, 2002. [Online]. Available: http://www.sciencedirect.com/science/article/pii/S0022311502011327

[65] J. W. Coenen, G. D. Temmerman, G. Federici, V. Philipps, G. Sergienko, G. Strohmayer, A. Terra, B. Unterberg, T. Wegener, and D. C. M. V. den Bekerom, "Liquid metals as alternative solution for the power exhaust of future fusion devices: status and perspective," *Physica Scripta*, vol. 2014, no. T159, p. 014037, 2014. [Online]. Available: http://stacks.iop.org/1402-4896/2014/i=T159/a=014037

[66] W. T. Hicks, "Evaluation of vapor pressure data of mercury, lithium, sodium, and potassium," *Journal of Chemical Physics*, vol. 38, no. 8, p. 1873, 1963.

[67] C. B. Alcock, V. P. Itkin, and M. K. Horrigan, "Vapour pressure equations for the metallic elements: 298–2500k," *Canadian Metallurgical Quarterly*, vol. 23, no. 3, pp. 309–313, 1984. [Online]. Available: https://doi.org/10.1179/cmq.1984.23.3.309

[68] M. Poradziński, I. Ivanova-Stanik, G. Pełka, and R. Zagórski, "Integrated core-sol-divertor modelling for demo with tin divertor," *Fusion Engineering and Design*, vol. 124, pp. 248 – 251, 2017, proceedings of the 29th Symposium on Fusion Technology (SOFT-29) Prague, Czech Republic, September 5-9, 2016. [Online]. Available: http://www.sciencedirect.com/science/article/pii/S0920379617305343

[69] P. Innocente, *J. Nucl. Mat.*, vol. 463, pp. 1138–1421, 2014.

[70] M. Apicella, V. Lazarev, I. Lyublinski, G. Mazzitelli, S. Mirnov, and A. Vertkov, "Lithium capillary porous system behavior as pfm in ftu tokamak experiments," *Journal of Nuclear Materials*, vol. 386-388, pp. 821 – 823, 2009, fusion Reactor Materials. [Online]. Available: http://www.sciencedirect.com/science/article/pii/S0022311508009938

[71] I. Lyublinski and A. Vertkov, "Technical letter report or the complete furniture of two lithium limiters to develop, manufacture, transport and install on ftu," Kurchatov Innovation Company, Tech. Rep., 2004.

[72] M. Iafrati, M. Apicella, L. Boncagni, I. Lyublinski, G. Mazzitelli, and A. Vertkov, "Ftu cooled liquid lithium upgrade," *Fusion Engineering and Design*, vol. 117, pp. 157 – 162, 2017. [Online]. Available: http://www.sciencedirect.com/science/article/pii/S0920379617300881

[73] M. L. Apicella, A. Buscarino, C. Corradino, L. Fortuna, G. Mazzitelli, and M. G. Xibilia, "Temperature model identification of ftu liquid lithium limiter," *IEEE Transactions on Control Systems Technology*, vol. 26, no. 3, pp. 1132–1139, May 2018.

[74] A. Buscarino, M. L. Apicella, C. Corradino, L. Fortuna, G. Mazzitelli, and M. G. Xibilia, "Modeling thermal behavior on the ftu liquid lithium limiter," *43rd EPS Conference on Plasma Physics*, p. 4, 2017. [Online]. Available: http://ocs.ciemat.es/EPS2016PAP/pdf/P5.011.pdf

[75] J. H. Lienhard, "Heat transfer," *J. Heat Transfer*, 2010.

[76] H. S. Carslaw and J. C. Jaeger, "Conduction of heat in solids," vol. -1, 01 1959.

[77] W. J. Cook and E. J. Felderman, "Reduction of data from thin-film heat-transfer gages: A concise numerical technique." *AIAA Journal*, vol. 4, no. 3, pp. 561–562, 1966. [Online]. Available: https://doi.org/10.2514/3.3486

[78] T. E. Oliphant, *Guide to NumPy*, 2nd ed. USA: CreateSpace Independent Publishing Platform, 2015.

[79] M. L. G. Oldfield, T. V. Jones, and D. L. Schultz, "On-line computer for transient turbine cascade instrumentation," *10.1109/TAES.1978.308624*, vol. AES-14, no. 5, pp. 738–749, Sept 1978.

[80] P. C. Stangeby, "Interpretation of langmuir, heat-flux, deposition, trapping and gridded energy analyser probe data for impure plasmas," *Journal of Physics D: Applied Physics*, vol. 20, no. 11, p. 1472, 1987.

[81] Y. Corre, E. Rachlew, M. Cecconello, R. M. Gravestijn, A. Hedqvist, B. Pégourié, B. Schunke, and V. Stancalie, "Radiated power and impurity concentrations in the extrap-t2r reversed-field pinch," *Physica Scripta*, vol. 71, no. 5, p. 523, 2005. [Online]. Available: http://stacks.iop.org/1402-4896/71/i=5/a=017

[82] C. Breton, C. de Michelis, and M. Mattioli, "Ionization equilibrium and radiative cooling of a high temperature plasma," *Journal of Quantitative Spectroscopy and Radiative Transfer*, vol. 19, no. 3, pp. 367 – 379, 1978. [Online]. Available: http://www.sciencedirect.com/science/article/pii/0022407378900705

[83] S. Loch, J. Colgan, M. Witthoeft, M. Pindzola, C. Ballance, D. Mitnik, D. Griffin, M. O'Mullane, N. Badnell, and H. Summers, "Generalised collisional-radiative model for light elements. a: Data for the li isonuclear sequence," *Atomic Data and Nuclear Data Tables*, vol. 92, no. 6, pp. 813 – 851, 2006. [Online]. Available: http://www.sciencedirect.com/science/article/pii/S0092640X06000283

[84] H. P. Summers, *The ADAS User Manual*, 2004, version 2.6. [Online]. Available: http://www.adas.ac.uk

[85] M. L. Apicella, G. Apruzzese, G. Mazzitelli, V. P. Ridolfini, A. G. Alekseyev, V. B. Lazarev, S. V. Mirnov, and R. Zagórski, "Lithization of the ftu tokamak with a critical

amount of lithium injection," *Plasma Physics and Controlled Fusion*, vol. 54, no. 3, p. 035001, 2012. [Online]. Available: http://stacks.iop.org/0741-3335/54/i=3/a=035001

[86] J. H. Lienhard, *A Heat Transfer Textbook*, J. of Heat Transfer, Ed., 2008.

[87] C. Pitcher, A. Carlson, C. Fuchs, A. Herrmann, W. Suttrop, J. Schweinzer, and M. Weinlich, "Routes to divertor detachment in asdex upgrade," *Journal of Nuclear Materials*, pp. 241–243, 696–700, 1977.

[88] G. G. van Eden, V. Kvon, M. C. M. van de Sanden, and T. W. Morgan, "Oscillatory vapour shielding of liquid metal walls in nuclear fusion devices," *Nature Communications*, vol. 8, p. 192, 2017. [Online]. Available: https://doi.org/10.1038/s41467-017-00288-y

[89] E. Vassallo, A. Cremona, E. Alves, F. Causa, G. Giacomi, G. Gervasini, G. Granucci, M. Iafrati, G. Maddaluno, R. Mateus, D. Minelli, V. Mellera, A. Nardone, M. Pedroni, D. Ricci, V. Rigato, N. Rispoli, and A. Uccello, "Deuterium retention and erosion in liquid sn samples exposed to d2 and ar plasmas in gym device," *PSI 2018 Proc.*, 2018, proceedings of the 23rd International Conference on Plasma-Surface Interactions in Controlled Fusion Devices.

[90] J. Loureiro, H. Fernandes, F. Tabarés, G. Mazzitelli, C. Silva, R. Gomes, E. Alves, R. Mateus, T. Pereira, H. Figueiredo, and H. Alves, "Deuterium retention in tin (sn) and lithium–tin (li–sn) samples exposed to ISTTOK plasmas," *Journal of Nuclear Materials*, 2016. [Online]. Available: //www.sciencedirect.com/science/article/pii/S2352179116300837

[91] I. Lyublinski and A. Vertkov, "Comparative assessment of application of low melting metals with capillary pore systems in a tokamak," *Fusion Engineering and Design*, vol. 89, no. 12, pp. 2953 – 2955, 2014. [Online]. Available: http://www.sciencedirect.com/science/article/pii/S0920379614005924

[92] I. E. Lyublinski, A. V. Vertkov, M. Y. Zharkov, O. N. Sevryukov, P. S. Dzhumaev, V. A. Shumskiy, and A. A. Ivannikov, "Selection of materials for tokamak plasma facing elements based on a liquid tin capillary pore system," *Journal of Physics: Conference Series*, vol. 748, no. 1, p. 012014, 2016. [Online]. Available: http://stacks.iop.org/1742-6596/748/i=1/a=012014

[93] V. Pericoli-Ridolfini, "Study of the scrape-off plasma of the frascati tokamak in ohmic discharges by means of langmuir probes," *Nuclear Fusion*, vol. 31, no. 1, p. 127, 1991. [Online]. Available: http://stacks.iop.org/0029-5515/31/i=1/a=012

[94] F. Alladio and F. Crisanti, "Analysis of mhd equilibria by toroidal multipolar expansions," *Nuclear Fusion*, vol. 26, no. 9, p. 1143, 1986. [Online]. Available: http://stacks.iop.org/0029-5515/26/i=9/a=002

[95] F. Alladio and P. Micozzi, "Experimental plasma equilibrium reconstruction from kinetic and magnetic measurements in the ftu tokamak," *Nuclear Fusion*, vol. 35, no. 3, p. 305, 1995. [Online]. Available: http://stacks.iop.org/0029-5515/35/i=3/a=I05

[96] J. L. Schwob, A. W. Wouters, S. Suckewer, and M. Finkenthal, "High-resolution duo-multichannel soft x-ray spectrometer for tokamak plasma diagnostics," *Review of Scientific Instruments*, vol. 58, no. 9, pp. 1601–1615, 1987. [Online]. Available: https://doi.org/10.1063/1.1139408

[97] F. Bombarda, G. Apruzzese, L. Carraro, L. Gabellieri, M. Puiatti, A. Romano, M. Valisa, B. Zaniol, M. Apicella, E. Giovannozzi, A. Grosso, M. Iafrati, G. Mazzitelli, V. Piergotti, G. Rocchi, A. Sibio, B. Tilia, and the FTU team, "High resolution euv spectroscopy on ftu with tin liquid limiter," *Proc. 45th EPS Conference on Plasma Physics*, p. 4, 2018. [Online]. Available: http://ocs.ciemat.es/EPS2018PAP/pdf/P1.1005.pdf

[98] G. M. Apruzzese, M. L. Apicella, M. Iafrati, G. Mazzitelli, L. Gabellieri, J. P. S. Loureiro, A. Romano, and FTU Team, "First spectroscopic results with tin limiter on ftu plasma," *Plasma Physics Reports*, vol. 44, no. 7, pp. 636–640, Jul 2018. [Online]. Available: https://doi.org/10.1134/S1063780X18070012

[99] A. R. Foster, "On the behaviour and radiating properties of heavy elements in fusion plasmas," Ph.D. dissertation, University of Strathclyde, 2008. [Online]. Available: http://www.adas.ac.uk/theses/foster_thesis.pdf

[100] T. Morgan, D. van den Bekerom, and G. D. Temmerman, "Interaction of a tin-based capillary porous structure with iter/demo relevant plasma conditions," *Journal of Nuclear Materials*, vol. 463, pp. 1256 – 1259, 2015, pLASMA-SURFACE INTERACTIONS 21. [Online]. Available: http://www.sciencedirect.com/science/article/pii/S0022311514008885

[101] G. Cenacchi, A. Taroni, and J. Project, *JETTO: A Free-boundary Plasma Transport Code (basic Version).*, ser. ENEA-RT-TIB–88-5. JET Joint Undertaking, 1988. [Online]. Available: https://books.google.it/books?id=APVYQwAACAAJ

[102] J. Loureiro, F. Tabarés, H. Fernandes, C. Silva, R. Gomes, E. Alves, R. Mateus, T. Pereira, H. Alves, and H. Figueiredo, "Behavior of liquid li-sn alloy as plasma facing material on ISTTOK," *Fus. Eng. Design*, 2017. [Online]. Available: //www.sciencedirect.com/science/article/pii/S0920379616307463

[103] H. Fernandes, C. Varandas, J. Cabral, H. Figueiredo, and R. Galvão, "Engineering aspects of the ISTTOK operation in a multicycle alternating flat-top plasma current regime," *Fusion Engineering and Design*, vol. 43, no. 1, pp. 101 – 113, 1998. [Online]. Available: http://www.sciencedirect.com/science/article/pii/S0920379698002634

[104] A. Kramida, Yu. Ralchenko, J. Reader, and and NIST ASD Team, NIST Atomic Spectra Database (ver. 5.5.6), [Online]. Available: `https://physics.nist.gov/asd` [2018, July 17]. National Institute of Standards and Technology, Gaithersburg, MD., 2018.

[105] H.-K. Chung, M. Chen, W. Morgan, Y. Ralchenko, and R. Lee, "Flychk: Generalized population kinetics and spectral model for rapid spectroscopic analysis for all elements," *High Energy Density Physics*, vol. 1, no. 1, pp. 3 – 12, 2005. [Online]. Available: http://www.sciencedirect.com/science/article/pii/S1574181805000029

[106] M. D. Coventry, J. P. Allain, and D. N. Ruzic, "D+, He+ and H+ sputtering of solid and liquid phase tin," *Journal of Nuclear Materials*, vol. 313-316, no. SUPPL., pp. 636–640, 2003.

[107] T. E. Faber, *Introduction to the theory of the liquid metals*, ser. Cambridge monograph on physics. Cambridge at the University Press, 1972.

[108] J. Barker, *Lattice theories of the liquid state*, ser. International encyclopedia of physical chemistry and chemical physics: Fluid state. Pergamon Press, 1963. [Online]. Available: https://books.google.pt/books?id=sjRRAAAAMAAJ

[109] D. Turnbull and R. E. Cech, "Microscopic observation of the solidification of small metal droplets," *Journal of Applied Physics*, vol. 21, no. 8, pp. 804–810, 1950. [Online]. Available: https://doi.org/10.1063/1.1699763

[110] J. D. Bernal, *Liquids: Structure, Properties, Solid Interactions*, ser. Elsevier Pub. Co., Amsterdam. Hughel, T. J., 1965.

[111] J. D. Bernal and J. L. Finney, "Random close-packed hard-sphere model. ii. geometry of random packing of hard spheres," *Discuss. Faraday Soc.*, vol. 43, pp. 62–69, 1967. [Online]. Available: http://dx.doi.org/10.1039/DF9674300062

[112] "Random packings and the structure of simple liquids. i. the geometry of random close packing," *Proceedings of the Royal Society of London A: Mathematical, Physical and Engineering Sciences*, vol. 319, no. 1539, pp. 479–493, 1970. [Online]. Available: http://rspa.royalsocietypublishing.org/content/319/1539/479

[113] V. A. Blatov, "Voronoi–dirichlet polyhedra in crystal chemistry: theory and applications," *Crystallography Reviews*, vol. 10, no. 4, pp. 249–318, 2004. [Online]. Available: https://doi.org/10.1080/08893110412331323170

[114] "The resistance of liquid metals," *Proceedings of the Royal Society of London A: Mathematical, Physical and Engineering Sciences*, vol. 146, no. 857, pp. 465–472, 1934. [Online]. Available: http://rspa.royalsocietypublishing.org/content/146/857/465

[115] L. Landau, E. Lifshitz, and L. Pitaevskij, *Statistical Physics: Part 2 : Theory of Condensed State*, ser. Landau and Lifshitz Course of theoretical physics. Oxford, 1980. [Online]. Available: https://books.google.pt/books?id=dEVtKQEACAAJ

[116] S. J. Cocking, "High frequency waves in liquid metals," *Advances in Physics*, vol. 16, no. 62, pp. 189–201, 1967. [Online]. Available: https://doi.org/10.1080/00018736700101315

[117] G. Grimvall, "The heat capacity of liquid metals," *Physica Scripta*, vol. 11, no. 6, p. 381, 1975. [Online]. Available: http://stacks.iop.org/1402-4896/11/i=6/a=009

[118] P. D. Desai, T. K. Chu, H. M. James, and C. Y. Ho, "Electrical resistivity of selected elements," *Journal of Physical and Chemical Reference Data*, vol. 13, no. 4, pp. 1069–1096, 1984. [Online]. Available: https://doi.org/10.1063/1.555723

[119] R. D. Allen, L. F. Glasier, and P. L. Jordan, "Spectral emissivity, total emissivity, and thermal conductivity of molybdenum, tantalum, and tungsten above 2300°k," *Journal of Applied Physics*, vol. 31, no. 8, pp. 1382–1387, 1960. [Online]. Available: https://doi.org/10.1063/1.1735847

[120] S. Krat, A. Popkov, Y. M. Gasparyan, A. Pisarev, P. Fiflis, M. Szott, M. Christenson, K. Kalathiparambil, and D. N. Ruzic, "Wetting properties of liquid lithium on lithium compounds," *Fusion Engineering and Design*, vol. 117, pp. 199 – 203, 2017. [Online]. Available: http://www.sciencedirect.com/science/article/pii/S0920379616304379

[121] J. Zhang and N. Li, "Analysis on liquid metal corrosion–oxidation interactions," *Corrosion Science*, vol. 49, no. 11, pp. 4154 – 4184, 2007. [Online]. Available: http://www.sciencedirect.com/science/article/pii/S0010938X0700128X

[122] A. Grigoriev, O. Shpyrko, C. Steimer, P. S. Pershan, B. M. Ocko, M. Deutsch, B. Lin, M. Meron, T. Graber, and J. Gebhardt, "Surface oxidation of liquid sn," *Surface Science*, vol. 575, no. 3, pp. 223 – 232, 2005. [Online]. Available: http://www.sciencedirect.com/science/article/pii/S0039602804013883

[123] I. Lyublinski and A. Vertkov, "The furniture of new liquid metal limiter to be installed on ftu," FLUORIT PLUS Ltd, Tech. Rep., 2016.

[124] O. Chopra and D. Smith, "Influence of temperature and lithium purity on corrosion of ferrous alloys in a flowing lithium environment," *Journal of Nuclear Materials*, vol. 141-143, pp. 584 – 591, 1986. [Online]. Available: http://www.sciencedirect.com/science/article/pii/0022311586900589

[125] L. R. Kelman, W. D. Wilkinson, and F. L. Yaggee, "Resistance of materials to attack by liquid metals," *Argonne National Laboratory*, vol. ANL-4417, p. 150, 1950.

[126] Y.-G. Deng and J. Liu, "Corrosion development between liquid gallium and four typical metal substrates used in chip cooling device," *Applied Physics A*, vol. 95, no. 3, pp. 907–915, Jun 2009. [Online]. Available: https://doi.org/10.1007/s00339-009-5098-1

[127] M. Hansen, K. Anderko, and R. Elliott, *Constitution of Binary Alloys*, ser. McGraw-Hill series in materials science and engineering. McGraw-Hill, 1958. [Online]. Available: https://books.google.it/books?id=MpNUAAAAMAAJ

[128] M. American Institute of Mining, *Pyrometry: The Papers and Discussion of a Symposium on Pyrometry Held by the American Institute of Mining and Metallurgical Engineers at Its Chicago Meeting, September, 1919, in Co_peration with the National*

*Research Council and the National Bureau of Standards*. The Institute, 1920. [Online]. Available: https://books.google.it/books?id=wDwrAAAAYAAJ

[129] V. Chawla, B. Sidhu, D. Puri, and s. Prakash, "Performance of plasma sprayed nanostructured and conventional coatings," vol. 44, pp. 56–62, 01 2008.

[130] G. Kaushal, H. Singh, and S. Prakash, "Surface engineering, by detonation-gun spray coating, of 347h boiler steel to enhance its high temperature corrosion resistance," *Materials at High Temperatures*, vol. 28, no. 1, pp. 1–11, 2011. [Online]. Available: https://doi.org/10.3184/096034011X12960473417949

[131] G. Sundararajan, D. S. Rao, G. Sivakumar, and S. V. Joshi, *Detonation Spray Coatings*. Boston, MA: Springer US, 2013, pp. 736–742. [Online]. Available: https://doi.org/10.1007/978-0-387-92897-5_704

[132] W. Möller and F. Besenbacher, "A note on the 3he + d nuclear-reaction cross section," *Nuclear Instruments and Methods*, vol. 168, no. 1, pp. 111 – 114, 1980. [Online]. Available: http://www.sciencedirect.com/science/article/pii/0029554X80912392

[133] A. Gurbich, "Sigmacalc recent development and present status of the evaluated cross-sections for iba," *Nuclear Instruments and Methods in Physics Research Section B: Beam Interactions with Materials and Atoms*, vol. 371, pp. 27 – 32, 2016, the 22nd International Conference on Ion Beam Analysis (IBA 2015). [Online]. Available: http://www.sciencedirect.com/science/article/pii/S0168583X15008940

[134] N. P. Barradas, C. Jeynes, and R. P. Webb, "Simulated annealing analysis of rutherford backscattering data," *Applied Physics Letters*, vol. 71, no. 2, pp. 291–293, 1997. [Online]. Available: https://doi.org/10.1063/1.119524

[135] Y. Acar, A. Akay, S. Beser, A. Canbay, H. Karadeniz, U. Kaya, B. Oner, and S. Sultansoy, "Future circular collider based lepton–hadron and photon–hadron colliders: Luminosity and physics," *Nuclear Instruments and Methods in Physics Research Section A: Accelerators, Spectrometers, Detectors and Associated Equipment*, vol. 871, pp. 47 – 53, 2017. [Online]. Available: http://www.sciencedirect.com/science/article/pii/S0168900217307866

[136] Y. Alexahin, C. M. Ankenbrandt, D. B. Cline, A. Conway, M. A. Cummings, V. Di Benedetto, E. Eichten, J.-P. Delahaye, C. Gatto, B. Grinstein *et al.*, "The case for a muon collider higgs factory," *arXiv preprint arXiv:1307.6129*, 2013.

[137] M. Antonelli, M. Boscolo, R. D. Nardo, and P. Raimondi, "Novel proposal for a low emittance muon beam using positron beam on target," *Nuclear Instruments and Methods in Physics Research Section A: Accelerators, Spectrometers, Detectors and Associated Equipment*, vol. 807, pp. 101 – 107, 2016. [Online]. Available: http://www.sciencedirect.com/science/article/pii/S0168900215013364

[138] M. Antonelli, E. Bagli, M. Biagini, M. Boscolo, G. Cavoto, P. Raimondi, and A. Variola, "Very Low Emittance Muon Beam using Positron Beam on Target," in *Proceedings, 7th International Particle Accelerator Conference (IPAC 2016): Busan, Korea, May 8-13, 2016*, 2016, p. TUPMY001. [Online]. Available: http://accelconf.web.cern.ch/AccelConf/ipac2016/papers/tupmy001.pdf

[139] F. Berends and G. Komen, "Soft and hard photon corrections for μ-pair production and bhabha scattering in the presence of a resonance," *Nuclear Physics B*, vol. 115, no. 1, pp. 114 – 140, 1976. [Online]. Available: http://www.sciencedirect.com/science/article/pii/0550321376902807

[140] W. Beenakker, F. Berends, and S. van der Marck, "Small-angle bhabha scattering," *Nuclear Physics B*, vol. 355, no. 2, pp. 281 – 294, 1991. [Online]. Available: http://www.sciencedirect.com/science/article/pii/055032139190114D

[141] R. Brandelik, W. Braunschweig, K. Gather, F. Kirschfink, K. Lübelsmeyer, H.-U. Martyn, G. Peise, J. Rimkus, H. Sander, D. Schmitz, D. Trines, W. Wallraff, H. Boerner, H. Fischer, H. Hartmann, E. Hilger, W. Hillen, G. Knop, L. Köpke, H. Kolanoski, R. Wedemeyer, N. Wermes, M. Wollstadt, H. Burkhardt, S. Cooper, J. Franzke, D. Heyland, H. Hultschig, P. Joos, W. Koch, U. Kötz, H. Kowalski, A. Ladage, B. Löhr, D. Lüke, H. Lynch, P. Mättig, K. Mess, D. Notz, J. Pyrlik, D. Quarrie, R. Riethmüller, W. Schütte, P. Söding, G. Wolf, R. Fohrmann, H. Krasemann, P. Leu, E. Lohrmann, D. Pandoulas, G. Poelz, O. Römer, P. Schmüser, B. Wiik, I. Al-Agil, R. Beuselinck, D. Binnie, A. Campbell, P. Dornan, D. Garbutt, T. Jones, W. Jones, S. Lloyd, J. Sedgbeer, K. Bell, M. Bowler, I. Brock, R. Cashmore, R. Carnegie, P. Clarke, R. Devenish, P. Grossmann, J. Illingworth,

M. Ogg, G. Salmon, J. Thomas, T. Wyatt, C. Youngman, B. Foster, J. Hart, J. Harvey, J. Proudfoot, D. Saxon, P. Woodworth, M. Holder, E. Duchovni, Y. Eisenberg, U. Karshon, G. Mikenberg, D. Revel, E. Ronat, A. Shapira, T. Barklow, T. Meyer, G. Rudolph, E. Wicklund, S. L. Wu, and G. Zobernig, "Electroweak coupling constants in the leptonic reactions e+e− -> e+e− and e+e− -> μ+μ− and search for scalar leptons," *Physics Letters B*, vol. 117, no. 5, pp. 365 – 371, 1982. [Online]. Available: http://www.sciencedirect.com/science/article/pii/0370269382907377

[142] S. Agostinelli, J. Allison, K. Amako, J. Apostolakis, H. Araujo, P. Arce, M. Asai, D. Axen, S. Banerjee, G. Barrand, F. Behner, L. Bellagamba, J. Boudreau, L. Broglia, A. Brunengo, H. Burkhardt, S. Chauvie, J. Chuma, R. Chytracek, G. Cooperman, G. Cosmo, P. Degtyarenko, A. Dell'Acqua, G. Depaola, D. Dietrich, R. Enami, A. Feliciello, C. Ferguson, H. Fesefeldt, G. Folger, F. Foppiano, A. Forti, S. Garelli, S. Giani, R. Giannitrapani, D. Gibin, J. G. Cadenas, I. González, G. G. Abril, G. Greeniaus, W. Greiner, V. Grichine, A. Grossheim, S. Guatelli, P. Gumplinger, R. Hamatsu, K. Hashimoto, H. Hasui, A. Heikkinen, A. Howard, V. Ivanchenko, A. Johnson, F. Jones, J. Kallenbach, N. Kanaya, M. Kawabata, Y. Kawabata, M. Kawaguti, S. Kelner, P. Kent, A. Kimura, T. Kodama, R. Kokoulin, M. Kossov, H. Kurashige, E. Lamanna, T. Lampén, V. Lara, V. Lefebure, F. Lei, M. Liendl, W. Lockman, F. Longo, S. Magni, M. Maire, E. Medernach, K. Minamimoto, P. M. de Freitas, Y. Morita, K. Murakami, M. Nagamatu, R. Nartallo, P. Nieminen, T. Nishimura, K. Ohtsubo, M. Okamura, S. O'Neale, Y. Oohata, K. Paech, J. Perl, A. Pfeiffer, M. Pia, F. Ranjard, A. Rybin, S. Sadilov, E. D. Salvo, G. Santin, T. Sasaki, N. Savvas, Y. Sawada, S. Scherer, S. Sei, V. Sirotenko, D. Smith, N. Starkov, H. Stoecker, J. Sulkimo, M. Takahata, S. Tanaka, E. Tcherniaev, E. S. Tehrani, M. Tropeano, P. Truscott, H. Uno, L. Urban, P. Urban, M. Verderi, A. Walkden, W. Wander, H. Weber, J. Wellisch, T. Wenaus, D. Williams, D. Wright, T. Yamada, H. Yoshida, and D. Zschiesche, "Geant4—a simulation toolkit," *Nuclear Instruments and Methods in Physics Research Section A: Accelerators, Spectrometers, Detectors and Associated Equipment*, vol. 506, no. 3, pp. 250 – 303, 2003. [Online]. Available: http://www.sciencedirect.com/science/article/pii/S0168900203013688

[143] J. Allison, K. Amako, J. Apostolakis, H. Araujo, P. A. Dubois, M. Asai, G. Barrand, R. Capra, S. Chauvie, R. Chytracek, G. A. P. Cirrone, G. Cooperman, G. Cosmo, G. Cuttone, G. G. Daquino, M. Donszelmann, M. Dressel, G. Folger, F. Foppiano,

J. Generowicz, V. Grichine, S. Guatelli, P. Gumplinger, A. Heikkinen, I. Hrivnacova, A. Howard, S. Incerti, V. Ivanchenko, T. Johnson, F. Jones, T. Koi, R. Kokoulin, M. Kossov, H. Kurashige, V. Lara, S. Larsson, F. Lei, O. Link, F. Longo, M. Maire, A. Mantero, B. Mascialino, I. McLaren, P. M. Lorenzo, K. Minamimoto, K. Murakami, P. Nieminen, L. Pandola, S. Parlati, L. Peralta, J. Perl, A. Pfeiffer, M. G. Pia, A. Ribon, P. Rodrigues, G. Russo, S. Sadilov, G. Santin, T. Sasaki, D. Smith, N. Starkov, S. Tanaka, E. Tcherniaev, B. Tome, A. Trindade, P. Truscott, L. Urban, M. Verderi, A. Walkden, J. P. Wellisch, D. C. Williams, D. Wright, and H. Yoshida, "Geant4 developments and applications," *IEEE Transactions on Nuclear Science*, vol. 53, no. 1, pp. 270–278, Feb 2006.

[144] J. Allison, K. Amako, J. Apostolakis, P. Arce, M. Asai, T. Aso, E. Bagli, A. Bagulya, S. Banerjee, G. Barrand, B. Beck, A. Bogdanov, D. Brandt, J. Brown, H. Burkhardt, P. Canal, D. Cano-Ott, S. Chauvie, K. Cho, G. Cirrone, G. Cooperman, M. Cortés-Giraldo, G. Cosmo, G. Cuttone, G. Depaola, L. Desorgher, X. Dong, A. Dotti, V. Elvira, G. Folger, Z. Francis, A. Galoyan, L. Garnier, M. Gayer, K. Genser, V. Grichine, S. Guatelli, P. Guèye, P. Gumplinger, A. Howard, I. Hřivnáčová, S. Hwang, S. Incerti, A. Ivanchenko, V. Ivanchenko, F. Jones, S. Jun, P. Kaitaniemi, N. Karakatsanis, M. Karamitros, M. Kelsey, A. Kimura, T. Koi, H. Kurashige, A. Lechner, S. Lee, F. Longo, M. Maire, D. Mancusi, A. Mantero, E. Mendoza, B. Morgan, K. Murakami, T. Nikitina, L. Pandola, P. Paprocki, J. Perl, I. Petrović, M. Pia, W. Pokorski, J. Quesada, M. Raine, M. Reis, A. Ribon, A. R. Fira, F. Romano, G. Russo, G. Santin, T. Sasaki, D. Sawkey, J. Shin, I. Strakovsky, A. Taborda, S. Tanaka, B. Tomé, T. Toshito, H. Tran, P. Truscott, L. Urban, V. Uzhinsky, J. Verbeke, M. Verderi, B. Wendt, H. Wenzel, D. Wright, D. Wright, T. Yamashita, J. Yarba, and H. Yoshida, "Recent developments in geant4," *Nuclear Instruments and Methods in Physics Research Section A: Accelerators, Spectrometers, Detectors and Associated Equipment*, vol. 835, pp. 186 – 225, 2016. [Online]. Available: http://www.sciencedirect.com/science/article/pii/S0168900216306957

[145] F. Nitti, A. Ibarra, M. Ida, P. Favuzza, T. Furukawa, F. Groeschel, R. Heidinger, T. Kanemura, J. Knaster, H. Kondo, G. Micchiche, M. Sugimoto, and E. Wakai, "The design status of the liquid lithium target facility of ifmif at the end of the engineering design activities," *Fusion Engineering and Design*, vol. 100, pp. 425 – 430, 2015. [Online]. Available: http://www.sciencedirect.com/science/article/pii/S0920379615302374

[146] H. Nakamura, P. Agostini, K. Ara, S. Cevolani, T. Chida, M. Ciotti, S. Fukada, K. Furuya, P. Garin, A. Gessii, D. Guisti, V. Heinzel, H. Horiike, M. Ida, S. Jitsukawa, T. Kanemura, H. Kondo, Y. Kukita, R. Lösser, H. Matsui, G. Micciche, M. Miyashita, T. Muroga, B. Riccardi, S. Simakov, R. Stieglitz, M. Sugimoto, A. Suzuki, S. Tanaka, T. Terai, J. Yagi, E. Yoshida, and E. Wakai, "Latest design of liquid lithium target in ifmif," *Fusion Engineering and Design*, vol. 83, no. 7, pp. 1007 – 1014, 2008, proceedings of the Eight International Symposium of Fusion Nuclear Technology. [Online]. Available: http://www.sciencedirect.com/science/article/pii/S0920379608001622

[147] S. Halfon, A. Arenshtam, D. Kijel, M. Paul, D. Berkovits, I. Eliyahu, G. Feinberg, M. Friedman, N. Hazenshprung, I. Mardor, A. Nagler, G. Shimel, M. Tessler, and I. Silverman, "High-power liquid-lithium jet target for neutron production," *Review of Scientific Instruments*, vol. 84, no. 12, p. 123507, 2013. [Online]. Available: https://doi.org/10.1063/1.4847158

[148] G. Feinberg, M. Paul, A. Arenshtam, D. Berkovits, D. Kijel, A. Nagler, and I. Silverman, "Lilit - a liquid-lithium target as an intense neutron source for nuclear astrophysics at the soreq applied research accelerator facility," *Nuclear Physics A*, vol. 827, no. 1, pp. 590c – 592c, 2009, pANIC08. [Online]. Available: http://www.sciencedirect.com/science/article/pii/S0375947409003960

# Conferences and publications

## Conferences

PSI XXIII Princeton USA – June 2018
23rd PSI – International Conference on Plasma Surface Interactions in Controlled Fusion Devices
Oral contribution: *Review of the experiments performed with liquid lithium and tin limiters in FTU*

19th ICPP Vancouver CA – June 2018
19th 19th International Congress on Plasma Physics
Invited oral contribution: *Experiments with liquid metals in the Frascati Tokamak Upgrade (FTU)*

7th HPTW East Lansing USA – June 2018
7th High Power Targetry Workshop
Poster: *Preliminary study of high power density target for the LEMMA proposal*

Seminar CNR Milan IT – Nov. 2017
Seminar at CNR-IFP-Milan on the liquid metals application in fusion relevant plasmas
Seminar title: *Brief review of the experiments performed with the liquid lithium and liquid tin limiters in FTU*

19th IOS-TG Frascati IT – Oct. 2017
19th International Tokamak Physics Activity (ITPA) -Integrated Operation Scenarios (IOS) Topical Group (TG)
Oral contribution: *FTU operations with liquid Li and Sn limiters*

ISLA-5 Moscow RU – Sept. 2017
5th International Symposium on Liquid metals Applications for fusion (ISLA-5)
Oral contribution: *Updated comparison between liquid lithium and liquid tin limiters in Frascati Tokamak Upgrade*

44th EPS Belfast UK – June 2017
44th European Physical Society Conference on Plasma Physics
Oral contribution: *Comparison between liquid lithium and liquid tin limiters in FTU*

PSI XXII Rome IT – June 2016
22nd PSI – International Conference on Plasma Surface Interactions in Controlled Fusion Devices
Poster: *Modeling of lithium vapour cloud observed on FTU*

ISLA-4 Granada ES – Sept. 2015
4th International Symposium on Liquid metals Applications for fusion (ISLA-4)
Oral contribution: *FTU Cooled Liquid Lithium Upgrade*

Publication list

1. S. Peruzzo, M. Bernardi, G. Berton, R. Cavazzana, S. Dal Bello, M. Dalla Palma, D. Marcuzzi, L. Grando, M. Iafrati, D. Rizzetto, A. Rizzolo, F. Rossetto, M. Siragusa, M. Spolaore, L. Trevisan, M. Utili, M. Zuin
   Technological challenges for the design of the RFX-mod2 experiment
   *Submitted to Fusion Engineering and Design*

2. F. Alladio, P. Micozzi, A. Mancuso, V. Zanza, G.M. Apruzzese, L. Boncagni, O. D'Arcangelo, E. Giovannozzi, L.A. Grosso, M. Iafrati, A. Lampasi, V. Piergotti, G. Rocchi, A. Sibio, B. Tilia, O. Tudisco, P. Buratti, F. Andreoli, V. Lazic, S. Magagnino, M. Pillon, S. Roccella, F. Crescenzi, A. Tuccillo, B. Tirozzi, G. Galatola Teka, F. Giammanco, P. Marsili, and D. Giulietti
   Proto-sphera, without toroidal magnets, produces and confines plasma tori inside magnetostatic fields
   *Submitted to Nature Physics*, 2018.

3. M.L. Apicella, M. Iafrati, G. Mazzitelli, R. Zagrski, G. Apruzzese, and C. Corradino
   Proto-sphera, without toroidal magnets, produces and confines plasma tori inside magnetostatic fields
   *Proceedings - International Conference on Plasma Surface Interactions in Controlled Fusion Devices*, 2018.

4. G.M. Apruzzese, M.L. Apicella, M. Iafrati, G. Mazzitelli, L. Gabellieri, J.P.S. Loureiro, A. Romano, and FTU Team
   First spectroscopic results with tin limiter on ftu plasma
   *Plasma Physics Reports*, 44(7):636–640, 2018.

5. F. Bombarda, L. Carraro, L. Gabellieri, A. Romano, B. Zaniol, B. Tilia, M.L. Apicella, G. Apruzzese, M. Iafrati, G. Mazzitelli, M.E. Puiatti, Valisa M., and the FTU team
   High resolution euv spectroscopy on ftu with tin liquid limiter
   *Special issue of Plasma Physics and Controlled Fusion, EPS - 45th Conference on Plasma Physics*, 2018.

6. A. Cremona, E. Vassallo, E. Alves, F. Causa, G. Giacomi, G. Gervasini, G. Granucci, M. Iafrati, G. Maddaluno, R. Mateus, D. Minelli, V. Mellera, A. Nardone, M. Pedroni, D. Ricci, D. Rigato, N. Rispoli, and A. Uccello
   Deuterium retention and erosion in liquid sn samples exposed to d2 and ar plasmas in gym device
   *Proceedings - PSI2018*, 2018.

7. M. Iafrati, M.L. Apicella, L. Boncagni, I. Lyublinski, G. Mazzitelli, and A. Vertkov
   Ftu cooled liquid lithium upgrade
   *Fusion Engineering and Design*, 117:1–8, 2017.

8. F. Alladio, P. Micozzi, G.M. Apruzzese, L. Boncagni, O. D'Arcangelo, E. Giovannozzi, L.A. Grosso, M. Iafrati, A. Lampasi, G. Maffia, A. Mancuso, V. Piergotti, G. Rocchi, A. Sibio, B. Tilia, O. Tudisco, and V. Zanza
The proto-sphera experiment, an innovative confinement scheme for fusion
*Proceedings - 19th International Spherical Torus Workshop (ISTW 2017)*, 09, 2017.

9. A. Vertkov, I. Lyublinski, M. Zharkov, A. Berlov, S. Mirnov, A. Dedov, A. Zakharenkov, M. Iafrati, and G. Mazzitelli.
The concept of lithium based plasma facing elements for steady state fusion tokamak-reactor and its experimental validation
*Proceedings - IAEA 2017*, 2017.

10. A. Vertkov, I. Lyublinski, M. Zharkov, G. Mazzitelli, M.L. Apicella, and M. Iafrati
Liquid tin limiter for ftu tokamak
*Fusion Engineering and Design*, 117:130–134, 2017.

11. G. Pucella, E. Alessi, L. Amicucci, B. Angelini, M.L. Apicella, G. Apruzzese, G. Artaserse, F. Belli, W. Bin, L. Boncagni, A. Botrugno, S. Briguglio, A. Bruschi, P. Buratti, G. Calabr, M. Cappelli, A. Cardinali, C. Castaldo, F. Causa, S. Ceccuzzi, C. Centioli, R. Cesario, C. Cianfarani, G. Claps, V. Cocilovo, F. Cordella, F. Crisanti, O. D'Arcangelo, M. De Angeli, C. Di Troia, B. Esposito, D. Farina, L. Figini, G. Fogaccia, D. Frigione, V. Fusco, L. Gabellieri, S. Garavaglia, E. Giovannozzi, G. Granucci, M. Iafrati, F. Iannone, M. Lontano, G. Maddaluno, S. Magagnino, M. Marinucci, D. Marocco, G. Mazzitelli, C. Mazzotta, A. Milovanov, D. Minelli, F.C. Mirizzi, A. Moro, S. Nowak, D. Pacella, L. Panaccione, M. Panella, V. Pericoli-Ridolfini, A. Pizzuto, S. Podda, G. Ramogida, G. Ravera, D. Ricci, A. Romano, C. Sozzi, A.A. Tuccillo, O. Tudisco, B. Viola, V. Vitale, G. Vlad, M. Zerbini, F. Zonca, M. Aquilini, P. Cefali, E. Di Ferdinando, S. Di Giovenale, G. Giacomi, A. Grosso, V. Mellera, M. Mezzacappa, A. Pensa, P. Petrolini, V. Piergotti, B. Raspante, G. Rocchi, A. Sibio, B. Tilia, R. Tulli, M. Vellucci, D. Zannetti, I. Bogdanovic-Radovic, D. Carnevale, A. Casolari, M. Ciotti, C. Conti, P.P. Dinca, V. Dolci, C. Galperti, M. Gospodarczyk, G. Grosso, L. Lubiako, M. Lungu, J.R. Martin-Solis, C. Meineri, F. Murtas, A. Nardone, F.P. Orsitto, E. Perelli Cippo, Z. Popovic, D. Ripamonti, A. Simonetto, and U. Tartar
Overview of the ftu results.
*Nuclear Fusion*, 57(10), 2017.

12. G. Ramogida, G. Calabro, F. Crisanti, M.L. Apicella, G. Artaserse, W. Bin, L. Boncagni, G. Brolatti, P. Buratti, M. Carlini, D. Carnevale, P. Costa, F. Crescenzi, A. Cucchiaro, D. Frigione, S. Garavaglia, M. Gospodarcyk, G. Granucci, M. Iafrati, A. Lampasi, G. Maddaluno, G. Maffia, F. Maviglia, G. Mazzitelli, R. Mazzuca, M. Moneti, A. Moro, G. Pucella, M. Reale, S. Roccella, F. Starace, A.A. Tuccillo, A. Vertkov, and P. Zito
D-shaped configurations in ftu for testing liquid lithium limiter: Preliminary studies

and experiments.
*Nuclear Materials and Energy*, 12:1082–1087, 2017.

13. F. Collamati, M. Antonelli, M. Boscolo, M. Biagini, O. Blanco-Garcia, A. Variola, A. Bacci, S. Liuzzo, P. Raimondi, I. Chaikovska, R. Cheab, M. Iafrati, L. Keller, and P. Sievers
Studies of a scheme for low emittance muon beam production from positrons on target
*PoS, EPS - HEP2017*, 531:157–162, 2017.

14. M. De Angeli, G. Maddaluno, P. Tolias, S. Ratynskaia, C. Castaldo, M.L. Apicella, G. Gervasini, F. Ghezzi, E. Giovannozzi, G. Granucci, G. Grosso, M. Iafrati, D. Iraji, E. Lazzaro, and Uccello A.
Pre-plasma mobilization of magnetic dust and possible interference with tokamak operations
*Proceedings - 16th International Conference on Plasma-Facing Materials and Components for Fusion Applications*, 2017.

15. P. Micozzi, F. Alladio, G.M. Apruzzese, L.Boncagni , Ocleto D'Arcangelo, Edmondo Giovannozzi, L.A. Grosso, M. Iafrati, A. Lampasi, G. Maffia, A. Mancuso, V. Piergotti, G. Rocchi, A. Sibio, B. Tilia, O. Tudisco, and V. Zanza
Obtainment of the phase1 full performances in proto-sphera and future perspectives of the experiment.
*Proceedings - EPR 2017 - The Exploratory Plasma and Fusion Research Workshop, Vancouver*, 117:130–134, 08, 2017.

16. M. Iafrati, G. Mazzitelli, M.L. Apicella, L. Boncagni, G.M. Apruzzese, I. Lyublinski, A. Berlov, A. Vertkov, G. Maddaluno, F. Crescenzi, A. Mancini, and FTU Team
Comparison between liquid lithium and liquid tin limiters in ftu
*Proceedings 44th EPS Conference on Plasma Physics*, O5.132, pages 1–4, 2017.

# Acknowledgments

My special thanks to the people without whom this work would have not been possible. First of all, I would like to thanks the world citizens, real employers of each researcher, without which it would not make sense to get busy every day attempting to leave the world a little better than we found it. I'm also grateful to wake up happy every morning having the possibility to play such an amazing discovery game.

Il primo ringraziamento è per Giuseppe Mazzitelli, mio mentore nel mondo della fisica del plasma, oltre che relatore delle mie tesi. A lui devo infatti tutta la mia riconoscenza per avermi fatto scoprire il Tokamak ed il mondo della fusione nucleare molti anni fa, un sera di settembre durante la settimana europea della ricerca. Durante questi anni sei stato un punto di riferimento sul quale ho sempre potuto contate, grazie Giuseppe.

Grazie Luca Boncagni, amico e collega, per la tua presenza, per i molteplici strumenti ed ammennicoli che mi hai dato ed insegnato ad utilizzare, per aver creduto nei progetti più strani condividendone risultati e fallimenti, per tutte le birre di lavoro spese a parlare di FTU.

Un ringraziamento speciale ai coniugi Maria Laura Apicella e Vincenzo Pericoli Ridolfini; a Maria Laura, colonna portante del team Metalli Liquidi di Frascati sin dagli albori, per le sue attente revisioni e le sue puntali parole di conforto; a Vincenzo per avermi introdotto allo sconfinato mondo delle sonde elettrostatiche, per tutti i suoi racconti – memoria storica dei laboratori di Frascati.

Un grazie ad Onofrio Tudisco per l'immancabile impegno e supporto con la sperimentazione, con il microndе e con la chimica e fisica in cucina. Grazie per le piacevolissime passeggiate in montagna tra paesaggi mozzafiato e lezioni di fisica del plasma. Un grazie ad Afra Romano e Simone Magagnino per l'aiuto giorno dopo giorno in sala controllo, per aver potuto condividere piacevolissimi momenti in compagnia dei loro meravigliosi bambini Alice e Filippo e per i disegni che lo testimoniano.

Un ringraziamento a Cristina Centioli, Oriana Scopetti, Lori Gabellieri per la loro preziosa disponibilità, aiuto e competenza. Un grazie speciale a tutti i tecnici ognuno dei quali mi ha insegnato qualcosa di speciale durante questo percorso, gli operatori di FTU, in particolare

Enzo Di Ferdinando, per le lezioni sugli impianti da vuoto, per tutte le dritte in campo motociclistico e per aver pazientamene condiviso gli spazi in sala controllo e sala sperimentale ogni giorno con gli ingombri lasciati dal sottoscritto. Grazie ai tecnici delle diagnostiche, in particolare Benedetto Tilia ed Andrea Grosso, per avermi insegnato a non avere fretta, per avermi fatto comprendere quanto la pazienza nel progettare e realizzare gli esperimenti sia fondamentale per la loro riuscita, grazie anche a Valerio Piergotti e Giuliano Rocchi. Un ulteriore ringraziamento a coloro senza i quali il Laboratorio Metallo Liquido non esisterebbe ovvero Valerio Cerri per la sua inestimabile esperienza nella progettazione di forni da vuoto, a Luigi Verdini per la sua competenza e per la realizzazione del sistema di controllo del forno, a Stefano Rueca, Marco Vellucci e Mario Mezzacappa per le centinaia di fili collegati insieme ed i puntuali caffè delle cinque.

Ferruccio Maierna, ti ringrazio di cuore per il tuo aiuto quotidiano, la tua officina è sempre stata aperta insieme alla tua disponibilità ed il tuo entusiasmo, non ti sei mai tirato indietro, non importava se bisognava riparare un riscaldatore da vuoto con il vetro oppure aiutare gli studenti del liceo per costruire la camera a nebbia, anche nei momenti più tristi sei stato presente con la tua maestria e la tua arte ad insegnarmi che tutto si più risaldare.

Un ringraziamento a Franco Alladio e Paolo Micozzi per avermi dato la possibilità di assistere alle operazioni di ProtoSphera, condividendo le emozioni della sala controllo.

Switch now back to English, thank you Alexey Vertkov, you introduced me in the use of liquid metals, you have been with me the first time I handled the liquid limiter, you have patiently answered all my questions and doubts and I am very grateful for this. Kind thanks to Alexander Berlov for him precious help during the tin limiter installation.

Many thanks to all the friend and the colleagues I met during these years and in particular to Zana, Peter, Stein, Oscar, with each of you I had the opportunity to spend nice moments, hiking the Apennines, enjoying a beer at sunset or in a pub in Princeton, walking near the Kremlin or sharing a good pasta in a room in Geneva, and from each of you I learned a lot.

Thanks to my Ph.D. Italian colleagues Adriano Mele, Antonio Castaldo, Giuseppe Galatola Teka, Matteo Vallar, Daniele Maggio, grazie ragazzi per questi bellissimi tre anni, per aver condiviso i nostri interessi (lavorativi e non) e per le fantastiche serate passate insieme in giro per l'Europa.

Now special thanks to the people I met during the amazing time spent in Lisbon. First of all, thank you João Simões Loureiro Pedro, we met in a sunny morning in Frascati during the first year of my Ph.D., we manage to share the office first in Italy and then in Lisbon. We share together a lot of adventure around the world and I have so good memories of that

since our first ISLA conference. Thank your for you support, for your help in Lisbon and for introducing me to the craft beer producing world.

Many thanks to Horacio Fernandes, for the amazing Kite lessons. Thank you, Rui Gomes, for your kind guidance during my time in Lisbon. Thanks to Bernardo for motorcycle ridings. Infinite thanks to Humberto Figueiredo, you made me discover climbing and more you showed me such amazing places in Portugal. Many thanks to Gonçalo, Cláudia, Duarte, Pedro, Sarah, Andrè and all the people I have met and collected fantastic memories in Lisbon. Obrigado meus amigos.

Un ringraziamento ai colleghi e le persone con le quali ho avuto la fortuna di lavorare godendo della bellezza unica del bacino del Brasimone, tra tutti Marco Utili per la sua disponibilità e voglia di mettersi in gioco, Alessandro Del Nevo per l'inestimabile esperienza con i metalli liquidi. Un grazie a Francesco Marra e Giovanni Pulci per aver giocato insieme ad un'inaspettata quanto fruttuosa avventura, a Roberto Cavazzana, Matteo Zuin e Mauro Della Palma per aver condiviso letteralmente il bello ed il cattivo tempo inseme in uno dei più strani compleanni che potesse mai capitarmi.

Un ringraziamento speciale alle persone che mi han fatto sentire a Milano come se fossi a casa, a Gustavo Granucci sempre presente per ogni domanda sulle operazioni di FTU, a Daria Ricci per avermi accompagnato nelle misure con GyM, ad Andrea Uccello ed Espedito Vassallo per loro prezioso aiuto e supporto ed ovviamente un ringraziamento speciale a Vittoria Mellera, tra una sonda di Langmuir ed un cioccolatino, per la sua immancabile professionalità. Un grandissimo ringraziamento lo devo a Mario Antonelli ed a tutto il team di LEMMA per l'opportunità di aver lavorato a questo fantastico ed estremamente stimolante progetto. Un ringraziamento anche a tutti le persone con le quali ho avuto la fortuna di condividere il tempo, e le notti, in sala di controllo al CERN, imparando da ognuno di voi. Grazie a Marco Calviani per avermi dato l'occasione di imparare così tanto confrontandomi con una realtà per me nuova quanto emozionante.

Ed ora un ringraziamento particolare al liceo G. Vailati di Genzano ed ai professori con i quali in questi anni abbiamo avuto modo di costruire un progetto e vederlo crescere, insieme agli studenti che ne hanno fatto parte. Grazie Massimiliano Giacometti, Marco Dreucci, Silvia Miozzi, Francesca Fabrizi, Paola Petrillo.

Un grazie alla mia famiglia per avermi supportato e sopportato, ai miei genitori, a mio fratello Raffaele e mia sorella Cristina. Ai miei amici, sempre presenti in questi anni, che mi hanno aiutato nelle difficoltà e gioito insieme nei momenti felici. Grazie Federico, Alessandro, Marco, Cristina, Allison, Luca, Marta, Claudio, Stefano, Giulia, Alice, Matteo.

Nonostante la speranza di aver ringraziato tutti, sono sicuro di non averlo fatto, quindi, chiunque tu sia a leggere e non trovarti in queste righe sappi che sei stato nei miei pensieri e lo sarai nuovamente appena ricorderò di aver dimenticato di inserirti tra queste righe.

*A poet once said, 'The whole universe is in a glass of wine.' We will probably never know in what sense he meant it, for poets do not write to be understood. But it is true that if we look at a glass of wine closely enough we see the entire universe. There are the things of physics: the twisting liquid which evaporates depending on the wind and weather, the reflection in the glass; and our imagination adds atoms. The glass is a distillation of the earth's rocks, and in its composition we see the secrets of the universe's age, and the evolution of stars. What strange array of chemicals are in the wine? How did they come to be? There are the ferments, the enzymes, the substrates, and the products. There in wine is found the great generalization; all life is fermentation. Nobody can discover the chemistry of wine without discovering, as did Louis Pasteur, the cause of much disease. How vivid is the claret, pressing its existence into the consciousness that watches it! If our small minds, for some convenience, divide this glass of wine, this universe, into parts – physics, biology, geology, astronomy, psychology, and so on – remember that nature does not know it! So let us put it all back together, not forgetting ultimately what it is for. Let it give us one more final pleasure; drink it and forget it all!*

Richard Feynman, Six Easy Pieces